



HAL
open science

Light-induced flows and pattern formation in suspensions of phototactic microalgae

Aina Ramamonjy

► **To cite this version:**

Aina Ramamonjy. Light-induced flows and pattern formation in suspensions of phototactic microalgae. Other [cond-mat.other]. Université Paris Cité, 2022. English. NNT : 2022UNIP7022 . tel-04127226

HAL Id: tel-04127226

<https://theses.hal.science/tel-04127226>

Submitted on 13 Jun 2023

HAL is a multi-disciplinary open access archive for the deposit and dissemination of scientific research documents, whether they are published or not. The documents may come from teaching and research institutions in France or abroad, or from public or private research centers.

L'archive ouverte pluridisciplinaire **HAL**, est destinée au dépôt et à la diffusion de documents scientifiques de niveau recherche, publiés ou non, émanant des établissements d'enseignement et de recherche français ou étrangers, des laboratoires publics ou privés.

Université de Paris

École doctorale Physique en Île-de-France 564

Laboratoire Matière et Systèmes Complexes

Light-induced flows and pattern formation in suspensions of phototactic microalgae

Par Aina Ramamonjy

Thèse de doctorat de physique

Dirigée par Philippe Brunet

Présentée et soutenue publiquement à Paris le 14 février 2022

Devant un jury composé de :

Rapportrice	Cécile Cottin-Bizonne, Directrice de recherche, Université Lyon 1
Rapporteur	Harold Auradou, Directeur de recherche, Université Paris-Saclay, <i>président</i>
Examinatrice	Salima Rafai, Chargée de recherche, Université Grenoble Alpes
Examineur	Christophe Goupil, Professeur des universités, Université de Paris
Directeur de thèse	Philippe Brunet, Directeur de recherche, Université de Paris
Co-encadrant	Julien Dervaux, Chargé de recherche, Université de Paris, <i>membre invité</i>



Abstract

The mechanism by which living organisms seek optimal light conditions, phototaxis, is a fundamental process for motile photosynthetic micro-organisms that rely on light to survive. Phototaxis is thus ultimately involved in virtually all natural processes and applications involving light-harvesting microbes, from bloom formation in aquatic environments to the diel vertical migration of phytoplankton, through the production of high-value chemical compounds in photobioreactors. At the crossing between active matter and complex fluid physics, this thesis aims at understanding the collective response, at the scale of a population, of the model photosynthetic micro-algae *Chlamydomonas reinhardtii* to complex space and time-dependent light fields.

In a first step, the phototactic response of these micro-organisms in dilute suspensions is characterized and is found to be highly sensitive and nonlinear. Next, we show that phototaxis can be exploited to generate self-sustained macroscopic flows in moderately concentrated, yet shallow, suspensions of *Chlamydomonas reinhardtii* using specific illumination patterns. These flows originate from the light-controlled local accumulation of the micro-algae which are negatively buoyant. This in turn creates density gradients which drive fluid flows, an hydrodynamic instability specific to active suspensions and known as bioconvection. In this regime, we find that the algal population self-organizes as a result of the coupling between self-generated flows and nonlinear phototaxis and it undergoes multiple symmetry breaking instabilities. These instabilities are also investigated theoretically using an asymptotic model of light-induced bioconvection.

Next, a fluorescence-based PIV setup is developed to allow for the direct quantification of bioconvective flows in a Hele-Shaw cell. The magnitude and structure of these flows are deciphered for the first time and contrasted with a classical model of bioconvection. In the last chapter of this thesis, we present a preliminary study on the effects of light-controlled bioconvection on the growth-rate of *Chlamydomonas reinhardtii* cultures, with in mind an application to photo-bioreactors.

Keywords phototaxis, bioconvection, microswimmers, active matter, suspensions



Résumé

Le mécanisme par lequel les organismes vivants recherchent des conditions de lumière optimales, la phototaxie, est un processus fondamental pour les micro-organismes photosynthétiques mobiles qui dépendent de la lumière pour survivre. La phototaxie est donc impliquée dans la quasi-totalité des processus naturels et des applications impliquant des microbes photosynthétiques, de la formation des efflorescences dans les environnements aquatiques à la migration verticale diurne du phytoplancton, en passant par la production de composés chimiques à haute valeur ajoutée dans les photo-bioréacteurs. Au croisement entre la matière active et la physique des fluides complexes, cette thèse vise à comprendre la réponse collective, à l'échelle d'une population, de la micro-algue photosynthétique modèle *Chlamydomonas reinhardtii* en présence de champs lumineux complexes dépendant de l'espace et du temps.

Dans un premier temps, la réponse phototactique de ces micro-organismes dans des suspensions diluées est caractérisée et s'avère être hautement sensible et non-linéaire. Ensuite, nous montrons que la phototaxie peut être exploitée pour générer des écoulements macroscopiques auto-entretenus dans des suspensions peu profondes de *Chlamydomonas reinhardtii* en utilisant des motifs d'illumination spécifiques et en augmentant l'intensité des effets collectifs. Ces écoulements proviennent de l'accumulation locale, contrôlée par la lumière, des micro-algues qui ont une flottabilité négative. Cette accumulation entraîne des gradients de densité qui déclenchent des écoulements. Cette instabilité hydrodynamique est spécifique aux suspensions actives et est connue sous le nom de bioconvection. Dans ce régime, nous constatons que la population d'algues s'auto-organise en raison du couplage entre les écoulements auto-générés et la réponse phototactique non-linéaire et qu'elle subit de multiples brisures de symétrie. Ces instabilités sont également étudiées théoriquement à l'aide d'un modèle asymptotique de bioconvection induite par la lumière.

Ensuite, une méthode de vélocimétrie par images de particules basée sur la fluorescence est développée pour permettre la quantification directe des écoulements de bioconvection dans une cellule de Hele-Shaw. L'amplitude et la structure de ces écoulements sont examinées pour la première fois et comparées à un modèle classique de bioconvection. Dans le dernier chapitre de cette thèse, nous présentons une étude préliminaire sur les effets de la bioconvection contrôlée par la lumière sur le taux de croissance des cultures de *Chlamydomonas reinhardtii*, avec pour objectif à long terme une application aux photo-bioréacteurs.

Mots-clés Phototaxie, bioconvection, micronageurs, matière active, suspensions

Remerciements

Je sais que je ne serais pas arrivé jusqu'ici tout seul et avant de rentrer dans mon manuscrit de thèse, je souhaiterais prendre le temps un certain nombre de personnes. Ce nombre est grand, j'oublierai peut-être de nommer certaines personnes et je les prie de m'excuser.

Merci Seigneur Je remercie Dieu, Père, Fils et Saint-Esprit, pour son amour pour moi chaque jour. Il n'y a que lui seul qui connaisse toutes les joies et les peines que j'ai traversées pendant cette aventure qu'est la thèse. Je prie que ce travail soit à sa gloire, à lui seul qui en connaît la vraie valeur.

Merci pour votre rôle aux différentes étapes de ma thèse

Je remercie Laurent Limat de m'avoir accueilli au laboratoire Matière et Systèmes Complexes de l'Université de Paris. Je remercie les directeurs successifs de l'école doctorale Physique en Île-de-France Jean-François Allemand et Frédéric Chevy ainsi que le directeur adjoint et l'assistante pour l'Université de Paris Philippe Lafarge et Monia Mestar.

Je tiens à remercier Salima Rifaï, Christophe Goupil, Cécile Cottin-Bizonne et Harold Auradou de m'avoir fait l'honneur de faire partie du jury de l'évaluation de ma thèse et pour leur intérêt porté à mon travail. Vos travaux sont pour moi des exemples de réflexion. Merci en particulier à Cécile Cottin-Bizonne et Harold Auradou qui ont accepté la lourde tâche d'être rapporteurs.

J'ai aussi eu la chance d'avoir Éric Clément et Adrian Daerr dans le comité de suivi de ma thèse. Merci pour vos réflexions et encouragements lors de nos réunions.

Je remercie François Heslot et Dario Vignoli pour leurs contributions significatives au projet "biomixing with light", respectivement dans la conception du dispositif expérimental et dans la mise en place des expériences.

Je remercie maintenant Julien Dervaux et Philippe Brunet qui m'ont encadré pendant ces années de doctorat à MSC. Vous m'avez inspiré de manière durable et je vous garderai comme exemples s'il m'arrive d'encadrer des étudiants. Julien, tu m'as beaucoup appris scientifiquement et dans la gestion de ma thèse. Tu as su me tirer vers l'avant et me réorienter aux bons moments. Ton enthousiasme et ta bonne humeur m'ont fait beaucoup de bien. Philippe, tu m'as appris à avoir une vision d'ensemble sur ma thèse. J'ai toujours aimé tes bonnes idées et aurais aimé pouvoir les mettre en oeuvre plus souvent.

J'ai apprécié ton calme et ta bienveillance. Votre disponibilité s'est particulièrement manifestée au moment de la rédaction de cette thèse et je vous en suis très reconnaissant.

Merci pour ces trois années aux laboratoires Je voudrais remercier les chercheurs permanents et les accompagnants à la recherche du laboratoire MSC pour leur accueil, notamment : Matthieu Roché, Christophe Coste, Michel Saint Jean, Florence Elias, Bérengère Abou, Julien Moukthar, Adrian Daerr, Chi-Tuong Pham, Alain Richert, Nathalie Luciani, Jean Hubert, Patrick Montastier, et Oune-Saysavanh Souramasing. Je remercie également les doctorants, post-doctorants ou stagiaires du laboratoire. En particulier, merci Rémy, Robin, Amandine, Quentin, Marie, Alicia, Dario, Chuanyu, David P., David M., Wei, Gueyu, Camille L., Jérémy, Thibaut. Merci à Camille G., Gabriel T., Alice et Alice, Irène et Paul pour l'organisation d'évènements pour les non-permanents. Enfin merci à Alice et Alice, Gabriel et Gabriel, Mathieu, Johann et Darius pour ces belles années passées ensemble, chères à mon coeur, et ce très beau séjour à la montagne.

Quelques enseignants, enseignants-chercheurs ou chercheurs m'ont beaucoup inspiré depuis ma jeunesse au collège Paul Bert de Cachan, au lycée et en CPGE à Lakanal, jusqu'au études supérieures à l'ESPCI et au doctorat. Je les remercie. Je voudrais citer Thomas Salez pour sa disponibilité pendant mon M2. Nos entretiens m'ont aidé à me diriger vers ma thèse avec Julien Dervaux et Philippe Brunet. Je remercie mes encadrantes et encadrants de stage qui m'ont formé et équipé pour le doctorat : Eloïse Chevallier et Amandine Cuenca au Laboratoire du Futur Solvay, Christian Kreis et Oliver Baümchen au Max-Planck Institute for Dynamics and Self-organization, André Estevez-Torres et Jean-Christophe Gallas au laboratoire Jean-Perrin.

“La vraie thèse c'est l'amitié”, (selon Berouke T). Je remercie le groupe d'amis d'enfance de Cachan qui ont eu du mal à suivre mes goûts successifs pour les mathématiques, la chimie et la physique mais qui m'ont soutenu. Merci en particulier à Robin et Charles, mes deux plus vieux amis ; et à Fabien A., Behrouz, Clément. Je remercie ensuite mes amis du lycée Lakanal. Merci Arthur, Rayane, Bruno, Elsa, Taman, Fabien K. Merci en particulier à l'Équipage : Jean-Côme, Berouke, Arnaud, Kévin, Robin, Sangsong et Baptiste, que du bonheur avec vous et merci pour votre soutien. Merci à mes amis et anciens camarades de l'ESPCI qui savent pour la plupart très bien ce qu'est une thèse. Merci particulièrement à Antoine, Bruno, Julia, Nassim, Julie, Murad, Constant, Raphaël.

Merci à la nouvelle famille que Jésus m'a donnée. Il s'agit de mes frères et soeurs chrétiens. Certains m'ont entouré de bienveillance depuis mon enfance, certains sont des amis proches. Je citerai “quelque personnes” de cette famille : Aser, Jonathan H., Adrien, Laurie, Daniel, Noémie, Naomi, Nathan D., Anne-Lise B., Laura et Jérémy,

Marie et Jonathan, Pierre-Alexandre, Lionel, Ary-Ela, Isabel, Michel, Anaïs, Aurélien, Marion D., Séverine, Pierre, Simon H., Aloysia, Daphné et Siméon, Anne-Gaëlle, Chloé, Estelle, Dalmace, Marie S., Marie et Nathan, Aimie, Cécile, Dylan et Laura, Anne-Lise C., Lauricia, Bénédicte, Thierry, Hermann, Sophie, Olivier M., Olivier F., Sarah-Line, Mathilde et Alban, Edwin, David, Marjorie, Caillou, Nicolas, Marion, Laetitia, Josh, Jasna, Sylvie et Raymond, Julien, Stéphane, Asido, Olivier et Marie-Cécile, Philippe et Anne, Florence et Marc, Pierre-Antoine et Marie-Edith, Edith, Sylvie et Malek, Arnold et Myriam, Armelle et Aloïse. À tous, merci pour ces doux moments passés ensemble et avec Dieu qui me renouvellent.

Merci à ma famille. Merci à mes cousins et cousines, à mes oncles et tantes et à mes grands-parents de m'avoir soutenu. Merci à mes frères Aro et Johary, vos chemins ressemblent au mien, en sont aussi très différents, et m'inspirent. Merci à mon papa et à ma maman : dès mon plus jeune âge, vous avez trouvé le juste équilibre entre remettre en questions mes choix, les soutenir, en être fiers et m'encourager.

Merci Seigneur

“Au commencement était celui qui est la Parole de Dieu, il était avec Dieu, il était lui-même Dieu. Au commencement, il était avec Dieu. Tout a été créé par lui, rien de ce qui a été créé n'a été créé sans lui. En lui résidait la vie, et cette vie était la lumière des hommes. [...] La Parole est devenue chaire, et a vécu parmi nous.”

Jean 1.1-14, la Bible



Contents

1	Introduction	17
1.1	Active suspensions	18
1.1.1	Definitions	18
1.1.2	Some phenomena in active suspensions	19
1.2	Microorganisms motility	21
1.2.1	Hydrodynamics of swimming microorganisms: some basics	21
1.2.2	Random and directed motions of swimming microorganisms	24
1.3	Bioconvection	25
1.3.1	Mechanisms in bioconvection caused by upward swimming	26
1.3.2	The bioconvection Rayleigh number	29
1.3.3	Main quantitative studies and other remarkable examples	30
1.3.4	Continuum models in bioconvection	32
1.3.5	Localized photo-bioconvection	34
1.3.6	Open questions in bioconvection	35
1.4	<i>Chlamydomonas reinhardtii</i> as a model phototactic microswimmer	36
1.4.1	Presentation	36
1.4.2	Methods for phototactic behavior analysis in <i>Chlamydomonas</i>	37
1.4.3	The eyespot and intracellular mechanisms in phototaxis	39
1.4.4	Phototaxis and motility	41
1.4.5	<i>Chlamydomonas</i> motion in the dark	46
1.4.6	Additional features	48
1.4.7	Concluding remarks and open issues	50
1.5	Outline of this thesis	50
2	<i>Chlamydomonas reinhardtii</i> phototactic susceptibility to light gradients	53
2.1	Phototaxis: a taxis in a vectorial field	54
2.2	Experimental setup	55
2.2.1	Principle of the experiments	55
2.2.2	Tuning of the light intensity gradients	56
2.2.3	Top view cell concentration imaging	56
2.3	Measurement of <i>Chlamydomonas reinhardtii</i> phototactic susceptibility	57

2.3.1	The Keller-Segel approach	57
2.3.2	<i>Chlamydomonas reinhardtii</i> phototactic susceptibility curve	59
2.4	Range of light detection in phototaxis	59
2.4.1	Detection threshold	60
2.4.2	Single photon detection in phototaxis	62
2.4.3	Critical inversion intensity and negative phototaxis	62
2.5	Discussion	63
2.5.1	Hypothesis of the unique dependence on light intensity	63
2.5.2	Time dependence of phototaxis	64
2.6	Conclusion	65
3	Pattern formation in localized bioconvection	67
3.1	Tuning collective effects: control parameters	68
3.1.1	Shaping of the light beam	68
3.1.2	Tuning the pseudo-Rayleigh number	69
3.2	Phase diagram and global properties of patterns	69
3.2.1	Classification of photo-bioconvection patterns	69
3.2.2	Global properties of photo-bioconvection patterns	72
3.3	Dendrites patterns	75
3.3.1	Kinetics	75
3.3.2	Wavelengths of dendrites	76
3.3.3	Validity and limit of the measurements wavelengths	77
3.4	Directional growth	78
3.4.1	Characterization of directional growth	78
3.4.2	Enhancing directional growth using inclination	80
3.4.3	Discussion	81
3.5	Conclusion	81
4	Asymptotic model for bioconvection in thin layers	83
4.1	Axisymmetric structures	84
4.1.1	Preliminaries	84
4.1.2	Structure of the primary convective roll	84
4.1.3	The effect of gyrotaxis	85
4.2	Hypothesis for the development of the asymptotic model	87
4.2.1	Dimensionless equations	88
4.2.2	Effective drifts	88
4.2.3	Timescales of the problem	90
4.2.4	Boundary conditions	90
4.2.5	Geometry $H \ll L$	90

4.2.6	Physical origin of the vertical drift \mathcal{T}_\perp	91
4.3	Derivation of the asymptotic model	92
4.3.1	Pressure and velocity fields	92
4.3.2	Orientation field	93
4.3.3	Depth-averaged cell concentration field	94
4.4	Physical interpretation of the model	95
4.4.1	A nonlinear diffusion-drift equation	95
4.4.2	Effect of advection	96
4.4.3	Effect of gyrotaxis	97
4.5	Analysis of the asymptotic model	98
4.5.1	Theoretical analysis	98
4.5.2	Instabilities produced by the model	99
4.5.3	Comparaison with experimental data	101
4.5.4	Discussion	104
4.6	Conclusion	105
5	Direct quantification of light-induced bioconvective flows	107
5.1	Experimental setup	108
5.1.1	Principle of the experiments	108
5.1.2	Cell concentration imaging and time dependent phototaxis	108
5.1.3	Fluorescent PIV	110
5.1.4	A typical experiment	112
5.2	Global analysis	114
5.2.1	Cell concentration fields	114
5.2.2	Flow fields	116
5.3	Relation between concentration and velocity fields structures	120
5.3.1	Convective roll length versus cell pattern length	120
5.3.2	The case of well separated cell patterns	121
5.3.3	The case of reduced space between cell patterns	121
5.4	Local analysis	123
5.4.1	Theoretical prediction	123
5.4.2	Data analysis	124
5.5	Discussion	127
5.5.1	Physical parameters controlling the flow fields	127
5.5.2	The surprising effect of cell concentration	127
5.5.3	A remark on instabilities	128
5.6	Conclusion	129

6	Stirring with light: a perspective	131
6.1	Cultures of photosynthetic microorganisms	132
6.2	Experimental setup	133
6.2.1	Time-dependent light-field for large-scale bioconvection	133
6.2.2	Microalgae preconditioning	135
6.2.3	Experimental protocol	136
6.3	Results	137
6.3.1	Sustained phototaxis	137
6.3.2	Effect of bioconvection on culture growth	138
6.4	Conclusion	138
7	Conclusion	141
7.1	Results	141
7.2	Outlook	143
8	Résumé détaillé en français	145
8.1	Introduction	146
8.1.1	Suspensions actives	146
8.1.2	Bioconvection	146
8.1.3	Le micronageur phototactique modèle <i>Chlamydomonas Reinhardtii</i>	148
8.1.4	Plan de la thèse	150
8.2	Susceptibilité phototactique de <i>Chlamydomonas</i> dans les gradients d'intensité lumineuse	151
8.2.1	Dispositif expérimental	151
8.2.2	Mesure de la susceptibilité phototactique	151
8.3	Formation de motifs avec la photo-bioconvection locale	152
8.3.1	Paramètres de contrôle	152
8.3.2	Diagramme de phase et propriétés globales des motifs de concentration	153
8.3.3	Caractérisation des instabilités en dendrites et de croissance direc- tionnelle	154
8.3.4	Modèle asymptotique pour la photo-bioconvection en couche mince	154
8.4	Quantification des écoulements de bioconvection induits par la lumière . .	155
8.4.1	Dispositif expérimental	155
8.4.2	Amplitude des écoulements	155
8.4.3	Relation entre les structures des champs de concentration et des vitesses	156
8.4.4	Analyse locale	158
8.5	Mélange par la lumière, une perspective	159

A	Microalgae preparation	161
A.1	Microalgae strain and culture medium	161
A.1.1	<i>Chlamydomonas reinhardtii</i> vegetative cells cultivation	161
A.1.2	Culture medium	162
A.2	Solid and liquid cultures preparation	163
A.2.1	Solid cultures	163
A.2.2	Synchronized liquid cultures	163
A.2.3	Unsynchronized liquid cultures	163
A.3	Microalgae suspensions preparation for experiments	163
A.3.1	Suspensions cells concentration measurements	163
A.3.2	Suspensions of arbitrary cells concentration	164
B	Pattern formation experiments : additional material and figures	165
B.1	Experimental procedure	165
B.2	Laser calibration	166
B.2.1	Green light intensity calibration	166
B.2.2	Green light intensity profiles acquisition	166
B.3	Top view cells concentration imaging calibration	167
B.4	Additional figures	168
C	Experiments in Hele-Shaw geometry: additional material and figures	169
C.1	Front view cells concentration imaging calibration	169
C.2	Tests on the time dependency of the phototactic response	170
C.3	Experiments on UV flashes and their biocompatibility in <i>Chlamydomonas reinhardtii</i>	170
C.4	Experimental procedures and data analysis	171
C.4.1	Hele-Shaw liquid chambers assembly	171
C.4.2	Fluospheres purification	171
C.4.3	Main experiments	171
C.4.4	Fluorescent PIV settings	172
C.5	Additional figures	173

CHAPTER 1

Introduction

1.1 Active suspensions

1.1.1 Definitions

Complex fluids refer to fluids that consist of a mixture of several phases, solid-liquid (suspensions), solid-gas (granular) or liquid-liquid (emulsions). In industry, they are engineered with specific properties : the right consistency of a sauce in the food industry, the right wetting and softening of a foam shaving in cosmetics. Complex fluids are also present in life science such as biological fluids (blood, lymph, ...) or suspensions of swimming microbes.

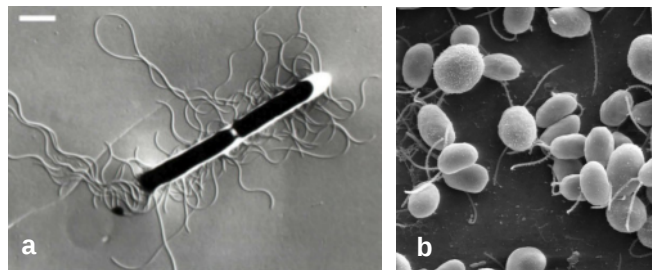


Figure 1.1: Two examples of swimming microorganisms. **a**, Electron micrograph of the bacterium *Bacillus subtilis* (Cisneros 2008). The image shows a cell dividing into two. White filaments are multiple flagella that the cell uses to self propel. The scale bar is 1 μm . **b**, Electron micrograph of the microalgae *Chlamydomonas reinhardtii* by the Dartmouth Electron Microscope Facility (Dartmouth College). Cells are approximately 10 μm of body size and use their two flagella to self-propel.

In this work, we are interested in suspensions of swimming microorganisms. Swimming microorganisms can be for example bacteria, like *Bacillus subtilis* (Figure 1.1.a) or microalgae, like *Chlamydomonas reinhardtii* (Figure 1.1.b). They are able to self-propel in their surrounding fluid and can be described as “active particles”, so that we call their suspensions “active suspensions”. Active suspensions are actually a class of active matter systems composed of “particles” capable of converting chemical energy into mechanical work for self-propulsion. Thus, the physics of active suspensions is at the intersection between active matter physics and complex fluids physics. It inherits two questions from these domains. How does active matter self-organize ? How are suspensions properties related to the properties of individuals ? Another question, more specific to active suspensions is: can we harvest the mechanical work produced by the microorganisms towards a larger scale in the fluid ? In the next paragraph, we give some examples of phenomena related to these questions.

1.1.2 Some phenomena in active suspensions

Self-organization

The animal kingdom exhibits fascinating behaviors like schools of fish or aerial flocks of birds or insects. The question of the self-organization is easily triggered by these observations, but it is also relevant for microbial life. In a study by Dombrowski et al. 2004, different scales of organization were observed in centimetric drops of bacterial suspension of *B.subtilis* (Figure 1.2), a rod-shaped bacterium of length $l \sim 5 \mu\text{m}$. At the scale of the whole drop (> 1000 times larger than the size of a bacterium), the suspension organizes in plumes, sliding along the meniscus (Figure 1.2.a). Thus, cells self-concentrate near the contact line. In this region, they reach a high volume fraction $\gtrsim 0.1$ and swim collectively with *vortices* and *jets* at a scale that is > 10 times larger than the size of a bacterium (Figure 1.2.b). These two phenomena have different physical origins. The formation of plumes of high concentration is a hydrodynamic pattern formation driven by macroscopic buoyancy differences in dilute suspensions of microorganisms denser than water. It was first termed “bioconvection” by Platt 1961 and can be seen as the biological analog of thermal convection. The collective swimming occurs is sometimes referred to as “bacterial turbulence” or “mesoscale living turbulence” (Wensink et al. 2012) and fundamentally relies on pairwise interactions between microbes in concentrated suspensions.

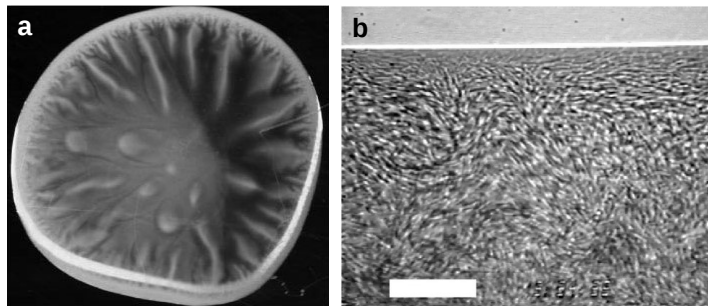


Figure 1.2: Different scales of organization in a bacterial fluid drop of *B.subtilis*. A sessile drop of diameter 1 cm is deposited on a horizontal Petri dish. **a**, Macroscopic pattern formation and self-concentration in the drop imaged from top view. Convective plumes of higher concentration appear (bright). Plumes are pulled down along the meniscus, leading to self-concentration near the contact line. **b**, Close-up on a region of very high concentration, near the contact line (white line) and viewed from below after self-concentration. Cells exhibit a collective swimming at the mesoscopic scale with *vortices* and *jets*. The scale bar is $35 \mu\text{m}$. From Dombrowski et al. 2004.

In nature, a self-organization phenomenon of much broader scale also takes place. Algal blooms consist of fast and very large accumulations of microalgae at the surface of water bodies (Figure 1.3). They are thought to be triggered by complex combinations of environmental conditions. They can be harmful, in particular because they often lead to a strong decrease in the amount of dissolved oxygen in water when the biomass is

decomposed at the end of the bloom.



Figure 1.3: Coccolithophore bloom off Brittany, France. Image taken by NASA on June 15, 2004.

Modification of suspensions properties

Swimming microorganisms can also modify their suspensions properties. For example, Sokolov and Aranson 2009 indirectly showed that the bacteria *Bacillus subtilis* lower the viscosity of their suspensions when compared to passive particles. The authors either measured the time decay of vortexes or the viscous torque exerted on a particle on freestanding suspensions films. Later, López et al. 2015 directly measured the rheologic response in suspensions of bacteria *Escherichia coli*. In particular, they found that in the semi-dilute regime and at low shear the system activity fully overcome viscous dissipation and the suspension behaves like a “superfluid” of vanishing viscosity. On the other hand, Rafai, Jibuti, and Peyla 2010 reported a significant increase of the macroscopic effective viscosity in suspensions of *Chlamydomonas reinhardtii* when compared to passive particles. They also reported a shear-thinning behavior. These results questions on what are the intrinsic differences between microalgae and bacteria which could explain the difference in the rheological properties of their suspensions.

Another example of a property of a suspension modified by active particles was provided by Wu and Libchaber 2000. In suspended thin bacterial films ($h \sim 10 \mu\text{m}$) of *Escherichia coli*, the authors measured positional fluctuations of beads as large as $10 \mu\text{m}$ diameter. They found that beads diffused as if the effective temperature (in Kelvin) of the bacterial bath was 100 times greater than room temperature due to collective motion.

A different type of active suspensions contains artificial motile systems. Active colloidal particles can be powered chemically, owing their self-propulsion to asymmetric chemical reactions at their surface in the presence of fuel. In such systems, an increase of the effective temperature was also found (Palacci et al. 2010).

Harvesting energy from active suspensions

In thin bacterial films of *B.subtilis*, Sokolov et al. 2010 studied the possibility to harvest energy from the collective motions of bacteria. They designed several microgears placed in bacterial thin films. Remarkably, collective motion induced gears rotation for gears

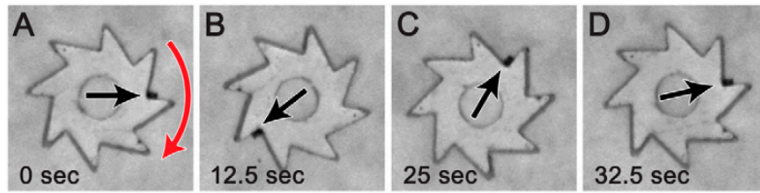


Figure 1.4: A microgear rotated by the collective motion of bacteria in a thin film. A microgear of polymeric material of 400 μm in diameter with asymmetric teeth is rotated in a thin film of a suspension of *B.subtilis*. Black arrows indicate the gears orientation and red arrows show the direction of rotation in the direction of the teeth slanted edges. Concentration of bacteria is 2×10^{10} cells/mL and the film thickness is 200 μm . From Sokolov et al. 2010.

with asymmetric teeth in the direction of the teeth slanted edges (Figure 1.4).

Some researches suggest that bioconvection could be used to induce self-bio-mixing in suspensions of microbes and improve microbial growth by better nutrient transport and cell distribution within the suspension (Sommer et al. 2017, Arrieta et al. 2019, Javadi et al. 2020). In particular, Arrieta et al. 2019 showed preliminary results of efficient convective self-bio-mixing with a spatiotemporal control of a light field to trigger bioconvection in suspensions of light sensitive microalgae, with potential application to algal photo-bioreactors.

1.2 Microorganisms motility

Some of the phenomena previously introduced can be partially understood by studying microorganisms motility and its consequences. We first introduce some hydrodynamics of swimming microorganisms related to hydrodynamics interactions and rheology in active suspensions. Then we introduce the random and directed motions of microorganisms relevant to bioconvection when microorganisms are denser than water.

1.2.1 Hydrodynamics of swimming microorganisms: some basics

Propulsion mechanisms

In their review, Lauga and Powers 2009 define a “microswimmer” as a cell that moves by deforming its body in a periodic way, although this definition excludes other motility mechanism developed by microbes such as vacuoles for buoyancy regulation in cyanobacteria. For example, *Chlamydomonas* cells use two flexible flagella that perform a breaststroke-like beating to propel forward (Figure 1.5.a). Bacteria such as *E.coli* or *B.subtilis* possess several flagella, each flagellum being attached to the membrane by a motor. Flagella coalesce to form a “flagellar bundle” that propel cells during motors rotation (Figure 1.5.b). In *E.coli* flagella are attached to the membrane at the same spot while in *B.subtilis* they surround the rod shaped cell.

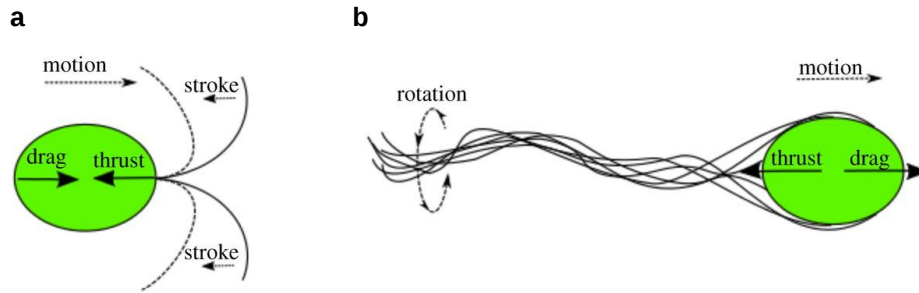


Figure 1.5: Sketch of flagellar propulsion mechanisms. **a**, A *Chlamydomonas* is propelled by its two flagella stroke. **b**, A bacterium is propelled by the coordinated rotation of its bundled flagella. From Gluzman, Karpeev, and Berlyand 2013.

Swimming at low Reynolds number

These microorganisms have developed locomotion in fluids at low Reynolds number, which is quite different from what larger animals experience. Reynolds number is the ratio of typical inertial forces to viscous forces in the fluid flow. At low Reynolds number, flow is dominated by viscous forces. In water $\rho \approx 10^3 \text{ kg/m}^3$, $\eta \approx 10^{-3} \text{ Pa}\cdot\text{s}$, a swimming bacterium such as *E.coli* with $v_s \approx 10 \text{ }\mu\text{m/s}$ and $l_s \sim 10 \text{ }\mu\text{m}$ experiences a Reynolds number $\text{Re} \sim 10^{-4} \ll 1$. Concerning swimming at low Reynolds number, an interesting and more specific interpretation of this number was proposed by Lauga and Powers 2009. A microswimmer of size $\sim l_s$ swimming with velocity v_s that suddenly stops deforming its body to swim coasts at a small distance d relatively to l_s due to the small inertia. In this case, the Reynolds number can be interpreted as the dimensionless coasting distance $\text{Re} \sim d/R_s$. Locomotion at low Reynolds number displays the following features : a microswimmer instantaneously stops propelling as soon as it stops deforming its body. Consequently, swimmers must display non-reciprocal body kinematics (Purcell 1976): this is often referred to as the scallop theorem. Finally, by flows fields around microswimmers can be described by a superposition of flow fields associated to point forces applied on the fluid at different locations. This approach is used in models of microswimmers described hereinafter.

Model with force dipole and flow fields around microswimmers

In canonical models of microswimmers related to hydrodynamics interactions in microswimmers suspensions (Hatwalne et al. 2004), a microorganism moves at a constant velocity, exerts no net force on the fluid (neutrally buoyant) and is a force dipole. Its flagella thrust and body viscous drag forces compose a force dipole that gives the flow field around the microswimmer. This flow decays with the distance from the active particle as $\sim \frac{1}{r^2}$. In these models, bacteria *E.coli* and *B.subtilis* and microalgae *Chlamydomonas* represent two types of model microswimmers. Both *E.coli* and *B.subtilis* push the fluid behind them to propel and are called *pusher* swimmers. They are modelled by a positive

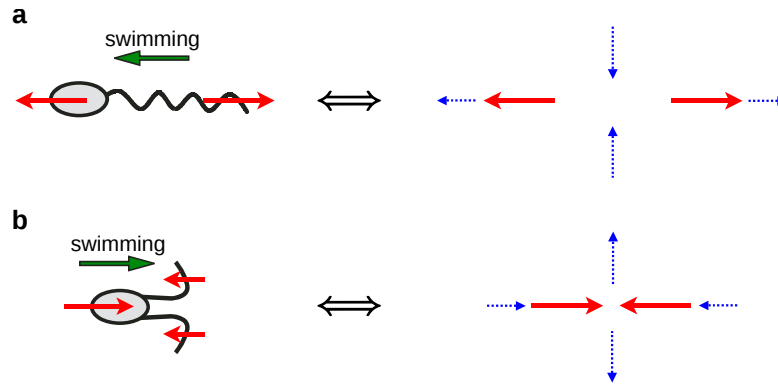


Figure 1.6: Equivalent force dipoles and flow fields associated to model pusher and puller microswimmers. Left : Schematic representations of model microswimmers on the left with local forcing on the fluid in solid red arrows. Right : The equivalent force dipoles (shown in red arrows) generate surrounding flows of directions indicated by blue dotted arrows. **a**, A pusher is equivalent to a positive force dipole. **b**, A puller is equivalent to a negative force dipole.

force dipoles which generates a flow field directed away from the cells along their swimming direction and towards the cells in the perpendicular direction (Figure 1.6.a). Microalgae *Chlamydomonas* pull the fluid in front of them to propel and are called *puller* swimmers. They are modelled by a negative force dipoles which generates a flow of opposite directions to those of a *pusher* (fig. 1.6.b).

Qualitative explanations of effective viscosity and collective motion

These models provide qualitative predictions for the increase or the decrease of the suspension effective viscosity by microswimmers and for some collective motions.

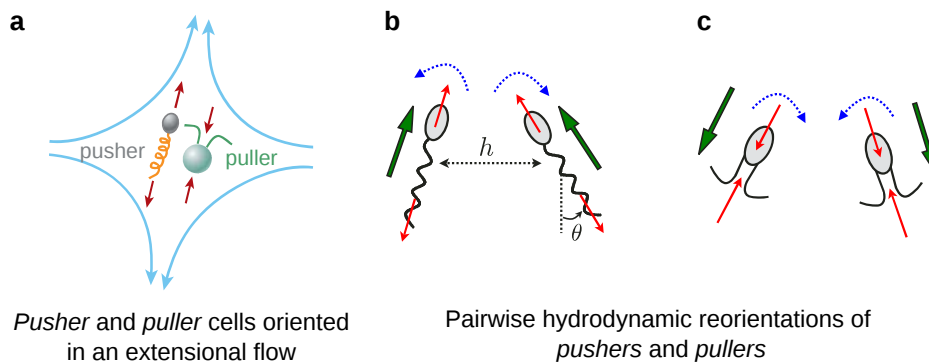


Figure 1.7: Pusher and puller in an extensional flow and pairwise interactions. **a**, Pusher and puller in an extensional flow (curved sky blue arrows). The force dipole (solid red arrows) of a pusher reinforces the flow whereas a puller retards the flow. **b,c**. Pairs of pushers and pullers with local forces exerted by cells on the fluid in solid red arrows and swimming directions in thick solid green arrows. By hydrodynamic interactions, cells reorient each other in directions indicated by dotted blue arrows. **b**, Two *pushers* approaching each other tend to align each other. **c**, Two *pullers* moving away from each other tend to anti-align each other.

A shear flow can be decomposed into a translational part, a rotational part, and an extensional part. If in a suspension subjected to a shear flow, *pushers* align and swim in the extensional direction of the flow, which is reasonable for elongated cells as *E.coli* or *B.subtilis*, then their force-dipoles reinforces the flow (Figure 1.7.a). Thus, cells actively lower the suspension effective viscosity. Force-dipole models also predict that two pusher coming close to each other tend to reorient and swim side-by-side (Figure 1.7.b), which can contribute to collective motion. A review of the phenomena qualitatively described above, other phenomena and new experimental challenges was proposed specifically for bacterial suspensions by Clement et al. 2016. Recently, the combined use of rheometry and imaging techniques helped to link the vanishing of the viscosity to collective motions in bacterial suspensions (Martinez et al. 2020).

A qualitative explanation can also be given to why so-called "bacterial turbulence" like that shown in Figure 1.2.b are not reported in *Chlamydomonas*. Two *pullers* modelled by force dipoles on a diverging course tend to reorient in opposite directions and further swim away from each other (Figure 1.7.c). In principle, *pullers* could also increase the shear viscosity by resisting a flow when oriented in its extensional direction (Figure 1.7.a). However, in *Chlamydomonas reinhardtii*, it is not obvious why cells would align in the extensional flow direction to increase the viscosity (Rafai, Jibuti, and Peyla 2010; Mussler et al. 2013).

To test these force dipoles models, flow fields were measured experimentally around *E.coli* (Drescher et al. 2011) and *Chlamydomonas reinhardtii* (Drescher et al. 2010). The flow field around *E.coli* was indeed well described by a positive force dipole. On the contrary, in *Chlamydomonas reinhardtii*, the flow field induced by a negative force dipole is only valid at distances $\gtrsim 7R_{CR}$ (cell radius) where the flow is already $\lesssim 1\%$ of the cell velocity. For smaller distances, the flow is better described by a force tripole that takes into account flagella separation. Then, it was finally proposed that *Chlamydomonas reinhardtii* increase the viscosity by resisting the flow vorticity (Levan et al. 2017).

At distances $\gtrsim 35R_{CR}$, the flow field around *Chlamydomonas reinhardtii* measured by Drescher et al. 2010 is well described by a force monopole that originates from microorganisms negative buoyancy. This cell property was neglected in the models described above but it is precisely the non-homogeneous repartition of a multitude of cells denser than water that leads to bioconvection. In the next paragraph, we introduce random and directed motions of swimming microorganisms that control their spatial repartition.

1.2.2 Random and directed motions of swimming microorganisms

Random motion

The repartition of swimming microorganisms in a still fluid is the result of a superimposition of their random and directed motions. On initial examination, single microorganisms trajectories are random in the absence of stimulus. Berg and Brown 1972

followed single cells trajectories in *E.coli*. Their motion consists of a series of straight runs in different directions interrupted by short times spent tumbling. This was termed run-and-tumble. Flagella rotate counter-clockwise and work in synchrony in the flagellar bundle during a run. During a tumble however, the clockwise rotation breaks the flagellar bundle : bacteria stop and randomly reorient in a new direction for the next run. This was modelled as a persistent random walk by Lovely and Dahlquist 1975. The authors explained that an effective isotropic diffusion coefficient D can be estimated from the swimmer velocity during run v_s and the direction correlation time τ_c as $D \sim v_s^2 \tau_c$. τ_c is related to the mean duration of a run and to the mean angle between successive runs. Similar behavior is also observed in *Chlamydomonas* (Hill and Häder 1997; Polin et al. 2009). Thus, microswimmers explore their environment in a diffusive-like behavior, with for each one a specific regulation of their swimming.

Taxes

Berg and Brown 1972 also observed that bacteria bias their random trajectories when swimming in a gradient of a chemical attractant. This response to an external stimulus is called a taxis. To find favorable conditions in heterogeneous environments, swimming microorganisms have developed a wide array of mechanisms to direct their motion as a response to external stimuli. They either detect and process external physico-chemical signals or are subjected to passive mechanical forces affecting their trajectories. Such a directed motion is termed taxis. In the case of chemotaxis in *E.coli*, cells actively tend to suppress directional changes in a gradient of an attractant. A taxis can be positive (towards a stimuli) or negative (away from a stimuli). *E.coli* swims towards nutrients by positive chemotaxis but also to avoid predators by negative chemotaxis away from chemicals secreted by predators.

Other taxes include magnetotaxis, geotaxis/gravitaxis, thermotaxis. An important taxis often found in photosynthetic microorganisms that seek optimal light intensities like *Chlamydomonas* is phototaxis, which enables directed motility in response to light. A typical feature of phototaxis is that there is a critical inversion intensity I_{crit} that separates positive phototaxis $I < I_{\text{crit}}$ and negative phototaxis $I > I_{\text{crit}}$. In section 1.4, we will describe in more details the phototactic ability of *Chlamydomonas reinhardtii*. It is especially relevant in bioconvection controlled by light in suspensions of these cells.

1.3 Bioconvection

In active suspensions where cells that have a density mismatch with the surrounding fluid, the local density depends on the local cell concentration. Bioconvection is the resulting hydrodynamic instability driven by gravity that originates from gradients of cell concentration. It is the biological analog of thermal convection with which

it shares many similarities but from which it also stands out. Cells repartition does not result solely from the combined effect of advection and diffusion because their taxis is also the driving force.

1.3.1 Mechanisms in bioconvection caused by upward swimming

Upward swimming

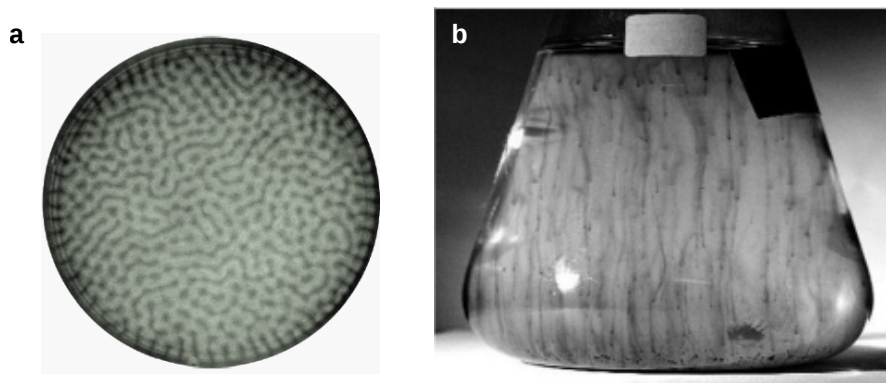


Figure 1.8: Bioconvection patterns in suspensions of upward swimming microorganisms **a**, Regularly spaced array of bioconvection plumes in a petri dish from top view with *Chlamydomonas augustae*. Concentration 1.5×10^7 cells/mL. Depth 0.2 cm. Width 5 cm. From Bees 1996. **b**, Falling bioconvection plumes in an Erlenmeyer flask of a suspension of *Chlamydomonas augustae* at $< 10^5$ cells/mL. From Williams and Bees 2011a.

Bioconvection can readily be seen in suspensions of microorganisms which are not only denser than their ambient medium, but also have the property to swim upward in average. In this situation, bioconvection patterns consist of plumes of higher cell concentration separated by regions of low cell concentration. Figure 1.8 presents typical patterns obtained in the laboratory under controlled conditions in the suspension of upward swimming microalgae *Chlamydomonas augustae*.

In fact, there are various mechanisms that make cells swim upward on average. In the experiments in bacterial drops by Dombrowski et al. 2004 (Figure 1.2.a), bacteria triggered bioconvection by swimming upward due to oxytaxis or aerotaxis, a particular case of chemotaxis towards oxygen. Plumes sliding was an additional Boycott effect due to the meniscus tilt. In the microalgae *Chlamydomonas*, there also exists a passive mechanism that orients *Chlamydomonas* upward on average which is negative gravitaxis (often only referred to as gravitaxis). In this case, a gravitational torque orients cells upward on average. It is generally assumed that the reason is that *Chlamydomonas* is bottom heavy, although another mechanism is also possible (Roberts 2006). Bees and Hill 1997 studied bioconvection where upward swimming was due to gravitaxis in *Chlamydomonas augustae* (which was mistakenly classified as *Chlamydomonas nivalis* according to Bees 2019). Williams and Bees 2011a performed bioconvection experiments

with vertical phototaxis due to bottom or top homogeneous illumination in suspensions of *Chlamydomonas augustae*.

In suspensions of microorganisms denser than water and swimming upward on average, two mechanisms can be involved in bioconvection. The first mechanism is an overturning mechanism where a vertical density gradient is destabilized. The second one is termed gyrotaxis. It is a competition between viscous torques and a reorientation torques that can cause cells to swim towards regions of locally downwelling fluid and away from upwelling fluid.

The overturning mechanism

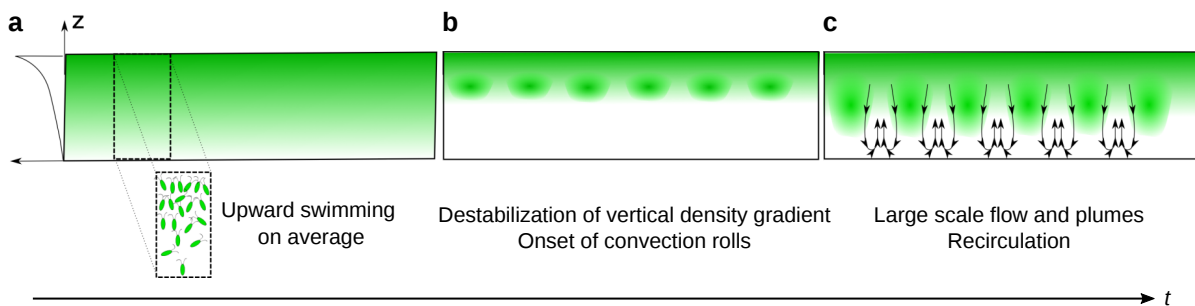


Figure 1.9: The overturning mechanism for bioconvection in three steps. **a**, Cell concentration c is higher near the upper surface because cells swim upward on average. Density ρ also gets higher because cells are denser than water. **b**, When the vertical density gradient is strong enough, it becomes unstable and convection rolls start to develop. **c**, Fully developed spontaneous bioconvection consists of a regularly spaced alternation of plumes of high concentration and regions of low concentration, associated with recirculation flows. Denser regions of high density sink whereas the flow is directed upward in regions of low density. On average, the unstable vertical density gradient originating from upward swimming is maintained and the instability is self-sustained.

Plesset and Winet 1974 first linked bioconvection to the Rayleigh-Taylor instability. The upward swimming was taken into account by considering that microorganisms formed a layer of density ρ_1 above a fluid layer of density ρ_0 , which is always unstable. Later, Childress, Levandowsky, and Spiegel 1975 proposed that the average upward swimming of microorganisms creates a vertical density gradient rather than a discontinuous separation between two regions of different densities (Figure 1.9.a). This gradient can become unstable (Figure 1.9.b), which generates self-sustained bioconvective flows associated with cell concentration patterns of plumes (Figure 1.9). It should be noted that cells swim upward only on average, and in competition with their random motion. Thus the vertical gradient density gradient is limited in amplitude and is only destabilized when high enough. This is controlled by the liquid height, the cell concentration, the cell bias toward the upper surface and the effective diffusion coefficient.

Gyrotaxis in bioconvection

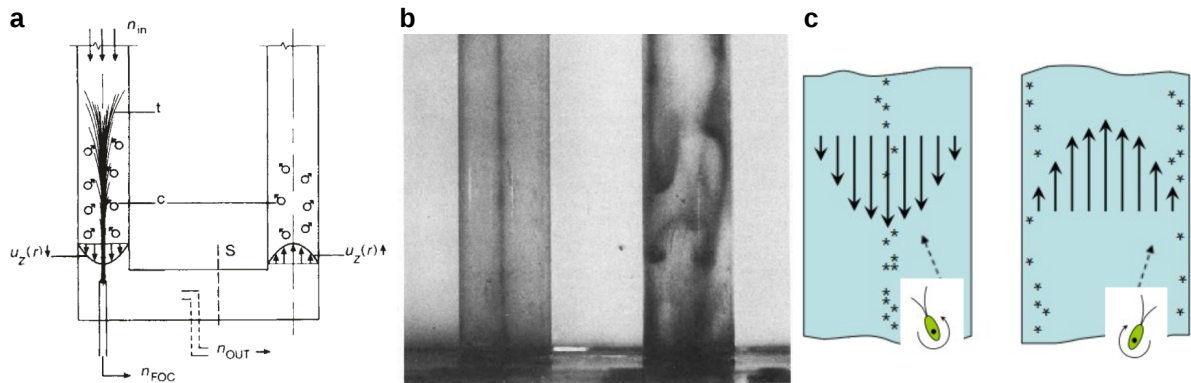


Figure 1.10: Gyrotactic accumulation in an imposed vertical flow of a suspension of gravitactic *Chlamydomonas nivalis*. **a**, Experimental setup. A flow of a suspension of *Chlamydomonas nivalis* is imposed in two vertical tubes connected by a horizontal section. The flow speed is typically $u_0 \approx 0.1$ cm/s in tubes of diameter $2R = 1.25$ cm with a suspension of global cell concentration $c_0 \approx 10^6$ cells/mL. **b**, Picture of the two vertical tubes. On the left, algae are focused along the axis of the imposed downward flow. Right : Algae accumulate at the periphery away from the axis of the imposed upward flow and form sinking plumes. **c**, Sketch of the gyrotactic effect depending on cells on the flow direction. Cells mean orientation (dashed arrows) results from a competition between flow vorticity (viscous torque indicated by rotating arrow) and their preferential vertical orientation. Left : a cell is oriented towards the center of the downward flow. Right : a cell is oriented towards the periphery.

Kessler 1985 demonstrated and explained the gyrotactic effect in suspensions of *Chlamydomonas nivalis*. In still fluids, these cells swim upward on average by gravitaxis. In the presence of fluid flows, they tend to swim towards downwelling fluid and away from upwelling fluid. The experimental setup and the demonstration by Kessler 1985 are shown in Figure 1.10.a,b while the phenomenon is sketched in Figure 1.10.c. The flow vorticity competes with the preferential orientation of cells. In *Chlamydomonas nivalis*, a gravitational torque tends to orient cells in the vertical direction while a viscous torque deviates cells from this preferential orientation.

Gyrotaxis was demonstrated in an imposed flow, and was quickly taken into account in the understanding of bioconvection Pedley, Hill, and Kessler 1988. Gyrotaxis is a mechanism for the spontaneous growth of concentration fluctuations. In gyrotactic bioconvection of upward swimming microorganisms, the establishment of an unstable vertical density stratification is not necessary : cells can be focused in any regions of locally downwelling fluid and amplify the downwelling by increasing the local density. Bioconvection with gyrotaxis also leads to smaller wavelengths and more focused patterns than with the overturning mechanism.

Gyrotaxis was initially introduced to describe the competition for a competition between viscous and gravitational reorientation torque. In all generality, any preferential

orientation driven by a passive or an active torque can compete with viscous torques and leads to a gyrotactic effect. In particular, Williams and Bees 2011b proposed a model for photo-gyrotaxis in *Chlamydomonas* as resulting from the competition between viscous torque and phototactic reorientation torque. They also suggest that the phototactic reorientation torque is stronger than the gravitational torque in gravitaxis, so that photo-gyrotaxis occurs at higher vorticities than gravi-gyrotaxis. Another example characterized by Waisbord et al. 2016. In this case, a competition between the flow vorticity and the preferential orientation of magnetotactic bacteria lead to a flow focusing further destabilized into a new pearling instability.

1.3.2 The bioconvection Rayleigh number

Qualitatively, the emergence of instabilities in bioconvection are controlled by a Rayleigh-like number, which compares the timescale of cells diffusive transport to their negative buoyancy-driven convective transport :

$$\text{Ra} = \frac{\tau_{\text{diff}}}{\tau_{\text{conv}}} \quad (1.1)$$

To define the Rayleigh number, we model a sinking plume in Figure 1.9.c by a blob of typical size H , with a horizontal cell concentration differential Δc with the surroundings and a density $\rho(\Delta c)$. Its convective transport timescale is obtained from its sinking velocity $v \sim H/\tau_{\text{conv}}$ given by the balance between negative buoyancy and viscous drag $(\rho(\Delta c) - \rho_0)gH^3 \sim \eta vH$. We find $\tau_{\text{conv}} \sim \eta/gH^3(\rho(\Delta c) - \rho_0)$. On the other hand, the blob can also spreads by diffusion with a timescale $\tau_{\text{conv}} \sim H^2/D$. Thus, the Rayleigh number can be written as :

$$\text{Ra} = \frac{\rho_0 g \beta H^3 \Delta c}{D \eta} \quad (1.2)$$

Above, $\beta = \frac{\rho(\Delta c) - \rho_0}{\rho_0 \Delta c}$ is actually independent of Δc in the typical range of cells volume fraction and quantifies the density difference between cells and the ambient medium. Indeed, we have at small volume fraction : $\rho(\Delta c) = \rho_0 + \phi(\Delta c) \Delta \rho_{\text{cell}} \underset{\phi \ll 1}{=} \rho_0 + \Delta c V_{\text{cell}} \Delta \rho_{\text{cell}}$. We find : $\beta = \frac{\Delta \rho_{\text{cell}}}{\rho_0} V_{\text{cell}}$, where V_{cell} and $\Delta \rho_{\text{cell}}$ are respectively the volume and the excess density above water of a cell. The diffusion coefficient and the viscosity are generally taken independent of the cell concentration so that the Rayleigh number is proportional to H^3 and to the magnitude of the horizontal cell concentration difference Δc . In particular, this reasoning suggests that once bioconvective flows are generated, their magnitude is controlled by horizontal density gradient, regardless of the fact that cells motion is biased in the vertical direction.

In practice, the horizontal cell concentration difference arising *in situ* cannot be easily imposed experimentally, in stark contrast with the temperature difference arising in thermal convection. Instead, we use the initial cell concentration c_0 as a typical scale for

the cells and we replace the Rayleigh number by a pseudo-Rayleigh number (keeping the same notation) :

$$\text{Ra} = \frac{\rho_0 g \beta H^3 c_0}{D \eta} \quad (1.3)$$

To give an order of idea in bioconvection in a suspension of *Chlamydomonas reinhardtii*, we typically have $V_{\text{CR}} \approx 500 \mu\text{m}^3$, $\Delta\rho_{\text{CR}} \approx 50 \text{ kg/m}^3$ and $\beta \approx 25 \mu\text{m}^3$. The typical order of magnitude of initial volume fraction is $\phi_0 \sim 10^{-3}$ (hence a volume fraction much smaller than that required for bacterial turbulence in certain pushers suspensions). Therefore, the relative density difference is actually very small : $\phi_0 \Delta\rho_{\text{CR}}/\rho_0 \sim 5 \times 10^{-5}$. The pseudo-Rayleigh number however can be quite large. To estimate Ra, we need a value of a diffusion coefficient. Because we work at the scale of a population, we use a value obtained from macroscopic measurements on large populations : $D \sim 10^{-7} \text{ m}^2/\text{s}$ (Polin et al. 2009, Dervaux, Capellazzi Resta, and Brunet 2017). For $H \sim 5 \text{ mm}$, $c_0 \sim 10^6 \text{ cells/mL}$, we have : $\text{Ra} \sim 500$. A critical pseudo-Rayleigh number above which bioconvection occurs spontaneously (in the absence of light) due to upward swimming of *Chlamydomonas reinhardtii* was reported in experimental studies by Yamamoto et al. 1992; Dervaux, Capellazzi Resta, and Brunet 2017: $\text{Ra}_c \sim 1500$.

1.3.3 Main quantitative studies and other remarkable examples

Although bioconvection was first documented more than a century ago Wager 1911, the two main quantitative studies are quite recent. Bees and Hill 1997 and Williams and Bees 2011a both studied bioconvection in suspensions of *Chlamydomonas augustae*. They focused mainly on the description of cell concentration patterns. To our knowledge, there are no quantitative study of bioconvective flow fields associated to cell concentration patterns in the litterature. In particular, they used Fourier analysis to extract the dominant wavelength of instabilities. Bees and Hill 1997 studied bioconvection with gravitaxis and gyrotaxis. Williams and Bees 2011a extended this study by also triggering vertical phototaxis using top or bottom illumination. In particular, these studies help to distinguish the overturning mechanism and the gyrotaxis mechanism in the experiments.

With Fourier analysis, Bees and Hill 1997 studied wavelength dependence on liquid height $2 \text{ mm} \leq H \leq 8 \text{ mm}$ and initial cell concentration $2 \times 10^6 \text{ cells/mL} \leq c_0 \leq 1.5 \times 10^7 \text{ cells/mL}$ (Figure 1.11). In their experiments, bioconvection was dominated by the gyrotactic focusing mechanism. They found that pattern evolved in time, with the global trend that their wavelength decreases with time. The initial wavelength scaled with the liquid height and only slightly depended on the initial cell concentration. In contrast, the wavelength of well developed patterns clearly decreased with increasing cell concentration and depended only little on liquid height. These results were attributed to a predominance of gyrotactic and non-linear effects in regions where the local concentration increases.

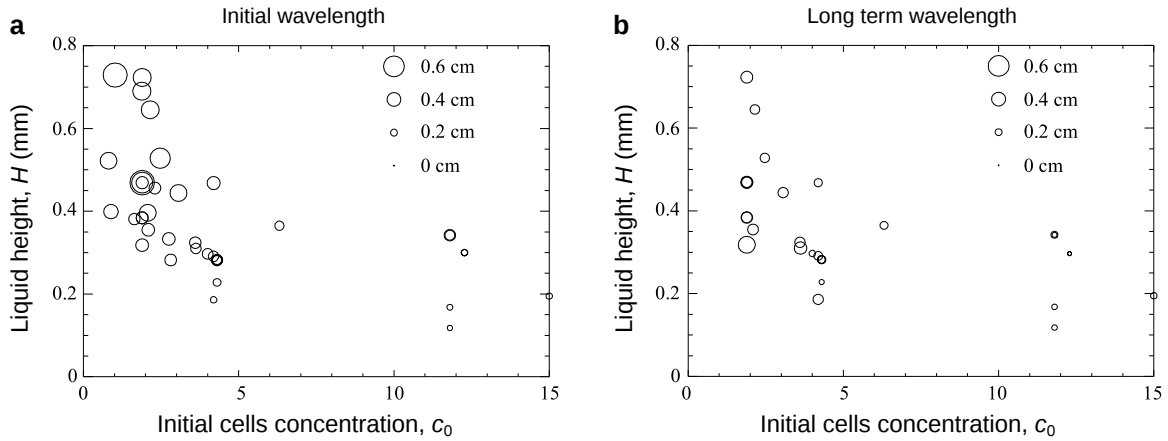


Figure 1.11: Effect of height, concentration and time on the wavelength of gyro-gravitactic bioconvection patterns in suspensions of *Chlamydomonas augustae*. **a**, Initial wavelength (30s after mixing) as a function of liquid height and initial cell concentration. **b**, Long term wavelength (10 min after mixing) as a function of liquid height and initial cell concentration. From Bees and Hill 1997.

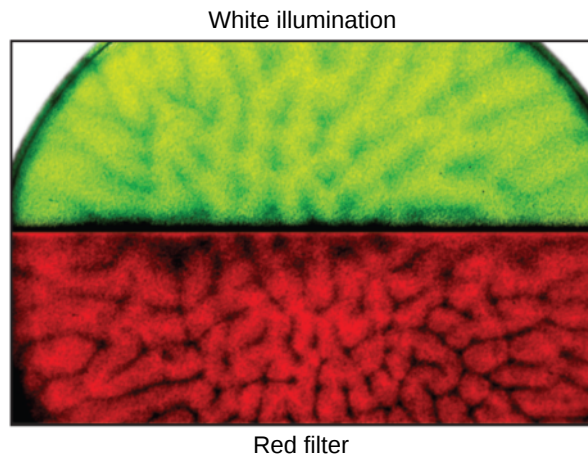


Figure 1.12: Effect of phototaxis in photo-gyro-gravitactic bioconvection. Bioconvection pattern in a suspension of *Chlamydomonas augustae* in a Petri dish (liquid height 4 mm, width 5 cm, concentration 10^6 cells/mL) observed from top view with two different illuminations from below. In the top half, a strong white light illumination from below elicits negative phototaxis and upward swimming. Bioconvection results from an interplay between phototaxis, gravitaxis and gyrotaxis. In the bottom half, a red light filter (660 nm) was placed on the light path. Cells do not respond to the red light illumination. Bioconvection results from an interplay between gravitaxis and gyrotaxis. From Williams and Bees 2011a, recolored in Bees 2019.

Williams and Bees 2011a used various illumination configurations in photo-gyro-gravitactic bioconvection of *Chlamydomonas augustae*. This experimental study aimed to combine gravitaxis and vertical phototaxis in order to create controlled gradients of cell concentration, also with significant influence of gyrotaxis. Because light was shone from above or from below, phototaxis occurred in the vertical direction and either supported or competed against gravitaxis, and as a result controlled the torque balance in gyrotaxis. When pho-

totaxis and gravitaxis worked hand in hand, cells tendency to swim upward was strong enough to suppress gyrotaxis. In this case, bioconvection was dominated by the overturning mechanism (Figure 1.12, top half). On the other hand, when phototaxis did not support gravitaxis, cells tendency to swim upward was weaker and bioconvection was dominated by gyrotaxis. This resulted in more focused plumes and smaller wavelengths than with the overturning mechanism (Figure 1.12, bottom half).

1.3.4 Continuum models in bioconvection

The example of gyrotaxis first demonstrated in 1985 (Kessler 1985) and then quickly included in theoretical models (Pedley, Hill, and Kessler 1988) shows that in bioconvection, experimental observations drive the development of theory. Reviews in the domain (Pedley 1992, Hill and Pedley 2005, Bees 2019, Javadi et al. 2020) also emphasize the strong desire to compare experimental results to theoretical predictions.

Main ingredients

Here, we give the flavor of the different continuum models. The main constituents of standard continuum models are momentum balance, flow incompressibility (which generally applies for aqueous active suspensions), cells conservation, and a description of the cells orientation field as a function of the flow.

The momentum balance describes the evolution of the velocity \vec{v} and pressure fields. The forces monopoles of non-neutrally buoyant cells are coarse-grained in an additional term which couples the pressure and the velocity fields to the cell concentration field c . Together with the incompressibility constraint, we have :

$$\rho_0 \left(\frac{\partial \vec{v}}{\partial t} + (\vec{v} \cdot \vec{\nabla}) \vec{v} \right) = \eta \Delta \vec{v} - \vec{\nabla} p_e + \rho_0 \beta c \vec{g} \quad \text{and} \quad \vec{\nabla} \cdot \vec{v} = 0 \quad (1.4)$$

Above, p_e is the excess pressure above hydrostatic pressure, $\beta = \frac{\Delta \rho_{\text{cell}}}{\rho_0} V_{\text{cell}}$ was introduced in the definition of the pseudo-Rayleigh number with V_{cell} and $\Delta \rho_{\text{cell}}$ the volume of a cell and its excess density above the density of water ρ_0 . Active stresses due to cells propulsion mechanisms are neglected in eq. (1.4), although they may become significant they become significant in concentrated suspensions (Pedley 2010).

The key equation of the model is the equation for the conservation of the number of cells in the suspension. Death and birth of cells for which the time-scale is much longer than that of typical bioconvection experiments are neglected. The cells conservation takes the form of an advection-drift-diffusion equation :

$$\frac{\partial c}{\partial t} = \vec{\nabla} \cdot \left(\underbrace{D \vec{\nabla} c}_{\text{diffusion}} - \underbrace{c \vec{v}_{\text{drift}}}_{\text{drift due to taxis}} - \underbrace{c \vec{v}}_{\text{advection}} \right) \quad (1.5)$$

The diffusive and the drift term describe the motility of the organisms in absence of flow while the advection term describes their recirculation by fluid flows. The diffusive

term originates from cells random motion and D is an effective diffusion coefficient. The drift term can be written $c\vec{v}_{\text{drift}} = c|v_{\text{drift}}|\vec{q}$ and describes a cells bias in a direction of unit vector \vec{q} at a speed v_{drift} due to a particular taxis (gravitaxis, chemotaxis, phototaxis, etc...).

In generality, \vec{q} differs from the microorganisms preferential orientation $q \neq \vec{e}_p$. \vec{q} is selected by a competition between the reorientation torque towards \vec{e}_p and the viscous torques exerted by the fluid. This is modelled by the equation of gyrotaxis :

$$\frac{\partial \vec{q}}{\partial t} = \frac{1}{2B}[\vec{e}_p - (\vec{e}_p \cdot \vec{q})\vec{q}] + \frac{1}{2}\vec{\omega} \times \vec{q} \quad (1.6)$$

On the right hand side of eq. (1.6), the first term tends to align cells along their preferential orientation \vec{e}_p . B is the gyrotactic parameter. It can be interpreted as the timescale of reorientation along \vec{e}_p when the flow is switched off. The second term corresponds to the rotation by the vorticity of the flow $\omega = \vec{\nabla} \times \vec{v}$. Note that this form of the equation of gyrotaxis is for spherical swimmers.

It should be noted that with chemotaxis, there is an additional coupling with an equation for the conservation of the chemoeffector that induces a chemotactic response.

Models without gyrotaxis

A continuum model was used for the first time by Childress, Levandowsky, and Spiegel 1975 to describe bioconvection due to gravitaxis in *Tetrahymena pyriformis*. At that time, gyrotaxis was not yet discussed in the context of bioconvection. The model consisted of equations (1.4,1.5) and cells were aligned with their preferential orientation $\vec{q} = \vec{e}_p$ given by upward swimming. The same model with \vec{e}_p given by the direction of a light intensity gradient was recently used in Dervaux, Capellazzi Resta, and Brunet 2017, and Arrieta et al. 2019 to describe bioconvection triggered by a light beam in suspensions of phototactic microalgae *Chlamydomonas reinhardtii*.

Deterministic models with gyrotaxis

After its discovery, gyrotaxis was included in bioconvection continuum models by Pedley, Hill, and Kessler 1988. At this stage, cells swimming direction \vec{q} was calculated in a deterministic way and the diffusion coefficient was written independently of \vec{q} . The authors explained that it is inconsistent because the diffusion coefficient should represent the probability of cell orientation which is biased around \vec{q} . They argued, however, that the model is still valid in the case of a weak bias of cells swimming in the direction \vec{q} .

Stochastic models with gyrotaxis

Later, Pedley and Kessler 1990 presented a stochastic model to resolve the inconsistency previously noted. In this new model, cells orientation \vec{q} is a random variable.

Its distribution is theoretically found by solving a Fokker-Planck equation based on the rate of change of \vec{q} , $\frac{\partial \vec{q}}{\partial t}$. It is the rate of change that is calculated deterministically with the gyrotaxis equation eq. (1.6). The drift due to taxis in eq. (1.5) is replaced by $v_{\text{drift}} \rightarrow |v_s| \langle \vec{q} \rangle$. Here, $\langle \vec{q} \rangle$ is not a unit vector anymore but is the ensemble average of \vec{q} and $|v_s|$ is the swimming speed of a microorganism. The diffusive tensor is calculated as a function of the distribution of \vec{q} , the speed of a swimmer $|v_s|$ and a correlation time τ_c .

1.3.5 Localized photo-bioconvection

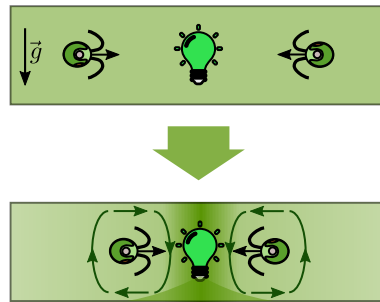


Figure 1.13: Mechanism in localized photo-bioconvection. Top : Cells diffusive behavior is biased by positive phototaxis along the horizontal light intensity gradient. Bottom : Cells accumulation at the center create a horizontal density gradient. Counter-rotating convection rolls with downward flow at the center originate from higher density at the center. They are self-sustained because on average, density remains higher at the center. Low and high concentration are represented in dim and dark green respectively.

In the study by Williams and Bees 2011a, the use of homogeneous light in bioconvection of the phototactic microalgae *Chlamydomonas* already demonstrated interesting features by selecting the mechanism of bioconvection between overturning mechanism and a gyrotactic mechanism, by either enhancing or opposing gravitaxis. Recently, another type of photo-bioconvection has emerged (Dervaux, Capellazzi Resta, and Brunet 2017; Arrieta et al. 2019) in suspensions of the phototactic microalgae *Chlamydomonas reinhardtii*. In these studies, no bioconvection patterns are observed in absence of light because cell concentration and liquid height are kept low enough (and so is the pseudo-Rayleigh number). Then, instead of using a homogeneous light field, a localized light beam is used to induce phototaxis along a light intensity gradient. Algae accumulate only locally and thus localized photo-bioconvection can be generated anywhere within the suspension. This novel mechanism is illustrated in Figure 1.13. It opens new possibilities to control bioconvective flows in space and time with complex inhomogeneous light fields, and under conditions of pseudo Rayleigh number much below the threshold for spontaneous - gravitactic driven - bioconvection.

In Dervaux, Capellazzi Resta, and Brunet 2017, cells accumulated around a vertical light beam projected at the center of a suspension in a horizontal Petri dish. In Arrieta

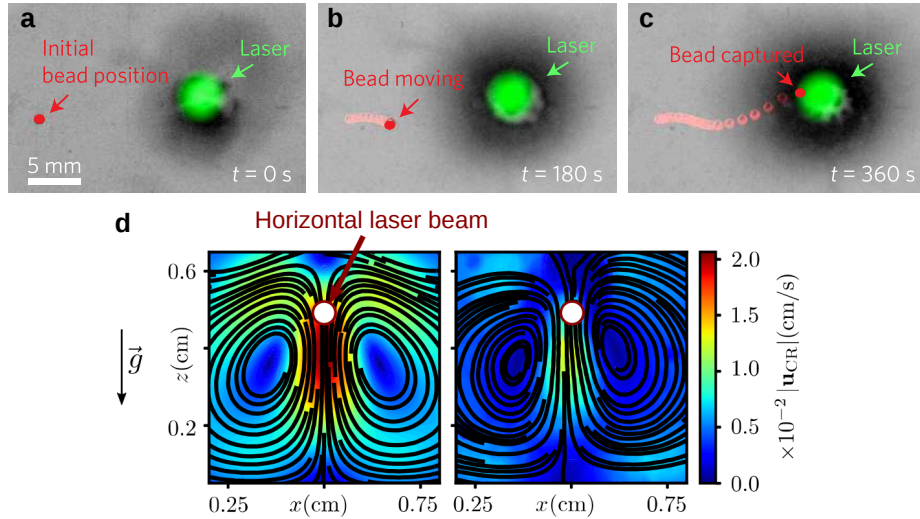


Figure 1.14: Flows signatures in localized photo-bioconvection. **a-c**, A suspension of *Chlamydomonas reinhardtii* in a horizontal Petri dish is imaged from top view. Bioconvection is triggered by cells accumulation around a vertical green light beam projected at the center of the suspension. Bioconvective flows are evidenced by the transportation of a floating glass bead at the free surface. From Dervaux, Capellazzi Resta, and Brunet 2017. **d**, A suspension of *Chlamydomonas reinhardtii* in a vertical Hele-Shaw cell is imaged from side view. Bioconvection is triggered by cells accumulation around a horizontal green light beam. Bioconvective flows are evidenced by cells recirculation. Left : Cells velocity field in numerical simulations. Right : cell velocity field in the experiments. From Arrieta et al. 2019.

et al. 2019, bioconvection was triggered in a vertical geometry around a horizontal light beam. Interestingly, both these studies provided first hydrodynamic signatures of bioconvective flows. These flows could be used as hydrodynamic tweezers and were evidenced by the transportation of a floating glass beat at the free surface (Figure 1.14.a). They were also evidenced by tracking the recirculation of cells (Figure 1.14.b).

1.3.6 Open questions in bioconvection

Advances in bioconvection are mainly driven by the description of cell concentration fields. Further insight could be obtained by looking at fluid velocity fields. What are the magnitude and the structure of bioconvective flows associated with cell concentration patterns ? In particular, this could provide new ways to test the hypotheses that cell-cell interactions can be neglected, as well as the possible dependence of the effective diffusion coefficient and the effective viscosity of suspensions with cell concentration in the range of volume fractions of bioconvection.

The emergence of the light control of flows in active suspensions opens new questions and possibilities (Javadi et al. 2020). In particular, can we tune inhomogeneous light fields to control bioconvection patterns and flows on demand ?

A remarkable instance of bioconvection was likely found in the alpine lake Cadagno in Switzerland by Sommer et al. 2017. The authors showed that the unusual presence of

thick homogeneous layers (~ 1 m) of uniform temperature and salinity in deep regions associated with high cells could be explained by a large scale bioconvective mixing induced by the oxygen-dependent bacterium *Chromatium okenii*. In the case of phototactic and photosynthetic microorganisms, can biomixing of gases and nutrients be controlled by light to enhance the growth-rate of suspensions, especially those used in photo-bioreactors ?

Continuum models of bioconvection including gyrotaxis are quite advanced. However, parameters related to behavior of microswimmers still need to be estimated from quantitative experiments. In this thesis, we worked with the phototactic microalgae *Chlamydomonas reinhardtii*. In the following section of the introduction, we present important results on *Chlamydomonas reinhardtii* random and phototactic motion.

1.4 *Chlamydomonas reinhardtii* as a model phototactic microswimmer

1.4.1 Presentation

The photoactive microalga *Chlamydomonas reinhardtii* has emerged as an important model microorganism in cellular biology, bioengineering and biophysics, from a fundamental point of view as well as for industrial applications. *Chlamydomonas reinhardtii* is the best-studied *Chlamydomonas* species, and many features *Chlamydomonas reinhardtii* behavior can be generalized to the whole genus and vice-versa. This green photosynthetic bi-flagellated cell (Figure 1.15.a) is found in fresh water. *Chlamydomonas reinhardtii* is widely studied for several reasons. It is used to study fundamental questions in life sciences such as metabolic pathways, photosynthesis or flagella-mediated locomotion (swimming or gliding). Its genome is fully sequenced. It has also been proposed as a potential production platform for biohydrogen and biofuel (Beer et al. 2009). A few words about the cultivation of *Chlamydomonas reinhardtii* in laboratories can be found in appendix A.

Chlamydomonas reinhardtii is also a model microswimmer for physicists. It has an almost spherical shape of diameter $10\ \mu\text{m}$ and is slightly denser than water with an excess density $\Delta\rho_{\text{CR}} \approx 50\ \text{kg/m}^3$. *Chlamydomonas reinhardtii* swims by performing non-reciprocal breaststrokes as required for self-propulsion at low Reynolds number (Figure 1.15.c) with forward effective strokes and backward recovery strokes. It rotates around its axis and follows an helical path (Figure 1.15.d). If the viewing distance is large enough, one can consider that the swimmer swims in a straight line along the helix axis with a velocity $v_{\text{CR}} \approx 50 - 100\ \mu\text{m/s}$. In a homogeneous environment, *Chlamydomonas reinhardtii* appears to follow a run-and-tumble dynamics but its trajectories can be biased by phototaxis. It is mostly phototactic to green and blue light and does not respond to red light and higher wavelengths.

In localized photo-bioconvection of *Chlamydomonas reinhardtii*, it is essential to quan-

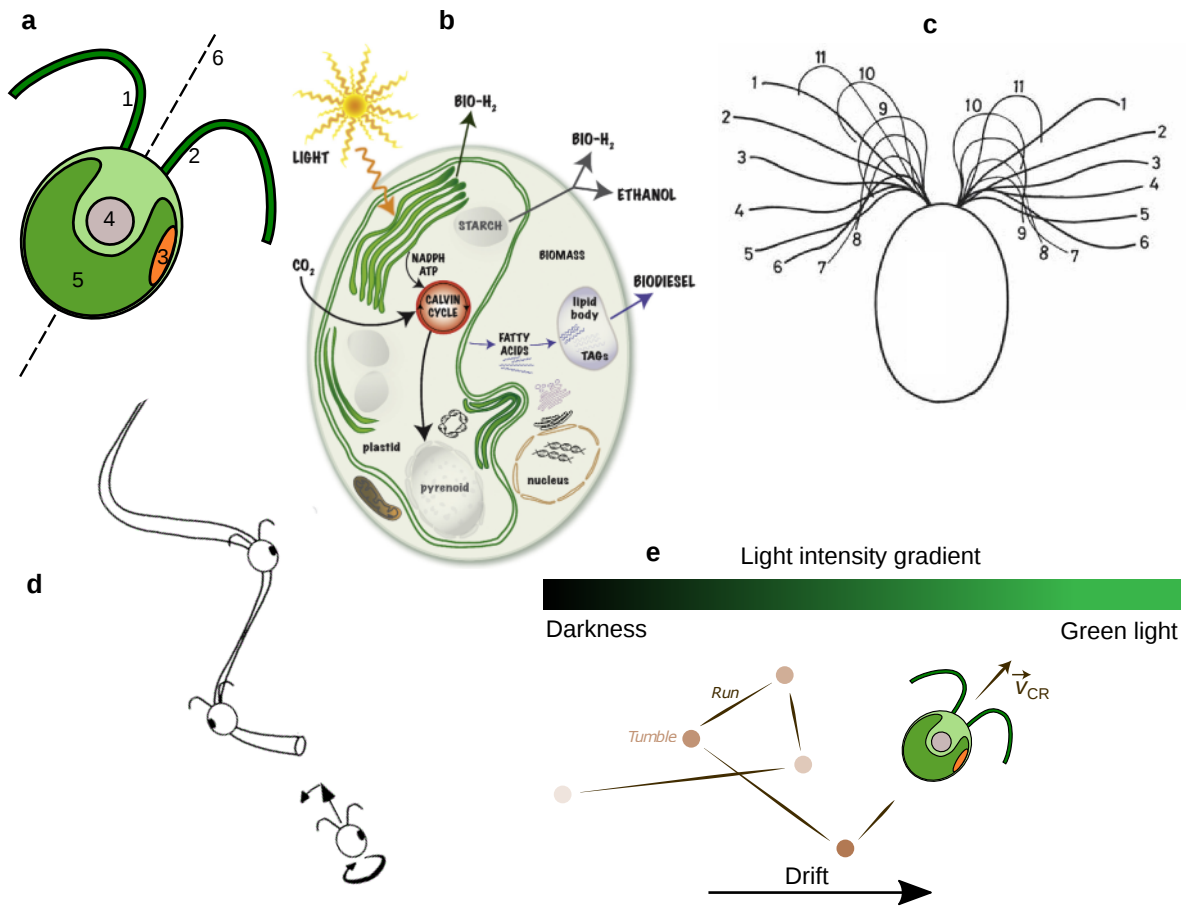


Figure 1.15: Presentation of *Chlamydomonas reinhardtii*. **a**, Minimal sketch of a *Chlamydomonas reinhardtii* cell. The cell body is a spheroid of diameter $\sim 10 \mu\text{m}$. It has two flagella attached to its anterior face, one on the *trans*- (1) and one on the *cis*- position relative to the eyespot (3) which detects light. The cells contains (non-exhaustive) a nucleus (4), a chloroplast (5) for photo-synthesis and has a posterior-anterior cell axis, or cell axis/body length axis (6). **b**, Metabolic pathways related to biofuel and biohydrogen production by cells (Beer et al. 2009). **c**, Decomposition of a beat of the flagella during swimming. The movements of the two flagella are not exactly identical and have an out-of-plane component (not shown here). From Ruffer and Nultsch 1985. **d**, As a result its flagella beating, a cell rotates around its body length axis and follows helical trajectories. **e**, Cell random trajectory biased by phototaxis.

tify the diffusive and phototactic behavior of cells, which will be the focus of this last section of the introduction. Historically, efforts in research dedicated to *Chlamydomonas* motility were first concentrated in understanding its phototaxis.

1.4.2 Methods for phototactic behavior analysis in *Chlamydomonas*

Phototaxis can be studied either on cell populations or on individual cells as illustrated in Figure 1.16 where a few examples of experimental methods are given.

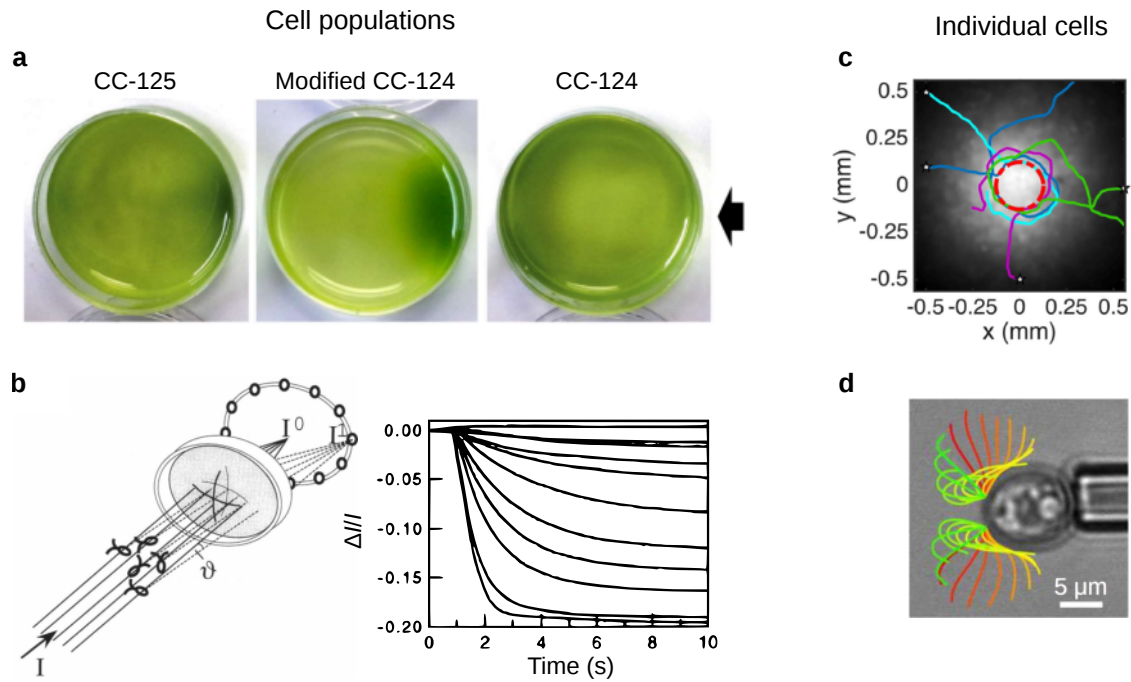


Figure 1.16: Examples of methods for phototactic behavior analysis of cells population or individual cells. **a**, The “dish test” for phototaxis assays. Suspensions of different *Chlamydomonas reinhardtii* strains contained in Petri dishes after 10 min of illumination from the right (black arrow). In the middle, strain CC-124 with modified expression of the gene *agg1*. (From Ide et al. 2016) **b**, Schematic representation of an infrared light scattering. Curves of the infrared scattered light intensity reflect the time course of orientation at different phototaxis stimulation irradiances. (From Schaller, David, and Uhl 1997) **c**, Individual trajectories of cells phototaxing around a light beam located at the center of the graph. (From Arrieta et al. 2017) **d**, Single cell held on a micropipette, here not to study phototaxis but for dynamical forces measurements. (From Böddeker et al. 2020)

Cells population phototaxis experiments

For cell populations, the most simple method for phototactic behavior analysis is the “dish test” (Figure 1.16.a). A Petri dish is filled with a suspension of cells and illuminated from one side. After a few minutes, cells accumulation on the illuminated side (here with CC-125 and modified CC-124) or on the opposite side (here CC-124) corresponds respectively to positive or negative phototaxis while no accumulation means no phototactic response. This simple test is very useful to quickly determine the phototactic sign of a strain, for example after a reagent was added to the medium or after a gene was modified. In Figure 1.16.a, it was used to evidence that a modification of the gene *agg1* can restore positive phototaxis of CC-124 (Ide et al. 2016). Schaller, David, and Uhl 1997 developed an infrared light scattering system to monitor the degree of orientation of a cell populations. *Chlamydomonas* cells are not exactly spherical so that the scattered infrared light intensity increases as more and more cells respond to an orienting actinic

light (a light source that triggers a photo-response) stimulus. This methods allows for quantitative measurements, at such as the measurement of the sensitivity to light intensity as a function of the wavelength (action spectra). This method is quite sensitive and the authors could measure how an initial orientation induced with a continuous light was transiently perturbed by dim light flashes.

Individual cells phototaxis experiments

Phototaxis of single cells can be studied by tracking individual trajectories in a light landscape as in Figure 1.16.c (Arrieta et al. 2017). Here, individual trajectories show loops around the light source, a feature that would not be accessible by studying the phototactic response of a population. Cells can be tracked only on finite portions of their trajectories, typically during tens of seconds and over submillimetric distances. The authors supplemented their individual cells phototaxis study with a population response study. Small portions of cell concentrations profiles could be estimated from individual trajectories and did match cell concentration profiles obtained from populations experiments. Individual cells experiments can also be performed with cells held on micropipette. A high-speed camera allows to track the flagellar beating as in Figure 1.16.d. In such a configuration, the eyespot can be stimulated and flagellar responses can be observed (Rüffer and Nultsch 1991; Harz and Hegemann 1991). In fact, fundamental steps in the understanding of phototaxis were possible thanks to individual cells experiments, in particular experiments with the micropipette technique.

1.4.3 The eyespot and intracellular mechanisms in phototaxis

General description of *Chlamydomonas* eyespot apparatus

The eyespot apparatus allows *Chlamydomonas* to sense light and to respond to it. It is located at the equator of the cell (the flagella basal body being one pole), with an offset of 45° counterclockwise from the flagella plane when the cell is viewed from behind with the *cis*-flagellum on the right. Figure 1.17 represents a cross section of the eyespot. Light is detected by channelrhodopsins photoreceptor proteins named ChR1 and ChR2 located on the cell plasma membrane. Below photoreceptors, the eyespot contains layers of carotenoid granules responsible for the orange color of the eyespot. Each layer is covered by a thylakoid double membrane. Carotenoid granule layers both reflect and attenuate light. When light comes from the inside of the cell, the “rear side”, it is blocked both by the cell body (attenuation) and the carotenoid layers (attenuation and reflection). When it comes from the outside of the cell, the “front side”, it is reflected after passing through the plasma membrane and thus amplified on the photoreceptors. Therefore, the eyespot works as a directional antenna for light coming from the “front side”.

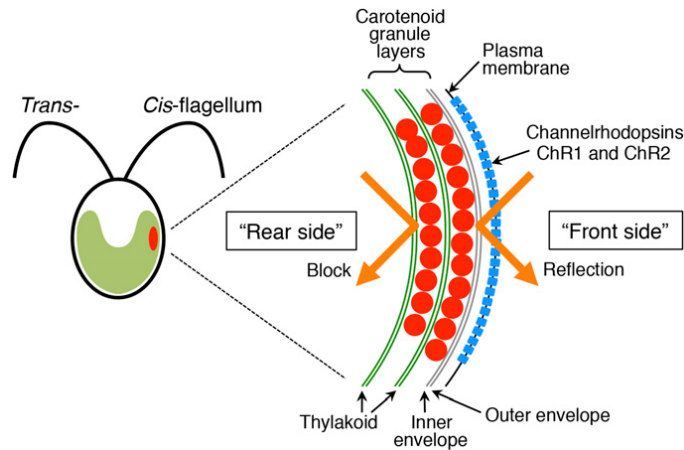


Figure 1.17: Schematic diagram of *Chlamydomonas reinhardtii* eyespot structure. The eyespot consists of carotenoid granule layers (red) and Channelrhodopsins (ChR1, ChR2; blue) photoreceptor proteins. The carotenoid layers reflect light (orange arrow): the signal from the inside of the cell (“rear side”) is blocked before the channelrhodopsins, while it is amplified from the outside of the cell (“front side”) on the channelrhodopsins. (From Ueki et al. 2016)

History of the research on *Chlamydomonas* eyespot apparatus

The research on *Chlamydomonas* eyespot apparatus really took off with first electron microscopy in 1980 and culminated when the photoreceptors were finally identified in 2001.

Carotenoid granule layers optics The carotenoid granule layers were observed with electron microscopy observations by Foster and Smyth 1980. The authors then explained that the eyespot can be considered as an absorbing quarter-wave mirror with reflection by constructive interferences. They theoretically predicted maximum reflectivity in blue light with a band width at half maximum reaching green light. For light coming from the “front side”, the authors noted that, interestingly, constructive interference between the incident light and the reflected light should give a maximum light intensity at the plasma membrane. Consequently, they postulated that photoreceptors, unidentified at that time, could be located on the membrane. Schaller and Uhl 1997 later measured a maximum reflectivity in green light, in contrast to the theoretical results. They also showed that the attenuation through the cell body and the carotenoid layers peaks in blue and is very poor in yellow.

Thus, the carotenoid granule layers optics and the eyespot location explained the directivity of light detection in blue-green light. They also gave a clue of the possible location of photoreceptors on the plasma membrane.

Investigation on photoreceptors for phototaxis In the same study by Foster and Smyth 1980, the authors proposed that photoreceptors should be rhodopsin proteins based on ac-

tion spectra of *Chlamydomonas*. They also estimated their minimal number per cell to be around 30000. Then, Foster et al. 1984 provided experimental evidence that photoreceptors in *Chlamydomonas* phototaxis indeed belong to the rhodopsin proteins family. From an initially blind mutant, they reconstituted phototaxis with action spectra consistent with non-blind strains by incorporating analogs of rhodopsin retinal chromophore.

Since *Chlamydomonas* phototaxis is intrinsically linked to its swimming mechanism, there should be a signaling path from the eyespot to the flagella. The first experimental data available were that intracellular calcium concentration $[Ca^{2+}]$ controls the balance of beating of the two flagella. Kamiya and Witman 1984 worked with demembrated cells to control intracellular calcium concentration with solutions of different submicromolar levels. *Cis*- and *trans*-flagella activities responded differently to calcium levels. After that, Harz and Hegemann 1991 measured calcium currents response to light stimulation. They worked with single cells held on micropipette. Following light stimulation, calcium photocurrents peak within tens of ms in the rhodopsin photoreceptors and then in the flagellar region. The conclusion was that rhodopsin communicates with flagella through Ca^{2+} channels. The understanding of light the light responses chain in *Chlamydomonas* after this study is shown in Figure 1.18.

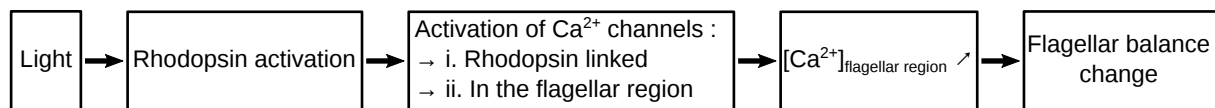


Figure 1.18: Diagram of the light responses chain in *Chlamydomonas* phototaxis. Based on the understanding after Harz and Hegemann 1991.

In particular, the extremely fast rise of calcium photoreceptors current after a brief light flash led to the conclusion that the rhodopsin and the calcium channel are intimately linked in a protein complex, or even within one single protein. This was verified ten years later, when the type of photoreceptor rhodopsin proteins were finally uncovered following the *Chlamydomonas* genome project. They were identified and named Channelrhodopsin ChR1 and ChR2 by Hegemann, Fuhrmann, and Kateriya 2001. They are light-activated cation channels, the first of their kind identified in the rhodopsin proteins family. They are indeed located at the plasma membrane, as predicted by Foster and Smyth 1980

1.4.4 Phototaxis and motility

Phototaxis of *Chlamydomonas* can be broken down into two requirements. The first one is to find the right phototactic orientation by turning towards or away from the light source. The second one is to keep and swim along this direction. Let us see how both are achieved in this section.

Helical motion

Key to the mechanisms of phototaxis that will be described in the following is the helical trajectory combined with cell rotation of *Chlamydomonas* which was documented by R uffer and Nultsch 1985. The authors showed that *Chlamydomonas* rotates counterclockwise around its body length axis at about 1-2 Hz. It also follows a helical swimming path due to an additional beat of a dominant flagellum every 20 beats, with a beat frequency of ~ 50 Hz. This dominant flagellum is directed outward with respect to the helix.

Phototactic turn mechanism

The prevailing phototactic turn mechanism was elucidated by R uffer and Nultsch 1991. The cell rotation around its body is essential to scan its light environment and the cell orients itself by a change in the flagellar in case of periodic illumination of the eyespot. The authors stimulated the eyespot of *Chlamydomonas* single cells held on micropipette and observed the flagellar response in beating pattern with a high-speed camera. They chose to periodically stimulate the eyespot with a frequency of 1-2 Hz to mimic light modulation due to rotation when swimming perpendicular to light. Their observations for a positively phototactic cell are represented in Figure 1.19.

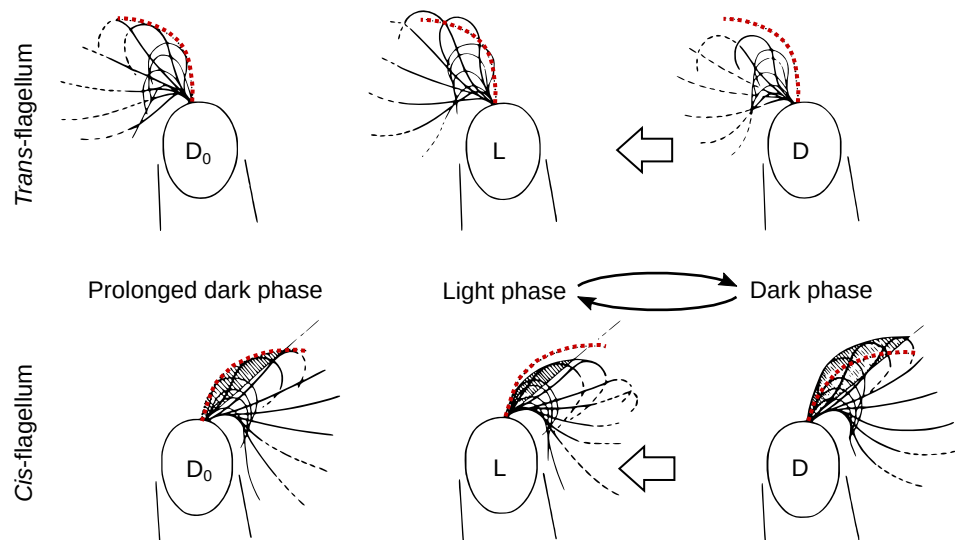


Figure 1.19: Changes of the flagellar beating pattern to light conditions of a positively phototactic *Chlamydomonas* cell held on a micropipette. *Trans*-flagellum and *cis*-flagellum are shown separately at different phases indicated on the cell body. D₀ : after a prolonged period without illumination. L, D : respectively light-on and light-off phases of pulsed irradiation at 2 Hz. During the light-on phase, the eyespot faces light coming from the right (white arrows). Dotted red light indicate the reference front amplitude of the D₀ beat with which to compare the L and D beats. (From R uffer and Nultsch 1991)

The flagella beating in periodic illumination was compared to the beating after a prolonged period without illumination. During the light-on phase, the *trans* and *cis*-

flagella respectively beat stronger and weaker. This is reversed during the light-off phase. How this enables a cell to orient itself toward light is illustrated in Figure 1.20.

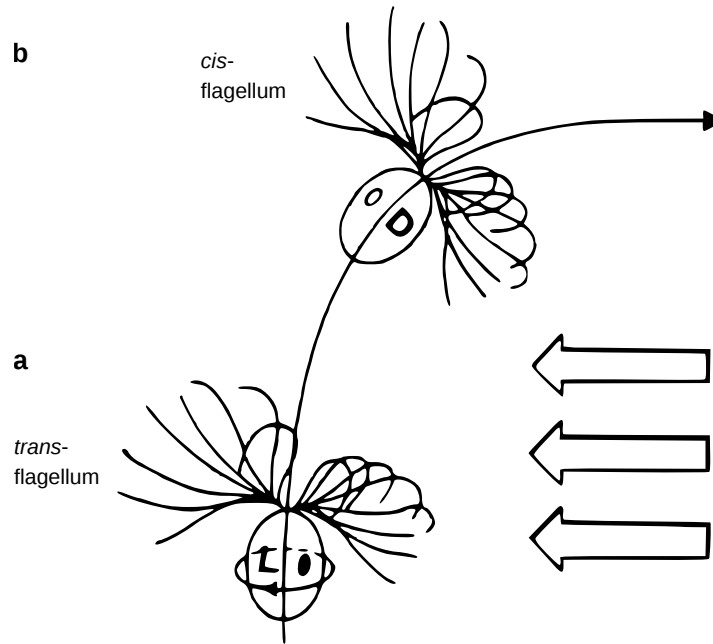


Figure 1.20: Schematic representation of positive phototactic turn in *Chlamydomonas*. The trajectory of the cell in unilateral light coming from the right (white arrows) is materialized by the curvilinear arrow. The eyespot is represented by an ellipse which is plain when facing the light (L) or empty when shaded by the cell body (D). L and D : respectively “light-on” and “light-off” as in Figure 1.19 but here from the rotating point of view of the eyespot. **a**, L-phase, stronger beat of the *trans*-flagellum. **b**, D-phase after a half rotation around the body length axis, stronger beat of the *cis*-flagellum. (From Ruffer and Nultsch 1991)

The authors proposed that a phototactic turn occurs when a cell initially swims perpendicularly to the light and consists of two steps. When the eyespot faces light coming from the front side, the *trans*-flagellum transiently beats stronger (Figure 1.20.a). The cell then makes an eighth turn towards light during half rotation around the body axis. During the second half rotation, the eyespot faces away from the light (Figure 1.20.b). It is then the *cis*-flagellum that transiently beats stronger and the cell makes an additional eighth turn. Finally after one cell body rotation, a quarter turn towards light has been completed. The flagella work the other way around for negative phototaxis. With this mechanism, the timescale of a phototactic turn is thus given by one body rotation and is of the order of ~ 1 s. This also justifies the equatorial location of the eyespot for phototactic turns to occur when the cell swims perpendicularly to light.

Keeping phototactic orientation

Schaller, David, and Uhl 1997 then pointed out that cell rotation a body length axis aligned with the direction of light can not produced different signals for positive or negative

phototaxis because the eyespot is located on the equator of the cell. An additional mechanism to keep the right phototactic orientation, away or towards from the light, should be proposed. The authors argued the right phototactic orientation should correspond to minimum photon absorption and thus reorientation probabilities. They explained that it is achieved by a shielding of the eyespot photoreceptors during the helical swimming path in between reorientations.

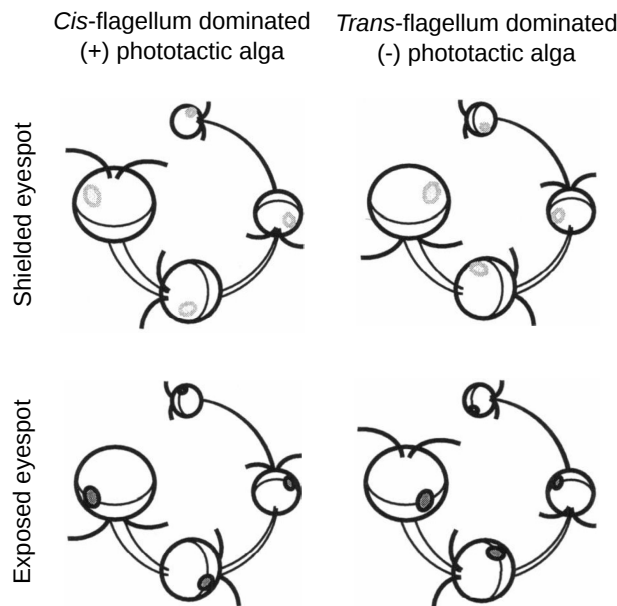


Figure 1.21: *Trans*- or *cis*- dominance dependency of the eyespot orientation relative to the helical swimming path of a *Chlamydomonas* cell. Schematic representation of the helical swimming path of *cis*- or *trans*- dominated algae swimming towards or away from a light coming from the observer. A dark shaded eyespot means that it faces light, while a lightly shaded eyespot means that light goes through the cell body first. (From Schaller, David, and Uhl 1997)

Figure 1.21 illustrates the role of the helical swimming path of an alga as understood by Schaller, David, and Uhl 1997 for a light coming from the observer and aligned with the helix axis. When the *cis*-flagellum dominates (left column), the eyespot is shielded if the helix is oriented towards light. This is due to the eyespot offset from the flagella plane. Photon absorption and reorientation probabilities are minimized, and this is helpful for positive phototaxis. If the helix is oriented away from light, photoreceptors are not shielded and it is likely that the cell will experience phototactic turn due to photons absorption. It is the other way around for a *trans*-flagellum dominated alga (right column). This reasoning suggests that *cis*-dominated cells should phototax positively while negatively phototactic cells should be *trans*-dominated. It was supported by an indirect observation (using light reflection by the eyespot) that the eyespot was raked forward/inward with respect to the helical path for a *trans*-dominated alga.

Phototaxis and flagellar dominance

The mechanisms for phototaxis proposed by R uffer and Nultsch 1991 and by Schaller, David, and Uhl 1997 were finally confirmed by direct observations of free swimming cells by Isogai, Kamiya, and Yoshimura 2000.

They found that the phototactic sign is indeed associated to a flagellar dominance. *Cis*-dominance (*trans*-dominance) was correlated to positive (negative) phototaxis. Then, they observed *in situ* phototactic turns in two steps predicted by R uffer and Nultsch 1991. They observed the behavior shown in Figure 1.19 for *cis*-dominated positive phototaxis and the reverse for *trans*-dominated algae. Finally, they saw that the natural dominance then helped to keep the right phototactic orientation by shielding the eyespot, as predicted by Schaller, David, and Uhl 1997.

However, it remains elusive how this flagellar dominance is regulated. How a the switch from positive to negative phototaxis occurs at high light intensity is not clear either.

Photo-gyrotaxis or photo-focusing

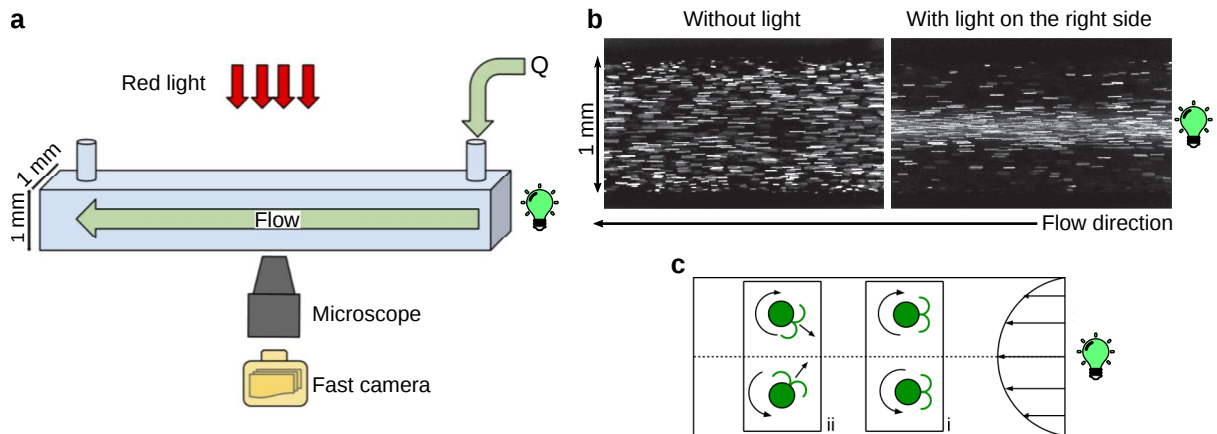


Figure 1.22: Experimental study to investigate the interaction between light-seeking algae and flow. **a**, . A Poiseuille flow of a *Chlamydomonas reinhardtii* suspension is imposed with a flow rate Q in a millifluidic channel. A light source is located on the right of the channel to attract microalgae. The cells transport is imaged from below. **b**, Cells trajectories. Cells are transported from right to left by the flow, their trajectories are represented by white rods obtained by superposing images. Left : without light, homogeneous cells density profile on the transverse direction. Right : with light on the right side, higher cell concentration at the center of the flow. **c**, Proposed mechanism for the photo-focusing of cells attracted by an upstream light source. i) Phototactic turn towards light. ii) Rotation by vorticity. (From Garcia, Rafai, and Peyla 2013)

The phototactic turn mechanism enabled to understand the coupling between flows and phototaxis in an experimental study which addressed this fundamental question. Garcia, Rafai, and Peyla 2013 used light to focus algae in a flow with the experimental setup sketched in Figure 1.22.a.

Chlamydomonas reinhardtii cells were subjected to a millifluidic flow. By turning on an attractive light upstream, a band of concentrated cells at the center of the channel was observed (Figure 1.22.b). This self-focusing was understood as gyrotactic effect : the mean cells orientation is the result of a competition between flow vorticity that rotates cells and phototactic turns towards light (Figure 1.22.c). This phenomenon was only observed when the shear rate was in the range $1 \text{ s}^{-1} \lesssim \dot{\gamma} \lesssim 3 \text{ s}^{-1}$. It corresponds to the inverse of a phototactic turn timescale. Below this range, the flow is too weak to rotate cells while above it, phototactic turns are too slow compared to cells rotation by the flow.

This experiment is the equivalent of the historical experiment gyrotactic focusing of gravitactic algae in downwelling flow by Kessler 1985. Here, light provides a greater control: focusing can be controlled for any flow direction and can be switched on and off on demand.

1.4.5 *Chlamydomonas* motion in the dark

We now present some results that reflect the current state of the art concerning *Chlamydomonas* motility in the absence of light.

Analysis of the mean square displacement

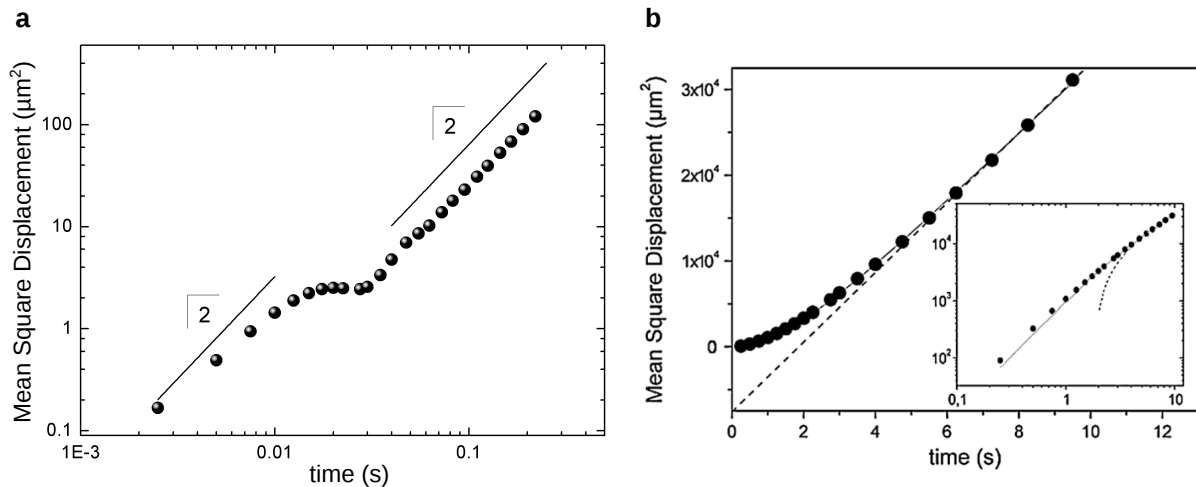


Figure 1.23: Mean square displacement (MSD) of *Chlamydomonas reinhardtii* cells as a function of time. **a**, Mean square displacement of cells as function of time at short time scales. From Garcia 2013. Solid lines represent a slope 2 on log scale. **b**, Mean square displacement of cells as a function of time Rafai, Jibuti, and Peyla 2010 entering the diffusive regime. The evolution of the MSD is well described by a persistent random walk of direction correlation time $\tau_c = 3.5 \pm 0.1 \text{ s}$. An estimate of the diffusion coefficient is $D = (1.0 \pm 0.2) \times 10^{-9} \text{ m}^2/\text{s}$. Inset : log-log plot.

The helical swimming of *Chlamydomonas* was well documented by Ruffer and Nultsch 1985 using high-speed microcinematography (see opening of section 1.4.4). Garcia et al. 2011, Garcia 2013, and Rafai, Jibuti, and Peyla 2010 extended these studies. They

reported the mean square displacement (MSD, $\langle r(t)^2 \rangle$) measured across cell population as a function of time, over a large range of timescales.

For $t < 0.3$ s, two ballistic regimes with $\langle r(t)^2 \rangle \propto t^2$ were found (Garcia et al. 2011; Garcia 2013, Figure 1.23.a). They are separated by a plateau at the period of flagella beating $1/f_b = 32$ ms. Thus, the first ballistic regime for $t < 1/f_b$ gives a speed $v_b = 130$ $\mu\text{m/s}$. At this timescale, the trajectories recorded are either forward with speed v_E due to effective strokes or backward with speed v_R due to recovery strokes with $v_E > v_S$ and with equal probabilities, which corresponds to the non-reciprocal body kinematics of the swimming strategy at low Reynolds number. Thus, v_b corresponds to the forward on average velocities difference over one beat cycle $v_b \approx 0.5 \times (v_E - v_R)$. The second ballistic speed for $t > 1/f_b$ is $v_a = 50$ $\mu\text{m/s}$. At this timescale, movements perpendicular to the helices axes average out in the MSD and v_a corresponds to the velocity of trajectories projected on the axes of the helices.

At larger timescale, a diffusive regime is observed with $\langle r(t)^2 \rangle \propto t$ (Figure 1.23.b). More precisely, the evolution of the MSD for $t > 0.3$ s gives a direction correlation time $\tau_c = 3.5 \pm 0.1$. The total duration of the trajectory remains quite small to estimate a diffusion coefficient D . Values as small as $D = (1.0 \pm 0.2) \times 10^{-9}$ m^2/s could be estimated (Rafai, Jibuti, and Peyla 2010).

Characterization of the diffusive behavior

Polin et al. 2009 investigated and identified the mechanism behind the random motion of *Chlamydomonas reinhardtii*. They found that it consists of stochastic switches between synchronous and asynchronous flagellar beatings. They observed these two states in high-speed movies of *Chlamydomonas reinhardtii* held by micropipettes (Figure 1.24.a). Long periods of synchronous beating were separated by short periods of asynchronous beating associated to a drift of the phase difference between the flagella. They also tracked individual trajectories consisting of long almost straight swimming and short period of sharp turns. They found that the the duration of turn t_{turn} and of asynchronous beating t_{drift} had nearly identical distributions (Figure 1.24.b). Thus, they showed that synchronous and asynchronous respectively lead to straight swimming and reorientations. At the macroscopic scale, they measured a collective diffusion coefficient by analyzing the spreading of cell concentration profiles (Figure 1.24.c). They found $D_{\text{exp}} = (0.68 \pm 0.11) \times 10^{-7}$ m^2/s . Dervaux, Capellazzi Resta, and Brunet 2017 and Arrieta et al. 2017 also measured similar values of collective diffusion coefficient (resp. $(0.85 \pm 0.15) \times 10^{-7}$ m^2/s and $(0.39 \pm 0.04) \times 10^{-7}$ m^2/s).

These values of collective diffusion coefficient measured at the macroscopic scale are much larger than the one estimated in Figure 1.23.b from MSD analysis ($D = (1.0 \pm 0.2) \times 10^{-9}$ m^2/s , Rafai, Jibuti, and Peyla 2010). Differences of speed and correlation time due to different strains and growth medium are not sufficient to explain this discrepancy between

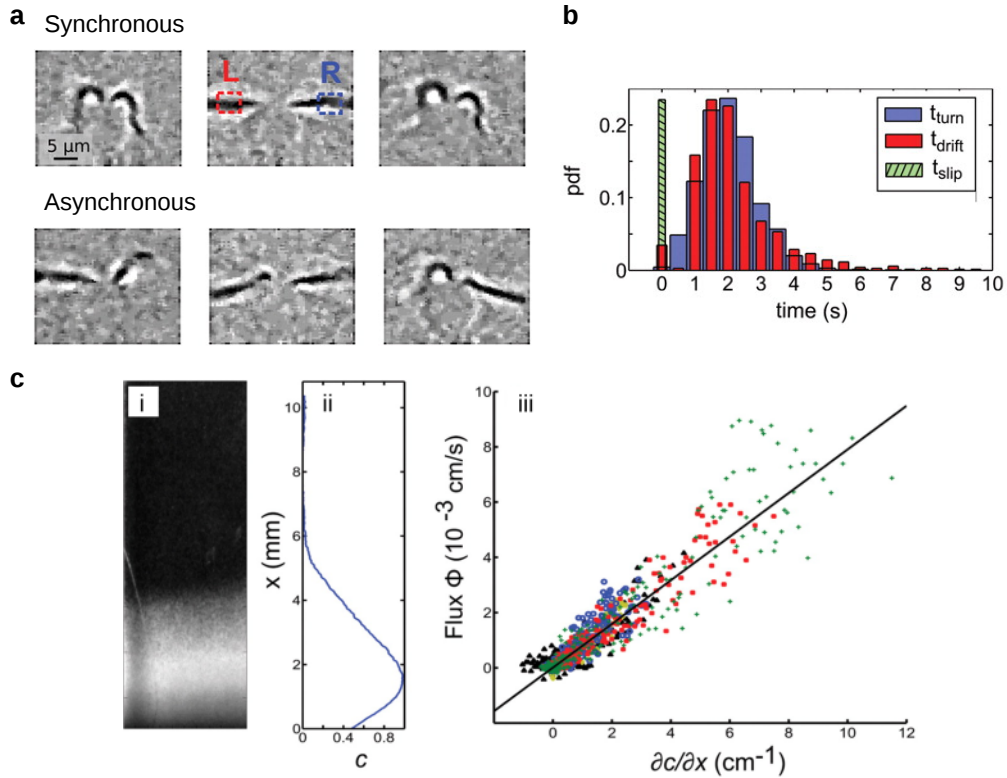


Figure 1.24: Characterisation of the run-and-tumble motion at both individual and population scales. **a**, Frames showing a synchronous flagella beating cycle (top images) and an asynchronous beating cycle (bottom images). **b**, Distributions of the duration of turns in trajectories (t_{turn}), periods of asynchronous beating (t_{drift}), and extra beats (“slips”, t_{slip}). **c**, Diffusion of a population of cells in a plastic cuvette. Cells were concentrated at the bottom of a plastic cuvette (i). The dynamics of concentration profiles (ii) was analyzed. Far from the bottom, concentration flux was measured as a function of the cell concentration gradient at various points in space and time (iii). According to Fick’s law, the linear relationship yields a collective diffusion coefficient $D_{\text{exp}} = (0.68 \pm 0.11) \times 10^{-7} \text{ m}^2/\text{s}$. From Polin et al. 2009.

measurements on cell populations and on individual cells. It should be noted that for it is very challenging experimentally to keep cells long enough in a large enough field of view to characterize their individual diffusive regime. As for macroscopic measurements, they should be performed on a range of cell concentration as large as possible to isolate the potential effects of concentration on the measured diffusion coefficient. In this work, since we performed experiments on cells population, we used $D = (0.85 \pm 0.15) \times 10^{-7} \text{ m}^2/\text{s}$ also obtained on a population scale and with the same strain in the same liquid medium as in our experiments (Dervaux, Capellazzi Resta, and Brunet 2017).

1.4.6 Additional features

Gravitaxis

Chlamydomonas is also (negatively) gravitactic. A gravitational torque orients cells upward on average in the absence of flows or phototaxis. There are two possible mecha-

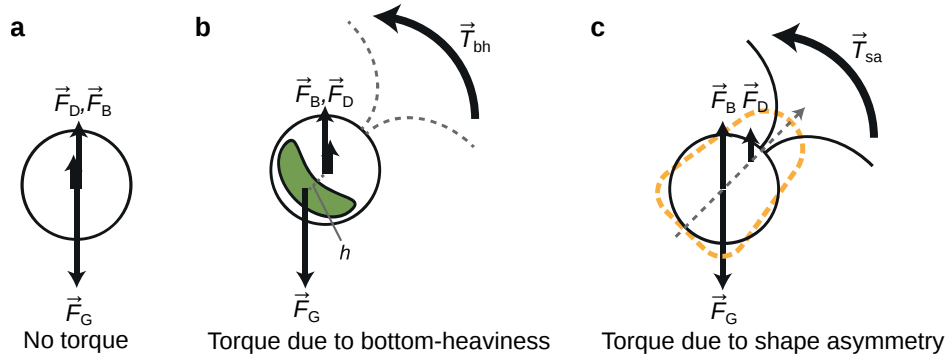


Figure 1.25: Possible mechanisms for gravitaxis in *Chlamydomonas reinhardtii*. Straight arrows represent the forces of buoyancy (\vec{F}_B), drag (\vec{F}_D) and gravity (\vec{F}_G) anchored at their centers of application. Gravitational torques (curved arrows) orient cells upward. **a**, Centers of \vec{F}_B , (\vec{F}_D and \vec{F}_G are all the same as the cell body center of geometry, resulting in a zero torque. **b**, A bottom-heaviness torque \vec{T}_{bh} is due to the posterior location of \vec{F}_G at a distance h from the geometric center. **c**, A shape asymmetry torque \vec{T}_{sa} is due to the anterior position of the center \vec{F}_D when the flagella are taken into account in the shape. From Kage et al. 2020.

nisms leading to the same effect, as explained by Roberts 2006 and shown in Figure 1.25. The gravitational torque either originates from bottom-heaviness (Figure 1.25.b) or from shape asymmetry (Figure 1.25.c). Gravitaxis due to bottom heaviness was often assumed (Pedley 1992; Hill and Pedley 2005; Bees 2019), although recent studies emphasize the contribution of shape (Kage et al. 2020). The upward gravitactic drift was found to be $v_d \sim 5 \mu\text{m/s}$ (Bean 1977; Polin et al. 2009).

Dependence of phototaxis on external factors

When studying phototaxis, one should keep in mind possible dependences on external factors. We give here some examples.

The dependence on culture growth was studied by Stavis and Hirschberg 1973 and Feinleib and Curry 1971. In particular, phototaxis is at its strongest during the exponential growth of cells. Stavis and Hirschberg 1973; Nultsch 1979 studied the effects of cations on phototaxis and motility in *Chlamydomonas reinhardtii*. They found inhibitions effects at high cations concentrations but also a specific transient boost following an addition of calcium at moderate concentration. Although photosynthesis is actually not needed for phototaxis (Stavis and Hirschberg 1973), the photosynthetic activity of cells can alter their phototaxis (Takahashi and Watanabe 1993). CO_2 can modify the critical inversion intensity between positive and negative phototaxis (Nultsch 1977). One can use reactive oxygen species (ROS) or ROS-scavengers to control the sign of phototaxis (Wakabayashi et al. 2011). Finally, a finding that stands out is that the effectiveness of phototaxis increases when lowering cells swimming speed due to better light detection (Choudhary, Baskaran, and Sharma 2019). In particular, this translates into a greater

phototactic effectiveness in concentrated suspensions ($> 3 \times 10^7$ cells/mL).

1.4.7 Concluding remarks and open issues

The role of flagella is well understood in *Chlamydomonas* random and phototactic motilities. During almost straight swimming, *Chlamydomonas* actually rotates around its body axis and follows a helical trajectory with a naturally dominant flagellum located outward. In random motion, changes in direction are due to short periods of asynchronous beating that result in sharp turns in cells trajectories. Phototaxis, whose sign is correlated to the natural flagellar dominance, relies on the other hand on opposite amplitude modulations of flagellar motion for reorientation and on shielding the eyespot to keep the phototactic orientation. Nevertheless there are still some open questions.

The origins of the regulations of random change of directions and phototactic reorientations remain open issues. It is also possible that there is an interplay between these regulations which has not been studied yet.

Diffusion coefficients can be measured either with cells population experiments or from individual cells. However, some discrepancies remain between measurements performed at these two different scales.

In phototaxis on the other hand, there is a lack of quantitative laws linking the directed biased velocity to the light intensity. In the context of bioconvection, this is in contrast with highly advanced models of gyrotaxis. Moreover, the difference between swimming in a light intensity gradient and swimming along the direction of propagation of light is often omitted and both are referred to as “swimming towards light”.

1.5 Outline of this thesis

The main goal of this thesis is to understand the collective response, at the scale of a population, of the model photosynthetic micro-algae *Chlamydomonas reinhardtii* to complex space and time-dependent light fields. The main goal is divided into the following objectives.

1. Propose a phenomenologic law of the phototactic velocity of a population of *Chlamydomonas reinhardtii* in light intensity gradients with a dependence on the light intensity.
2. Study the self-organization of cells when bioconvective flows are induced by phototaxis in localized photo-bioconvection with a control on both the heterogeneous illumination and the pseudo-Rayleigh number.
3. Quantify the magnitude and structure of bioconvective flows for the first time, investigate their relationship with the cell concentration field and compare them with a classical model of bioconvection.

4. Study a possible effect of long sustained light-controlled bioconvection on the growth-rate of *Chlamydomonas reinhardtii* cultures, with in mind an application to photo-bioreactors.

In chapter 2, the objective 1 is addressed using an experimental setup with a vertical light beam of controlled light intensity radial profile projected on thin layers of dilute suspensions of *Chlamydomonas reinhardtii*. The phototactic susceptibility to light intensity gradients is measured as a function of the light intensity at the population scale.

Next, the same experimental setup is used in a different regime to tackle the objective 2 in chapter 3. The pseudo-Rayleigh number is increased to induce bioconvective flows and we study the formation of pattern in localized photo-bioconvection with an additional spatial control of the heterogeneous illumination. The chapter 4 is then devoted to investigate theoretically the experimental observations of the chapter 3 in an asymptotic model of light-induced bioconvection which implements the phototactic susceptibility measured in chapter 2.

In chapter 5, a fluorescence based experimental setup is developed to conduct the first quantitative study of bioconvective flows (objective 3). Bioconvection is triggered by phototaxis in suspensions contained in vertical Hele-Shaw cells. The magnitude and the structure of the flow fields are quantified. The relationship between the cell concentration and the flow fields is also investigated and comparison with a classical model of bioconvection is proposed.

Finally, in chapter 6, an original experimental setup able to induce sustained and unstationary bioconvective flows over timescale comparable to the cell division timescale is presented, together with preliminary results on the influence of bioconvection on the growth-rate of *Chlamydomonas reinhardtii* cultures (objective 4).

A summary of the findings and a brief outlook are given as a conclusion in chapter 7. Additional methods and data are given in appendices A to C.

CHAPTER 2

***Chlamydomonas reinhardtii* phototactic susceptibility to light gradients**

In this chapter, we investigate the phototactic response of *Chlamydomonas reinhardtii* populations in heterogeneous light fields in the absence of flow. In particular, our goal is to find a phenomenologic law that describes the phototactic behavior *Chlamydomonas reinhardtii* in light intensity gradients with a dependence on light intensity. First, we introduce the two possible phototaxes: either along the direction of light propagation or along light intensity gradients. Then, we present an experimental setup used to measure the phototactic susceptibility to light intensity gradients at the population scale. We finally try to link this macroscopic measurement to properties of individual cells.

2.1 Phototaxis: a taxis in a vectorial field

Prevailing mechanisms in *Chlamydomonas* phototactic motility aim to explain how cells find an orientation towards light and keep this orientation. But because a light field is a vector field, swimming towards light can have two meanings : either swimming towards the direction from which light comes from, or towards increasing light intensities. Thus, there are two possible phototaxes and it remains unclear whether cells orient themselves in the light propagation direction, in the direction of light intensity gradient, or both.

Bennett and Golestanian 2015 proposed a simple swimming model for *Chlamydomonas* to better understand what drives phototaxis. It relied on a modulation of the flagellar balance by the light intensity received by the eyespot, in addition to a natural *cis*- or *trans*-dominance. A phase-shift between light and darkness, and noise to check for robustness were also added. They analytically derived that in their model, the swimmer is able to measure light intensity temporal derivative within its reference frame, which translates into light intensity gradient within the laboratory reference frame. Their model was then tested in numerical simulations of cells trajectories. They recovered essential features of *Chlamydomonas* motility : its rotation around its body-length axis, its helical path, its random walk in the dark and phototaxis when exposed to light. This is a good indication that *Chlamydomonas* should be able to detect light intensity gradients, although it is not known how at the subcellular level.

In most experiments involving phototaxis, directional light was used so that it could not be distinguished whether phototaxis was along the light intensity gradient or along the direction of propagation of light. The situation is quite different when a localized light beam is used as in our experiments and in recent studies (Giometto et al. 2015; Dervaux, Capellazzi Resta, and Brunet 2017; Arrieta et al. 2017; Arrieta et al. 2019). In this case, the directions of light propagation and light intensity gradient are at right angle to each other. Thus, there is a possible competition between phototaxes along those two directions. In Arrieta et al. 2017, the drift velocity of individual cells was measured and showed a similar radial profile shape than that of the light intensity gradient. In Dervaux, Capellazzi Resta, and Brunet 2017; Arrieta et al. 2019, experimental data of cells spatial repartition were well reproduced with a phototactic drift proportional to the light intensity gradient. But then, with the prevailing motility mechanism in phototaxis, it is unclear how a cell can both shield its eyespot to keep the right phototactic orientation and measure light intensity gradients at the same time. It is possible that the a drift proportional to the light intensity gradient only exists at timescales larger than the characteristic time between reorientations.

2.2 Experimental setup

In this section, we describe the experimental setup that we used to investigate how cells collectively respond to light intensity gradients.

2.2.1 Principle of the experiments

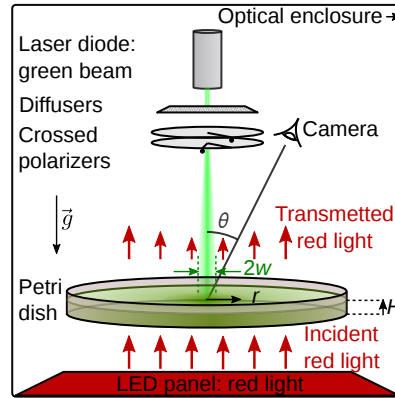


Figure 2.1: Sketch of the experimental setup used to measure *Chlamydomonas* phototactic response. A Petri dish contains a suspension of *Chlamydomonas reinhardtii* whose horizontal motion is directed by a green light beam. A camera is used to image the cell concentration field from above by measuring the amount of red light transmitted through the suspension. The experimental setup is kept in a dark enclosure.

The experimental setup is sketched in Figure 2.1. A levelled Petri dish (horizontality $\pm 0.05^\circ$, diameter 139 mm) was filled with an algal suspension of initial cell concentration c_0 to a desired liquid height H and placed in an optical enclosure. We turned on an actinic green light beam (532 nm) projected at the center of the Petri dish to establish an heterogeneous light environment. Cells response to the actinic light was monitored by measuring the cell concentration field. Because cells do not phototax in red light, this was achieved by measuring the amount of red light transmitted through the suspension. This experimental setup was adapted from Dervaux, Capellazzi Resta, and Brunet 2017 with an additional control of the green light beam width.

In all generality, the cells spatial organization results from a coupling between their phototaxis along the horizontal green light gradient, their diffusive behavior and their recirculation by bioconvection. In order to measure the phototactic response in the absence of flows, the pseudo-Rayleigh number was kept low enough to prevent bioconvective flows from arising in these experiments. We kept $H \approx 1$ mm and c_0 in the range $(1.5 - 3.0) \times 10^6$ cells/mL. The green light intensity gradient was tuned by widening the light beam and controlling the maximum light intensity at the center.

The detailed experimental protocol can be found in the appendices (appendix B.1).

2.2.2 Tuning of the light intensity gradients

To tune the light intensity gradient, we performed experiments with different beam profiles. We initially had a thin gaussian laser beam of known light intensity radial profile. Our goal was then to spread this light beam and still know the light intensity profile. We placed stacked diffusers on the light beam path to spread it out. The number of stacked diffusers between 0 and 4 defined a unique normalized light intensity radial profile while the maximum light intensity at the center was adjusted with crossed polarizers.

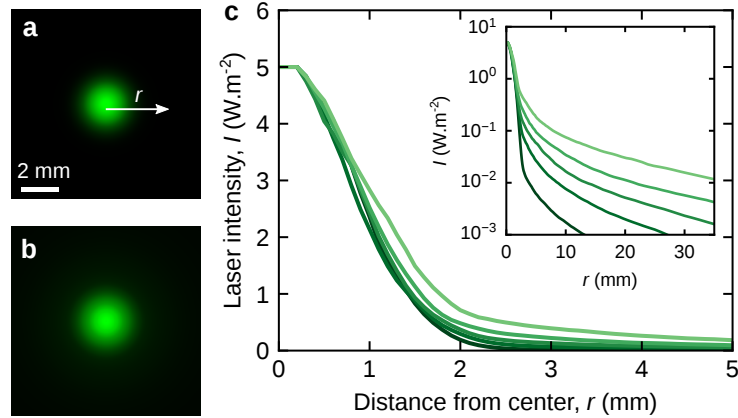


Figure 2.2: Laser beams of 5 different widths at fixed maximum light intensity. **a, b,** Images of laser beams reconstructed from their light intensity profiles. The green pixel intensities range from 0 to 255 and are proportional to the light intensity with 255 corresponding $5 \text{ W}/\text{m}^2$. The images shown are for the smallest (**a**) and the largest beam width (**b**). **c,** Radial profiles of the laser intensity with a fixed maximum light intensity of $I_{\text{max}} = 5 \text{ W}/\text{m}^2$.

After calibration (see appendix B.2), laser light intensity profiles could be precisely acquired over several decades of light intensity on the green channel of the images. 5 light beams with from 0 to 4 diffusers on their path are shown in Figure 2.2, here with a fixed maximum light intensity of $5 \text{ W}/\text{m}^2$. On the reconstructed images and on the lin-lin laser intensity radial profile, we see that the beams have gaussian profiles of similar widths close to the center, with only a minor effect of the diffusers in this part. However, the inset log-linear plot shows that the profiles have non-gaussian tails of significantly different widths due to the diffusers.

2.2.3 Top view cell concentration imaging

We used the red light transmitted through the suspension to measure the cell concentration field. After calibration, red light intensity could be converted to depth averaged cell concentration knowing the liquid height H .

The Figure 2.3 shows the time course of cells accumulation around the light beam. gives an example of a pattern formation from an initially homogeneous cell concentration field. After the laser was turned on at $t = 0$, cells accumulation around the location of the

laser was occurring within tens of minutes. A steady state was typically reached within an hour.

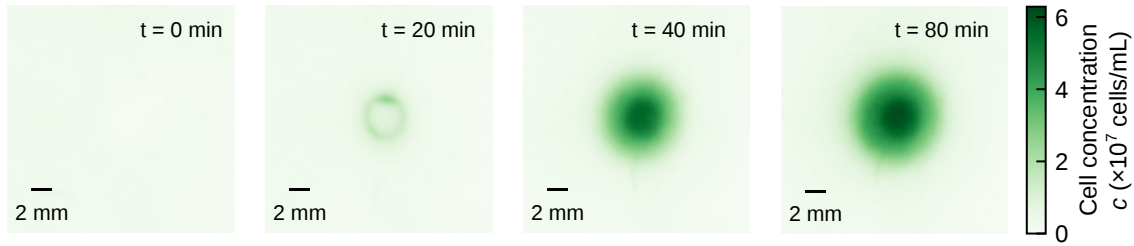


Figure 2.3: Time course of cells accumulation around the light beam. Top view of the cell concentration fields showing cells accumulation around the light beam. The green light beam was turned on at $t = 0$. $c_0 = 3 \times 10^6$ cells/mL, $H = 1$ mm, $Ra = 10$, $I_{\max} = 10$ W/m².

2.3 Measurement of *Chlamydomonas reinhardtii* phototactic susceptibility

With the experimental setup described previously, we let cells phototaxing in light intensity profiles of different spreadings and irradiances ranges in conditions where convection could be neglected. With a Keller-Segel model, we measured the phototactic susceptibility to light intensity gradients as a function of the spacially swept light intensity.

2.3.1 The Keller-Segel approach

After the green light was turned on, we monitored the cell concentration field until a steady state was reached. In these experiments, it shared the radial symmetry of the light field. Figure 2.4 shows that the effect of light intensity on phototaxis is visible on the concentration field. At low maximum light intensity, cells show only positive phototaxis and their concentration monotonously increases towards the center of the light beam (Figure 2.4.a). Upon increasing the maximum light intensity, an inversion from positive to negative phototaxis occurs and the maximum cell concentration is reached at a non-zero distance from the center of the light beam (Figure 2.4.b).

We now theoretically analyze these curves to extract the phototactic susceptibility. We performed experiments with very thin layers of algae suspensions, $H \simeq 1$ mm. In these conditions, recirculation flows generated by fluid density gradients can be neglected in the algal mass transport. This will be confirmed in the next chapters. We thus propose a Keller-Segel framework in which the stationary cell concentration field results from the balance between the cells phototactic flux that creates inhomogeneities and the diffusive flux that arises from concentration gradients.

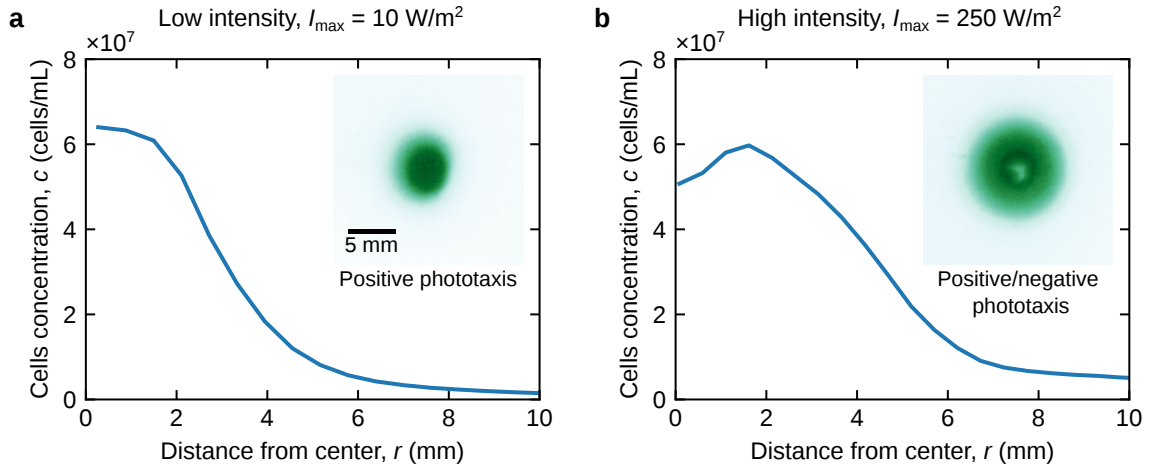


Figure 2.4: Stationary cell concentration radial profiles for different maximum light intensities. Insets images show the corresponding cell concentration fields. Here, the imposed light intensity radial profiles have the same relative shape but differ from their maximum values at the center. **a**, $c_0 = 2.6 \times 10^6$ cells/mL, $H = 1.0$ mm, $Ra = 10$, $I_{\max} = 10$ W/m². **b**, $c_0 = 2.5 \times 10^6$ cells/mL, $H = 1.2$ mm, $Ra = 16$, $I_{\max} = 250$ W/m².

$$D\vec{\nabla}c = c\vec{v}_{drift}$$

The velocity drift is controlled by light intensity gradient and we write : $\vec{v}_{drift} = \chi(I)\vec{\nabla}I$. χ is the phototactic susceptibility to light intensity gradients that we let depend on the spatially swept light intensity I . Then, given the radial symmetry of the experiments, the balance between diffusion and phototaxis reads :

$$D\frac{\partial c}{\partial r} = c\chi(I(r))\frac{\partial I}{\partial r}$$

The phototactic susceptibility can be obtained from gradients of cell concentration and light intensity at any point of the radial profiles.

$$\chi = (D\frac{\partial c}{\partial r}) / (c\frac{\partial I}{\partial r}) \quad (2.1)$$

For a single experiment, $\chi(r)$ can be calculated from the formula derived above, using $D = (0.85 \pm 0.15)10^{-7}$ m².s⁻¹ (see section 1.4.5). Knowing the light intensity profile $I(r)$, we thus obtain a parametric curve $\{I(r), \chi(r)\}$ (see Figure 2.5).

In Figure 2.5, the light intensity range is given by the fact that light intensity radial profiles typically decay by a factor 10^4 over a few tens of mm in the camera field of view. Here, only positive phototaxis is observed in this range ($\chi > 0$). The susceptibility is much higher at low light intensity and then decays by 5-6 orders of magnitude.

In order to characterized *Chlamydomonas reinhardtii* phototactic response over a wide range of light intensities, we performed a series of experiments by changing light beams.

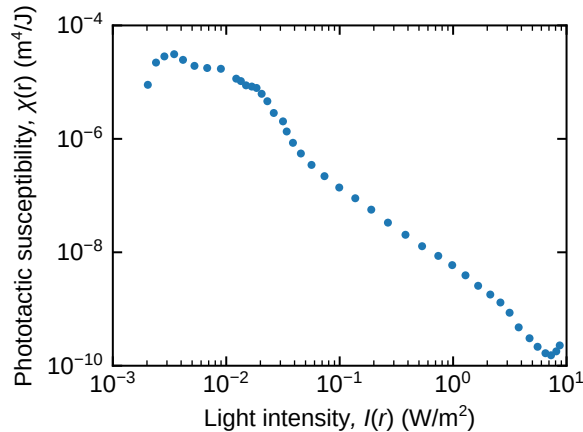


Figure 2.5: Parametric representation $\{I(r), \chi(r)\}$ of the phototactic susceptibility from a single experiment. Calculated from the stationary cell concentration radial profile in Figure 2.4.a.

By varying the maximum value at the center by 3 orders of magnitude, we obtained a total light intensity range of 7 decades (10^{-4} to 10^3 W/m²) in the series of experiments.

2.3.2 *Chlamydomonas reinhardtii* phototactic susceptibility curve

The parametric curves $\{I(r), \chi(r)\}$ obtained by changing light beams are plotted together on a bi-symmetric logarithmic plot in Figure 2.6 (light grey curves).

The curves overlap each other and are well described by a master curve of the phototactic susceptibility on 7 decades of green light intensity. Both positive and negative phototaxis are well described by a nonlinear function of light intensity. This finding is similar to the study by Giometto et al. 2015 in the phytoplankton *Euglena gracilis*, where the authors also used a Keller-Segel model to analyze concentration profiles around a light beam.

At very low light intensity, no sensitivity to light intensity gradients is detected. Above a clear detection threshold intensity I_{th} , cells show positive phototaxis ($\chi(I) > 0$). The susceptibility decays as $\sim I^{-1.5}$ over 5 orders of magnitude of light intensity, highlighting in particular an enhanced sensitivity at low light intensity. At a critical inversion light intensity I_{crit} , cells switch from positive to negative phototaxis with a change of sign of $\chi(I)$. The negative phototactic susceptibility then further increases (the cells become more and more repelled by the light) as the light intensity further increases above I_{crit} . The detection threshold and the critical inversion intensity that delimit the range of positive phototaxis are reported in Table 2.1.

2.4 Range of light detection in phototaxis

We obtained two remarkable values of light intensity in the curve of the susceptibility to light intensity gradients : a detection threshold intensity and a critical inversion intensity

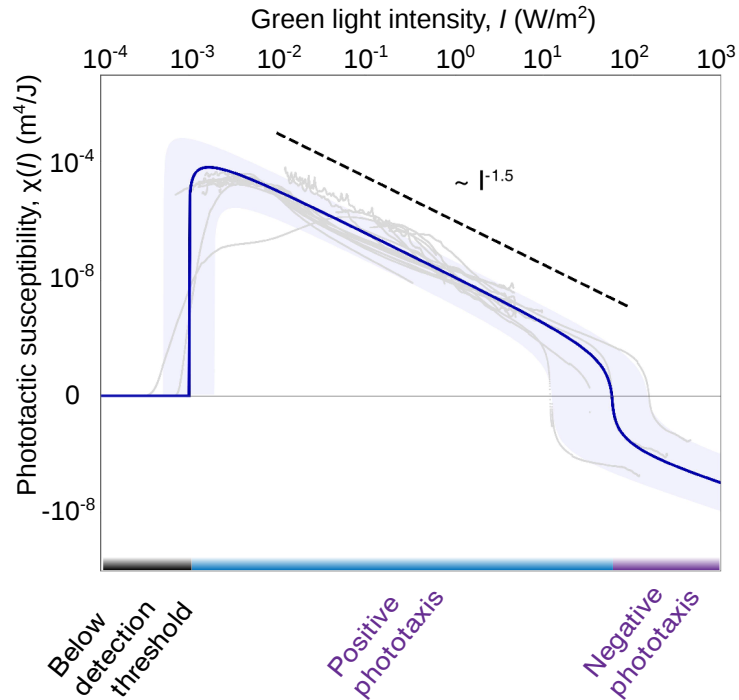


Figure 2.6: Measurement of *Chlamydomonas Reinhardtii* phototactic susceptibility. The graph is a bi-symmetric logarithmic plot of the phototactic susceptibility $\chi(I)$. It is obtained by plotting the transform $\text{sign}(\chi) \cdot \log(C[1 + |\chi|/C])$ as a function of $\log(I)$. The constant C , here of value $10^{-12} \text{ m}^4/\text{J}$, is arbitrary and removes the singularity of the log-log representation near $\chi = 0$. Light grey curves correspond to individual experiments and are fitted by a master curve in blue.

Symbol	Meaning	Value
I_{th}	Detection threshold intensity	$(1.2 \pm 0.7) \times 10^{-3} \text{ W/m}^2$
I_{crit}	Critical inversion intensity separating positive and negative phototaxis	$101 \pm 81 \text{ W/m}^2$

Table 2.1: Light intensity range of positive phototaxis in *Chlamydomonas Reinhardtii*. The light intensity range of positive phototaxis is determined from the phototactic susceptibility curve. It goes from a detection threshold intensity to a critical intensity separating positive and negative phototaxis.

from positive to negative phototaxis. This allows us to discuss the range of light detection in phototaxis of *Chlamydomonas reinhardtii*.

2.4.1 Detection threshold

Detection threshold intensities were previously measured for phototaxis in directional light by varying the homogeneous light intensity from one experiment to the other. Feinleib and Curry 1971 measured threshold intensity for phototaxis with both cell populations and individual cells methods. In cell populations experiments, they measured the rate of light-induced algae accumulation, while trajectories were analyzed in individual cells experiments. Both Foster et al. 1984; Hegemann, Hegemann, and Foster 1988, performed dish tests and measured rates of algae depletion on the illuminated side of negatively pho-

totactic suspensions. Schaller, David, and Uhl 1997 measured the degree of orientation under continuous illumination with their light scattering system on cell populations. In all those studies, light stimulus-response curves do not show marked threshold but the response continuously increases with intensity at dim irradiance. Thus threshold intensities are obtained by interpolation to zero response of intensity-response curves. They are given in Table 2.2. Threshold light intensity values obtained from cells population experiments were close to each other were around 10^{-3} W/m², close to our own measurement. On the other hand, it is not clear why threshold intensity measured with individual cells method was one order of magnitude higher (10^{-2} W/m²) than that obtained with population experiments. It is possible that individual cells experiments are more subject to sampling bias.

Threshold irradiance		Measured by
photons.m ⁻² .s ⁻¹	W.m ⁻²	
3×10^{15}	1×10^{-3}	1
3×10^{16}	1×10^{-2}	2
5×10^{15}	2×10^{-3}	3
5×10^{15}	2×10^{-3}	4
2×10^{15}	1×10^{-3}	5

Table 2.2: Reported values of light irradiance threshold for *Chlamydomonas reinhardtii* phototaxis in directional light. Values are rounded to 1 significant digit.

- 1: Feinleib and Curry 1971, population experiments.
- 2: Feinleib and Curry 1971, individual cells experiments.
- 3: Foster et al. 1984, population experiments.
- 4: Hegemann, Hegemann, and Foster 1988, population experiments.
- 5: Schaller, David, and Uhl 1997, population experiments.

Our experiments on a population scale with light intensity gradients gave a threshold light intensity close to values obtained in cells population experiments with directional light. This is a good indication that the two possible phototaxes share the same detection system. These values correspond to a photons density flux of $\sim (3 - 5) \times 10^{15}$ photons.m⁻².s⁻¹. The number of rhodopsin photoreceptors in each cell is $N_r \sim 30000$ (Foster and Smyth 1980), with an absorption cross section $\sigma_r \sim 1.5 \times 10^{-20}$ m² per rhodopsin and a quantum efficiency for activation $\Phi_r \sim 0.67$ (Foster and Smyth 1980; Beckmann and Hegemann 1991). It can thus be estimated that a remarkably symbolic value of **1 photon/cell/s** is absorbed at threshold light intensity. This timescale of 1s is still much larger than that of photocurrents reaching a peak after light stimulation (tens of milliseconds, Harz and Hegemann 1991), it thus provides an indirect measurement that single photon absorption events are sufficient to trigger photomovement response in *Chlamydomonas reinhardtii*.

2.4.2 Single photon detection in phototaxis

The minimum number of photons necessary to trigger a photomovement response in *Chlamydomonas reinhardtii* was specifically studied by Hegemann and Marwan 1988. They compared light stimulus-response curves to theoretical Poisson distribution curves to evidence the probabilist nature of *Chlamydomonas reinhardtii* phototaxis. They could evaluate the minimum number of photon required for a phototactic turn. This method was first applied by Hecht, Shlaer, and Pirenne 1942 to show that 5-8 events occur at threshold of human vision.

Hegemann and Marwan 1988 used 50 ms light flashes on tracked individual cells. In the analysis of the experiments, the probability that exactly n photon produce a direction change was treated as a Poisson process of expected value α . α is the average number of effective photons per cell, i.e. photons that do contribute to a movement :

$$\alpha = F \cdot N_r \cdot \sigma_r \cdot \Phi_r \cdot k_{\text{eff}}$$

F is the photon exposure (given by irradiance \times flash duration). N_r , σ_r and Φ_r are the number of photoreceptors per cell, their absorption cross section and their quantum efficiency for activation. k_{eff} is the effective yield for an activated rhodopsin to contribute to a direction change. In the formula above, the product $\Phi_r \cdot k_{\text{eff}}$ means that an effective photons should activate a photoreceptor and that this absorption should lead to a movement response.

Then, the frequencies $R(F)$ of direction changes at a photon exposure F corresponds to the probability $P\{N \geq n\}(\alpha)$ that n or more photons are effective at an average number of effective photons $\alpha(F)$. This is shown in Figure 2.7. Since $\log(\alpha) = \log(F) + \log(N_r \sigma_r \Phi_r k_{\text{eff}})$, a horizontal offset X was applied to the stimulus-response curves to fit Poisson distributions. The theoretical curves shapes depend on n . The best fit was obtained for a minimum number of photon required $n = 1$, that is to say phototactic turn is a single-photon event.

The effective yield for an activated rhodopsin to contribute to a direction change was also evaluated. From the value of the horizontal shift X applied to fit stimulus-response data points with theoretical curves and which corresponds to $X = \log(N_r \sigma_r \Phi_r k_{\text{eff}})$ (where both N_r , σ_r and Φ_r are known), the authours found $k_{\text{eff}} \sim 0.05$. Detection threshold light intensities could then be further interpreted. The average value of 1 photon-activated photoreceptor/cell/s at threshold irradiances (see section 2.4.1) can be multiplied by k_{eff} to give 0.05 photomovement response/cell/s. The authors concluded that cells experienced tens of rotation between phototactic turns at these threshold irradiances.

2.4.3 Critical inversion intensity and negative phototaxis

A similar calculation to that of section 2.4.1 can be performed at the critical inversion intensity $I_{\text{crit}} \sim 100 \text{ W/m}^2$. We can estimate that $\sim 80\,000$ photons/cell/s are absorbed

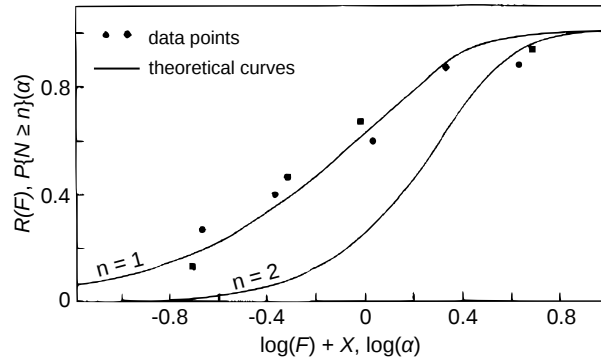


Figure 2.7: Light-induced direction changes stimulus-response curves compared to Poisson distribution.

(From Hegemann and Marwan 1988)

Stimulus-response data points, $R(F)$ vs $\log(F) + X$ with : R the frequency of direction changes, F the light exposure, X the applied horizontal shift to data points curves in order to fit Poisson distribution.

Poisson distribution theoretical curves (for $n=1,2$), $P_n(\alpha)$ vs $\log(\alpha)$ with : α the average number of effective photons, $P_n(\alpha)$ the probability that n or more events occur at averaged value α .

by the $\sim 30\,000$ photoreceptors/cell at I_{crit} . According to photocurrents measurements by Kuhne et al. 2019, the timescale of Channelrhodopsin-2 relaxation to its dark-adapted state is ~ 250 ms, so that they can be photoisomerized only a few times every second. This would mean that a majority ($\sim 70\%$) of rhodopsin photoreceptors are continuously photoisomerized at I_{crit} .

Thus, the full range of photoisomerization states from single activation to almost full continuous activation is used in the positive phototaxis irradiance range of *Chlamydomonas reinhardtii*. Nevertheless, the negative phototactic susceptibility still increases with stronger irradiances $I > I_{\text{crit}}$. It highlights the open question of the molecular mechanisms that control *Chlamydomonas reinhardtii* negative phototactic response. Although very meaningful, these conclusions at I_{crit} should be taken carefully because it was previously observed that the inversion from positive to negative phototaxis is much more sensitive to external factors such as CO_2 tension and age of the culture compared to detection threshold (Nultsch 1977; Feinleib and Curry 1971).

2.5 Discussion

2.5.1 Hypothesis of the unique dependence on light intensity

Our measurement of the phototactic susceptibility can be compared to a previous estimate in Dervaux, Capellazzi Resta, and Brunet 2017. The authors estimated a constant phototactic susceptibility of $\sim 1 \times 10^{-7} \text{ m}^4/\text{J}$ without taking a dependence on light intensity and below the critical inversion intensity with $I_{\text{max}} = 5 \text{ W/m}^2$. From the pho-

totactic susceptibility curve, we can calculate the average value over the range of light intensity with the same value of $I_{\max} = 5 \text{ W/m}^2$. We find $\chi|_{\text{avg}} = \frac{1}{I_{\max} - I_{\text{th}}} \int_{I_{\text{th}}}^{I_{\max}} \chi(I) dI \approx 5 \times 10^{-8} \text{ m}^4/\text{J}$, which is close to the previous estimation.

In the determination of the phototactic susceptibility, we assumed that it only depends on light intensity. Choudhary, Baskaran, and Sharma 2019 reported a dependence of phototaxis on cell concentration. For concentrations $> 3 \times 10^7 \text{ cells/mL}$, they found that light detection is enhanced due to a lowering of cells swimming speed. Nevertheless, they found relative variations (by a factor 2) that are negligible compared to those we found with light intensity. In all generality, the phototactic susceptibility can also depend on cell concentration via the effective diffusion coefficient in the formula eq. (2.1).

An additional vertical drift along the direction of propagation of the light beam could be neglected in this experimental setup according to Dervaux, Capellazzi Resta, and Brunet 2017. Finally, the phototactic susceptibility could also depend on the light intensity gradient. We note that we partially decoupled light intensity and its gradient in the determination of χ by using light beams of different shapes and maximum intensities. Yet, the parametric curves $\{I(r), \chi(r)\}$ still collapsed on a master curve. *a posteriori*, this is good indications that dependency of χ on light intensity gradient can be neglected with the light beams used in our experiments. We also check that the drift velocities calculated from the phototactic susceptibility remain reasonable in our experiments using the definition $\vec{v}_{\text{drift}} = \chi \vec{\nabla} I$. In pattern formation experiments presented in the next chapter, we used light beams with fixed $I_{\max} = 5 \text{ W/m}^2$. In this case, we can calculate $\chi|_{\text{avg}} \times |\vec{\nabla} I|_{\max} \sim 200 \text{ }\mu\text{m/s}$, which is still comparable to the swimming speed of *Chlamydomonas reinhardtii*.

2.5.2 Time dependence of phototaxis

We obtained the phototactic susceptibility curve at rather long timescale ($\sim 1\text{h}$). Nevertheless, it should be noted that phototaxis also displays some interesting time-dependent features. An example is a self-adaptation to light exposure reported by Arrieta et al. 2017. They observed cells orbiting around a light source as if optimal light intensity was found but then cells left their orbit and the field of view.

We also observed a time dependent phototactic response in side view imaging experiments in Hele-Shaw cells (see appendix C.2). In these experiments, the field of view allowed to image the whole length of Hele-Shaw cells. We observed that each time the light beam was turned on, we first observed negative phototaxis during $\sim 5 \text{ min}$ with algae accumulation at the sides, away from the light beam. Then, positive phototaxis was observed with later accumulation around the light beam. We are currently not able to explain this behavior. Thus, the phototactic susceptibility that we measured should be interpreted as a response at long timescale.

2.6 Conclusion

In this chapter, we discussed that there are two possible phototaxes: either along the direction of light propagation or along light intensity gradients. In this work, we developed an experimental setup to study the interaction between algae and controlled light intensity gradients within shallow suspensions. With very thin layers, we used a Keller-Segel approach to determine the phototactic susceptibility to light gradients as a function of the spatially swept light intensity. Such a macroscopic approach does not model the mechanisms that regulate phototaxis along light intensity gradients but offers a robust and quantitative description of its effect at the population scale. We obtained a curve of the phototactic susceptibility over several light intensity gradients. It features a detection threshold, a higher sensitivity at low light intensities and a critical inversion intensity from positive to negative phototaxes. The value of the detection threshold that we found for phototaxis in light intensity gradients is consistent with values previously reported for phototaxis in directional light, corresponding to a remarkably symbolic value of 1 photon/cell/s. Thus, the two phototaxes likely share the same detection system for which it was shown that single photon absorption events are sufficient to trigger photomovement response. Here, we also found that the full range of isomerization states of the photoreceptors is used in the positive phototaxis range of *Chlamydomonas reinhardtii*, which leaves the question of the mechanism behind negative phototaxis open.

Let us now tune the intensity of the collective effects in *Chlamydomonas reinhardtii* suspensions by increasing the magnitude of the Rayleigh number.

CHAPTER 3

Pattern formation in localized bioconvection

In the previous chapter, we characterized the phototactic response of populations of *Chlamydomonas reinhardtii* in shallow suspensions illuminated with heterogeneous light fields. Here, the same system is used but in a different regime. Keeping the heterogeneity of the light field as a critical control parameter, we now tune the collective effects by changing the pseudo-Rayleigh number to trigger bioconvective flows in *Chlamydomonas reinhardtii* suspensions. We aim at understanding the cells self-organization in these sustained self-generated flows by characterizing light-induced pattern formation in localized photo-bioconvection. First, we show the role of the two control parameters - the pseudo-Rayleigh number and the width of the light beam - on the formation of different patterns. Then, we characterize separately and in detail several light-induced instabilities observed in the experiments.

3.1 Tuning collective effects: control parameters

We used the experimental setup presented in the previous chapter. In this chapter, we tuned the intensity of the collective effects by increasing the magnitude of the Rayleigh number as in previous studies of localized photo-bioconvection (Dervaux, Capelazzi Resta, and Brunet 2017; Arrieta et al. 2019) where a thin light beam was used. Here, we introduced a new parameter which is the width of the light beam to tune light intensity gradients.

3.1.1 Shaping of the light beam

We used the width of the light beam to tune light intensity gradients at fixed maximum light intensity. In the previous chapter, we identified the positive phototaxis range in *Chlamydomonas reinhardtii* to be: $10^{-3} \text{ W/m}^2 \lesssim I \lesssim 10^2 \text{ W/m}^2$ (section 2.3.2). Here, we fixed the maximum light intensity at $I_{\max} = 5 \text{ W/m}^2$ to remain within the range of positive phototaxis. Qualitatively, a larger beam width then corresponds to two effects : it broadens the spatial range of phototaxis and it weakens the magnitude of light intensity gradients.

# diffusers	Beam width	
	σ , Gaussian width	w , with $I(r = w)/I_{\max} = 0.005$
0	$0.79 \pm 0.02 \text{ mm}$	$2.7 \pm 0.1 \text{ mm}$
1	$0.79 \pm 0.01 \text{ mm}$	$5.0 \pm 0.5 \text{ mm}$
2	$0.81 \pm 0.01 \text{ mm}$	$7.5 \pm 0.7 \text{ mm}$
3	$0.85 \pm 0.01 \text{ mm}$	$11.1 \pm 0.6 \text{ mm}$
4	$0.98 \pm 0.01 \text{ mm}$	$20 \pm 1 \text{ mm}$

Table 3.1: Green light beams widths. The gaussian beam width σ and its error are determined by the gaussian fit of the light intensity profiles. The beam width w is evaluated at $I/I_{\max} = 0.005$ cooresponds to a light intensity threshold of $2.5 \times 10^{-2} \text{ W/m}^2$ at fixed $I_{\max} = 5 \text{ W/m}^2$. The error takes into account the ajustement of the maximum light intensity at the center.

Let us now defined the beam width. As explained in section 2.2.2, the use of diffusers to widen the initially gaussian light beam gave 5 light intensity radial profiles shown in Figure 2.2. Given the low intensity threshold for detection ($I_{\text{thresh}} \sim 10^{-3} \text{ W/m}^2$), we chose an arbitrary threshold at $I(r = w)/I_{\max} = 0.005$ to define a beam width w for each of these profiles, which corresponds to $I(r = w) = 2.5 \times 10^{-2} \text{ W/m}^2$ at fixed $I_{\max} = 5 \text{ W/m}^2$. As discussed in section 2.2.2, the light intensity radial profiles have similar gaussian shape at the center but significant different tails. The high sensitivity of *Chlamydomonas reinhardtii* phototaxis at low light intensity justifies now that the beam width w can be defined in the tails of the light intensity radial profiles. The values of the beam widths w are given in Table 3.1, together with the values of the gaussian widths σ for

comparison. Note that the beam width defined at the detection threshold for phototaxis I_{thresh} could have also been used as a meaningful measure of the beam width.

3.1.2 Tuning the pseudo-Rayleigh number

Let us recall the pseudo-Rayleigh number :

$$\text{Ra} = \frac{\rho_0 \beta H^3 c_0}{D\eta} \quad (3.1)$$

The pseudo-Rayleigh number is controlled by both the initial cell concentration c_0 and the liquid height H . The initial cell concentration could be adjusted in the range $c_0 \sim 10^6 - 10^7$ cells/mL using the procedure described in appendix A.3 although most of the time, c_0 was the cell concentration of grown liquid cultures $c_0 \sim (1.5 - 3.0) \times 10^6$ cells/mL. In practice, the pseudo-Rayleigh number Ra was mostly controlled with the liquid height $1 \text{ mm} \leq H \leq 5 \text{ mm}$. We obtained a range of pseudo-Rayleigh number : $\text{Ra} \sim 10 - 1000$.

3.2 Phase diagram and global properties of patterns

3.2.1 Classification of photo-bioconvection patterns

We observed different photo-bioconvection patterns that we report in Figure 3.1 when varying both the Rayleigh number and the beam width. We observed *round* patterns (3.1.a), *waves* emission (3.1.b), *dendrites* (3.1.c), and *directional growth* (3.1.d,e). We obtained the phase diagram of these instabilities as a function of the pseudo-Rayleigh number Ra and the relative beam width w/H (Figure 3.1.f). It gives the domain of existence of *round*, *waves* and *dendrites* on which *directional growth* is superimposed.

Primary instability

Round patterns were observed at low Ra. They were first documented by Dervaux, Capellazzi Resta, and Brunet 2017 as the primary pattern formation of localized photo-bioconvection for thin light beams ($w/H < 1$) and low Ra. In this study, we showed that if Ra remains low, they still appear at large beam width ($w/H > 1$). In *round* patterns, the cell concentration field reaches a steady state that keeps the symmetry of the light beam. It results from a coupling between lateral phototaxis, diffusion and convection. Because only positive phototaxis occurs with $I_{\text{max}} = 5 \text{ W/m}^2$, cell concentration monotonically increases towards the center. Dervaux, Capellazzi Resta, and Brunet 2017 underlined that although the overall shape of *round* patterns did not significantly change when increase Ra, the appearance of convection was testified by the discrepancy between the experimental concentration radial profile and that predicted by the balance between diffusive and phototaxis fluxes, for $\text{Ra} \gtrsim 20$. Above this value, convection arising from

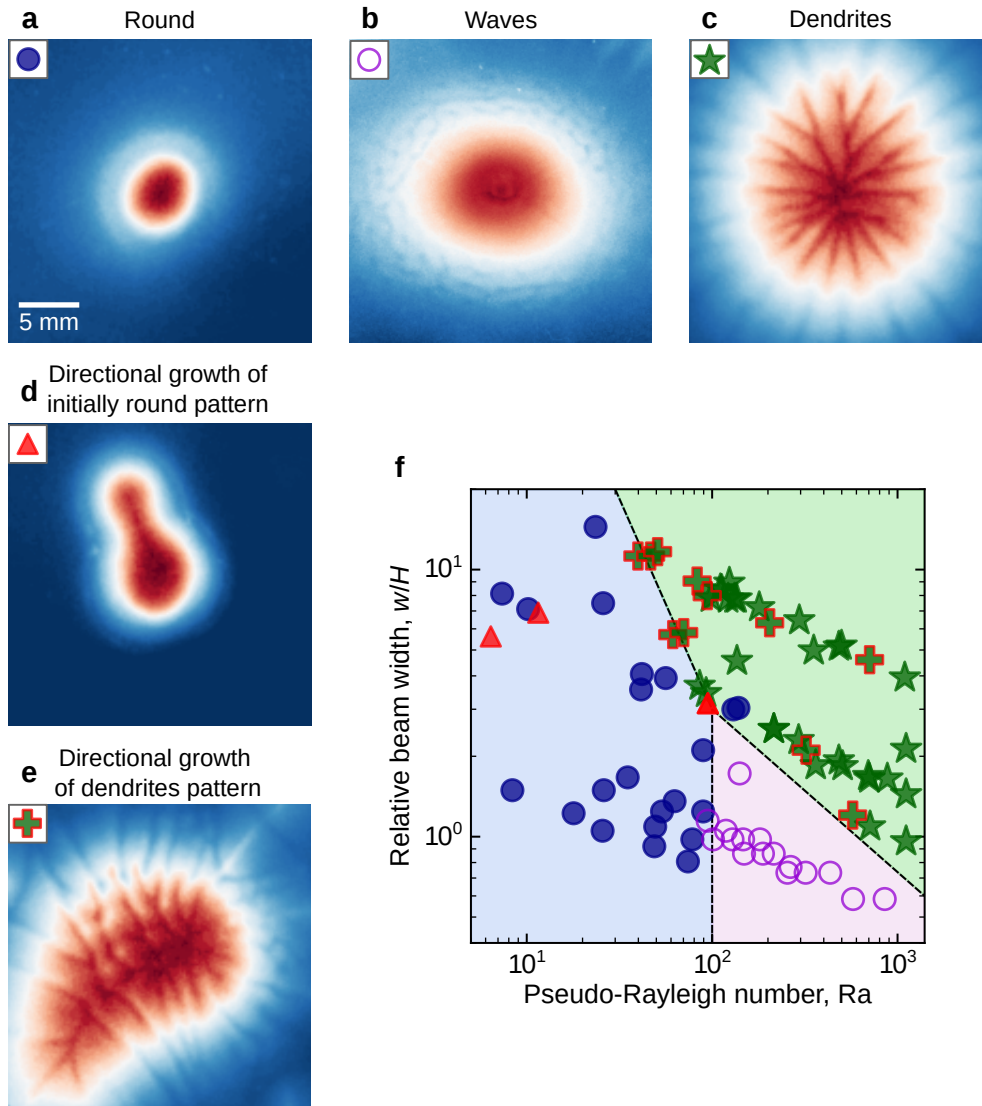


Figure 3.1: Phase diagram of photo-bioconvection patterns. **a-e**, Cell concentration fields imaged from top view of the different types of patterns observed in photo-bioconvection experiments. Images are centered around the light beam. Colormap with low concentrations in dark blue, high concentrations in dark red and maximum brightness for intermediate concentrations. The 3 main patterns are round, waves and dendrites. **a**, Stationary round pattern. **b**, Waves of concentration propagating radially from the center to the periphery. **c**, Dendrites pattern with splits into branches of high concentration and a stationary radial extension. **d**, **e**, Unstationary directional growth during pattern formation for initially round patterns (**d**, growth towards bottom left of the image) and dendrites (**e**, growth towards top of the image). **f**, Occurrences of the different patterns types are plotted in a phase diagram as a function of the pseudo-Rayleigh number Ra and the relative beam size w/H . Boundaries are a guide for the eyes to delimit the domains of existence of round, waves and dendrites patterns that are respectively colored in pale blue, green and violet.

density gradients becomes significant.

A sketch of the convection mechanism in localized photo-bioconvection was proposed in the introduction (section 1.3.5, Figure 1.13) with downward flow at the center due to

cells accumulation by positive phototaxis. Here, given the radial symmetry of the problem, we expect that the flow consists of a main toroidal convection roll with a downwelling flow at the center, a flows respectively directed towards and away from the center in the upper and in the lower parts of the suspension. We expect convection flow velocities to scale with cell concentration gradients as $\vec{v} \propto \vec{\nabla}c$, but convection flows cannot be studied quantitatively with this experimental setup. Still, the flow directed towards the center at the surface was confirmed by the transportation of a floating bead at the free surface towards the center at a velocity $> 100 \mu\text{m/s}$ (Dervaux, Capellazzi Resta, and Brunet 2017). The chapter 5 will be dedicated to quantative measurements of bioconvective flows.

Secondary instabilities

Waves, *dendrites*, and *directional growth* are secondary instabilities that break either the initial radial symmetry imposed by the light beam or the time invariance of the pattern. They arise when increasing either the pseudo-Rayleigh number Ra or the light beam size ($w > H$), or both.

Waves are emitted when the beam width is kept small ($w/H \lesssim 1$) above a critical pseudo-Rayleigh number ($\text{Ra} \gtrsim 100$). In this regime, round patterns start forming but their time invariance break. A concentrated region remains in the center and waves of intermediate concentration propagates away from this region. The wave velocity measured as a function of Ra in Dervaux, Capellazzi Resta, and Brunet 2017. Their appearance was understood as a photo-gyrotactic instability. In numerical simulations, algal concentration close to the center is higher in the lower part of the suspension because of the structure of the primary convection rolls (downward flow at the center). Then, when the Ra further increases, the flow vorticity increases and deviates cells from their preferential radial orientation as illustrated in Figure 3.2. Thus a layer of high concentration is formed just above the bottom of the Petri dish and is destabilized by gravity when dense enough. Finally, advection by the primary toroidal flow generates waves of concentration. In the work that we present here, we precised the domain of existence of *waves* emission in the phase diagram of photo-bioconvection patterns, but we did not further characterize this instability.

Dendrites patterns were observed by widening the light beam and at high pseudo-Rayleigh number. For $w/H \gtrsim 3$, we observed the transition from *round* to *dendrites* patterns above a critical Ra . This threshold in Ra was lowered when increasing w/H and was in the range 40 – 100 in the experiments. For $\text{Ra} > 100$, the transition from *waves* to *dendrites* was observed when increasing $w > H$. Close to this boundary, we sometimes observed *dendrites* superimposed with *waves* emission (see appendix B.4, Figure B.3).

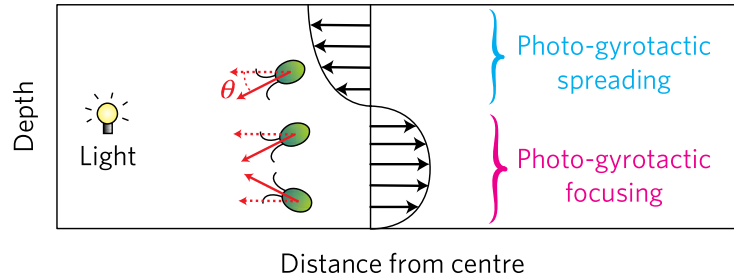


Figure 3.2: Sketch of the effect of photo-gyrotaxis in the presence of a recirculation flow Cells are attracted towards the light beam located at the center. In the upper part of the suspension, the flow is directed to the center with a free surface and cells are slightly oriented towards the bottom because of gyrotaxis. In the lower part of the suspension, cells are concentrated at the center of the Poiseuille flow.

In *dendrites* instability, the orthoradial invariance of the light beam is lost but the pattern still reaches a stationary state. Branches of high concentration are separated by spaces of lower concentrations. From center to periphery, they exhibit splitting and their number increases, so that their spacing is a well-defined quantity seemingly selected by a physical mechanism. We shall give more details on this dendrites instability in section 3.3.

Directional growth was observed at high beam width ($w/H > 1$), either growing from initially round patterns at low pseudo-Rayleigh number Ra or mixed with dendrites at higher Ra . In both case, the same phenomenology is observed. Cell concentration patterns are initially centered but are destabilized and a finger grows in a given direction while the patterns remain anchored around the light beam. For $w/H > 1$, *directional growth* occurred quite randomly accross the whole range of Ra , and mostly at low to intermediate values. This instability will be discussed in more details in a dedicated section.

3.2.2 Global properties of photo-bioconvection patterns

Before describing in details the different instabilities, we take a step back and investigate the effect of both the pseudo-Rayleigh number and the size of the light beam on global properties of cell concentration patterns. For this, we focus on *round*, *waves* and *dendrites patterns*. In the absence of *directional growth*, cell concentration patterns are centered around the light beam and have a fixed radial extension. Thus, concentration fields can be averaged over time and along the angular coordinate θ .

Figure 3.3 shows stationary cell concentration profiles obtained with different values of the beam width and of the pseudo-Rayleigh number. In all cases, cell concentration c monotonically decreases with distance from center r . It is maximum at the center $c_{\max} = c(r = 0)$. It then decays and sometimes reaches a limit value within the range of distance from center range for which cell concentration measurements were best calibrated ($r < 30$ mm), as in Figure 3.3.a. This limit should be c_0 for infinite systems : $c(r) \xrightarrow{r \rightarrow \infty} c_0$. Thus, we defined two global properties of cell concentration patterns based on c_0 and on

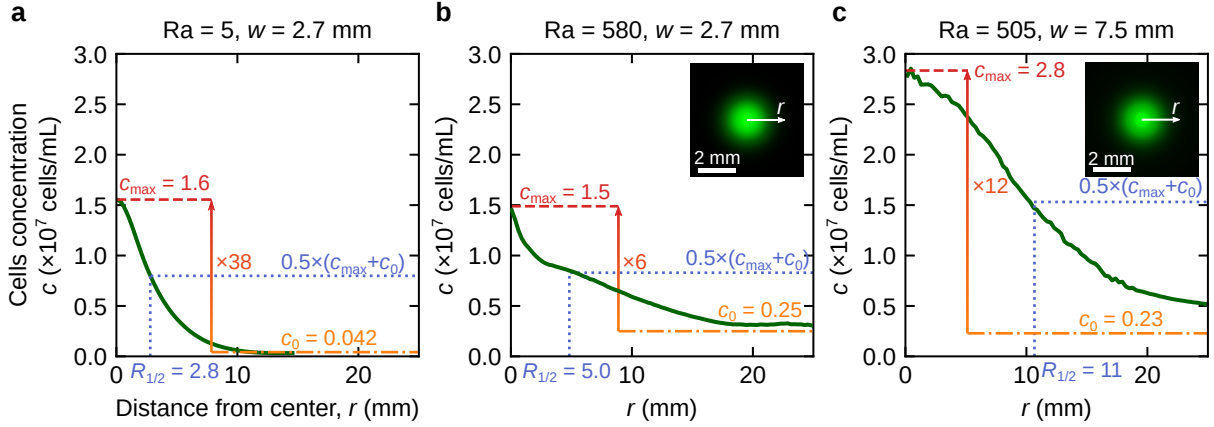


Figure 3.3: Stationary cell concentration radial profiles at different pseudo-Rayleigh numbers and beam widths. Concentration profiles are averaged over the last 10 minutes of the experiments and along $\theta = [0; 2\pi]$. They are more or less spread out as a function of the pseudo-Rayleigh number Ra and the beam width w , which is quantified by two properties. The maximum concentration c_{\max} is compared to the initial concentration c_0 . The distance from center at which the monotonically decreasing concentration reaches $c = 0.5 \times (c_{\max} + c_0)$ defines a pattern radius $R_{1/2}$. **a-b**, At fixed $w = 2.7$ mm, Ra is increased. **a**, $Ra = 5$ ($H = 1.7$ mm, $c_0 = 4.2 \times 10^5$ cells/mL). **b**, $Ra = 580$ ($H = 4.2$ mm, $c_0 = 2.5 \times 10^6$ cells/mL). **b-c**, w is increased at similar Ra . **c**, $w = 7.5$ mm, $Ra = 505$ ($H = 4.1$ mm, $c_0 = 2.3 \times 10^6$ cells/mL). In (b) and (c), the inset are reconstructed images of the light beam where the pixel intensity values range from $[0, 255]$ and are proportional to the light intensity with 255 corresponding 5 W/m^2 . The reconstructed images are not distinguishable to the eye although the two beam widths differ in the tail of the light intensity radial profiles.

radial profiles $c(r)$. First, the relative maximum concentration c_{\max}/c_0 quantifies the concentrating power of the light beam. Then, pattern radius $R_{1/2}$ is defined at $c(r = R_{1/2}) = 0.5 \times (c_{\max} + c_0)$. It should be related to the size of primary convection rolls, a relationship that will be tested when measuring flow fields in a dedicated experimental setup (chapter 5). At first sight, it seems that increasing Ra strongly decreases c_{\max}/c_0 and the size of the concentrated region increases with the width of the light beam.

The analysis described above was performed for all experiments in the absence of directional growth. The relative maximum concentration c_{\max}/c_0 is plotted against the pseudo-Rayleigh number Ra for different beam sizes w in Figure 3.4.a. Data reveal a global trend that c_{\max}/c_0 decreases with Ra . The maximum value of c_{\max}/c_0 for $Ra \rightarrow 0$ indicates that there is a maximum concentration factor A that can be reached in our system in the absence of flow. A should depend on I_{\max} , on the total number of algae I_{\max} and on their collective diffusion coefficient. No significant effect of the beam size is observed on the normalized maximum cell concentration and data are well grouped together for $w \geq 5.0$ mm. It should be however that the decay of c_{\max}/c_0 with Ra is more pronounced for $w = 2.7$ mm. Because experiments with $w = 2.7$ mm were first performed with smaller Petri dishes than that of experiments with $w \geq 5.0$ mm (see Figure 3.4

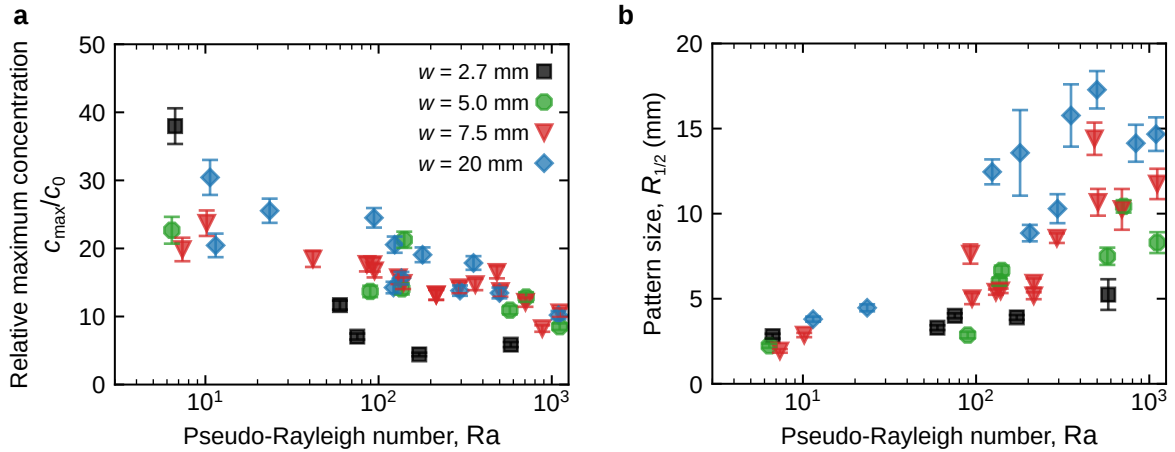


Figure 3.4: Effect of the pseudo-Rayleigh number and the beam width on two global properties of cell concentration patterns. Relative maximum concentration c_{\max}/c_0 and pattern size $R_{1/2}$ as a function of the pseudo-Rayleigh number Ra at different beam widths w . Each point corresponds to a single experiment. Experiments with $w = 2.7$ mm were first performed with a Petri dish diameter 8.4 mm while other experiments were later performed with a Petri dish of larger diameter, 13.9 mm. Error bars take into account both the precision of the local cell concentration measurements by red light transmission, and variability when averaging cell concentration profiles over time and along $\theta = [0; 2\pi]$.

caption), the deviation from the other experiments can be interpreted as an effect of the side of Petri dish rather than an effect of the beam width. Indeed, c_{\max}/c_0 should not only depend on Ra but also on $N_{\text{cells,tot}} = c_0\pi\frac{D_{\text{petri}}^2}{4}H$. Then, since we mostly controlled Ra with H , $N_{\text{cells,tot}}$ mostly depends on the Petri dish diameter D_{petri} at fixed Ra and $\{c_{\max}/c_0; Ra\}$ curves can be differentiated by Petri dish diameter.

Figure 3.4.b shows patterns sizes $R_{1/2}$ measured as a function of the pseudo-Rayleigh number Ra for different beam widths w . For $w = 2.7$ mm, we observe a slight increase of $R_{1/2}$ with Ra , by a factor 2 – 3 when Ra is increased by 2 orders of magnitude. This effect becomes much more pronounced when increasing the beam width. If $R_{1/2}$ does not depend on much w at low Ra , it does however significantly increase with w at high Ra . This is a direct effect of the higher sensitivity of the nonlinear phototactic susceptibility to the low light intensities in the tails of the light beams radial profiles.

In conclusion, concentrating power c_{\max}/c_0 decays and pattern size $R_{1/2}$ increases when the pseudo-Rayleigh number Ra is increased. Thus convection spreads cell concentration patterns out. $R_{1/2}$ also increases with w : larger beam widths contribute to a wider range of localized bioconvection by attracting algae that are further away from the center. It should be noted that for low $Ra \lesssim 20$, the both c_{\max}/c_0 and $R_{1/2}$ are largely independent of Ra , so that in this range of parameter values collective effects are indeed negligible as we assumed in the previous chapter when measuring the phototactic susceptibility.

3.3 Dendrites patterns

3.3.1 Kinetics

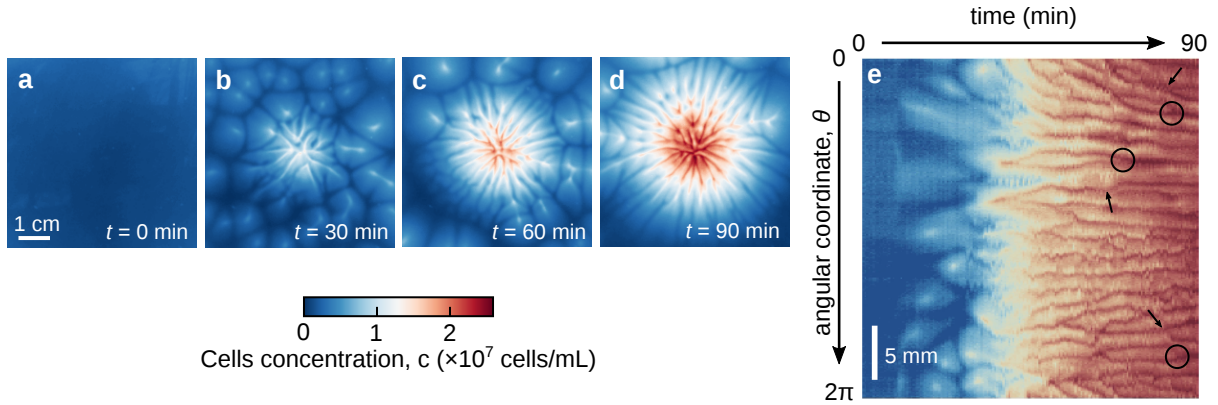


Figure 3.5: Kinetics of dendrites formation. a-d, cell concentration field imaged from top view at different times during an experiment showing the formation of dendrites. The light beam at the center is turned on at $t = 0$. From an homogeneous cell concentration field (a), aggregates dots of intermediate concentrations move towards the center (b) where branches are splitting and growing with increasing concentration at the center (c) before reaching a stationary state (d). e, For the same experiment, kymograph of the cell concentration as a function of time and the angular coordinate θ at a fixed distance 5 mm from the beam center. Arrows show splitting events while merging events are circled. $Ra = 1100$ ($H = 0.51$ mm, $c_0 = 2.6 \times 10^6$ cells/mL), $w = 20$ mm.

We first studied the formation of *dendrites* patterns from an initially homogeneous state in Figure 3.5.

Transitory regime

In a transitory regime, spots of intermediate algae concentrations form in the suspension within the first tens of minutes (Figure 3.5). This dots instability is reminiscent of spontaneous bioconvection that originates from an upward swimming of micro-organisms. We did not study it quantitatively but we report here several observations. Dots appear in a region around the light beam whose area increases when increasing either the beam width w or the pseudo-Rayleigh number Ra . Their spacing also seems to increase with the liquid height H .

Formation of branches

Close to the center, cell concentration increases with time and the concentration fields self-organizes in branches of intermediate to high concentration that grow radially (Figure 3.5). The evolution of branches with time exhibits a complex kinetics of splittings and merging shown by a kymograph of the evolution of angular concentration profiles with time at a fixed distance from center in Figure 3.5.e. These events seem to accommodate for

a regular spacing between branches. The pattern eventually reaches a stationary state of maximum radial extension (Figure 3.5) in which we studied the spacing between branches.

3.3.2 Wavelengths of dendrites

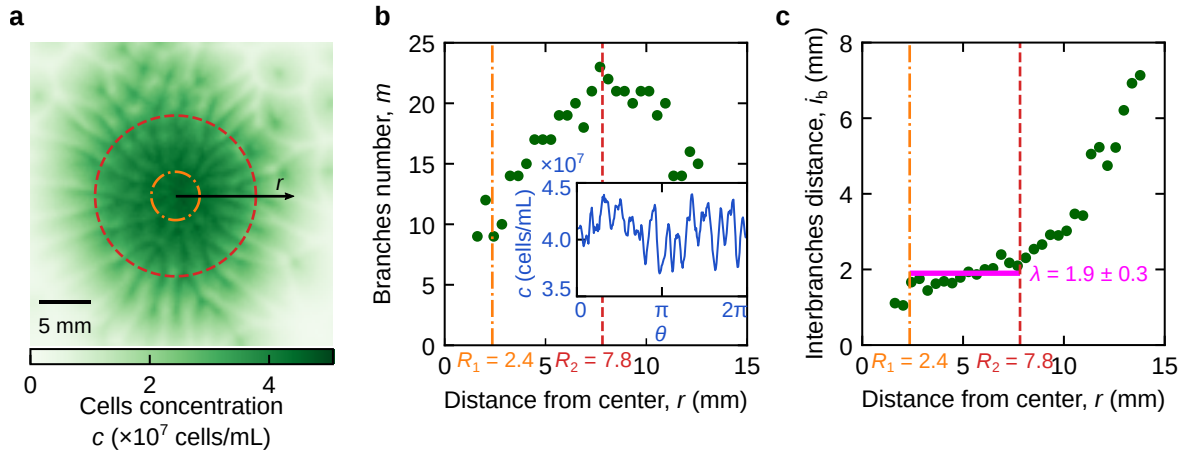


Figure 3.6: Analysis of branches number and interbranches distance in dendrites patterns. **a**, cell concentration field of a dendrites pattern with fully developed branches whose number and spacing can be measured as a function of the distance r from the center of the light beam. **b**, The number of branches $m(r)$ is measured radially as the number of intersections with the centered circle of radius r . This is obtained by peak detection in orthoradial cell concentration profiles (see inset for which $r = 4$ mm). **c**, The interbranche distance $i_b(r)$ is evaluated as the side length of a regular $m(r)$ -sided polygon inscribed in a circle of radius r . An orthoradial wavelength λ can be defined between $r = R_1$ and $r = R_2$ where the branches split (b) and their spacing only slightly increase (c) (see main text). $\lambda = 1.9 \pm 0.3$ mm. $Ra = 180$ ($H = 0.28$ mm, $c_0 = 8.4 \times 10^6$ cells/mL) and $w = 20$ mm.

We mainly studied *dendrites* patterns in their stationary state. Figure 3.6 illustrates our analysis to extract an orthoradial wavelength from a stationary *dendrites* pattern (fig. 3.6.a). Figure 3.6.b shows the evolution of the number m of a pattern branches obtained from peak detection in orthoradial concentration profiles as a function of the distance from the center of the light beam r . In Figure 3.6.c, the interbranche distance i_b is plotted against r . At a given r , the branches spacing $i_b(r)$ is calculated from the number of branches $m(r)$ as the side length of a regular $m(r)$ -sided polygon inscribed in a centered circle of a radius r :

$$i_b(r) = 2r \sin\left(\frac{\pi}{m(r)}\right) \quad (3.2)$$

Radial profiles of $m(r)$ and $i_b(r)$ can be decomposed in different parts. There exists a domain $R_1 \leq r \leq R_2$ in which m increases because of radial splittings. R_1 is the minimum distance from the center at which branches can be counted with peak detection. R_2 is the distance from center at which m is maximum. In this domain, the branches spacing

i_b stays close to an orthoradial wavelength λ . After r exceeds R_2 , m stays on a plateau and then drops when reaching the branches maximum radial extension while i_b strongly increases with r . Between R_1 and R_2 , there is a competition between the establishment of an orthoradial wavelength and the initial radial symmetry so that the spacing i_b slightly increases with r . We however defined an orthoradial wavelength λ in this domain as the averaged spacing weighted by distance from center. This is equivalent to unroll all circles of radiuses $R_1 \leq r \leq R_2$ and then computing the average spacing. We thus have for the orthoradial wavelength :

$$\lambda = \frac{\int_{R_1}^{R_2} r i_b(r) dr}{\int_{R_1}^{R_2} r dr} \quad (3.3)$$

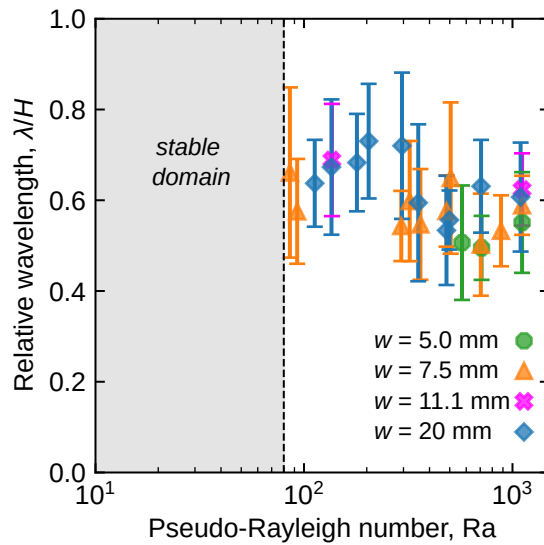


Figure 3.7: Orthoradial wavelengths of dendrites patterns. Relative wavelength λ/H as a function of the pseudo-Rayleigh number Ra at different beam widths w . Each point correspond to a single experiment. Error bars take into account the variability both when averaging the branches spacing i_b along the distance from center and when averaging over the wavelength over time during the last 10 minutes of the experiments.

We analyzed the experiments with *dendrites* patterns as explained above. We found domains $R_1 \leq r \leq R_2$ on which orthoradial wavelengths were calculated using the formula 3.3. Normalized orthoradial wavelengths λ/H are plotted against the pseudo-Rayleigh number Ra for different beam widths w . Error bars (see Figure 3.7 caption) are relatively large. This is mainly due to the fact that i_b slightly increases with r . Although the domain of existence of dendrites patterns in the phase diagram depends on the beam size, no effect of w is observed on the wavelength. Given the error bars, the relative wavelength is largely independant of Ra with $\lambda/H = 0.63 \pm 0.08$.

3.3.3 Validity and limit of the measurements wavelengths

Our analysis allows to define an orthoradial wavelength in a simple way compared to other methods that could have been used to measure characteristic lengths of *dendrites*

patterns. As a complement, a method to measure average radial distance between splittings points could have been developed and this distance could have been compared to the orthoradial wavelength that we defined. Bees and Hill 1997 used Fourier transform to extract dominant wavelengths of bioconvection patterns in suspensions of single-celled alga *Chlamydomonas nivalis*. In fact, a Fourier analysis could have enabled to extract both the average radial distance between splitting points and the orthoradial wavelength.

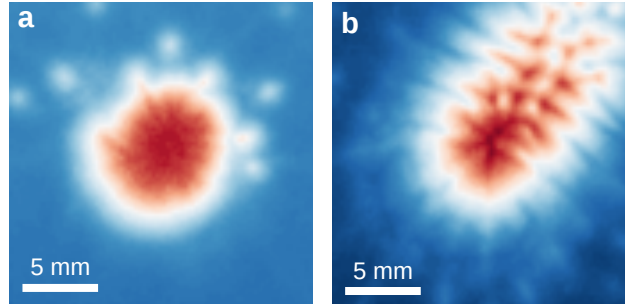


Figure 3.8: Other dendrites patterns. **a**, Emerging dendrites with branches barely visible and a stationary radial extension. $Ra = 95$ ($H = 1.4$ mm, $c_0 = 1.1 \times 10^7$ cells/mL) and $w = 11.1$ mm. **b**, Dendrites mixed with unstationary directional growth. $Ra = 85$ ($H = 2.2$ mm, $c_0 = 2.4 \times 10^6$ cells/mL) and $w = 20$ mm.

Also, we did not measure wavelengths on all *dendrites* patterns. Close to the transition from *round* to *dendrites patterns*, patterns were sometimes hedgehog-like (see Figure 3.8.a), only exhibiting emerging dendrites. In these cases, still counted as *dendrites* in the phase diagram, our method for orthoradial wavelength determination do not apply. Our analysis does not apply to *dendrites* with *directional growth* either, for which we see a periodic development of branches perpendicularly to the direction of growth (Figure 3.8.b).

3.4 Directional growth

3.4.1 Characterization of directional growth

Although directional growth could occur for both initially round patterns or dendrites patterns, the phenomenology is the same in both cases.

Figure 3.9 shows the kinetics of this unstationary instability on an example of a single experiment. On the images, we see the formation of an initially centered pattern with a maximum concentration at the center which eventually grows in a well defined direction θ_0 . As it grows directionally, the pattern also remains anchored at the location of the light beam. Here, the direction of growth is also materialized by a line of high concentration (Figure 3.9.c). For dendrites with directional growth, the direction of growth is perpendicular to periodic branches (see Figure 3.8.b and Figure 3.1.e). This growth cannot not be predicted at the beginning of the experiment when the Petri dish is levelled

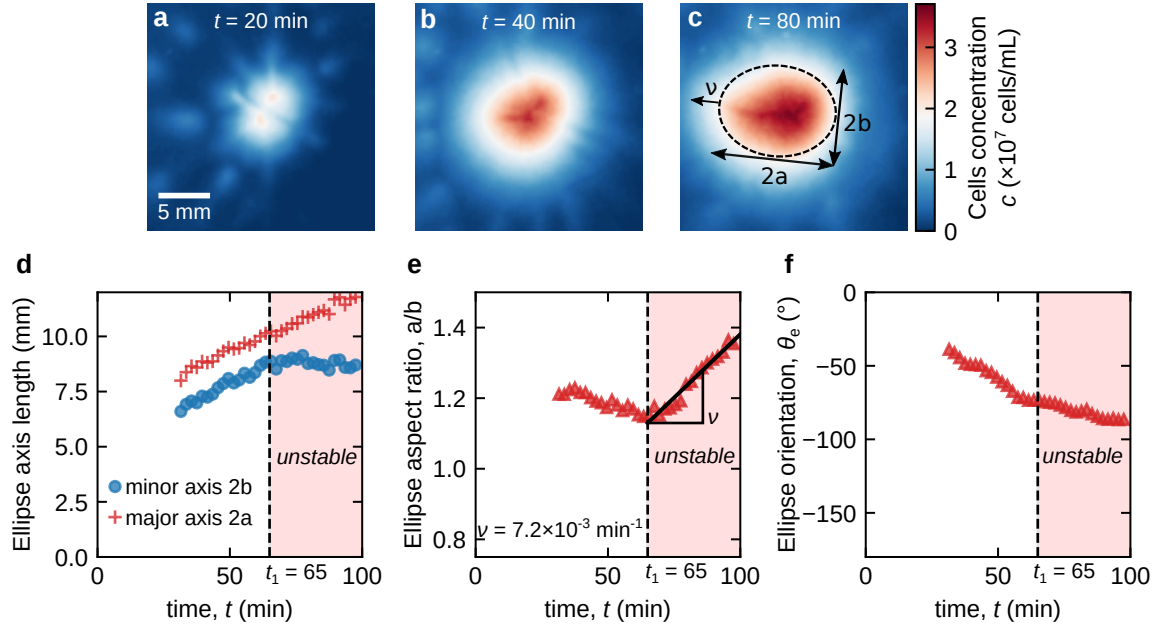


Figure 3.9: Dynamics of directional growth. **a-c**, cell concentration field imaged from top view at different times during an experiment showing directional growth. The light beam was turned on at $t = 0$. Cells accumulate around the light beam (a), reaching a maximum concentration at the center (b). The patterns eventually grow in a well defined direction θ_0 away from the center (here towards the left of the image) with an aspect ratio growth rate $\nu > 0$. **c-f**, The region for which $c(r, \theta, t) > \frac{c_{\max}(t)}{2}$ can be described by an ellipse of orientation θ_e and of major and minor axis lengths $2a$ and $2b$. The evolution of its axis lengths (d), aspect ratio (e) and orientation (f) with time allow to quantify directional growth kinetics. For $t > t_1$, the slope estimate and standard deviation of a linear fit of the aspect ratio gives an anisotropy growth rate $\nu = (7.2 \pm 0.6) \times 10^{-3} \text{ min}^{-1}$. $\text{Ra} = 95$ ($H = 0.24 \text{ mm}$, $c_0 = 2.2 \times 10^6 \text{ cells/mL}$) and $w = 7.5 \text{ mm}$.

(horizontality $\pm 0.05^\circ$). However, we shall see that it can be triggered by an inclination of the Petri dish.

We first quantified directional growth of patterns when it occurred in the experiments. For this, we modelled patterns by ellipses of parameters major and minor axis lengths $2a$, $2b$, aspect ratio a/b and orientation θ_e (Figure 3.9.c). We studied the time evolution of these parameters (Figure 3.9.d-f). Data reveal that there is a clear time t_1 at which directional growth starts. For $t < t_1$, the ellipse grows with a constant aspect ratio close to 1 and there is not any fixed orientation at this stage. For $t > t_1$, the system then finds a fixed direction of growth $\theta_e \simeq C^{st}$. The minor axis length $2b$ reaches a plateau while the major axis length $2a$ still increases. The aspect ratio increases linearly with time, which can be fitted to extract the growth rate of the anisotropy ν .

We measured the anisotropic growth rate ν for all occurrences of directional growth as a function of the pseudo-Rayleigh number Ra . Data are plotted in Figure 3.10.a. Measured anisotropy growth rates ν are of the order of $\sim 10^{-2} \text{ min}^{-1}$. Patterns sizes are typically tens of $\sim 10 \text{ mm}$, so that this corresponds to drift velocities of the order of a

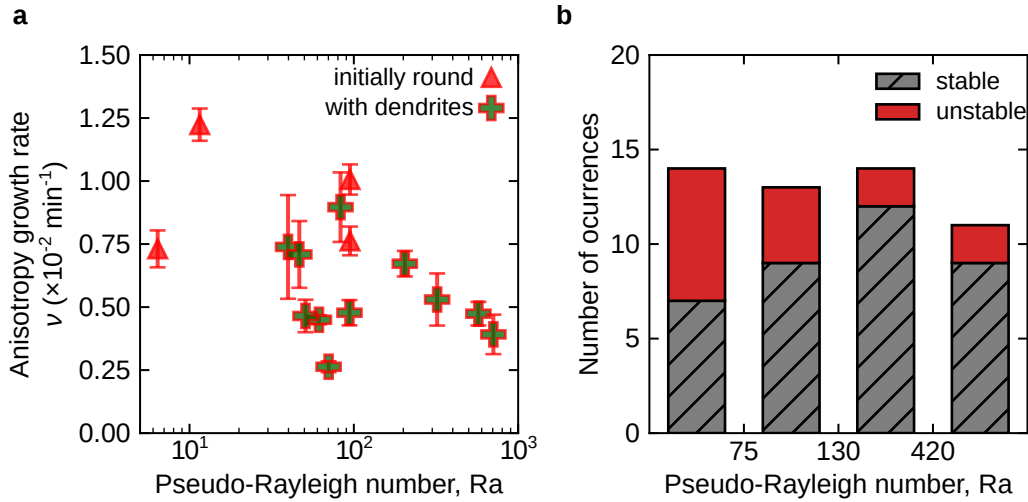


Figure 3.10: Effect of the pseudo-Rayleigh number on directional growth. **a**, Anisotropy growth rate of experiments showing directional growth as a function of the pseudo-Rayleigh number. Each point correspond to a single directional growth occurrence. Growth rates and error bars were measured as explained in Figure 3.9. **b**, Statistics of directional growth occurrences in intervals of pseudo-Rayleigh number for beam widths $w \geq 5.0$ mm. Labels “unstable” and “stable” correspond respectively to occurrence and non-occurrence of directional growth.

few $\mu\text{m/s}$. This is much smaller than the expected velocity of the primary convection roll ($> 100 \mu\text{m/s}$). We observed a decrease of the anisotropy growth rate when increasing the pseudo-Rayleigh number Ra.

To further investigate the effect of the Ra, we studied the statistics of occurrence of directional growth as a function of Ra. Noting that directional growth did not occur for $w < 5$ mm, we counted its number of occurrences for experiments with $w \geq 5$ mm in intervals of Ra (see Figure 3.10.b). Data reveal that directional growth mostly occurs at rather low to intermediate values Ra.

3.4.2 Enhancing directional growth using inclination

To better understand the underlying mechanisms from which directional growth originates, we carried out experiments with a slight inclination of the Petri dish, as illustrated in a schematic view in Figure 3.11.a.

In these experiments, we worked at fixed pseudo-Rayleigh number $Ra = 140$ with 3 beam widths $w = 5.0$, 7.5 , and 20 mm because *directional growth* occurred mainly at intermediate Ra and w/H in the main experiments. We found that directional growth was indeed triggered by a slight inclination α of the Petri dish and patterns grew towards the lower side of the Petri dish, *i.e.* the side where the layer thickness is the largest. We measured their anisotropy growth rate ν as a function of α . For $w = 5.0$ mm, we measured $\nu < 4.0 \times 10^{-3} \text{ min}^{-1}$. For $w = 7.5$ and 20 mm, ν increased from 1.5×10^{-2} to $1.7 \times 10^{-1} \text{ min}^{-1}$ for α increasing from 0.1 to 1.0° . The value of $1.5 \times 10^{-2} \text{ min}^{-1}$ for $\alpha = 0.1 \pm 0.05^\circ$ is found to be a close upper limit of the values of anisotropy growth rate measured with a

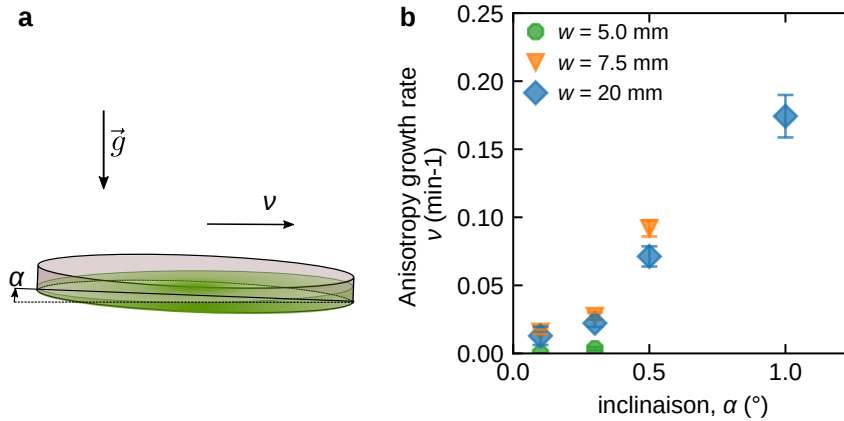


Figure 3.11: Experiments of directional growth of photo-bioconvection patterns with a slight inclination of the suspension. **a**, Principle of the experiments. An inclination $0.1 \pm 0.05^\circ \leq \alpha \leq 1.0 \pm 0.05^\circ$ of the Petri dish with respect to the horizontal is imposed and triggers directional growth towards the lower side of the Petri dish. **b**, Anisotropy growth rates as a function of the Petri dish inclination for different beam widths w at fixed pseudo-Rayleigh number $Ra = 140$.

levelled Petri dish (Figure 3.10.a). This is consistent with a possible defect of horizontality $< 0.1^\circ$ in the main experiments. In any case, the *directional growth* instability reveals a striking increase of the system sensitivity to any slight asymmetry when the beam width is increased.

3.4.3 Discussion

The mechanism behind this instability is not well understood at this stage. The higher concentration along the axis of growth in Figure 3.9.c is an indication that gyrotactic focusing could be involved. The stabilizing effect of Ra on the other hand is intriguing because bioconvection instabilities usually appear when increasing Ra . The role of w can be discussed qualitatively. A first effect of increasing w is to lower the magnitude of the light intensity gradients, which in turn weakens the phototactic restoring attraction towards the center. On the other hand, increasing w also enlarges the spatial range of localized photo-bioconvection. These two effects might play different roles at different distances from the light beam center.

3.5 Conclusion

We studied how cells self-organize in bioconvective flows triggered locally by light. We found that pattern formation in the cell concentration field is controlled by both the Rayleigh number Ra and the beam width w . We first emphasized the role of both these parameters on global properties of cell concentration patterns. Then, we found that different instabilities are under the control of Ra and w . In particular, we showed that when the beam width is comparable or wider than the suspension depth, the cell

concentration field undergoes instabilities with striking breakings of the initial radial symmetry. We found the domain of existence of these instabilities and characterized them separately. *Dendrites* instabilities were found at high Ra and w/H with a well-defined orthoradial wavelength that scales with the liquid height H . *Directional growth* instability occurred mostly at low to intermediate Ra for large w/H . Its anisotropy growth rate is the direct illustration of the system high sensitivity to any slight asymmetry when the beam width is increased.

CHAPTER 4

Asymptotic model for bioconvection in thin layers

This chapter is devoted to the development of an asymptotic theoretical model that captures several qualitative and quantitative features of the experimental observation performed in the previous chapter.

4.1 Axisymmetric structures

4.1.1 Preliminaries

Let us first write the general equations describing the collective behavior of a suspension of *Chlamydomonas reinhardtii* cells in the presence of a heterogeneous light-field. We shall use a continuum deterministic model with gyrotaxis of the form given in section 1.3.4.

$$\begin{aligned}
\text{Incompressibility : } & \vec{\nabla} \cdot \vec{v} = 0 \\
\text{Velocity and pressure fields : } & \rho_0 \frac{\partial \vec{v}}{\partial t} = \eta \Delta \vec{v} - \vec{\nabla} p_e - \rho_0 \beta c g \vec{e}_z \\
\text{Cells conservation : } & \frac{\partial c}{\partial t} = \vec{\nabla} \cdot \left(\underbrace{D \vec{\nabla} c}_{\text{diffusion}} - \underbrace{c |v_{\text{drift}}| \vec{q}}_{\text{drift due to taxis}} - \underbrace{c \vec{v}}_{\text{advection}} \right) \\
\text{Gyrotaxis : } & \frac{\partial \vec{q}}{\partial t} = \frac{1}{2B} [\vec{e}_p - (\vec{e}_p \cdot \vec{q}) \vec{q}] + \frac{1}{2} \omega \times \vec{q}
\end{aligned} \tag{4.1}$$

Despite their complexity, the equations above can be studied numerically if we restrict ourselves to the plane spanned by the unit vectors $\{\vec{e}_r, \vec{e}_z\}$.

4.1.2 Structure of the primary convective roll

Let us first show that the formation of the primary instability can be modeled with the continuum model for bioconvection recalled above without the need to include gyrotaxis. We only consider a phototactic drift which steers cells along the imposed light intensity gradient $\frac{\partial I}{\partial r}$, where in the absence of gyrotaxis, cells are strictly oriented, on average, along their preferential orientation \vec{e}_p :

$$\begin{aligned}
|v_{\text{drift}}| &= \chi \left| \frac{\partial I}{\partial r} \right| \\
\vec{q} &= \vec{e}_p \quad \text{and} \quad \vec{e}_p = \text{sign} \left(\chi \frac{\partial I}{\partial r} \right) \vec{e}_r
\end{aligned} \tag{4.2}$$

A continuum model for localized photo-bioconvection in a radial light intensity in the absence of gyrotaxis is thus :

$$\begin{aligned}
\text{Incompressibility : } & \vec{\nabla} \cdot \vec{v} = 0 \\
\text{Velocity and pressure fields : } & \rho_0 \frac{\partial \vec{v}}{\partial t} = \eta \Delta \vec{v} - \vec{\nabla} p_e - \rho_0 \beta c g \vec{e}_z \\
\text{Cells conservation : } & \frac{\partial c}{\partial t} = \vec{\nabla} \cdot \left(D \vec{\nabla} c - c \chi \frac{\partial I}{\partial r} \vec{e}_r - c \vec{v} \right)
\end{aligned} \tag{4.3}$$

The nonlinear system of equations (4.3) restricted to the (\vec{e}_r, \vec{e}_z) -plane (i.e. a radial cross section of the Petri dish) describes the evolution of four scalar fields (pressure p_e , concentration c , velocity \vec{v} in (\vec{e}_r, \vec{e}_z)). They can be solved numerically with the green light intensity radial profile $I(r)$ used in the experiments as an input. An example of such a numerical resolution with COMSOL is presented in Figure 4.1.

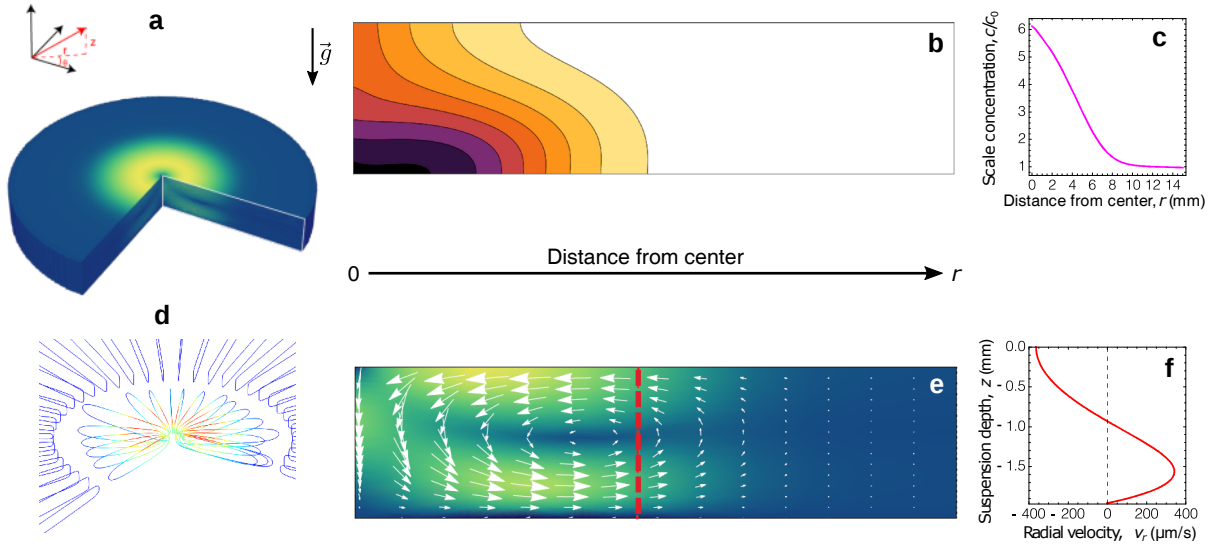


Figure 4.1: Numerical simulation of the primary convection roll without gyrotaxis. **a**, The axisymmetry enables to work in a cross section in a vertical (\vec{e}_r, \vec{e}_z)-plane and to reconstruct the 3D fields by revolution around the vertical axis. **b**, Side view of the stationary cell concentration field. The colormap brightness increases by steps from white for low concentration to black for high concentration. Contour lines are iso-cell concentration lines. **c**, Radial profile of the depth averaged scaled concentration c/c_0 . **d**, Detail of the streamlines of the principal toroidal convective roll near the light source. The second counter-rotating toroidal roll can be seen further away from the center of the light source. Red portions of the streamlines correspond to high velocities and blue portions to low velocities. **e**, Side view of the stationary velocity field. White arrows : local velocity vectors. The colormap brightness increases from chinese blue for low velocity to yellow for high velocity. **f**, Vertical profile of the radial velocity at a fixed distance away from the center (dashed red line in d.).

The formation of the main *round* patterns instability is recovered. Numerical simulations give access to data that cannot be measured in the experiments : data of the cells repartition along the suspension depth (Figure 4.1.b) and data of the velocity field (Figure 4.1.d,e.f). In the primary convection roll, the flow structure is toroidal (Figure 4.1.d).

The flow is directed downward at the center of the light source and as a result, the cell concentration field is pushed towards the bottom. As illustrated in (Figure 4.2.a.b.c), this effect is enhanced at high Rayleigh number since the magnitude of the flow velocity increases with the Rayleigh number. When the Rayleigh number is low on the other hand, the cell concentration is almost constant across the thickness of the suspension (Figure 4.2.a). As the distance from the center increases, the vertical velocity becomes negligible and the flow is almost horizontal (Figure 4.1.e).

4.1.3 The effect of gyrotaxis

The 2D model above without gyrotaxis is stable within the range of parameters explored in the experiments. In the study by Dervaux, Capellazzi Resta, and Brunet 2017, it was found that *waves* emission could be reproduced in 2D numerical simulations by

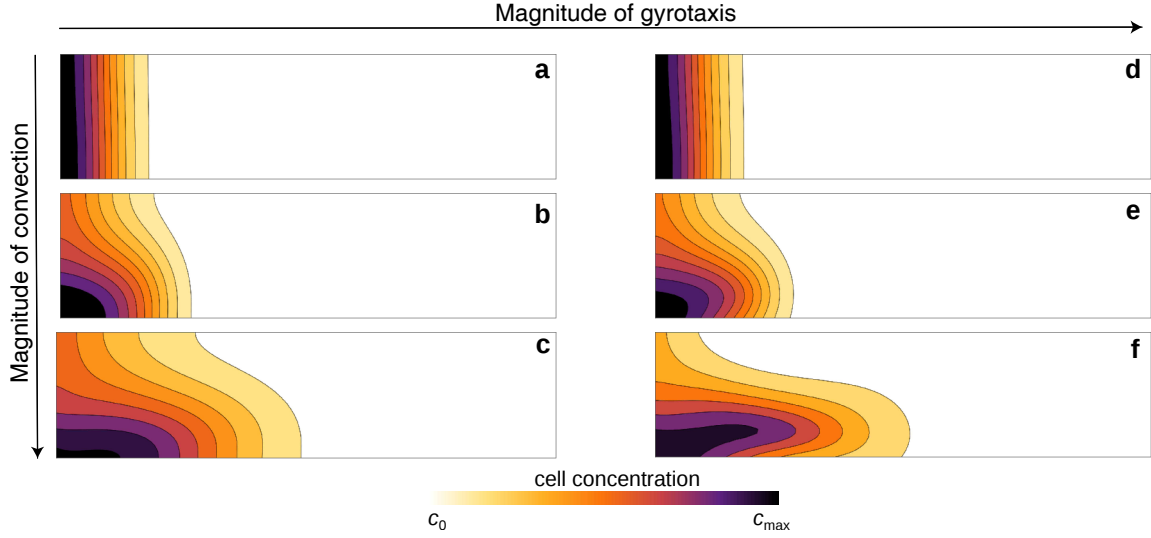


Figure 4.2: Effect of the Rayleigh number and of gyrotaxis on the cell concentration field. The magnitude of convection is controlled by 3 values of the pseudo-Rayleigh number. From top to bottom: 0.1, 1 and 100. The magnitude of gyrotaxis is controlled by 2 values of the gyrotactic timescale. On the left column, $B = 0$ s corresponds to the case without gyrotaxis. On the right column, $B = 1$ s. Contours lines show iso-cell concentration lines.

introducing gyrotaxis and a deviation of cells orientation with respect to their preferential direction $\vec{q} \neq \text{sign}(\chi \frac{\partial I}{\partial r}) \vec{e}_r$. The equations for a 2D model with gyrotaxis are :

$$\begin{aligned}
 \text{Incompressibility : } & \vec{\nabla} \cdot \vec{v} = 0 \\
 \text{Velocity and pressure fields : } & \rho_0 \frac{\partial \vec{v}}{\partial t} = \eta \Delta \vec{v} - \vec{\nabla} p_e - \rho_0 \beta c g \vec{e}_z \\
 \text{Cells conservation : } & \frac{\partial c}{\partial t} = \vec{\nabla} \cdot (D \vec{\nabla} c - c \chi \frac{\partial I}{\partial r} \vec{q} - c \vec{v}) \\
 \text{Gyrotaxis : } & \frac{\partial \vec{q}}{\partial t} = \frac{1}{2B} [\vec{e}_r - (\vec{e}_r \cdot \vec{q}) \vec{q}] + \frac{1}{2} \omega \times \vec{q}
 \end{aligned} \tag{4.4}$$

While gyrotaxis only has a weak effect on both the fluid flow and the depth-integrated cell concentration field, it does impact significantly the repartition of cell across the thickness of the suspension, as seen in (Figure 4.2.d.e.f). Qualitatively, in the presence of gyrotaxis, the dense layer of cell induced by the primary convective roll is slightly shifted above the bottom of the Petri dish. More precisely, the dense layer is located around the local maximum of the flow velocity. Because this cell-rich layer has a higher density than the cell-poor layer below, it ultimately undergoes a gravitational instability above a threshold in the Rayleigh number, as illustrated in (Figure 4.3). Because this secondary instability is advected by the primary convective roll, it manifests itself as rings of high concentration propagating outward from the center of the Petri dish. The wave velocity predicted by these numerical simulations was found to be in good agreement with experimental results (Dervaux, Capellazzi Resta, and Brunet 2017). Note that at that time,

a constant value was used for the phototactic susceptibility χ in the model. Best fits to experimental cell concentration profiles enabled authors to find the timescale of algae phototactic re-orientation along the direction \vec{e}_r of the light gradient when the flow is switched off : $B = 1.2 \pm 0.2$ s, in agreement with previous models (Williams and Bees 2011b; Garcia, Rafai, and Peyla 2013).

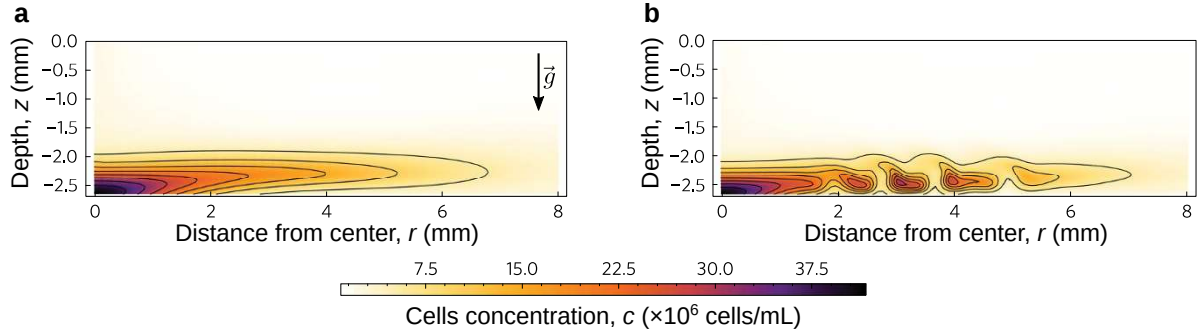


Figure 4.3: Numerical simulation of waves emission with gyrotaxis. Side views of the cell concentration fields obtained in 2D numerical simulations with gyrotaxis. Contours lines show iso-cell concentration lines. **a**, In the presence of gyrotaxis, there is a gap between the cells dense layer in the lower part of the suspension and the bottom of the Petri dish. **b**, Later, *waves* are emitted. The dense layer is destabilized by gravity and breaks into clusters of high cell concentration advected by the flow. $Ra = 125$ ($H = 2.5$ mm and $c_0 = 1.8 \times 10^6$ cells/mL), $w = 2.7$ mm. From Dervaux, Capellazzi Resta, and Brunet 2017.

4.2 Hypothesis for the development of the asymptotic model

Numerical simulations restricted to the (\vec{e}_r, \vec{e}_z) -plane cannot reproduce the orthoradial breaking of the radial symmetry observed in *dendrites* or in *directional growth*. However attempting a numerical resolution of a 3D model with gyrotaxis would require code optimization and/or numerical resources that are not within our reach. Indeed, including gyrotaxis in (\vec{e}_r, \vec{e}_z) required to solve numerically 6 scalar fields equations (pressure p_e , concentration c , velocity \vec{v} in (\vec{e}_r, \vec{e}_z) , orientation \vec{q} in (\vec{e}_r, \vec{e}_z)) and already took around 1 week of calculation (with COMSOL Multiphysics 5.3, on a desktop PC with 8 cores) in the unstable regime. In order to make further progress, we may take advantage of the fact that our experiments are performed in a thin layer geometry $H \ll L$. We therefore chose to simplify the model by developing an asymptotic model, tailored to describe the limit $H/L \ll 1$. As we shall see, this approach, together with additional simplifying hypotheses that we introduce in this section, allows us to reduce the systems of vectorial equation shown above to a single nonlinear partial differential equation describing the depth-averaged cell concentration in the suspension. In a second step, analytical solutions to this equation and numerical results will be presented and confronted to experimental data.

4.2.1 Dimensionless equations

We first rewrite in a dimensionless form the general equations (4.1) that describe the spatio-temporal evolution of the flow, pressure, concentration and orientation fields. We scale lengths by the liquid height H , time by the diffusion time scale H^2/D , concentrations by the global cell concentration c_0 , velocities by D/H and pressure by $\eta D/H^2$. To simplify the writing, we keep the same notations for both dimensioned and dimensionless space-time coordinates (r, θ, z, t) , fields $(\vec{v}, c, p_e, \omega)$ and operators $(\frac{\partial}{\partial t}, \vec{\nabla}, \Delta)$. Dimensionless equations take the following form :

$$\text{Incompressibility : } \vec{\nabla} \cdot \vec{v} = 0 \quad (4.5)$$

$$\text{Velocity and pressure fields : } \frac{\rho_0 D}{\eta} \frac{\partial \vec{v}}{\partial t} = \Delta \vec{v} - \vec{\nabla} p_e - (\text{Ra} \cdot c) \vec{e}_z = 0 \quad (4.6)$$

$$\text{Cells conservation : } \frac{\partial c}{\partial t} = \vec{\nabla} \cdot \vec{\mathcal{J}} \text{ with } \vec{\mathcal{J}} = \vec{\nabla} c - |\mathcal{T}_{\text{drift}}| c \vec{q} - c \vec{v} \text{ the mass flux} \quad (4.7)$$

$$\text{Gyrotaxis : } G_y \frac{\partial \vec{q}}{\partial t} = \frac{1}{2} [\vec{e}_p - (\vec{e}_p \cdot \vec{q}) \vec{q}] + \frac{1}{2} G_y \cdot (\vec{\omega} \times \vec{q}) = \vec{0} \quad (4.8)$$

They reveal that in this model, the system is governed by the following dimensionless numbers:

$$\begin{aligned} \text{The pseudo-Rayleigh number, } \text{Ra} &= \frac{\rho_0 g \beta H^3 c_0}{D \eta} \\ \text{The drift number, } \mathcal{T}_{\text{drift}} &= \frac{v_{\text{drift}} H}{D} \\ \text{The gyrotactic number, } G_y &= \frac{B D}{H^2} \end{aligned} \quad (4.9)$$

We already defined the pseudo-Rayleigh number Ra as the ratio of the time scale of diffusion to the time scale of convection. We see here that it quantifies the coupling of the velocity \vec{v} and pressure fields p_e with the concentration field c . The drift number $\mathcal{T}_{\text{drift}}$ compares the ratio of the time scale of diffusion to the time scale of cells drift. It increases as cells swimming is more biased. Finally, the gyrotactic number G_y compares the time scale of reorientation to the time scale of diffusion. It is alone hard to interpret because the algae re-orientation time scale B is usually compared to a characteristic time scale of the flow. Later, we will in fact see that, indeed, the gyrotactic effect is controlled by the product $G_y \cdot \text{Ra}$ which compares the time scale of re-orientation to the time scale of convection.

4.2.2 Effective drifts

In the dimensionless cell conservation and gyrotaxis equations (4.7,4.8), we need to specify the drift term and the orientations vectors. We consider two drifts : a phototactic drift due to the light intensity gradient of preferential radial direction and an additional

drift of preferential vertical direction. We shall discuss the origin of this vertical drift later in this section. We thus replace the generic single drift term with two drifts terms and make the hypothesis that they are additive. Each drift term has its own dimensionless drift velocity and orientation unit vector :

$$|\mathcal{T}_{\text{drift}}|c\vec{q} \rightarrow |\mathcal{T}_{\parallel}|c\vec{q}_{\parallel} + |\mathcal{T}_{\perp}|c\vec{q}_{\perp} \quad (4.10)$$

The dimensionless phototactic drift number \mathcal{T}_{\parallel} depends on space via the light intensity gradient and the phototactic susceptibility. In the model, the second term \mathcal{T}_{\perp} does not depend either on space or on time for simplicity and we shall obtain its value from comparison of the model with experimental results.

$$\mathcal{T}_{\parallel}(r) = \chi(I(r))\frac{\partial I}{\partial r}(r)\frac{H}{D} \quad \text{and} \quad \mathcal{T}_{\perp} = \frac{v_{\perp}H}{D} \quad (4.11)$$

\vec{q}_{\parallel} and \vec{q}_{\perp} are respectively radial and vertical vectors in the absence of flow. In the presence of flow however, they can have non-zero θ -components due to gyrotaxis. $q_{\perp,\theta}$ originates from the r -component of the vorticity acting on the vertical drift whereas $q_{\parallel,\theta}$ originates from the z -component of the vorticity acting on the radial drift. To further simplify the analysis, we write those θ -components as perturbations around known preferential horizontal and vertical orientations. Thus the radial and vertical components are known and we have :

$$\begin{aligned} \vec{q}_{\parallel} &= \text{sign}(\mathcal{T}_{\parallel})\vec{e}_r + q_{\parallel,\theta}\vec{e}_{\theta}, \quad |q_{\parallel,\theta}| \ll 1 \\ \vec{q}_{\perp} &= \text{sign}(\mathcal{T}_{\perp})\vec{e}_z + q_{\perp,\theta}\vec{e}_z, \quad |q_{\perp,\theta}| \ll 1 \end{aligned} \quad (4.12)$$

In the perturbative limit where $|q_{\parallel,\theta}|, |q_{\perp,\theta}| \ll 1$, \vec{q}_{\parallel} and \vec{q}_{\perp} are quasi-unit vectors. Finally, we construct a total unit orientation vector \vec{q}_{tot} on which to apply the gyrotaxis equation as the weighted sum of the two orientations unit vectors \vec{q}_{\parallel} and \vec{q}_{\perp} :

$$\vec{q}_{\text{tot}} = \frac{|\mathcal{T}_{\parallel}|}{\mathcal{T}}\vec{q}_{\parallel} + \frac{|\mathcal{T}_{\perp}|}{\mathcal{T}}\vec{q}_{\perp} \quad \text{with} \quad \mathcal{T} = \sqrt{\mathcal{T}_{\perp}^2 + \mathcal{T}_{\parallel}^2} \quad (4.13)$$

By construction, we have a similar expression for the total preferential orientation $\vec{e}_{\text{p,tot}}$ appearing in the gyrotactic equation 4.8. Then \vec{q}_{tot} can also be rewritten with a perturbation on $\vec{e}_{\text{p,tot}}$. We have :

$$\vec{e}_{\text{p,tot}} = \frac{|\mathcal{T}_{\parallel}|}{\mathcal{T}} \text{sign}(\mathcal{T}_{\parallel})\vec{e}_r + \frac{|\mathcal{T}_{\perp}|}{\mathcal{T}} \text{sign}(\mathcal{T}_{\perp})\vec{e}_z \quad (4.14)$$

$$\vec{q}_{\text{tot}} = \vec{e}_{\text{p,tot}} + \underbrace{q_{\text{tot},\theta}}_{|q_{\text{tot},\theta}| \ll 1} \vec{e}_{\theta} \quad \text{with} \quad q_{\text{tot},\theta} = \frac{|\mathcal{T}_{\parallel}|}{\mathcal{T}}q_{\parallel,\theta} + \frac{|\mathcal{T}_{\perp}|}{\mathcal{T}}q_{\perp,\theta} \quad (4.15)$$

4.2.3 Timescales of the problem

Additional simplifications can be obtained by evaluating the characteristic timescales involved in the problem. The diffusion timescale is the longest timescale in the problem with $\frac{H^2}{D} \gtrsim 10$ s with $H \gtrsim 1$ mm. The viscous timescale is $\frac{H^2 \rho_0}{\eta} \gtrsim 1$ s. Finally, the time scale for phototactic reorientation is $B \sim 1$ s. The respective ratios of the viscous and of the phototactic reorientation timescales over the diffusion time scale are thus : $\frac{D \rho_0}{\eta} \sim 0.1$, $G_y \lesssim 0.1$

We can thus drop the time-derivative terms in both the flow and pressure fields equation (4.6) as well as in the gyrotaxis equation (4.8). In other words, we consider that the pressure p_e , velocity \vec{v} and orientation fields $\vec{q}_{\parallel}, \vec{q}_{\perp}, \vec{q}_{\text{tot}}$ instantaneously adjust to the slowly varying concentration field c .

At this stage, we can rewrite the dimensionless equations as follows :

$$\text{Velocity and pressure fields : } \Delta \vec{v} = \vec{\nabla} p_e + (\text{Ra} \cdot c) \vec{e}_z = 0 \quad (4.16)$$

$$\text{Cell conservation : } \frac{\partial c}{\partial t} = \vec{\nabla} \cdot \vec{\mathcal{J}} \text{ with } \vec{\mathcal{J}} = \vec{\nabla} c - c |\mathcal{T}_{\parallel}| \vec{q}_{\parallel} - c |\mathcal{T}_{\perp}| \vec{q}_{\perp} - c \vec{v} \quad (4.17)$$

$$\text{Gyrotaxis : } (\vec{e}_{\text{p,tot}} \cdot \vec{q}_{\text{tot}}) \vec{q}_{\text{tot}} - \vec{e}_{\text{p,tot}} = G_y \cdot (\vec{\omega} \times \vec{q}_{\text{tot}}) \quad (4.18)$$

Note that this simplification implicitly assumes that gyrotaxis (or vorticity) is weak enough to allow the existence of stationary solutions to the gyrotaxis equation (4.8). Indeed, at large vorticities, no such solutions exist and cells rotate continuously.

4.2.4 Boundary conditions

We also need to specify the boundary conditions. At the bottom and at the free surface, we have :

$$\vec{v}(r, \theta, z = 0, t) = \vec{0} \text{ no slip condition at the bottom} \quad (4.19)$$

$$\frac{\partial v_r}{\partial z}(r, \theta, z = 1, t) = \frac{\partial v_{\theta}}{\partial z}(r, \theta, z = 1, t) = 0 \text{ vanishing shear at the free surface} \quad (4.20)$$

$$v_z(r, \theta, z = 1, t) = 0 \text{ constant thickness} \quad (4.21)$$

For simplicity, we assume that the system is infinite in the radial direction, so that the following conditions must also apply :

$$\lim_{r \rightarrow \infty} \vec{v}(r, \theta, z, t) = \vec{0} \text{ and } \lim_{r \rightarrow \infty} c(r, \theta, z, t) = C^{\text{st}} \quad (4.22)$$

4.2.5 Geometry $H \ll L$

We now take advantage of the geometry to reduce the dimensionality of the model, noting that the thickness H (typically 1 – 5 mm in the experiments) is much smaller

than the lateral extension L (typically 10 cm in the experiments). The lubrication approximation consists in developing the model equation in powers of the small parameter H/L and to retain only the first term in this development. At leading order in H/L , the incompressibility condition, together with the condition of constant thickness of the fluid layer, implies that the vertical component of the fluid flow vanishes :

$$v_z = 0 \quad (4.23)$$

In practice, this lubrication approximation is only valid for distances from the center $r > H$ (see primary convection roll toroidal structure in Figure 4.1.d). We also assume that the cell concentration field is stationary in the vertical dimension with vanishing vertical mass flux :

$$\mathcal{J}_z = 0 \Leftrightarrow \frac{\partial c}{\partial z} - c\mathcal{T}_\perp = 0 \quad (4.24)$$

This integrates to :

$$c(r, \theta, z, t) = c_{\parallel}(r, \theta, t)e^{z\mathcal{T}_\perp} \quad (4.25)$$

The next step in the development of an asymptotic model consists in integrating the model equations over the liquid thickness ($\int_0^1 \dots dz$), as in classical lubrication theory (Reynolds 1886). Before proceeding to this step however, let us briefly discuss the physical origin of the vertical drift \mathcal{T}_\perp introduced in our model.

4.2.6 Physical origin of the vertical drift \mathcal{T}_\perp

In classical continuum models for bioconvection, vertical drifts terms account for taxes in the vertical direction which are typically gravitaxis, phototaxis due to homogeneous top or bottom light, or aerotaxis toward/away from the free surface. For gravitaxis of *Chlamydomonas reinhardtii*, we typically have : $\mathcal{T}_\perp \sim 0.01 - 0.1$. In our experiments, possible causes of cells vertical swimming can be gravitaxis, upward phototaxis in the direction of propagation of the green widened light beam, or possible weak phototaxis due to bottom red light illumination. These vertical taxes were neglected in the previous section modeling the structure of the primary convective roll and the emission of *waves*.

In the proposed asymptotic model with gyrotaxis and a vertical drift $|\mathcal{T}_\perp|\vec{q}_\perp$, the first effect of \mathcal{T}_\perp is seen in the inhomogeneous cells repartition along the vertical direction for $\mathcal{T}_\perp \neq 0$ (eq. (4.25)). Cells accumulate at the top (resp. bottom) for $\mathcal{T}_\perp > 0$ (resp. $\mathcal{T}_\perp < 0$) in a region of size $\sim \frac{1}{|\mathcal{T}_\perp|}$. In this model with $v_z = 0$, the vertical drift term $|\mathcal{T}_\perp|\vec{q}_\perp$ enables to take phenomenologically into account the effect of the neglected vertical velocity ($v_z = 0$ assumed) clearly visible on cells repartition in the vertical direction, as shown in the previous section. But then, to distinguish between an effect of the advection by flow and an actual vertical taxis with a vertical cell orientation, two vertical drifts $\mathcal{T}_{\perp, \text{flow}}\vec{e}_z$ and $|\mathcal{T}_{\perp, \text{taxis}}|\vec{q}_{\perp, \text{taxis}}$ should be included in the model. Only the orientation $\vec{q}_{\perp, \text{taxis}}$ should

be taken into account in the total cell orientation \vec{q}_{tot} in the gyrotaxis equation (4.8). For simplicity, we take a unique effective vertical drift $|\mathcal{T}_\perp|\vec{q}_\perp$ with \vec{q}_\perp taken into account in \vec{q}_{tot} , whether \mathcal{T}_\perp originates from the flow or from a vertical taxis. In fact, it is still possible that in the experiments, the vertical downward flow at the center also orients the cells in the direction of the gravity field, in addition to pushing them towards the lower part of the suspension, but this is merely speculative.

4.3 Derivation of the asymptotic model

In this section, we derive an asymptotic model describing the evolution of the depth-averaged cell concentration field \bar{c} which can be compared to the experiments. We first obtain the pressure p_e and velocity fields \vec{v} as a function of the concentration field c . Then, we look for the orientations fields $\vec{q}_\parallel, \vec{q}_\perp, \vec{q}_{\text{tot}}$ knowing the vorticity from the flow field. Finally, we use the solutions for $\vec{v}, \vec{q}_\parallel, \vec{q}_\perp$, all expressed in term of the cell concentration field c , in the cell conservation equation that we integrate over the vertical coordinate. We obtain a nonlinear drift-diffusion equation for the depth-averaged cell concentration field given at the end of this section.

4.3.1 Pressure and velocity fields

Using the simplifications of the previous section, the equation (4.6) describing the flow and pressure fields reduces to, at dominant H/L order and projected on $(\vec{e}_r, \vec{e}_\theta, \vec{e}_z)$:

$$\frac{\partial^2 v_r}{\partial z^2} = \frac{\partial p_e}{\partial r} \quad (4.26)$$

$$\frac{\partial^2 v_\theta}{\partial z^2} = \frac{1}{r} \frac{\partial p_e}{\partial \theta} \quad (4.27)$$

$$\frac{\partial p_e}{\partial z} = -\text{Ra} \cdot c \quad (4.28)$$

Using the boundary conditions (4.19) and (4.20), we find :

$$p_e(r, \theta, z, t) = -\frac{\text{Ra}}{\mathcal{T}_\perp} c_\parallel(r, \theta, t) + c_1(r, \theta, t) \quad (4.29)$$

$$v_r(r, \theta, z, t) = -\text{Ra} f(z) \frac{\partial c_\parallel}{\partial r}(r, \theta, t) + \frac{z(z-2)}{2} \frac{\partial c_1}{\partial r}(r, \theta, t) \quad (4.30)$$

$$v_\theta(r, \theta, z, t) = -\frac{\text{Ra}}{r} f(z) \frac{\partial c_\parallel}{\partial \theta}(r, \theta, t) + \frac{z(z-2)}{2r} \frac{\partial c_1}{\partial \theta}(r, \theta, t) \quad (4.31)$$

$$\text{where: } f(z) = \frac{e^{z\mathcal{T}_\perp} - z\mathcal{T}_\perp e^{\mathcal{T}_\perp} - 1}{\mathcal{T}_\perp^3}$$

c_1 is determined by first integrating the continuity equation (4.5) over the suspension depth and then using the boundary conditions of an infinite system (4.22). We successively

obtain :

$$\Delta c_1(r, \theta, t) = \text{Ra} \underbrace{\frac{3[2(1 + \mathcal{T}_\perp) + e^{\mathcal{T}_\perp}(\mathcal{T}_\perp^2 - 2)]}{2\mathcal{T}_\perp^4}}_{h(\mathcal{T}_\perp)} \Delta_{\parallel} c_{\parallel}(r, \theta, t) \quad (4.32)$$

$$\text{and then, } c_1(r, \theta, t) = \text{Ra} h(\mathcal{T}_\perp) c_{\parallel}(r, \theta, t) \quad (4.33)$$

Finally, the pressure and velocity fields can be expressed as :

$$p_e(r, \theta, z, t) = \text{Ra} \left(\frac{-e^{z\mathcal{T}_\perp}}{\mathcal{T}_\perp} + h(\mathcal{T}_\perp) \right) c_{\parallel}(r, \theta, t) \quad (4.34)$$

$$\vec{v}(r, \theta, z, t) = \text{Ra} \left(-f(z) + \frac{z(z-2)}{2} h(\mathcal{T}_\perp) \right) \vec{\nabla} c_{\parallel}(r, \theta, t) \quad (4.35)$$

It is worth noting that, because the pressure field is linearly related to the concentration field, the lubrication approximation yields a Darcy-like model where the horizontal velocity field is proportional to both the pseudo-Rayleigh number and the horizontal cell concentration gradient :

$$\vec{v} \propto \text{Ra} \vec{\nabla} c_{\parallel} \quad (4.36)$$

In chapter 5, quantitative measurements of experimental velocity fields will be presented and eq. (4.36) is precisely the kind of remarkable relationships with the cell concentration field that we will investigate.

4.3.2 Orientation field

We then solve the gyrotaxis equation for the total cell orientation \vec{q}_{tot} . At first order in $q_{\text{tot},\theta}$, the gyrotaxis equation (4.18) reads :

$$q_{\text{tot},\theta} \vec{e}_\theta = \mathbf{G}_y \cdot \vec{\omega} \times \vec{e}_{\text{p,tot}} \quad (4.37)$$

In the right hand side of eq. (4.37), the vorticity is :

$$\omega_r = -\frac{\partial v_\theta}{\partial z} \quad (4.38)$$

$$\omega_\theta = \frac{\partial v_r}{\partial z} \quad (4.39)$$

$$\omega_z = 0 \quad (4.40)$$

We note the absence of vorticity of \vec{e}_z axis (eq. (4.40)). We thus find that the only contribution to the θ -component of the total orientation \vec{q}_{tot} is $q_{\perp,\theta}$ which comes from the vorticity of axis \vec{e}_r acting on the vertical drift and we have :

$$q_{\parallel,\theta} = 0, \quad q_{\perp,\theta} \neq 0 \quad \text{and} \quad q_{\text{tot},\theta} = \frac{|\mathcal{T}_{\perp}|}{\mathcal{T}} q_{\perp,\theta} \quad (4.41)$$

Then the gyrotaxis equation yields :

$$q_{\text{tot},\theta} = G_y \cdot \frac{\partial v_{\theta}}{\partial z} \frac{\mathcal{T}_{\perp}}{\mathcal{T}} \quad \text{and} \quad q_{\perp,\theta} = G_y \cdot \frac{\partial v_{\theta}}{\partial z} \text{sign}(\mathcal{T}_{\perp}) \quad (4.42)$$

4.3.3 Depth-averaged cell concentration field

We then look for the depth-averaged cell concentration field, which we note \bar{c} and is the observable in the experiments. From eq. (4.25), we have :

$$\bar{c}(r, \theta, t) = \int_0^1 c(r, \theta, z, t) dz = \frac{e^{\mathcal{T}_{\perp}} - 1}{\mathcal{T}_{\perp}} c_{\parallel}(r, \theta, t) \quad (4.43)$$

We integrate the cells diffusion-advection equation with use of the solutions for the velocity (4.35) and orientation fields (4.41, 4.42) and of the formula (4.43). We find a nonlinear diffusion-drift equation :

$$\frac{\partial \bar{c}}{\partial t} = \vec{\nabla} \cdot [(1 + \alpha \bar{c}) \vec{\nabla} \bar{c} - \bar{c} \vec{\nu}_{\text{eff}}] \quad (4.44)$$

Where :

$$\alpha = \text{Ra} \cdot \left(\frac{1 + e^{2\mathcal{T}_{\perp}}(3 - 2\mathcal{T}_{\perp}) - 4e^{\mathcal{T}_{\perp}}}{2\mathcal{T}_{\perp}^3(e^{\mathcal{T}_{\perp}} - 1)} + \frac{3[e^{\mathcal{T}_{\perp}}(\mathcal{T}_{\perp}^2 - 2) + 2(\mathcal{T}_{\perp} + 1)]^2}{4(e^{\mathcal{T}_{\perp}} - 1)\mathcal{T}_{\perp}^6} \right) \quad (4.45)$$

$$\vec{\nu}_{\text{eff}} = \mathcal{T}_{\parallel} \vec{e}_r + \text{Ra} \cdot G_y \cdot \left(\frac{e_{\perp}^{\mathcal{T}} - 1}{2\mathcal{T}_{\perp}} + \frac{3(\mathcal{T}_{\perp} - e_{\perp}^{\mathcal{T}} + 1)(e_{\perp}^{\mathcal{T}}(\mathcal{T}_{\perp}^2 - 2) + 2(\mathcal{T}_{\perp} + 1))}{2(e_{\perp}^{\mathcal{T}} - 1)\mathcal{T}_{\perp}^4} \right) \frac{1}{r} \frac{\partial c_{\parallel}}{\partial \theta} \vec{e}_{\theta} \quad (4.46)$$

We note that the drift term $\vec{\nu}_{\text{eff}}$ has a θ -component proportional to $\vec{\nabla} c_{\parallel} \cdot \vec{e}_{\theta}$ (and thus to $\vec{\nabla} \bar{c} \cdot \vec{e}_{\theta}$). Therefore, eq. (4.44) can be rewritten with an anisotropic nonlinear effective diffusion matrix :

$$\frac{\partial \bar{c}}{\partial t} = \vec{\nabla} \cdot (\mathbf{D} \cdot \vec{\nabla} \bar{c} - \bar{c} \mathcal{T}_{\parallel} \vec{e}_r) \quad (4.47)$$

$$\mathbf{D} = \begin{pmatrix} 1 + \alpha \bar{c} & 0 \\ 0 & 1 + (\alpha - \gamma) \bar{c} \end{pmatrix} = \begin{pmatrix} 1 + \alpha_0 \text{Ra} \cdot \bar{c} & 0 \\ 0 & 1 + (\alpha_0 - \gamma_0 G_y) \text{Ra} \cdot \bar{c} \end{pmatrix} \quad (4.48)$$

$$\text{with } \alpha_0 = \frac{1 + e^{2\mathcal{T}_{\perp}}(3 - 2\mathcal{T}_{\perp}) - 4e^{\mathcal{T}_{\perp}}}{2\mathcal{T}_{\perp}^3(e^{\mathcal{T}_{\perp}} - 1)} + \frac{3[e^{\mathcal{T}_{\perp}}(\mathcal{T}_{\perp}^2 - 2) + 2(\mathcal{T}_{\perp} + 1)]^2}{4(e^{\mathcal{T}_{\perp}} - 1)\mathcal{T}_{\perp}^6} \quad (4.49)$$

$$\text{and } \gamma_0 = \frac{e_{\perp}^{\mathcal{T}} - 1}{2\mathcal{T}_{\perp}} + \frac{3(\mathcal{T}_{\perp} - e_{\perp}^{\mathcal{T}} + 1)(e_{\perp}^{\mathcal{T}}(\mathcal{T}_{\perp}^2 - 2) + 2(\mathcal{T}_{\perp} + 1))}{2(e_{\perp}^{\mathcal{T}} - 1)\mathcal{T}_{\perp}^4} \quad (4.50)$$

The model with gyrotaxis and vertical drift therefore reduces, in the asymptotic limit $H/L \ll 1$ to a single (r, θ, t) nonlinear anisotropic diffusion-drift equation describing the evolution of the depth-averaged concentration fields \bar{c} (4.47) where information of the vertical direction is contained in the dependence of the nonlinear coefficients of the effective diffusion matrix on the vertical drift \mathcal{T}_\perp (4.49, 4.50).

4.4 Physical interpretation of the model

Before proceeding to the analysis of the model, let us first provide a physical interpretation of the nonlinear diffusion-drift equation describing the evolution of the depth-averaged cell concentration :

$$\frac{\partial \bar{c}}{\partial t} = \vec{\nabla} \cdot (\mathbf{D} \cdot \vec{\nabla} \bar{c} - \bar{c} \mathcal{T}_\parallel \vec{e}_r)$$

4.4.1 A nonlinear diffusion-drift equation

The time evolution of \bar{c} results from the competition between two fluxes: an anisotropic nonlinear diffusive flux $\mathbf{D} \cdot \vec{\nabla} \bar{c}$ and a phototactic drift $\bar{c} \mathcal{T}_\parallel \vec{e}_r$ of the Keller-Segel type. We note that the form of the phototactic drift simply carries over from the full three-dimensional model (up to an integration across the thickness of the suspension) and its interpretation remains identical: cells move in the radial light intensity gradient with a velocity that depends on the local value of the light intensity field. The anisotropic nonlinear effective diffusion matrix \mathbf{D} , on the other hand, incorporates several effects of distinct physical origins that we now discuss. We first note that it can be decomposed as the sum of three terms in the $(\vec{e}_r, \vec{e}_\theta)$ basis :

$$\mathbf{D} = \underbrace{\begin{pmatrix} 1 & 0 \\ 0 & 1 \end{pmatrix}}_{\text{linear diffusion}} + \underbrace{\begin{pmatrix} \alpha_0(\mathcal{T}_\perp)\text{Ra} \cdot \bar{c} & 0 \\ 0 & \alpha_0(\mathcal{T}_\perp)\text{Ra} \cdot \bar{c} \end{pmatrix}}_{\text{advection}} + \underbrace{\begin{pmatrix} 0 & 0 \\ 0 & -\gamma_0(\mathcal{T}_\perp)\text{G}_y\text{Ra} \cdot \bar{c} \end{pmatrix}}_{\text{gyrotaxis}} \quad (4.51)$$

The linear contribution corresponds to the random motion of *Chlamydomonas reinhardtii* cells. Nonlinear contributions originate from advection and gyrotaxis (second and third terms in the decomposition above). The advective term is isotropic and is due to the primary convective roll induced by cells accumulation at the center of the light beam. It is driven by the pseudo-Rayleigh number Ra and its magnitude is controlled by a convective coefficient α_0 . This convective coefficient depends on the dimensionless vertical velocity drift \mathcal{T}_\perp and we note that its sign is opposite to that of \mathcal{T}_\perp . Anisotropy is due to the gyrotactic term which creates an orthoradial diffusive flux. γ_0 is a gyrotactic coefficient. It is not only multiplied by the gyrotactic number G_y but also by the pseudo-Rayleigh number Ra . This means that both $\text{G}_y \neq 0$ and a high enough Ra are necessary conditions

to observe gyrotactic instabilities.

4.4.2 Effect of advection

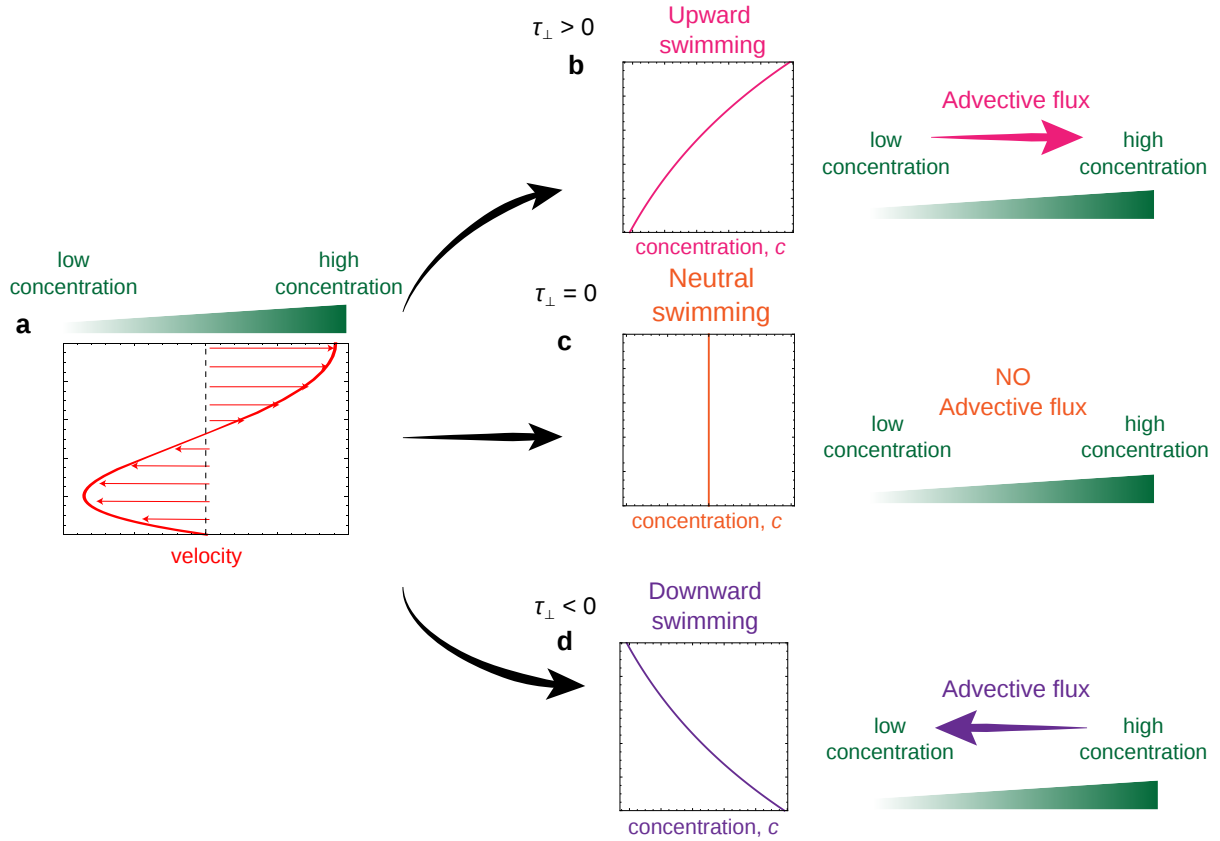


Figure 4.4: Effect of advection on the cell concentration in the asymptotic model. Left : A horizontal (radial or orthoradial) cell concentration gradient and its corresponding velocity vertical profile. Middle : the repartition of cells along the vertical coordinate is given by the sign of \mathcal{T}_\perp . Right : direction of the depth-averaged advective flux with respect to the direction of the cell concentration gradient. On each graph, the vertical axis is that of the vertical coordinate z . See main text for a discussion.

The physical origin of the advective term is sketched in Figure 4.4. A cell concentration gradient creates a convective flow, which magnitude is given by $\vec{v} \propto \text{Ra} \vec{\nabla} \bar{c}$ (see eq. (4.36)), and where the surface velocity is directed from the low toward the high concentration region (Figure 4.4.a). As a consequence, the advective mass flux $\bar{c} \vec{v}$ is of the form $\bar{c} \text{Ra} \vec{\nabla} \bar{c}$ with a proportionality coefficient α_0 . This advective term is indeed equivalent to a diffusive flux with a nonlinear diffusion coefficient $\alpha_0 \bar{c} \text{Ra}$. Now the direction of this advective flux of cells (the sign of α_0) depends on where the cells are located and three possibilities can be distinguished. i) When the cells are preferentially located near the free surface ($\mathcal{T}_\perp > 0$ and Figure 4.4.b), they are mostly advected by the flow in the upper layer of the suspension and thus the mass flux is directed from the low toward the high cell concentration regions ($\alpha_0 < 0$). Since this effective diffusive flux reinforces the concentration gradient, we expect

this regime to be prone to instabilities. ii) When cells are homogeneously distributed across the thickness of the suspension ($\mathcal{T}_\perp = 0$ and Figure 4.4.c), the resulting mass flux vanishes ($\alpha_0 = 0$). iii) When cells are preferentially located near the bottom of the suspension ($\mathcal{T}_\perp < 0$ and Figure 4.4.d), the mass flux is directed from the high toward the low cell concentration regions ($\alpha_0 > 0$).

4.4.3 Effect of gyrotaxis

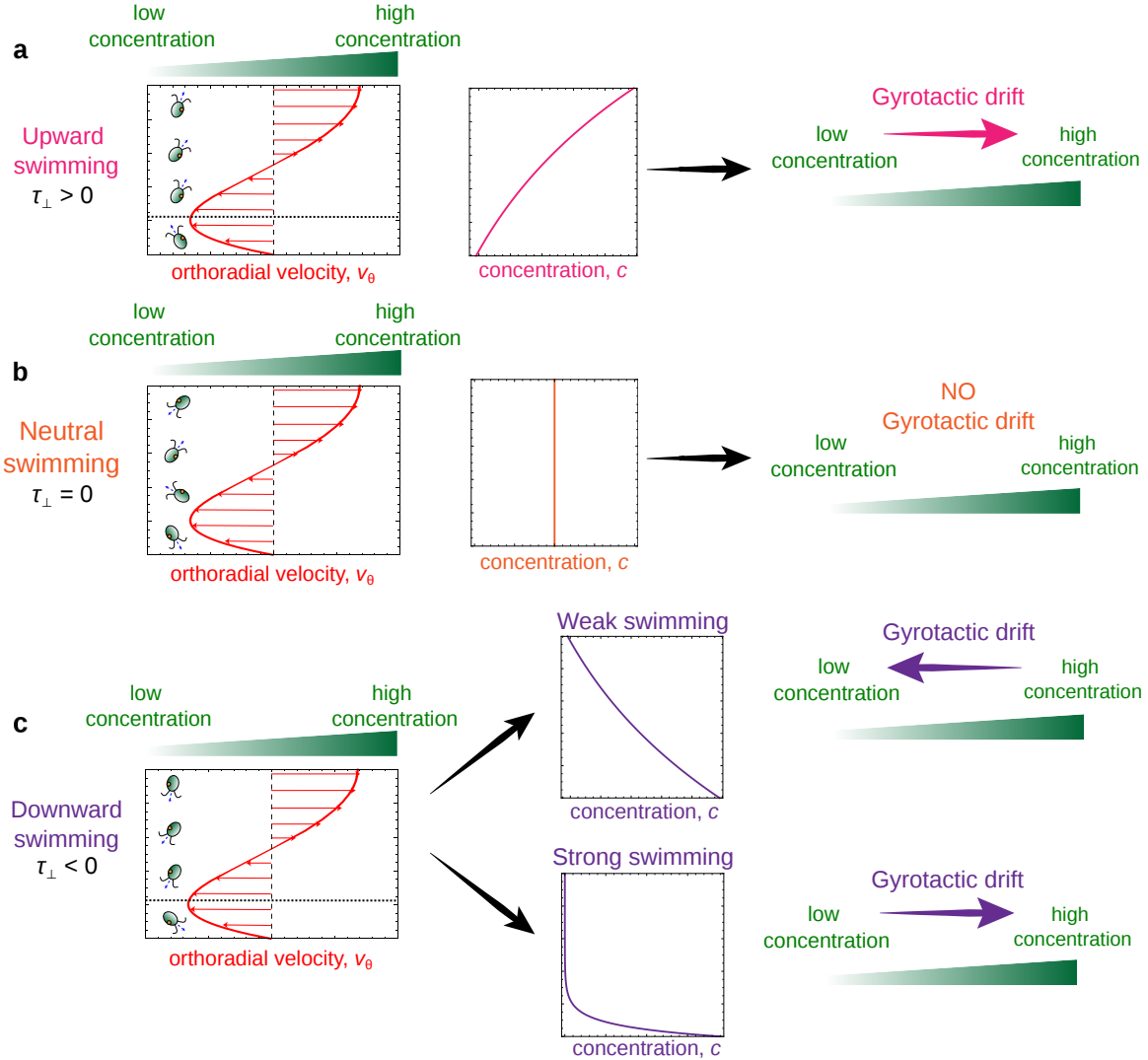


Figure 4.5: Effect of gyrotaxis on the cell concentration in the asymptotic model. Left : An orthoradial cell concentration gradient and the corresponding vertical profile of the orthoradial velocity. Cells are represented with an orientation \vec{q}_\perp corresponding to the competition between the vertical component of their preferential orientation and the vorticity of the flow. Middle : the repartition of cells along the vertical coordinate is given by the sign of \mathcal{T}_\perp . Right : direction of the depth-averaged gyrotactic drift with respect to the direction of the cell concentration gradient. On each graph, the vertical axis is that of the vertical coordinate z . See main text for a discussion.

The effect of gyrotaxis is sketched in Figure 4.5. Note that in this asymptotic model,

gyrotactic effects are only considered along the orthoradial direction (see eq. (4.51)). As previously, several cases must be distinguished. i) When cells tend to move toward the free surface ($\mathcal{T}_\perp > 0$ and Figure 4.5.a), the vorticity of the fluid flow rotates the cells away from their preferred vertical upward orientation. Close to the bottom of the container (below the dotted line), this rotation induces a drift in the direction of the low concentration while this drift is oriented toward the high concentration in the upper regions (above the dotted line). Since the microorganisms are preferentially located in the upper part of the suspension for $\mathcal{T}_\perp > 0$, the depth-averaged gyrotactic drift is oriented toward the highly concentrated region ($\gamma_0 > 0$) and gyrotaxis can therefore enhance fluctuations in concentration. ii) When cell have no preferential orientation ($\mathcal{T}_\perp = 0$ and Figure 4.5.b), then there is no gyrotactic effect ($\gamma_0 = 0$). iii) In the case where algae tend to move preferentially downward ($\mathcal{T}_\perp < 0$ and Figure 4.5.c), the fluid flow vorticity will again rotate the cells away from their preferential vertical orientation. Near the bottom of the dish (below the dotted line), the counter-clockwise rotation induces a drift toward the concentrated region of the suspension while, in the upper regions (above the dotted line), the rotation is clockwise and induces a drift toward the region of low concentration. In this case of preferential downward swimming, the depth-averaged effect of gyrotaxis however, is slightly more complex than before. When this swimming is not too strong, then the cell concentration is almost constant throughout the thickness and the resulting effect of gyrotaxis across the suspension thickness is a drift directed toward the region of low concentration. In that case, gyrotaxis acts as an enhanced diffusion ($\gamma_0 < 0$). On the other hand, when downward swimming is very strong, algae will be almost entirely located near the bottom of the suspension. Because gyrotaxis in this region is in the opposite direction, the depth-averaged gyrotactic drift will this time be directed toward highly concentrated regions ($\gamma_0 > 0$), again providing a potential instability mechanism.

4.5 Analysis of the asymptotic model

4.5.1 Theoretical analysis

As sketched previously, both the convective and the gyrotactic coefficient α_0 and γ_0 and their respective effects depend on the dimensionless vertical velocity drift \mathcal{T}_\perp . Their evolution as a function of \mathcal{T}_\perp is represented in Figure 4.6 (note that we plot $-\gamma_0$). When algae are preferentially located near the bottom of the suspension ($\mathcal{T}_\perp < 0$), $\alpha_0 > 0$ and the primary convection rolls spreads the concentration field out, acting as an additional outward diffusive flux. For $\mathcal{T}_\perp > 0$, $\alpha_0 < 0$, we have seen that advection reinforces the concentration gradient, which makes this regime prone to instabilities. For $1 + \alpha_0 \text{Ra} \cdot \bar{c} < 0$, the cell concentration field becomes unstable in the radial direction.

For stability analysis in the orthoradial direction, we need to sum the curves of α_0

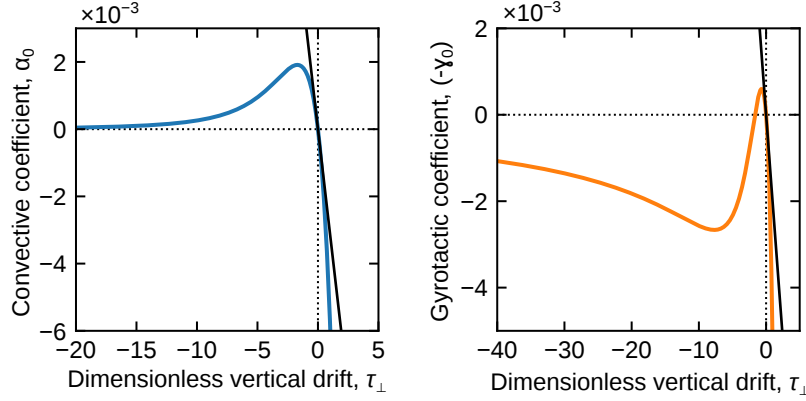


Figure 4.6: Evolution of the convective and gyrotactic coefficients α_0 and $(-\gamma_0)$ with the dimensionless vertical drift \mathcal{T}_\perp . Curves are obtained with formulas of eq. (4.49) and eq. (4.50). Tangents to these curves at $\mathcal{T}_\perp = 0$ are obtained using first order expansions around $\mathcal{T}_\perp \rightarrow 0$: $\alpha_0 \xrightarrow{\mathcal{T}_\perp \rightarrow 0} \frac{-1}{320} \mathcal{T}_\perp$ and $\gamma_0 \xrightarrow{\mathcal{T}_\perp \rightarrow 0} \frac{1}{48} \mathcal{T}_\perp$.

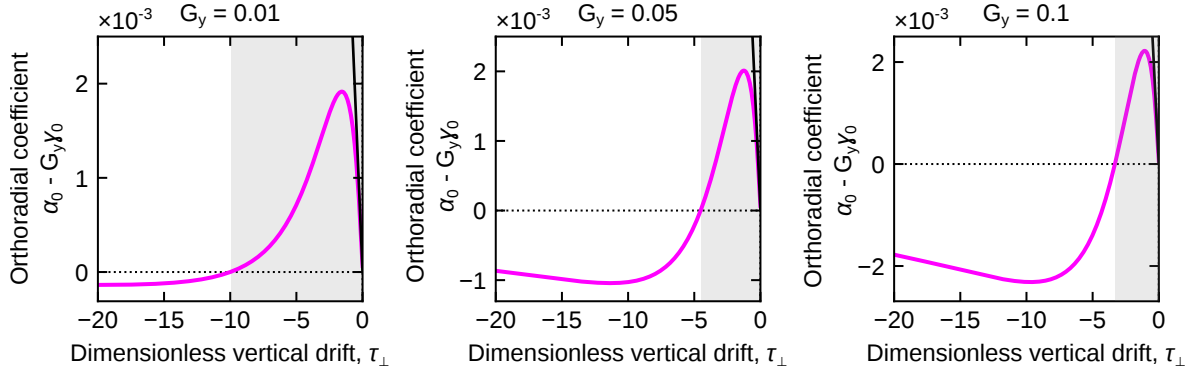


Figure 4.7: Nonlinear orthoradial diffuson coefficient $\alpha_0 - G_y \gamma_0 > 0$ at different gyrotactic number G_y . Curves are obtained with the formulas of eq. (4.49) and eq. (4.50). Tangents to these curves at $\mathcal{T}_\perp = 0$ are obtained using first order expansions around $\mathcal{T}_\perp \rightarrow 0$ (see Figure 4.6). In grey domains, $\alpha_0 - G_y \gamma_0 > 0$.

and $-\gamma_0$ by modulating the second with the gyrotactic number G_y . This is represented in Figure 4.7 for different values of G_y . This sum exhibits two zeros : one is always at $\mathcal{T}_\perp = 0$ and the other zero is always < 0 (Figure 4.7.a,b,c). In the interval where $\alpha_0 - G_y \gamma_0 > 0$ between the two zeros, shown as grey domains in Figure 4.7, the cell concentration field is always stable in the θ -direction. Outside this stable domain, $\alpha_0 - G_y \gamma_0 < 0$ and the concentration field is potentially unstable in the orthoradial direction if the combined effect of gyrotaxis and advection overcome the stabilizing effect of diffusion, i.e if the sum $1 + \alpha_0 - G_y \gamma_0$ is negative.

4.5.2 Instabilities produced by the model

Whether it be in the \vec{e}_r radial or in the \vec{e}_θ orthoradial direction, we note that cell concentration field is potentially unstable when $\alpha_0 < 0$ or $\alpha_0 - G_y \gamma_0 < 0$. In this case, in-

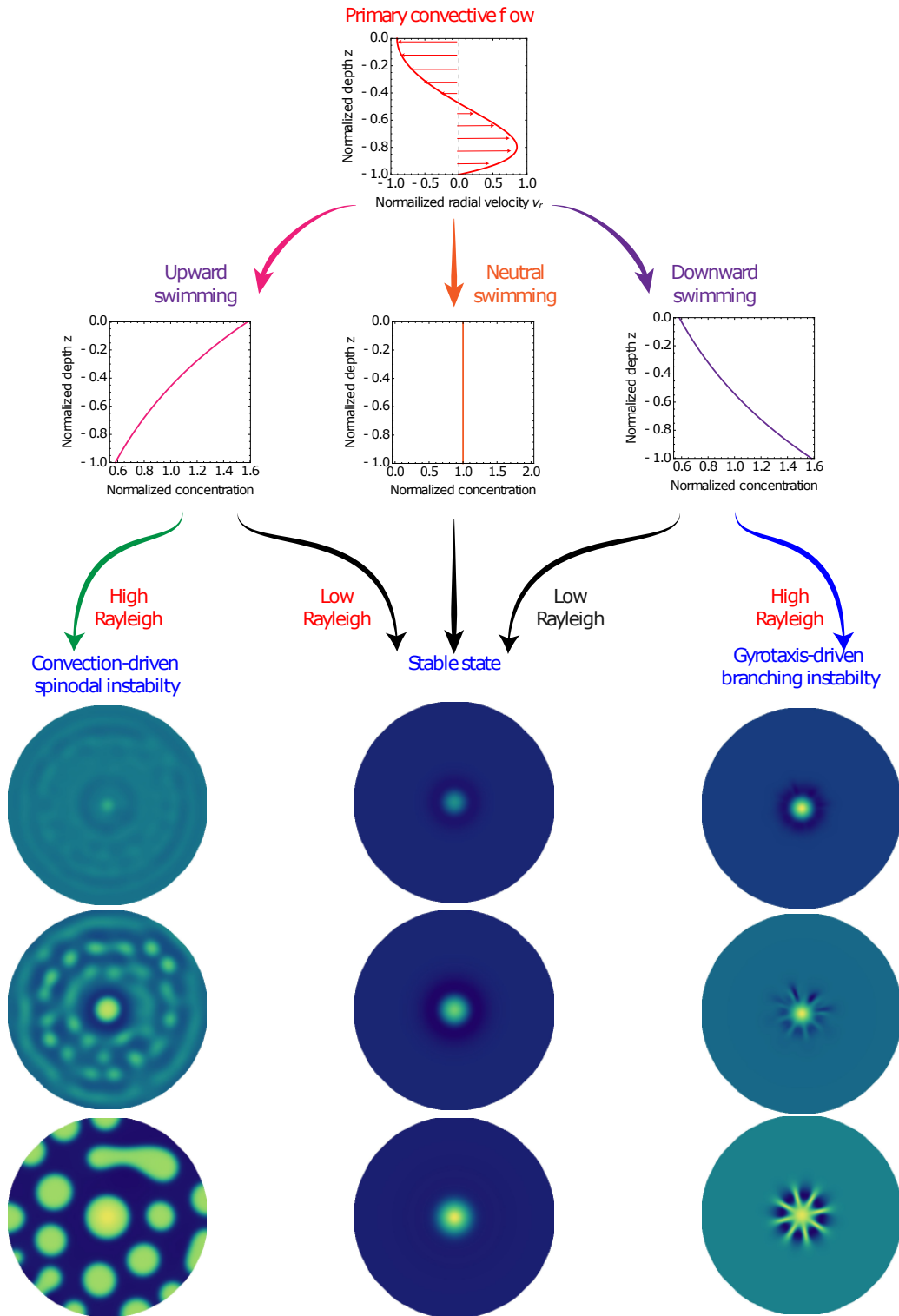


Figure 4.8: Instabilities predicted by the model. Left column : $1 + \alpha_0 \text{Ra} \cdot \bar{c} < 0$ and $1 + (\alpha_0 - G_y \gamma_0) \text{Ra} \cdot \bar{c} < 0$. Middle column : $1 + \alpha_0 \text{Ra} \cdot \bar{c} > 0$ and $1 + (\alpha_0 - G_y \gamma_0) \text{Ra} \cdot \bar{c} > 0$, for $\mathcal{T}_\perp = 0$ or at low enough Ra. Right column : $1 + \alpha_0 \text{Ra} \cdot \bar{c} > 0$ and $1 + (\alpha_0 - G_y \gamma_0) \text{Ra} \cdot \bar{c} < 0$. Note that a small higher-order term $\epsilon^2 \Delta^2 \bar{c}$ is added to the nonlinear diffusion equation to avoid the failure of the computation in the unstable regime.

stabilities only develop at high enough pseudo-Rayleigh number Ra and cell concentration \bar{c} .

We show the different instabilities produced by the model in numerical simulations in Figure 4.8. First, the cell concentration field keeps the radial symmetry of the light beam either for $\mathcal{T}_\perp = 0$ at all pseudo-Rayleigh number Ra or at low enough Ra for $\mathcal{T}_\perp \neq 0$. When the vertical drift is directed upward $\mathcal{T}_\perp > 0$, we always have $\alpha_0 < 0$ and $\alpha_0 - G_y \gamma_0 < 0$. In this case the concentration field is unstable in both the radial and the orthoradial direction at high enough $\text{Ra} \cdot \bar{c}$ and a convection-driven spinodal instability develops (left column). We use the term spinodal to qualify the instability since it is associated with a negative diffusion coefficient, as in the classical Cahn-Hilliard equation. When the vertical drift is directed downward $\mathcal{T}_\perp < 0$, we always have $\alpha_0 > 0$. Convection is always a stabilizing effect when cells are located near the bottom boundary of the suspension. In the orthoradial direction, the sign of $\alpha_0 - G_y \gamma_0$ depends on the values of \mathcal{T}_\perp and G_y . In this case, the concentration field is unstable only in the orthoradial direction when $\alpha_0 - G_y \gamma_0 < 0$ at high enough $\text{Ra} \cdot \bar{c}$ and a gyrotaxis-driven branching instability develops (right column).

Thus, the asymptotic model qualitatively reproduces two instabilities observed in the experiments. The convection-driven spinodal instability resembles the dots instability observed in the transitory regime of the experiments (see section 3.3.1, Figure 3.5). The gyrotaxis-driven branching instability resembles the *dendrites* instability observed in the experiments.

4.5.3 Comparaison with experimental data

We now compare theoretical predictions of the asymptotic model to experimental data. First, we compare the axi-symmetric solution of the concentration field to experimental radial concentration profiles. In this process, we find the best values of α_0 , \mathcal{T}_\perp and γ_0 . This allows us to finally look into predictions of boundaries in the phase diagram.

Prediction of global properties of cell concentration patterns

The radially symmetric solution of the concentration field in the asymptotic model involves the convective coefficient α_0 but the not gyrotactic coefficient γ_0 and is :

$$\frac{c_{\text{eq}}(r)}{c_0} = \frac{1}{\alpha_0 \text{Ra}} W \left(A \alpha_0 \text{Ra} \exp \left[\int_0^r \frac{\chi(r')}{D} \frac{\partial I}{\partial r'} dr' \right] \right) \quad (4.52)$$

W is the Lambert function defined by the relation $y = W(ye^y)$. A is found by the global conservation of the total number of cells and depends on the maximum light intensity I_{max} . We do not compare directly this solution to individual θ -averaged concentration radial profiles obtained in the experiments. Instead, global properties of cell concentration patterns c_{max}/c_0 and $R_{1/2}$ defined in the previous chapter are fitted by theoretical predictions.

We first note that c_{eq}/c_0 monotonically decreases with the distance from the center r because the Lambert function W is increasing on \mathbb{R}_+ while $\chi(r) \frac{\partial I}{\partial r} < 0$. Thus, the maximum concentration is obtained at the center :

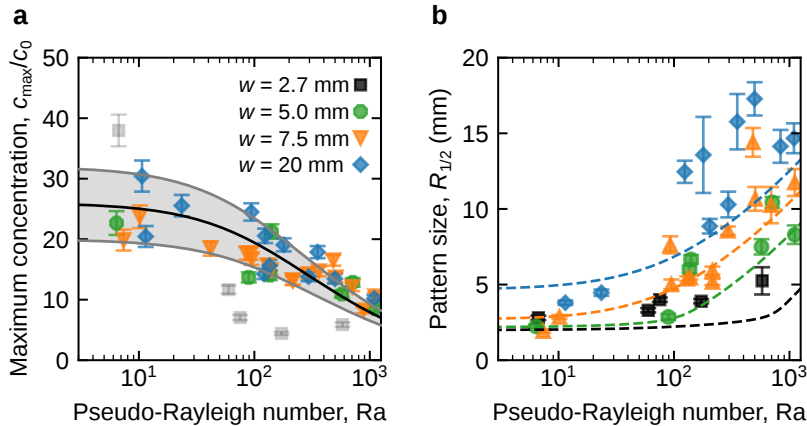


Figure 4.9: Comparison between models theoretical predictions and experimental data of cell concentration patterns global properties. Global properties of cell concentration patterns as a function of the pseudo-Rayleigh number Ra . Data points : experimental data at different beam widths w . Lines : theoretical predictions from the asymptotic model. **a**, Relative maximum concentration c_{\max}/c_0 . Experiments are compared to theoretical curves only for $w \geq 5$ mm. Data with $w = 2.7$ mm for which the Petri dish was smaller (see Figure 3.4.a) was smaller are shown with an opacity of 25% but not fitted. Theoretical curves are given by eq. (4.53) with $A = 26 \pm 6$ and $\alpha_0 = (1.5 \pm 0.2) \times 10^{-4}$ (best fit in black and error bar represented by the grey shaded area). **b**, Pattern size $R_{1/2}$. For theoretical, the equation $c_{\text{eq}}(r) = \frac{1}{2}(c_{\max} + c_0)$ is solved numerically as a function of Ra for different w . $c_{\text{eq}}(r)$ is given by the formula of eq. (4.52) with best estimates $A = 26$ and $\alpha_0 = 1.5 \times 10^{-4}$ obtained previously. From lowest to highest curve : $w = 2.7$ mm (black), $w = 5.0$ mm (green), $w = 7.5$ mm (orange), $w = 20$ mm (blue).

$$\frac{c_{\text{eq,max}}}{c_0} = \frac{c_{\text{eq}}(r=0)}{c_0} = \frac{1}{\alpha_0 Ra} W(A\alpha_0 Ra) \quad (4.53)$$

This theoretical prediction (4.53) is found to be in good agreement with experimental data in Figure 4.9.a. The model predicts that the relative maximum concentration $c_{\text{eq,max}}/c_0$ decreases with the pseudo-Rayleigh number Ra independently on the beam width w . Because $W(y) \xrightarrow{y \rightarrow 0} y$, we have $c_{\text{eq,max}}/c_0 \xrightarrow{Ra \rightarrow 0} A$, so that A can remarkably be interpreted as the maximum concentration concentration factor in the absence of flow discussed in the previous chapter. Best fit to data points is obtained for $A = 26 \pm 6$ and a convective coefficient $\alpha_0 = (1.5 \pm 0.2) \times 10^{-4}$.

The theoretical predictions of the pattern sizes $R_{1/2}$ are obtained by computing equilibrium cell concentration profiles $c_{\text{eq}}(r)/c_0$ for all Ra and light fields $I(r)$ using the values of A and α_0 found previously. The comparison with experimental data is shown in Figure 4.9.b. The trends found in the experiments are qualitatively captured by the model. In particular, the nonlinear higher sensitivity to low light intensities of the phototactic is needed to capture the effect of widening light beams only in the tail of their light intensity radial profiles.

Value of the dimensionless vertical drift \mathcal{T}_\perp

The value of the convective $\alpha_0 = (1.5 \pm 0.2) \times 10^{-4}$ obtained by fitting experimental data of c_{\max}/c_0 corresponds to two possible negative value of the dimensionless vertical drift \mathcal{T}_\perp as evidenced by variations of α_0 with \mathcal{T}_\perp (Figure 4.6.a). Either $\mathcal{T}_\perp = -12.6 \pm 0.7$ or $\mathcal{T}_\perp = -0.05 \pm 0.01$. In the experiments, we typically have $G_y \sim 0.01 - 0.1$. In this range of G_y , the model predicts that the cell concentration field is always stable in the orthoradial direction (see Figure 4.7) for $\mathcal{T}_\perp = -0.05$. We keep $\mathcal{T}_\perp = -12.6 \pm 0.7$ for which the model predicts the branching instability at high enough Ra in the range of G_y of the experiments. This corresponds to $|v_\perp| \sim 300 \mu\text{m/s}$, which is larger than the swimming speed of *Chlamydomonas reinhardtii* ($\sim 100 \mu\text{m/s}$). This value should not be interpreted literally but rather as an indication that the vertical drift \mathcal{T}_\perp in the model indeed originates from the downward flow at the center of the primary convection roll.

Theoretical phase diagram

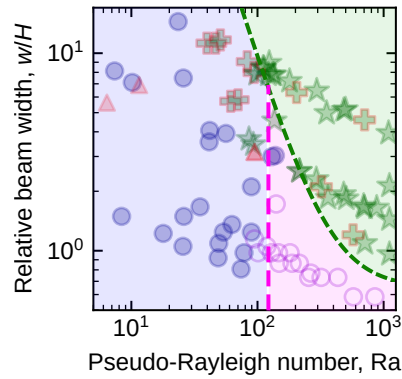


Figure 4.10: Theoretical phase diagram of photo-bioconvection patterns. Data points : experiments (see 3.1 for markers). Lines : theoretical boundaries. Green curve : prediction by the asymptotic model of the $\{Ra, w/H\}$ boundary between *round* patterns and *dendrites* patterns. Using the radially symmetric solution $c_{\text{eq}}(r)/c_0$, the boundary corresponds to $1 + (\alpha_0 - G_y \gamma_0) Ra \cdot c_{\text{eq}}(r = H)/c_0 = 0$ for the different light beams of widths w (justification of $r = H$ in the main text). Vertical pink line : the prediction by the 2D model with gyrotaxis of the critical pseudo-Rayleigh number above which *round* patterns break into *waves* emission is also added up to the intersection with the green curve.

Finally, the asymptotic model predicts a boundary between *round* and *dendrites* patterns in the phase diagram (Figure 4.10). Using a preferential cells location at the bottom with $\mathcal{T}_\perp = -12.6$ previously found, the value of γ_0 is fixed which allows us to find the domain of existence of *dendrites*. In the model, the branching instability develops when $1 + (\alpha_0 - G_y \gamma_0) Ra \cdot \bar{c} < 0$. The corresponding boundary in the phase diagram can thus be found using the radially symmetric solution c_{eq} and should correspond to $1 + (\alpha_0 - G_y \gamma_0) Ra \cdot c_{\text{eq,max}}/c_0 = 0$. However, because the hypothesis of $v_z = 0$ is only

valid for $r > H$, we use the condition $1 + (\alpha_0 - G_y \gamma_0) \text{Ra} \cdot c_{\text{eq}}(r = H)/c_0$ instead. We also included the boundary between *round* patterns and *waves* emission predicted by the previous 2D model in (\vec{e}_r, \vec{e}_z) with gyrotaxis.

4.5.4 Discussion

Origin of the dendrites instability

The gyrotaxis-driven branching instability of strong downward drift found in this asymptotic model qualitatively displays the same orthoradial breaking of the initial radial symmetry as the *dendrites* instability observed in the experiments. Moreover, the same domain of existence at high pseudo-Rayleigh number Ra and large beam width w/H is found in the phase diagram. We thus propose that the formation of *dendrites* in the experiments is also due to a gyrotactic coupling between a strong downward drift due to the primary light-induced convective flow and the vorticity of the flow.

We should also emphasize the role of the large beam width w/H as follows. When $\alpha_0 - \gamma_0 G_y < 0$, the branching instability is an instability of high $\text{Ra} \cdot \bar{c}$, i.e. high pseudo-Rayleigh number and high concentration. However, because the model fails to hold for distances $r < H$, we evaluated the condition of high concentration at $r = H$ where the concentration is high enough only when w/H is large enough. In the experiments, the first effect of increasing the beam width is that larger cell concentration patterns are observed. Thus, the *dendrites* instability might be seen as a gyrotaxis-driven instability of high pseudo-Rayleigh and large pattern size.

Finally, although the model does predict threshold values of the parameters for the instabilities, it does not predict any wavelength. Wavelengths are likely to be of order of the suspension thickness H where the hypotheses of the model fail to hold.

From the dots instability to the dendrites instability

The spinodal instability and the gyrotaxis-driven branching instability respectively reproduce the dots instability observed in the transitory regime of the experiments and the long term *dendrites* instability. However, in the model, these two instabilities are mutually exclusive because of opposite signs of \mathcal{T}_\perp . In the experiments, it is in fact likely that a dependence of the migration of cells along the vertical direction on both space and time explains the switch from the dots instability to the *dendrites* instability. This switch could well occur in the time course of the establishment of the main convective roll, but we did not take this into account in our simplified asymptotic model.

Work towards directional growth

The model does not reproduce the *directional growth* instability observed in the experiments. This is possibly due to the hypothesis of an infinite system which forbids the formation of a fixed direction of growth as in the experiments. In the experiments, this

fixed direction seems to be given by a slight defect of horizontality which is hard to include in the model because it breaks the hypothesis of constant thickness. Instead, theoretical and numerical works in progress look to adapt the asymptotic model to the case of a system of finite size with a slightly de-centered light beam in order to create a potentially fixed direction of growth (by creating a non-radially symmetric primary convective roll).

4.6 Conclusion

We developed an asymptotic model of light-controlled bioconvection with gyrotaxis. The model was developed in the limit $H/L \ll 1$ with additional simplifying hypotheses. A single nonlinear partial differential equation describing the depth-averaged cell concentration could be obtained where information of the vertical direction was contained in the dependence on an effective vertical drift term. This nonlinear equation enabled to capture the effect of advection by the primary convective roll and gyrotaxis in a nonlinear and anisotropic effective diffusion matrix.

This approach enabled to reproduce the *dendrites* instability observed in the experiments. According to the model, the *dendrites* instability originates from a gyrotactic coupling between the strong downward drift due to the primary light-induced convective flow and the vorticity of the flow. This occurs in cell concentration patterns whose large size is controlled by a large beam width. Global properties of cell patterns and threshold for the development of instabilities could also be reproduced by the model.

The structure of the flow field was a key ingredient in the model to predict the formation of instabilities. However, it could not be compared to any experimental data. In the next chapter, we develop an experimental setup to study quantitatively both the magnitude and the structure of bioconvective flows and compare them to classical bioconvection models.

CHAPTER 5

Direct quantification of light-induced bioconvective flows

The aim of this chapter is to investigate the intensity and the structure of light-induced bioconvective flows, to pinpoint the physical mechanisms controlling these flows, and to compare flow fields to cell concentration fields. First, I present the experimental setup that we developed to this end in a confined geometry. Then, I describe separately the concentration fields and the flow fields generated in this specific confined geometry. At the global scale, I then compare the structures of the flow and cell concentration fields. Finally, I present an investigation at the local scale of the relationship between variations of the cell concentration field and of the velocity field.

5.1 Experimental setup

5.1.1 Principle of the experiments

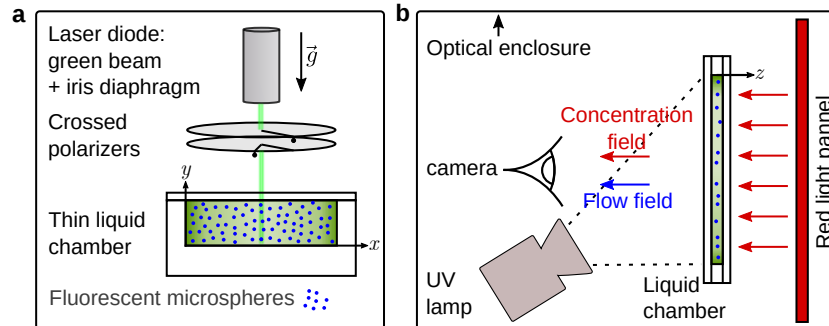


Figure 5.1: Sketches of the experimental setup used to study light-controlled bioconvection flows. A vertical Hele-Shaw liquid chamber contains a suspension of *Chlamydomonas reinhardtii* cells whose horizontal motion is directed by a green light beam. The camera is used to image both the cells repartition and the associated convective flows in the vertical plane (\vec{e}_x, \vec{e}_y) (averaged in the direction of confinement \vec{e}_z). The concentration field is obtained by measuring the amount of red light transmitted through the suspension. Fluorescent microspheres are used as passive tracers to obtain the velocity field. They absorb UV light and emit blue light. The experimental setup is kept in a dark optical enclosure. **a**, Front view (from the camera) of the experimental setup (red panel not shown). **b**, Top view (from crossed polarizers) of the experimental setup.

We developed an experimental setup to conduct a quantitative study of hydrodynamics flows arising from light-controlled bioconvection. The setup allowed to image both the cell concentration and velocity fields in a vertical Hele-Shaw cell. It is sketched in Figure 5.1 and an actual picture is shown in Figure 5.2. A vertical green light beam (532nm, gaussian, millimetric width, I_{\max}) was projected at the center of a suspension of *Chlamydomonas reinhardtii* to trigger phototaxis. The suspension was imaged with a camera whose axis \vec{e}_z was perpendicular to the vertical plane of the Hele-Shaw liquid chamber (\vec{e}_x, \vec{e}_y). The cell concentration field was acquired using red light transmission. A custom Particle Imaging Velocimetry technique with fluorescent particles was developed to obtain the fluid velocity field. We used fluorescent microspheres illuminated with widefield UV flashes (with an intensity kept as low as possible to remain harmless for cells) as passive tracers. They absorb in UV light (365nm) and emit in blue light (415 nm). The design of Hele-Shaw liquid chambers is illustrated in Figure 5.3.

5.1.2 Cell concentration imaging and time dependent phototaxis

We used the red light transmitted through the suspension to measure the cell concentration field. After calibration (details in appendices, appendix C.1), pixel intensity values on red channel of the images could be converted into thickness averaged (in the z -direction) local cell concentration $c(x, y)$.

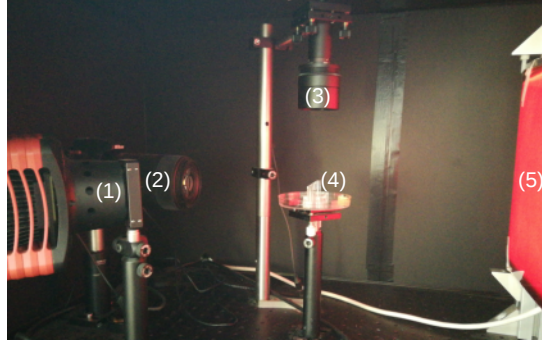


Figure 5.2: Experimental setup to study light-controlled bioconvection flows. Picture of the experimental setup. (1) UV lamp. (2) Camera. (3) Laser and crossed polarizers. (4) Liquid chamber on its holder. (5) Red filters on a white LED panel.

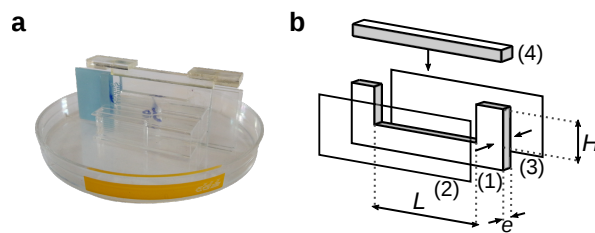


Figure 5.3: Design of liquid chambers. **a**, Picture of a liquid chamber on its holder. **b**, Sketch of the assembly of a liquid chamber. (1) The liquid chamber is cut from a plexiglas plate. (2), (3), Two microscope slides are glued on the sides. (4) A cover is cut from a plexiglas plate and lays on top of the liquid chamber. The cutting marks are shown in grey and do not intersect the path of the laser beam.

In the development of the measurements protocol, we first investigated the cells phototactic response in this geometry. We monitored their concentration field during 20 min following the activation of the green beam. We observed an interesting time dependency of the response to light. This is illustrated in Figure 5.4.

During the first minutes, cells displayed negative phototaxis and swam away from the light source. This was evidenced by an accumulation of cells near the lateral boundaries of the liquid chamber (Figure 5.4.a,b). The cell concentration field reached a pseudo steady state and did not vary much during a few minutes. After ~ 10 min, cells started to show positive phototaxis. It first resulted in mixed patterns with cells accumulation both at the sides and at the center (Figure 5.4.c). Eventually, only accumulation around the laser beam was observed (Figure 5.4.d). The reproducibility of this time dependency was checked with several tests. First, we used consecutive green light on-off cycles. Then, we also tested different green light intensities and cells conditioning prior to the experiments. Details of these tests can be found in appendices (appendix C.2). In all cases tested, negative phototaxis was observed in the first minutes of the experiments (sometimes mixed with positive phototaxis), and followed by accumulation around the light beam.

The time dependency of phototaxis left us with the choice to do measurements on bioconvection flows and cell patterns either with negative phototaxis or with positive

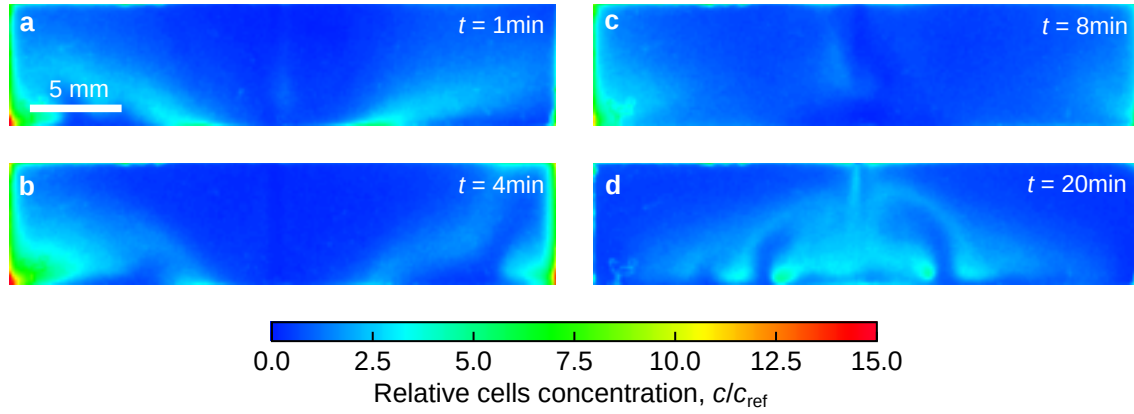


Figure 5.4: Front view imaging of the interaction between algae and light. The cell concentration field shows a time dependent phototactic response. At $t = 0$, the vertical green light beam is turned on and projected at the center of the suspension. The maximum green light intensity is $I_{\text{max}} = 125 \text{ W/m}^2$. **a,b**, Negative phototaxis with cells accumulation at the sides of the liquid chamber. **c**, Mixed response with negative phototaxis and minor positive phototaxis at the center. **d**, Positive phototaxis with cells accumulation at the center. $c_0/c_{\text{ref}} = 2$ with $c_{\text{ref}} = 3 \times 10^6 \text{ cells/mL}$, $H = 7 \text{ mm}$, $L = 30 \text{ mm}$. Prior to the experiments, cells were kept in white light (2.5 kLux) during 30 min.

phototaxis. This choice will be justified at the end of this section. Although this transient light response behavior is not well understood and escape from our full control, the fact that negative phototaxis is first observed is consistent with the classification of the strain CC-124 used here as negatively phototactic mutant, albeit in a different culture medium (Ide et al. 2016). In the experiments by Arrieta et al. 2019 in a similar confined geometry, the strain CC-125 was used and only positive phototaxis was observed.

5.1.3 Fluorescent PIV

We developed a custom Particle Image Velocimetry (PIV) technique with light-fluorescent passive tracers to image bioconvection flows. PIV is an optical technique to image flow fields by tracking illuminated passive tracers particles advected by fluid flows.

Principle of classical PIV

A classical PIV setup is shown in Figure 5.5.a. Tracer particles are usually illuminated by a high-intensity laser sheet and the scattered light intensity is captured by a camera. The laser sheet defines a plane of measurement within the flow. Displacement are measured by imaging tracers twice within a short time interval δt . Images are divided into squares named interrogation windows containing several tracer particles. When all the particles within an interrogation window have moved homogeneously (Figure 5.5.b), the local displacement $V\delta t$ is determined by images correlation (Figure 5.5.c). Repeating this procedure for all the interrogation windows yields the tracer velocity - and hence flow velocity - for the investigated field of view. This can also be repeated at different times t_0, t_1, t_2, \dots to access velocity temporal variations.

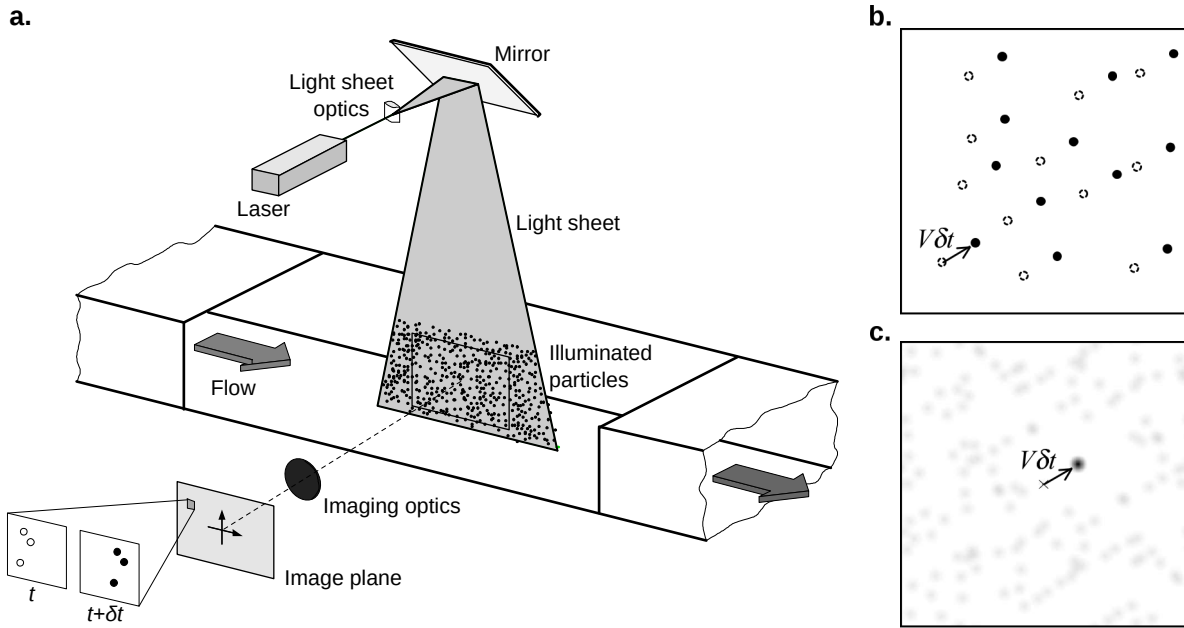


Figure 5.5: Measurement principle of classical PIV. **a**, Typical PIV setup (from Kompenhans et al. 2000). **b**, Positions of the passive tracers inside an interrogation window at two successive images at t and $t + \delta t$. **c**, The correlation between the two images gives the local displacement $V\delta t$.

Principle of Fluorescent Particle Image Velocimetry

In our system, classical light-scattering PIV could not be used because light would also be scattered by *Chlamydomonas reinhardtii* cells. The highly diffusive nature of concentrated suspensions of *Chlamydomonas reinhardtii*, associated with their inhomogeneous spatial repartition, would induce a very heterogenous scattered light field, no suitable for PIV analysis. We thus used fluorescent tracers for which the wavelengths of absorption and emission differ from each other. Then, we adapted tracers illumination to *Chlamydomonas reinhardtii* high sensitivity to light. In our study, we used the separation of the RGB channels of the images to measure both the flow field and the concentration field. It was preferable not to use blue or green light pulses to which cells could show phototactic or photoshock responses. In principle, we could have used particles excited in red light. However, we did not have the mean to measure the corresponding infra-red fluorescence. We finally turned to a UV lamp to excite fluorescent particles. We also expected the flow to be quasi 2D because of the lateral confinement. Thus, we used widefield flashes to illuminate the whole volume instead of a light sheet and we measured the light emitted by the fluorescent particles rather than the light scattered by the particles as commonly used in classical PIV. We imaged the particles in the whole volume by setting the camera depth of field to the Hele-Shaw liquid chamber thickness.

Fluorescent microspheres

We used fluorescent microspheres as particle tracers that absorb UV light at 365 nm and emit blue light at 415 nm. Given the field of view needed to obtain flow field over large region (a few centimeters), we used quite large particles (radius $r_s = 7.5 \mu\text{m}$) for visualization. Because they are denser than water (density $\rho_0 + \Delta\rho_s = 1.06 \text{ g/cm}^3$), they could be subjected to sedimentation. The sedimentation speed in the absence of flow is the Stokes velocity :

$$v_s = \frac{2r_s^2 g \Delta\rho_s}{9\eta}$$

With values given by the supplier, the sedimentation speed is $8 \mu\text{m/s}$, corresponding to 1 mm every 2 minutes. In theory, the typical magnitude of bioconvection flows ($\sim 100 \mu\text{m/s}$) is enough to keep beads in suspension. In practice, the limiting factor is the time needed for the system to generate strong enough flows. In particular, beads sometimes completely sedimented at the center before flows were generated by positive phototactic accumulation around the light beam. Performing experiments with the fast negative phototactic response helped in minimizing the amount of sedimentation

Range of UV flashes biocompatibility

UV flashes were kept as low in intensity as possible for biocompatibility, but this was limited by particles visibility on the images. We found an optimal UV intensity of $\sim 10 \text{ W/m}^2$ for periodic flashes of 500 ms every 1500 ms. We investigated the biocompatibility of such UV flashes with *Chlamydomonas reinhardtii* (details in appendices, appendix C.3). We found that a few tens of UV flashes can safely be used without effect on cells during the experiments.

5.1.4 A typical experiment

Negative phototaxis

Finally, we performed experiments with negative phototaxis in order to image flows as soon as possible after beads seeding. Algal suspensions seeded with fluorescent beads were placed in the liquid chamber. After the green light beam was turned on, structures of high cell concentration formed at the liquid chamber sides due to negative phototaxis (Figure 5.4.a,b). The evolution of the cell concentration field was monitored during $0 \lesssim t \lesssim 5 \text{ min}$, until the negative phototaxis pseudo steady state was reached. Then, we imaged the fluid velocity field with fluorescent PIV using only a few UV flashes (from 5 to 10). The total duration of the flow field acquisition was $\sim 15 \text{ s}$, much shorter than the time scale of variations of the concentration field (a few minutes). We also recall that the ratio of momentum diffusion and cells diffusion timescales is $\frac{D\rho_0}{\eta} \sim 0.1$, so that we can assume that the velocity field instantaneously adjusts to the cell concentration field. Therefore, the velocity field could be compared to the last image of the cell concentration

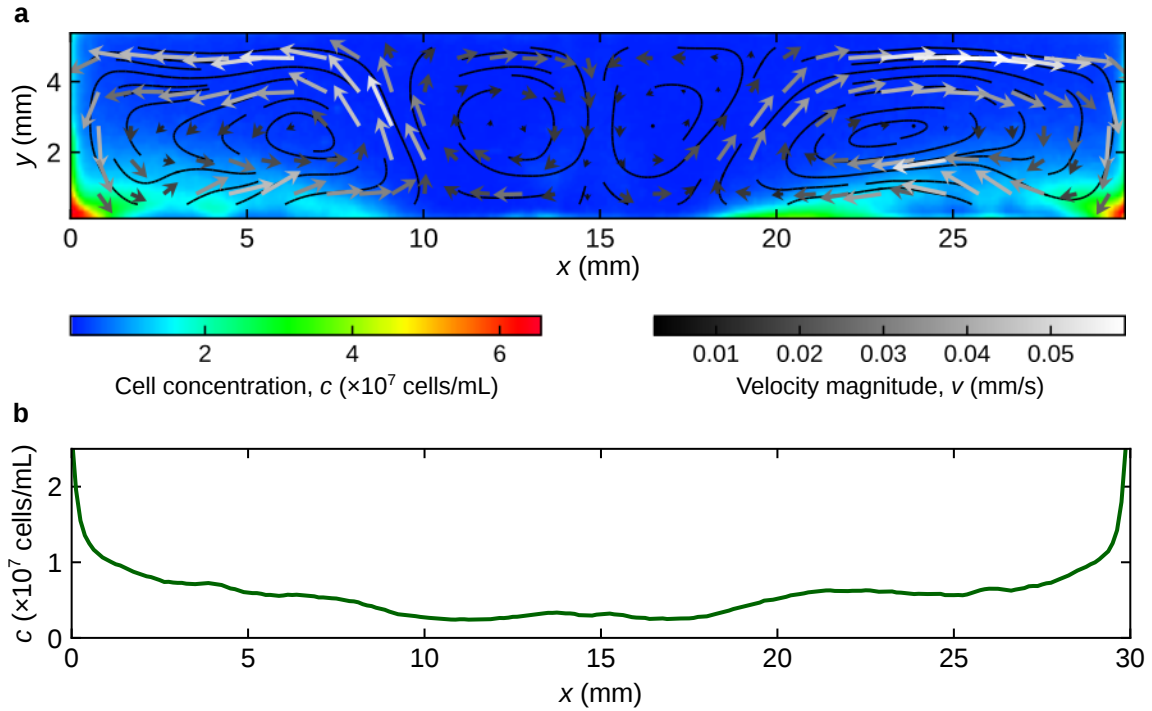


Figure 5.6: Superimposition of cell concentration and velocity fields acquired from front view. **a**, A quiver plot displays velocity vectors on a colormap of the cell concentration field. A velocity vector magnitude is indicated by both its arrow length and color. Streamlines in solid black lines are tangent to velocity vectors. **b**, The concentration field is averaged along y and plotted against x . $c_0 = 6 \times 10^6$ cells/mL, $H = 6$ mm, $L = 30$ mm. At $t = 0$ the green light beam was turned on with $I_{\max} = 125$ W/m². The cell concentration field corresponds to the pseudo-steady state that was reached during the negative phototactic response after 5 min. Then, the flow field was measured with fluorescent PIV.

field. A typical concentration field in the negative phototaxis pseudo steady state and the associated velocity field are superimposed in (Figure 5.6). Two cell patterns are well defined on both sides. The associated velocity fields is dominated two large convective rolls nears the edge of the chamber. The velocity is directed downward at the sides due to the locally higher density (see y -averaged cell concentration lateral profile, Figure 5.6). This creates a recirculation flow away from the sides edges.

It should be noted that in this situation of negative phototaxis, regions of high cell concentration that correspond to low pixel intensities on the red channel of the images are hard to distinguish from the liquid chamber side walls for $x \rightarrow \{0, L\}$. This explains the large increases observed for $x \rightarrow \{0, L\}$ in the y -averaged cell concentration fields (Figure 5.6.b). On the other hand, even when it was possible to image positive phototaxis-induced flows around the centered light beam, more complex and unsteady cell concentration and velocity fields were observed due to reduced viscous friction away from the side edges (see Figure C.5 in appendices).

Range of experimental parameters

In the experiments presented in the following, we carefully studied the separated effects of both the initial cell concentration $3 \times 10^6 \text{ cells/mL} \leq c_0 \leq 15 \times 10^6 \text{ cells/mL}$ and liquid height $4 \text{ mm} \leq H \leq 9 \text{ mm}$ in a range of reasonable horizontal sizes $20 \text{ mm} \leq L \leq 30 \text{ mm}$, with a fixed thickness $e = 2.1 \text{ mm}$.

It should be noted that the liquid chamber geometry plays a crucial role in this study. The thin thickness $e = 2.1 \text{ mm}$ stabilizes the system thanks to the predominance of viscous friction. For example, spontaneous gyro-gravitactic is expected for *Chlamydomonas* suspensions of infinite thickness in the range of suspension heights H (4 – 9 mm) and cell concentrations c_0 ($(3 - 15) \times 10^6 \text{ cells/mL}$) explored in these experiments (Bees and Hill 1997), but was not observed due to the confined thickness e . This allowed to work at higher cell concentrations and liquid heights than those used in Petri dishes. In particular, increasing the liquid height H delayed beads sedimentation during flows generation. The confined thickness also enabled to use widefield UV flashes instead of light sheets traditionally used in PIV.

5.2 Global analysis

Cell concentration and velocity fields are first quantified independently in this section. To study cell concentration fields, we defined global properties that describe their structure and inhomogeneities. From velocity fields, we characterized the structure and the intensity of the flows.

5.2.1 Cell concentration fields

Figure 5.7 shows several side views of cell concentration fields at different values of initial cell concentration c_0 and liquid chamber height H . At low c_0 and H (Figure 5.7.a), cells are essentially located against the sides of the liquid chamber. When either c_0 or H increases (Figure 5.7.a,b) cells repartition along the vertical coordinate y becomes highly asymmetric. This could not be measured in pattern formation experiments observed from top view. Here, we introduce a pattern length L_{pattern} that quantifies that quantifies the convection-dependent cell pattern size in the lower part of the suspension. For that, cell patterns on the left and right sides were delimited by two curves of iso-concentration ($\{(x_l(y), y) | 0 \leq y \leq H\}$, $\{(x_r(y), y) | 0 \leq y \leq H\}$, see caption). Then, we defined L_{pattern} as the maximum lateral pattern extension in the lower part of the suspension :

$$L_{\text{pattern}} = \begin{cases} \max\{x_l(y)\}_{0 \leq y \leq H/2} & \text{on the left side} \\ \max\{L - x_r(y)\}_{0 \leq y \leq H/2} & \text{on the right side} \end{cases} \quad (5.1)$$

We investigated the effect of the global concentration c_0 and liquid height H of the algae suspension on the cell pattern length L_{pattern} in Figure 5.8. At fixed c_0 , L_{pattern}

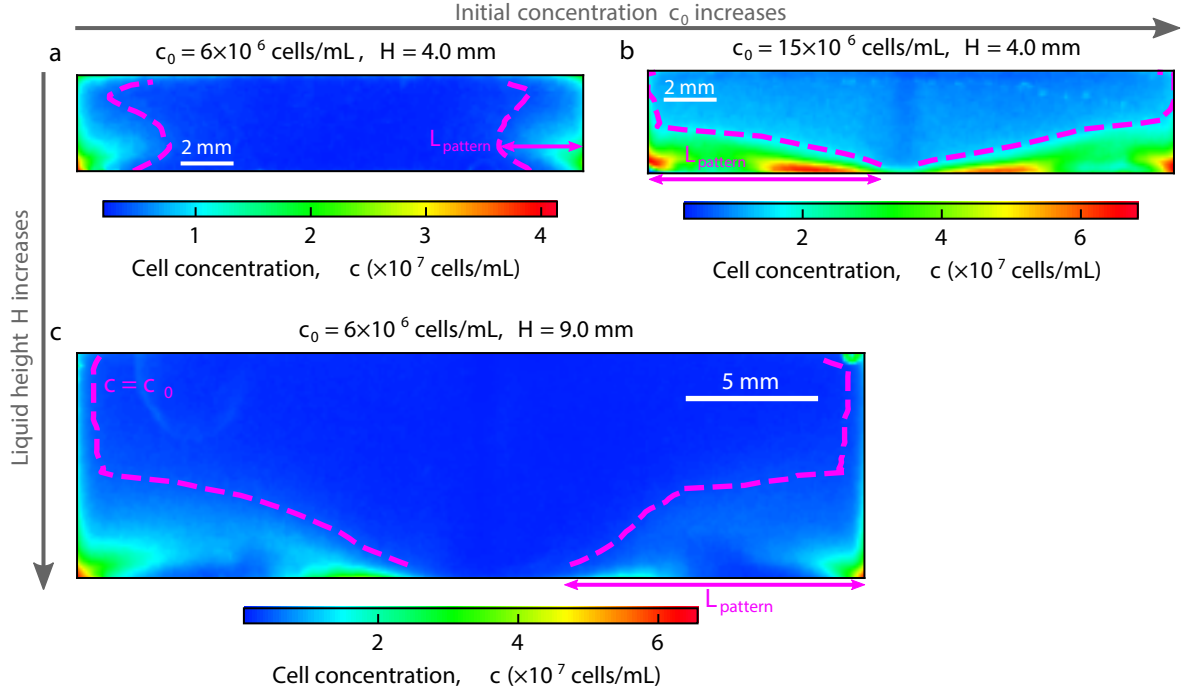


Figure 5.7: Front views of cell concentration fields at different initial cell concentrations and liquid chamber heights. Cell patterns can be delimited by dashed magenta curves $\{(x_l(y), y) \mid 0 \leq y \leq H\}$ on the left and $\{(x_r(y), y) \mid 0 \leq y \leq H\}$ on the right that verify $c(x, y) = c_0$. We respectively defined a cell pattern length L_{pattern} and concentration c_{pattern} as its maximum lateral pattern extension and its averaged Cell concentration.

increases with and scales with the liquid height $L_{\text{pattern}} \propto H$ (Figure 5.8.a). We also normalized data by the liquid chamber length L . It should be noted that the theoretical upper limit for a single measurement is $L_{\text{pattern}}/L \leq 1$ (with equality in the hypothetical case of a pattern localized on one edge side and spreading out to the opposite edge side). Now, measurements on left and right sides average out to $L_{\text{pattern}}/L \leq 1/2$. Normalized data reveal that when H increases relatively to L , L_{pattern}/L increases towards its limit $1/2$. For different geometries $\{H, L\}$, we also found that L_{pattern}/L increases with c_0 (Figure 5.8.b). For $c_0 \geq 1.2 \times 10^7$ cells/mL, regions of high concentration are fully spread out along half the liquid chamber length and L_{pattern}/L saturates at $L/2$.

We then tried to quantify the system ability to concentrate cells. In pattern formation experiments observed from top view, the height-averaged maximum cell concentration c_{max} was introduced to this end. Here, with negative phototaxis, the measurement of c_{max} is prone to error at $x = 0, L$. Instead, we defined c_{pattern} as the mean concentration inside

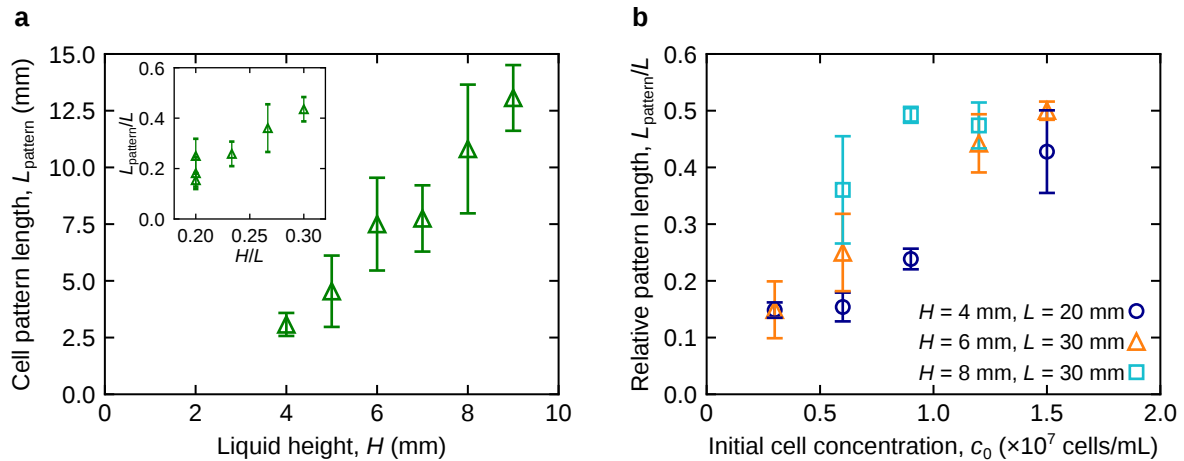


Figure 5.8: Effect of liquid height and cell concentration on cell pattern length. **a**, Cell pattern length as a function of liquid height at fixed initial cell concentration $c_0 = 6 \times 10^6$ cells/mL. The liquid chamber length L is not fixed and we have $\{(H, L)\} = \{(4, 20), (5, 25), (6, 30), (7, 30), (8, 30), (9, 30)\}$ (in mm) in this data set. The inset shows the same data set normalized by the liquid chamber length L . **b**, Relative cell pattern length L_{pattern}/L as a function of the initial cell concentration c_0 at different geometries $\{H, L\}$. For the different graphs, one point corresponds to the mean value for 3 experiments at fixed (H, L, c_0) triplet, knowing that there are two measures for each experiment (left and right sides). In particular, $L_{\text{pattern}}/L \leq 1/2$ when averaging over the two sides. Error bars show standard deviations.

highly concentrated regions :

$$c_{\text{pattern}} = \begin{cases} \frac{\int_0^H \int_0^{x_l(y)} c(x,y) dx dy}{\int_0^H \int_0^{x_l(y)} dx dy} & \text{on the left side} \\ \frac{\int_0^H \int_{L-x_r(y)}^L c(x,y) dx dy}{\int_0^H \int_{L-x_r(y)}^L dx dy} & \text{on the right side} \end{cases} \quad (5.2)$$

Figure 5.9 shows the evolution of the cell pattern concentration c_{pattern} as a function of the initial cell concentration c_0 . We found that patterns are less concentrated relatively to c_0 when increasing c_0 . Surprisingly, we did not find any effect of the liquid chamber height H on the cell pattern relative concentration c_{pattern}/c_0 .

5.2.2 Flow fields

We now characterize bioconvective flows associated to the previously analyzed cell concentration fields.

Figure 5.10 shows the analysis performed on velocity fields. Qualitatively, one can observe two main convection rolls on the velocity field shown in Figure 5.10.a, with significant flow speeds (dark blue) between $0 \text{ mm} \leq x \lesssim 7 \text{ mm}$ and $24 \text{ mm} \lesssim x \leq 30 \text{ mm}$. We quantified this observation with lateral profiles of the horizontal and vertical velocities (Figure 5.10.b). First, we note that the y -averaged vertical velocity is highest close to the sides edges of the Hele-Shaw cell (the flow field resolution does not enable to

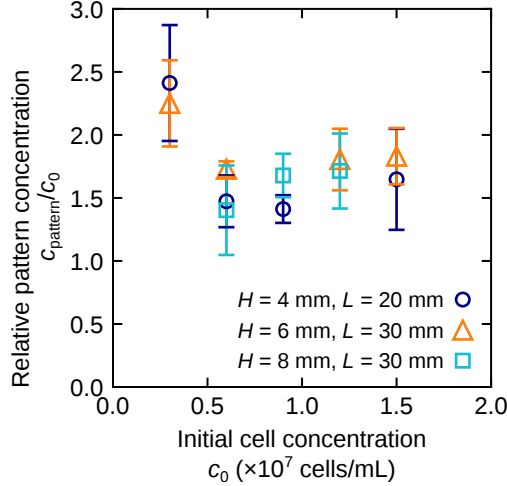


Figure 5.9: Relative cell pattern concentration as a function of the initial cell concentration at different geometries $\{H, L\}$. One point corresponds to the mean value for 3 experiments at fixed (H, L, c_0) triplet, knowing that there are two measures for each experiment (left and right sides). Error bars show standard deviations.

capture the no-slip boundary conditions). Thus, we defined the sinking velocity as the height-averaged downward velocity in the vicinity of the side edges :

$$v_{\text{sink}} = \begin{cases} \frac{-1}{H} \int_0^H v_y(x = \delta, y) dy & \text{on the left side} \\ \frac{-1}{H} \int_0^H v_y(x = L - \delta, y) dy & \text{on the right side} \end{cases} \quad (5.3)$$

where $\delta \approx 0.5$ mm

Vertical profiles of the vertical velocity close to the side edges are shown in Figure 5.10.c. They have a well-defined maximum value that could have also been used as a measure of the sinking velocity. For example, we have on the right side a maximum downward velocity $\max |v_y(x \approx L, y)| = 70 \mu\text{m/s}$ and an average downward velocity $v_{\text{sink}} = 40 \mu\text{m/s}$.

Next, we note that convection rolls occupy all vertical space and we studied their extension along the horizontal axis. A typical lateral profile of the y -averaged horizontal recirculation velocity magnitude is also plotted on Figure 5.10.b also. The horizontal velocity first increases as the distance from the sides edges increases, reaches a maximum value, and then decreases to zero. In this decrease, the distance from the side edge at which the maximum velocity is divided by 2 defines the length $L_{\text{roll},1/2}$ of a convective roll.

We measured the sinking velocity v_{sink} at different liquid heights H and initial cell concentration c_0 . First, Figure 5.11.a shows the evolution of v_{sink} with H at fixed c_0 . The variability from one experiment to the next is quite large as shown by error bars. Data reveal that the sinking velocity increases and scales with the liquid height $v_{\text{sink}} \propto H$. Figure 5.11 shows a surprising evolution of v_{sink} with c_0 for different H . For $c_0 \leq 9 \times 10^6$

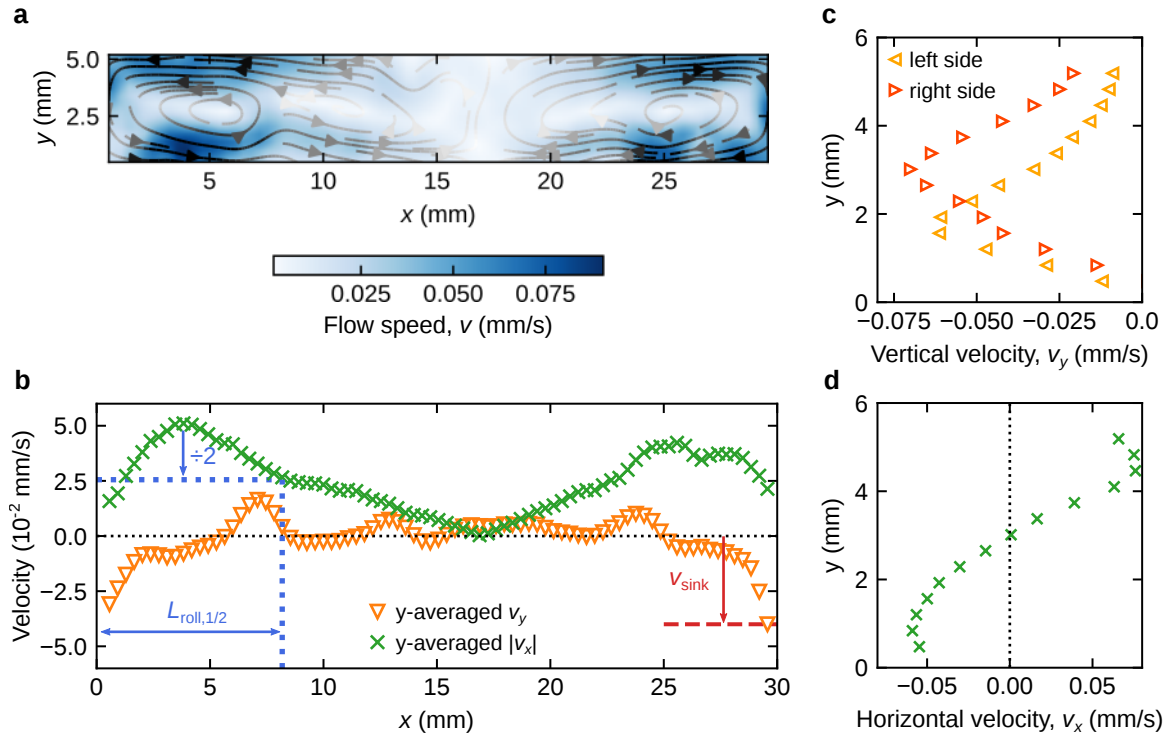


Figure 5.10: Example of a velocity field analysis. **a**, A velocity field represented by a colormap of the flow speed and streamlines tangent to velocity vectors. **b**, Lateral profiles of the horizontal and vertical velocities $|v_x|$ and v_y averaged along the vertical coordinate y . The sinking velocity v_{sink} is defined as the y -averaged downward velocity at the sides. Starting from the left or the right side edges, the convection roll length $L_{\text{roll},1/2}$ is defined as the distance until the y -averaged horizontal velocity decays to half of its maximum value. **c**, **d**. Velocity profiles along the vertical coordinate y . In **c**, Vertical velocity $v_y(y)$ at ~ 0.5 mm from the sides of the liquid chamber ($x \approx \{0, L\}$). **d**, Horizontal velocity $u_x(y)$ at $x = 5$ mm. Note that the flow field resolution does not enable to capture the no-slip boundary conditions at either $y = \{0, H\}$ or $x = \{0, L\}$.

cells/mL, the v_{sink} does not depend much on c_0 and still increases with H . For larger $c_0 \geq 1.2 \times 10^7$ cells/mL, v_{sink} decreases when c_0 increases and the effect of H is less pronounced.

Then, we measured convection rolls lengths $L_{\text{roll},1/2}$ in the experiments. We keep in mind a possible correlation with cell patterns lengths L_{pattern} but we first focus on the effect of c_0 and H on $L_{\text{roll},1/2}$. Figure 5.12.a shows the evolution of $L_{\text{roll},1/2}$ with H at fixed $c_0 = 6 \times 10^6$ cells/mL. We see that $L_{\text{roll},1/2}$ increases with H , but not as strongly as L_{pattern} does (Figure 5.8.a). Again, we normalized data by the liquid chamber length L (Figure 5.12.a, inset). For a single measurement, the upper limit is $L_{\text{roll},1/2}/L \leq 1$. Then, measurements on both sides average out to $L_{\text{roll},1/2}/L \leq 1/2$. Moreover, because $L_{\text{roll},1/2}$ is defined at half of the maximum horizontal velocity, this upper limit is further lowered. In the inset, $L_{\text{roll},1/2}/L$ initially increases with H/L , then reaches a maximum plateau value of $L_{\text{roll},1/2}/L \approx 0.35$. Thus, convection rolls length $L_{\text{roll},1/2}$ is controlled by H only

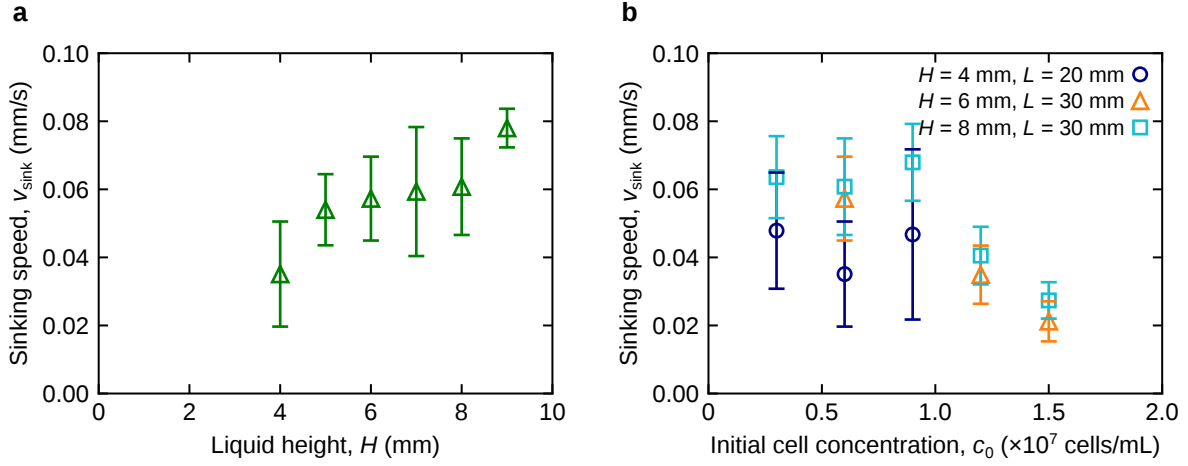


Figure 5.11: Effect of liquid height and initial cell concentration on the sinking velocity. **a**, Sinking velocity v_{sink} as a function of the liquid height H at fixed initial cell concentration $c_0 = 6 \times 10^6$ cells/mL. The liquid chamber length L also varies and we have $\{(H, L)\} = \{(4, 20), (5, 25), (6, 30), (7, 30), (8, 30), (9, 30)\}$ in mm in this data set. **b**, Sinking velocity v_{sink} as a function of the initial cell concentration c_0 at different geometries $\{H, L\}$. For the different graphs, one point corresponds to the mean value for 3 experiments at fixed (H, L, c_0) triplet, knowing that there are two measurements for each experiment (left and right sides). Error bars show standard deviations.

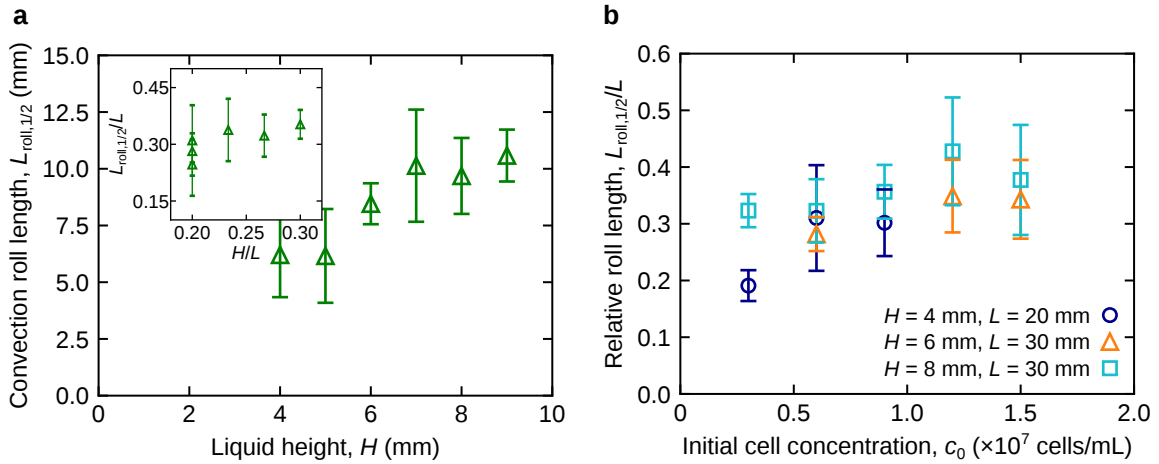


Figure 5.12: Effect of liquid height and initial cell concentration on the convection roll length. **a**, Convection roll length $L_{\text{roll},1/2}$ as a function of liquid height H at fixed initial cell concentration $c_0 = 6 \times 10^6$ cells/mL. The liquid chamber length L is not kept fixed and we have $\{(H, L)\} = \{(4, 20), (5, 25), (6, 30), (7, 30), (8, 30), (9, 30)\}$ in mm in this data set. The inset shows the same data set with $L_{\text{roll},1/2}/L$ normalized by L . **b**, Relative convection roll length $L_{\text{roll},1/2}/L$ as a function of the initial cell concentration c_0 at different geometries $\{(H, L)\}$. For the different graphs, one point corresponds to the mean value for 3 experiments at fixed (H, L, c_0) triplet, knowing that there are two measurements for each experiment (left and right sides). Error bar shows standard deviations.

for small aspect ratios H/L above which it is quickly limited by the horizontal size L . We observe the same saturation in the evolution of $L_{\text{roll},1/2}/L$ with c_0 in Figure 5.12 where

the relative convection roll length only slightly increases with c_0 .

5.3 Relation between concentration and velocity fields structures

In the previous section, cell concentration and velocity fields were analyzed separately. In this section, we compare them with each other. More precisely, we compare the structure of bioconvective flows to the structure of cell concentration patterns.

5.3.1 Convective roll length versus cell pattern length

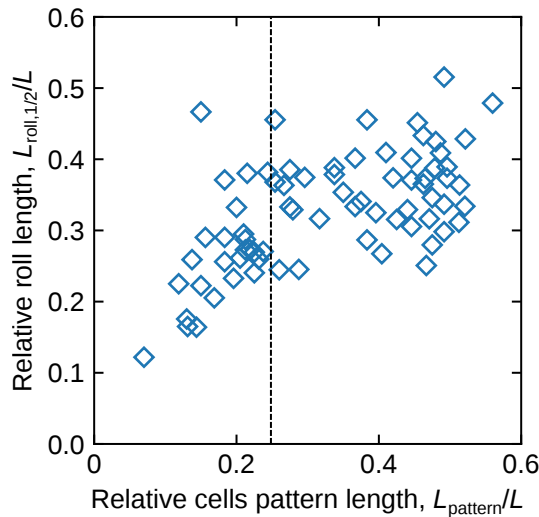


Figure 5.13: Correlation between the lengths of convection rolls and cell patterns. One point corresponds to one measurement of both the relative cell pattern length L_{pattern}/L and the relative convection roll length $L_{\text{roll},1/2}/L$ on the same side in one experiment. A vertical black dashed line separates at $L_{\text{pattern}}/L = 0.25$ separates the graph into two regions.

We used the measurements of L_{pattern} and $L_{\text{roll},1/2}$ introduced in the previous section and that respectively quantify cell concentration patterns spreading and convection rolls elongation. We looked into a possible correlation between these two lengths. To better investigate their relationship, we dropped the averaging of data over several experiments. Instead, the normalized roll size $L_{\text{roll},1/2}/L$ is plotted Figure 5.13 as a function of the corresponding pattern size L_{pattern}/L for each individual experiment. The graph of Figure 5.13 shows two distinct regimes, below and above $L_{\text{pattern}}/L \simeq 0.25$. In the left region of the graph, there is a positive correlation between L_{pattern}/L and $L_{\text{roll},1/2}/L$. In the right region of the graph, there is no correlation between cell patterns and convection rolls lengths and $L_{\text{roll},1/2}/L$ saturates.

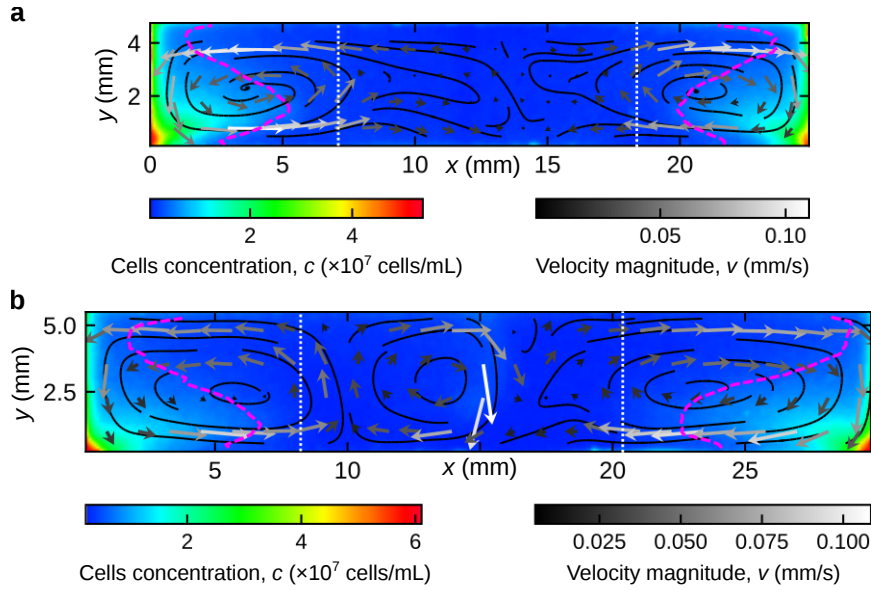


Figure 5.14: Front views of typical flow and concentration fields for $L_{\text{pattern}}/L \leq 0.25$. Colormaps of cell concentration fields on which velocity vectors and streamlines of the flow field are superimposed. Dashed magenta curve : cell patterns limits (def. in Figure 5.7). Dotted vertical white lines : main convective rolls typical lengths $L_{\text{roll},1/2}$ from the sides (def. in Figure 5.10). In these two experiments, cell patterns are well separated and $L_{\text{roll},1/2}$ is not limited by the total length L . In **b**, there are two additional rolls at the center due to a slight positive phototaxis. **a**, $c_0 = 6 \times 10^6$ cells/mL, $H = 6$ mm, $L = 30$ mm. **b**, $c_0 = 6 \times 10^6$ cells/mL, $H = 5$ mm, $L = 25$ mm.

5.3.2 The case of well separated cell patterns

Let us focus here on the left region of the graph of Figure 5.13. We have $L_{\text{pattern}}/L \leq 0.25$ and cell patterns on the left and right sides are well separated. In terms of experimental parameters, this region of the graph corresponds to low initial cell concentrations c_0 or low liquid heights H relatively to the horizontal size L (see Figure 5.8). In this region, both cell pattern length L_{pattern} and convection rolls length $L_{\text{roll},1/2}$ scale with H (Figure 5.8.a, Figure 5.12.a) and there is a positive correlation between the two. Typical examples of such cell concentration and velocity fields are shown in Figure 5.14. The characteristic convection rolls length $L_{\text{roll},1/2}$ is slightly larger than L_{pattern} and is not limited by the total length L . In most of the cases ($> 3/4$ of experiments), the flow speed decreases towards the center and only two main convective rolls are observed (Figure 5.14.a). In some cases ($< 1/4$ of the experiments), we observed an additional flow directed downward at the center induced by a little accumulation by positive phototaxis to which the system is very sensitive.

5.3.3 The case of reduced space between cell patterns

On the right region of the graph in Figure 5.13, we have $L_{\text{pattern}}/L \geq 0.25$ and the separation between regions of high concentration is reduced. We enter this region by increasing either the initial cell concentration c_0 or the aspect ratio H/L . While cell

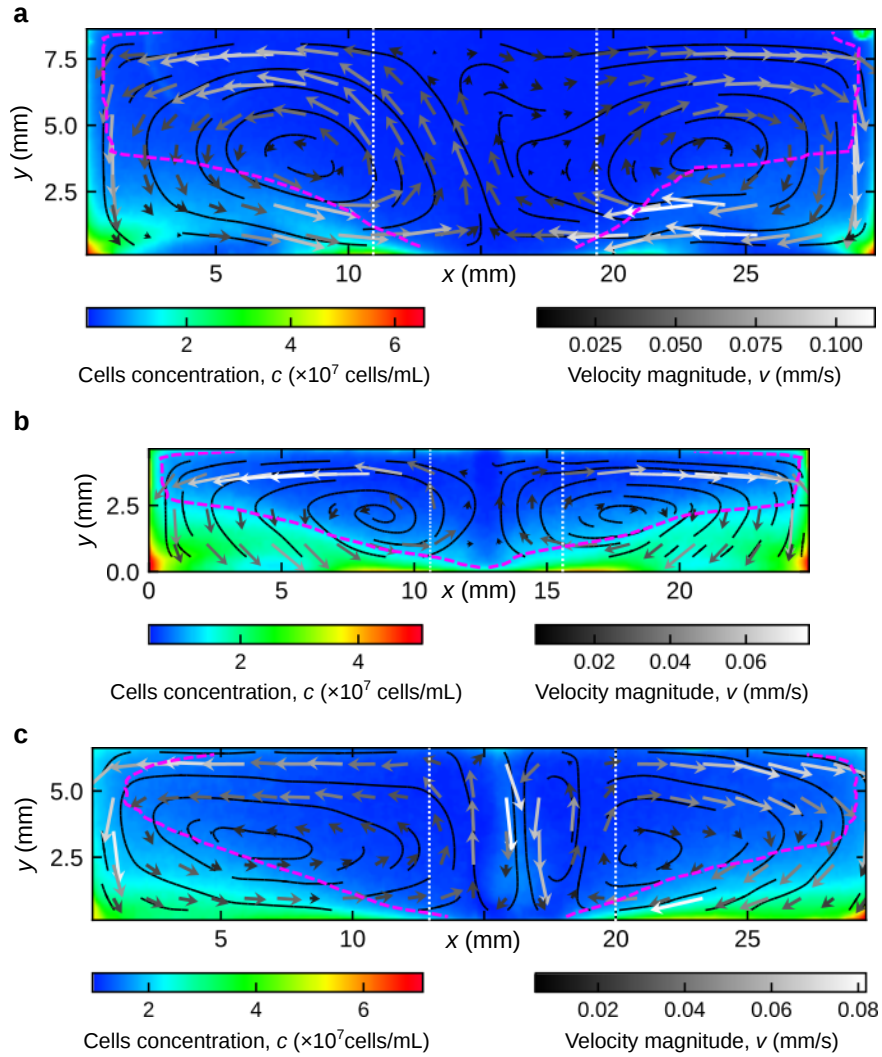


Figure 5.15: Side views of typical flow and concentration fields for $L_{\text{pattern}}/L \geq 0.25$. See legend in Figure 5.14. In these experiments, there is only a small separation of cell patterns and $L_{\text{roll},1/2}$ is limited by the total length L . In **c**, there are two additional rolls at the center due to a slight positive phototaxis. **a**, $c_0 = 6 \times 10^6$ cells/mL, $H = 9$ mm, $L = 30$ mm. **b**, $c_0 = 1.5 \times 10^7$ cells/mL, $H = 5$ mm, $L = 25$ mm. **c**, $c_0 = 1.5 \times 10^7$ cells/mL, $H = 7$ mm, $L = 30$ mm.

patterns length still increases with H (Figure 5.8), $L_{\text{roll},1/2}/L$ saturates (Figure 5.12) whereas L_{pattern}/L still increases with H and c_0 . Thus the correlation between the lengths of cell patterns and convection rolls is lost. Figure 5.15 gives a few examples of typical cell concentration and velocity fields for $L_{\text{pattern}}/L \geq 0.25$. Convection rolls are limited by the horizontal size : $L_{\text{roll},1/2}/L \approx 0.35$. In particular, we can have $L_{\text{roll},1/2} < L_{\text{pattern}}$. In Figure 5.15.a, cell pattern spreading is due to a large value of liquid height $H = 9$ mm whereas it is due to a large value of $c_0 = 1.5 \times 10^7$ cells/mL in Figure 5.15.b. Again, in some cases ($< 1/4$ of the experiments), we observed an additional flow directed downward induced by a slight positive phototaxis (Figure 5.15.c).

5.4 Local analysis

After looking at the macroscopic scale, we investigate in this section the local relationship between variations of the cell concentration field and variations of the fluid velocity field. Then, we compare this prediction to experimental data.

5.4.1 Theoretical prediction

Let us first that the ratio of the viscous and cells diffusion timescales is $\frac{D\rho_0}{\eta} \sim 0.1$. Thus we suppose that velocity and pressure fields instantaneously adjust to the Cell concentration field and we have :

$$\eta\Delta\vec{v} = \vec{\nabla}p_e - \rho_0\beta cg\vec{e}_y \quad (5.4)$$

We suppose that the liquid chamber thickness e of axis \vec{e}_z is much smaller than both its height H and length L : $e \ll H, L$. However, we note that $2/9 \leq e/H \leq 1/2$ and $e \ll H$ is taken for simplicity. We neglect both the velocity v_z and variations of the concentration field in the \vec{e}_z direction :

$$c = c(x, y) \quad (5.5)$$

$$\vec{v} = v_x\vec{e}_x + v_y\vec{e}_y \quad (5.6)$$

Then, we work at leading order in e/H and e/L and project the flow and pressure fields vectorial equation (5.4) on $\vec{e}_x, \vec{e}_y, \vec{e}_z$:

$$\eta\frac{\partial^2 v_x}{\partial z^2} = \frac{\partial p_e}{\partial x} \quad (5.7)$$

$$\eta\frac{\partial^2 v_y}{\partial z^2} = \frac{\partial p_e}{\partial y} - \rho_0\beta cg \quad (5.8)$$

$$\frac{\partial p_e}{\partial z} = 0 \quad (5.9)$$

Using the no-slip boundary conditions at $z = \pm e/2$ and equations (5.7,5.9), we find :

$$p_e = p_e(x, y) \quad (5.10)$$

$$v_x(x, y, z) = \frac{1}{2\eta} \left[z^2 - \frac{e^2}{4} \right] \frac{\partial p_e}{\partial x}(x, y) \quad (5.11)$$

In particular, the horizontal velocity follows a Poiseuille profile in the \vec{e}_z direction of z -averaged velocity given by :

$$\bar{v}_x(x, y) = \frac{-e^2}{12\eta} \frac{\partial p_e}{\partial x}(x, y) \quad (5.12)$$

Formula (5.8) indicates that the y velocity also follows a Poiseuille profile in the \vec{e}_z and is thus given by :

$$v_y(x, y, z) = \frac{-6}{e^2} \left[z^2 - \frac{e^2}{4} \right] \bar{v}_y(x, y) \quad (5.13)$$

We use the above form for v_y in eq. (5.8), which gives :

$$-\frac{12\eta}{e^2} \bar{v}_y - \frac{\partial p_e}{\partial y} = -\rho_0 \beta g c \quad (5.14)$$

Then, by differentiating with respect to x and using the relationship eq. (5.12), we find :

$$\frac{\partial \bar{v}_y}{\partial x} - \frac{\partial \bar{v}_x}{\partial y} = \frac{\rho_0 \beta e^2}{12\eta} \frac{\partial c}{\partial x} \quad (5.15)$$

We now introduce the flow stream function such that :

$$\bar{v}_x = -\frac{\partial \psi}{\partial y} \quad \text{and} \quad \bar{v}_y = \frac{\partial \psi}{\partial x} \quad (5.16)$$

Finally, we find :

$$\Delta \psi = B_{\text{th}} \frac{\partial c}{\partial x} \quad \text{where} \quad B_{\text{th}} = \frac{\rho_0 \beta g e^2}{12\eta} \quad (5.17)$$

Summary

We used a continuum model of bioconvection in which we assume that the velocity and pressure fields instantaneously adjust to the cell concentration field. We take advantage of the laterally confined geometry in the liquid chamber thickness direction (\vec{e}_z) to reduce the dimensionality of the problem. The model predicts a linear relationship between the stream function Laplacian and the local horizontal cell concentration gradient.

From the expression of the proportional coefficient B_{th} , we anticipate that fitting to experimental data should be highly sensitive to *Chlamydomonas reinhardtii* cells diameter $2R_{\text{CR}}$ because $\beta = \frac{\Delta r_{\text{hoCR}}}{\rho_0} V_{\text{CR}}$ varies with R_{CR}^3 . Using $2R_{\text{CR}} = 10 \mu\text{m}$ and a cell volume $V_{\text{CR}} = 500 \mu\text{m}^3$, we expect $B_{\text{th}} = 10^{-8} \text{ cm}^4/\text{s}$.

5.4.2 Data analysis

From experimental cell concentration and fluid flow fields data, we calculated local values of horizontal cell concentration gradients $\frac{\partial c}{\partial x}(x, y)$ and flow stream function Laplacian $\Delta \psi(x, y)$ and investigated their relationship. This analysis was first performed on single experiments as illustrated in Figure 5.16. It should be noted that the analysis was performed only within a flow area at some millimetric distance from the lateral edges $d_1 \leq x \leq L - d_2$ (see caption). The graph shows a linear domain for small concentration gradients $|\frac{\partial c}{\partial x}| < \times 10^7 \text{ cells}/\text{m}^4$. For a typical concentration scale of $1 \times 10^7 \text{ cells}/\text{mL}$, this would correspond to spatial variation over distances $> 1 \text{ cm}$, and thus to relatively

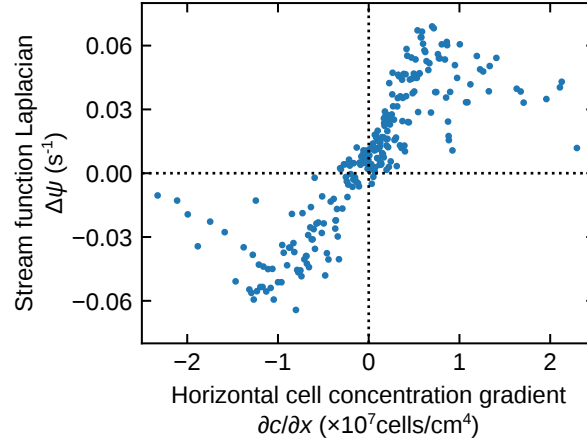


Figure 5.16: Stream function Laplacian as function of the horizontal cell concentration gradient for a single experiment. Different points correspond to $\frac{\partial c}{\partial x}$ and $\Delta\psi$ measured at different locations (x, y) of the cell concentration and velocity fields. More precisely, the sets of points corresponds to $\{(\frac{\partial c}{\partial x}, \Delta\psi(x, y)) \mid d_1 \leq x \leq L - d_2, 0 \leq y \leq H\}$, where cuts by $d_1, d_2 \approx 1$ mm enabled to limit the range horizontal range to $|\frac{\partial c}{\partial x}| \lesssim 5 \times 10^7$ cells/cm⁴. Raw data were sorted by ascending order of $\frac{\partial c}{\partial x}$ and the median value was taken every 3 points to obtain a graph to reduce both the number of points and their dispersion. $c_0 = 6 \times 10^6$ cells/mL, $H = 6$ mm, $L = 30$ mm.

weak cell concentration gradient given the length $L = 2$ cm. For higher values of $|\frac{\partial c}{\partial x}|$, the graph abruptly deviates from the linear regime and $|\Delta\psi|$ decreases towards zero with increasing $|\frac{\partial c}{\partial x}|$.

Subsequently, data of $\{(\frac{\partial c}{\partial x}, \Delta\psi)\}$ for all experiments were grouped together (Figure 5.17). Because this representation is based on the spatial derivatives of the experimental data, it exhibits of course a large amount of dispersion. Data were filtered to uncover the global trend. The corresponding solid line red curve shows a linear domain for $|\frac{\partial c}{\partial x}| < 0.3 \times 10^7$ cells/mL. The theoretical prediction of the model (eq. (5.17)) was tested on this linear domain and gave a proportional coefficient $B_{\text{exp}} = (0.55 \pm 0.3) \times 10^{-8}$ cm⁴/s, in good agreement with the expected theoretical value $B_{\text{th}} = 10^{-8}$ cm⁴/s. The relative deviation of B_{exp} from B_{th} could be attributed to values of cell diameter and volume of $8 \mu\text{m}$ and $250 \mu\text{m}^3$ smaller than the typical values of $10 \mu\text{m}$ and $500 \mu\text{m}^3$ used to estimate B_{th} . Although there are other possible sources of deviation, this would be in agreement with variations of *Chlamydomonas reinhardtii* cells diameter from one strain to another (Gallaher et al. 2015).

In Figure 5.17, we notice that the range of horizontal cell concentration in which there is a linear relationship with the stream function Laplacian is more restricted than that of the single experiment analyzed in Figure 5.16. Thus, we looked to identify what controls the deviation from the linear domain. In Figure 5.18, data are separated by initial initial cell concentration c_0 of the experiments. This additional step in the analysis shows that the higher the initial cell concentration, the sooner $\Delta\psi$ deviates from the linear

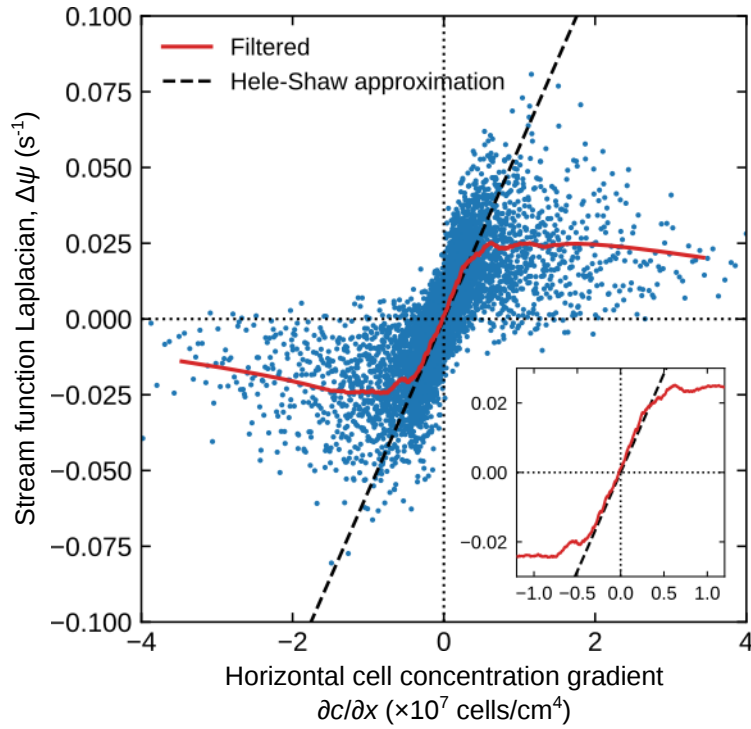


Figure 5.17: Relationship between the stream function Laplacian and the horizontal cell concentration gradient in the experiments. Data points of all experiments obtained as described in Figure 5.16 are all plotted together. Solid red line curve : data were filtered using local polynomial regression. Filtered data show a linear domain fitted with a straight line (dashed black line) of slope $B_{\text{exp}} = (0.55 \pm 0.3) \times 10^{-8} \text{ cm}^4/\text{s}$ passing through the origin representing the Hele-Shaw approximation eq. (5.17). Inset : zoom on the linear domain with the same quantities and units as in the main plot.

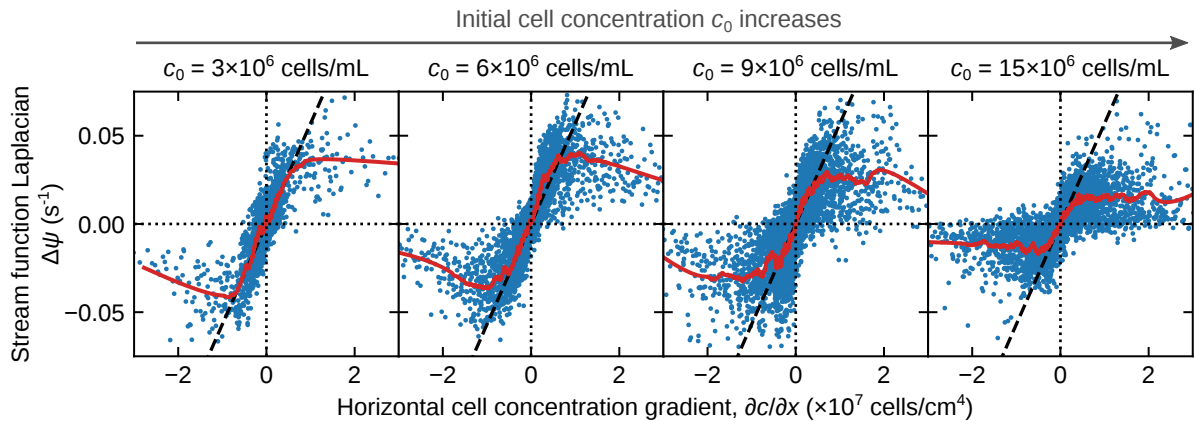


Figure 5.18: Relationship between the stream function Laplacian and the horizontal cell concentration gradient in the experiments at different initial cell concentration. For each graph, both the data points and the filtered data curve (solid red line) were obtained for the experiments at a given initial cell concentration c_0 as in Figure 5.17. The dashed black line on the other side corresponds to the unique linear fit obtained for all experiments in Figure 5.17.

relationship with $\frac{\partial c}{\partial x}$.

5.5 Discussion

5.5.1 Physical parameters controlling the flow fields

We found that all lengths in the geometry of the system play a different role. At the macroscopic scale global properties, we found that global properties scale with the liquid height H but are limited by the horizontal length L . At the local scale, we found that the linear relationship between $\Delta\psi$ and $\frac{\partial c}{\partial x}$ is well described by a proportional coefficient with the thickness to the square e^2 . Therefore, the system is not controlled by the pseudo-Rayleigh number defined for an extended system of height H as $\text{Ra} = \frac{\rho_0 \beta g c_0 H^3}{D\eta}$. In this confined geometry, fluid flows are controlled by the number $Bth = \frac{\rho_0 \beta g e^2}{12\eta}$ on a local scale while macroscopic properties of the flow and cell concentration fields are controlled by the large lengthscale H until H becomes comparable to L at which point roll size and pattern size saturate. However, we found some surprising effects arising at high initial cell concentration c_0 that we discuss below.

5.5.2 The surprising effect of cell concentration

We found some interesting effects of increasing the initial cell concentration c_0 . We found a decrease of the sinking velocity v_{sink} (Figure 5.11.b). We also found an effect of c_0 on the deviation from the linear relationship between the stream function Laplacian and the horizontal cell concentration gradient (Figure 5.18). We note that the decrease of v_{sink} with c_0 is in contrast to numerical results by Arrieta et al. 2019. We should stress that they did not measure directly fluid velocities but used swimming cells as tracers instead, which is fundamentally different. Still, their numerical simulations predicts higher cells recirculation velocities when increasing c_0 . In their experiments however, they only mention an effect of c_0 on plume formation. Possible explanations of the surprising effects of c_0 in our experiments are a significant increase of the effective viscosity at higher cell concentrations, edges effects or possible cell-cell interactions.

Rafai, Jibuti, and Peyla 2010 performed the first direct experimental macroscopic measurement of the effective viscosity in suspensions of *Chlamydomonas reinhardtii* (Figure 5.19). They found a significant increase of the effective viscosity η_{eff} with living cells compared to suspensions with dead cells, as predicted for puller-type cells by Ishikawa and Pedley 2007. They performed experiments at different shear rates $\dot{\gamma}$ and volumic fractions ϕ . They found a shear thinning behavior for with a maximum viscosity at $\dot{\gamma} \approx 4 \text{ s}^{-1}$. At 5 s^{-1} , η_{eff} was doubled when ϕ increased from 0 to 0.15. In our experiments however, the volume fraction and the shear rate are quite lower. The volume fraction can locally reach at most $\phi_{\text{max}} \sim 0.03$ while the typical shear rate can be estimated to $\dot{\gamma} \sim \frac{v}{e} \sim 0.05 \text{ s}^{-1}$. Additionnaly, effects of locally high cell concentrations in our experiments could also be

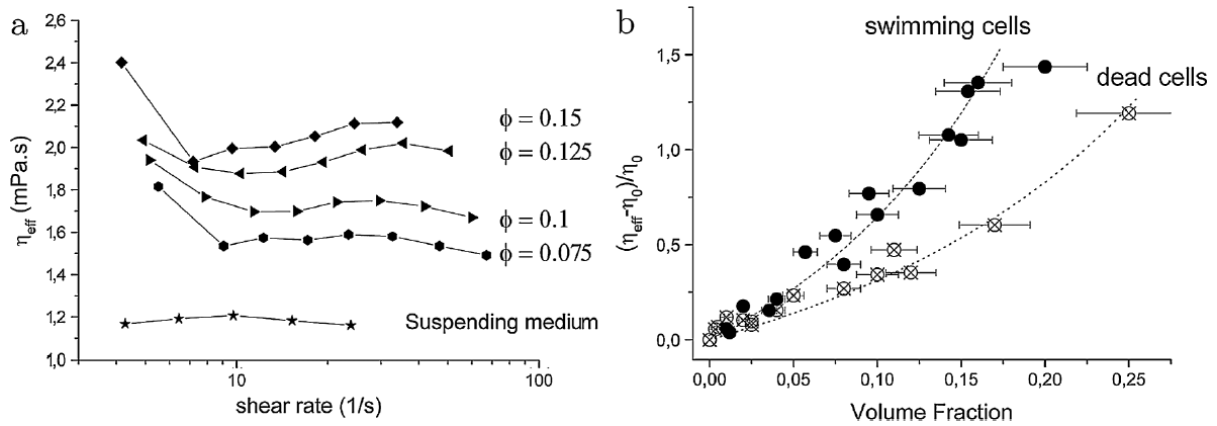


Figure 5.19: Measurements of the effective viscosity of *Chlamydomonas reinhardtii* suspensions by Rafai, Jibuti, and Peyla 2010. **a**, Effective viscosity as a function of the shear rate at different volume fractions. **b**, Reduced viscosity as a function volume fraction at shear rate $\dot{\gamma} = 5 \text{ s}^{-1}$. η_0 is the viscosity of the suspending medium. Measurements were performed in cone-plate geometry at imposed stress.

coupled to edge effects. This is because regions of high concentration are located close to edges in the negative phototaxis situation. Concerning possible cell-cell interaction, we refer to flow field measurements around *Chlamydomonas reinhardtii* by Drescher et al. 2010. They found that the fluid velocity around the swimmer is $\geq 1\%$ of its velocity for distances $\leq 7R_{\text{CR}}$. This correspond to volume fraction of a few % or more and the authors concluded that in this range that we approach in our experiments, cell-cell hydrodynamic interactions are possible.

Experimental data could be further analyzed better to investigate these hypotheses. The measurement of v_{sink} could be supplemented with the calculation of the viscous energy dissipation (under the hypothesis of a constant viscosity) to see if this quantity also decreases or instead increases with c_0 . Concerning the relationship between $\Delta\psi$ and $\frac{\partial c}{\partial x}$, the effect of the concentration could be further investigated by looking at local concentration values $c(x, y)$ associated to different regions of the graphs $\{(\frac{\partial c}{\partial x}(x, y), \Delta\psi(x, y))\}$. Additional numerical experiments might also shed light on the physical mechanisms underlying the departure of the experimental data from the theoretical prediction, in particular by quantifying the effect of boundaries on fluid flows.

5.5.3 A remark on instabilities

So far, we have not discussed the effect of gyrotaxis in these experiments. In Petri dishes experiments presented in chapter 3, photo-gyrotaxis in the vertical plane focused algae in a dense layer above the bottom of the suspension because of opposite flow direction and cells preferential orientation. This eventually led to outward waves emission when the dense layer was unstable. Here, a similar photo-gyrotactic effect in the vertical plane was also observed. Figure 5.20 shows some examples. We observed the detachment of cell concentration patterns from the bottom of the suspension (Figure 5.20.a,b), and in rare

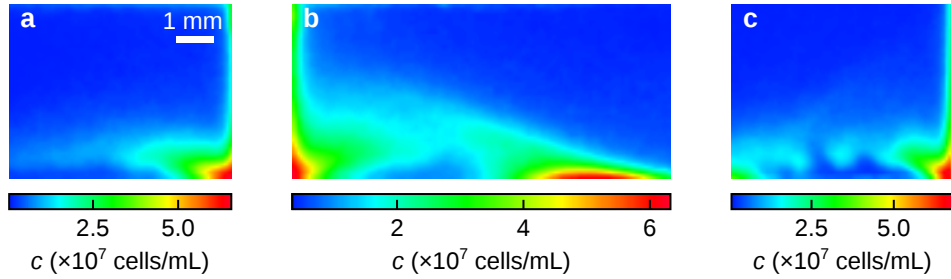


Figure 5.20: Instabilities in cell concentration patterns. Front views of cell concentration fields represented with the same scale. **a**, A concentrated layer is visible above the bottom of the suspension on the right-hand side of a concentration field map. $c_0 = 6 \times 10^6$ cells/mL, $H = 5$ mm, $L = 25$ mm. **b**, A bridge-like structure above the bottom of the suspension on the left-hand side of a concentration field map. $c_0 = 1.2 \times 10^7$ cells/mL, $H = 5$ mm, $L = 25$ mm. **c**, Breaks into clusters of high concentration on the bottom-right corner of a concentration field map. $c_0 = 6 \times 10^6$ cells/mL, $H = 9$ mm, $L = 2$ mm.

instances breaks into clusters of high concentration (Figure 5.20.c). We did not study in depth cell patterns photo-gyrotactic instabilities in these experiments. To give a simple picture, we think that high velocities and/or well separated cell patterns are necessary to observe these instabilities. The first condition is limited by viscous friction due to the thin thickness e while the second one is limited by the liquid chamber length L .

5.6 Conclusion

In conclusion to this chapter, we reported the first experimental quantitative study where bioconvection cell patterns and fluid flows were acquired simultaneously.

We developed a setup that enabled us to quantitatively study of bioconvection flows acquired simultaneously with concentration fields. We successfully adapted a custom fluorescent PIV technique, harmless and non-intrusive for the cells, to measure flow fields. In establishing a measurement protocol, we found some interesting time dependent features of the phototactic response in *Chlamydomonas reinhardtii* CC-124 with negative phototaxis followed by positive phototaxis.

In this negative phototaxis situation, we studied cell concentration fields consisting of cell patterns located at the side edges of the liquid chamber and spreading on the bottom of the suspension. We characterized the structure and the flow speed of the main convection rolls associated to those cell patterns with a flow directed downward close to the side edges.

In particular, we found that both the cell patterns spreading, the flow intensity and the convection rolls elongation, respectively described by L_{pattern} , v_{sink} and $L_{\text{roll},1/2}$, all increase with the liquid height H . We also found that L_{pattern} and $L_{\text{roll},1/2}$ increase with c_0 . On the contrary, v_{sink} unexpectedly decreases with c_0 at high concentration. Next, the experimental setup enabled the first comparison of bioconvective flows velocity fields

to their associated cell concentration fields. We compared the structures of cell patterns and convective rolls. We found that a positive correlation between their relative lengths L_{pattern}/L and $L_{\text{roll},1/2}$ but only when cell patterns located on both sides were well separated. Finally, we looked at the local scale and found a relationship between local variations of the cell concentration and of the fluid velocity. Experimental data are well described by a theoretical prediction of a linear relationship between the stream function Laplacian $\Delta\psi$ and the horizontal cell concentration gradient $\frac{\partial c}{\partial x}$ only at low concentration gradients. We found that experimental data deviate sooner from this prediction at high initial cell concentration c_0 . The surprising effects arising at high cell concentration are yet to be understood.

CHAPTER 6

Stirring with light: a perspective

The results presented in this chapter have been (partly/mostly) obtained during the internship of Dario Vignoli, which I co-supervised.

In this short chapter, we build upon the knowledge presented so far in this manuscript and investigate a question with potential important practical applications: can we use light to stir biological suspensions and enhance culture growth ?

We do not fully answer this question but, rather, we present an original experimental setup able to induce sustained bioconvective flows over timescale comparable to the cell division timescale and we show preliminary results on the influence of bioconvection on cell culture growth.

6.1 Cultures of photosynthetic microorganisms

Thanks to their ability to grow using carbon dioxide and light as their sole energy source, photosynthetic microorganisms are a natural source of biomass, which can then be converted into biofuels (Alam, Mobin, and Chowdhury 2015). Until the end of the last century, this abundant source of third generation biofuels was largely under-exploited in comparison with oil. More recently, the inevitable shrinking of fossil fuels, resulting in rising prices, combined with the awareness of their close link with climate change, has re-launched worldwide research aimed at producing biofuels (biohydrogen, biodiesel, biokerosene) in a sustainable and profitable way. An other application of microorganisms is the production of a wide range of chemical compounds for the medical, pharmaceutical, cosmetic and food industries (Mata, Martins, and Caetano 2010). Microalgae, like *Chlamydomonas reinhardtii*, are the most represented microorganisms in these applications. They are mostly cultivated in conventional fermenters (Figure 6.1, left), or sometimes in natural sites, in the sea or in raceways (Figure 6.1, right).



Figure 6.1: Typical setups for the culture of photosynthetic micro-organisms. **Left** A photo-bioreactor for moss culture (Freiburg University). **Right** An open raceway pond

The scientific community is mainly faced with two challenges to make biofuels both economically sustainable and profitable, which are to improve the photosynthetic processes and to develop efficient photobioreactors. Concerning bioreactors, high economical and energetical costs may originate from the large amount of mechanical work required in many processes such as mixing, or gas compression and transfer (Huang et al. 2017).

In theory, a way to reduce the cost of the mechanical work needed is to utilize the mechanical work already produced by the swimming microorganisms at the microscopic scale. The associated fundamental question is: can we harvest the mechanical work produced by the microorganisms towards a larger scale in the fluid? Upon the knowledge presented so far in this manuscript, bioconvection could induce a significant level of mixing

by the microorganisms themselves.

The goal of this short chapter is to quantify the effect of bioconvection on the growth of culture of microalgae. To this end, we have developed an opto-mechanical setup capable of projecting a wide variety of time and space-dependent optical patterns, at definite optical wavelengths, over a suspension of microalgae in order to trigger large-scale bioconvective flows. We also designed an experimental protocol tailored to sustain these flows over timescale comparable to the biological timescale of cell division. In order to assess the influence of bioconvection on *Chlamydomonas reinhardtii* culture growth, we monitored over time the cell concentration of the algal suspensions, with and without bioconvection.

6.2 Experimental setup

6.2.1 Time-dependent light-field for large-scale bioconvection

In order to induce complex flow fields on demand, and induce large-scale bioconvection, we have develop in collaboration with François Heslot an experimental device allowing us to project spatially and temporally structured light fields onto active suspensions. Because of the extreme light-sensitivity of photosynthetic micro-organisms, devices based on conventional LCD screens, projectors or digital micromirror devices (DMD) cannot be used because of their excessive light leakage (for example, even when turn to a black state, the light leaking between pixels or even through the filter of a LCD screen is strong enough to trigger an active response from *Chlamydomonas reinhardtii*). Consequently, a dedicated experimental device involving fast-speed oscillating mirrors and a laser beam equipped with a shutter has been developed. A sketch of the setup is shown in Figure 6.2.a. Briefly, a strong green laser beam (532 nm, 100mW), is first dimmed using crossed polarizers and then projected onto two small mirrors oscillating on perpendicular axes driven by high-speed servo motors. After being reflected by the two mirrors, the green laser dot finally reaches the algal suspension. By modulating the amplitude and frequency of the current driving the servo motors, the angular position of each mirror can be tuned independently and, consequently, the position of the laser dot onto the suspension can be controlled with a high spatial and temporal resolution. A shutter is also present along the beam path to further tune the resulting patterns. The oscillation of the mirrors is controlled using audio files converted by a digital-analog converter (DAC) and further amplified to drive the servo motors oscillation.

In order to study the influence of bioconvection on the growth of *Chlamydomonas reinhardtii* cultures, two spatio-temporal light patterns were chosen.

A pattern appearing as a *rotating bar* to the naked eye, and mimicking a magnetic stirrer, was used to trigger large scale bioconvection in the algal suspension. The pattern was generated by oscillating the laser dot at a high frequency (100Hz) along the radial

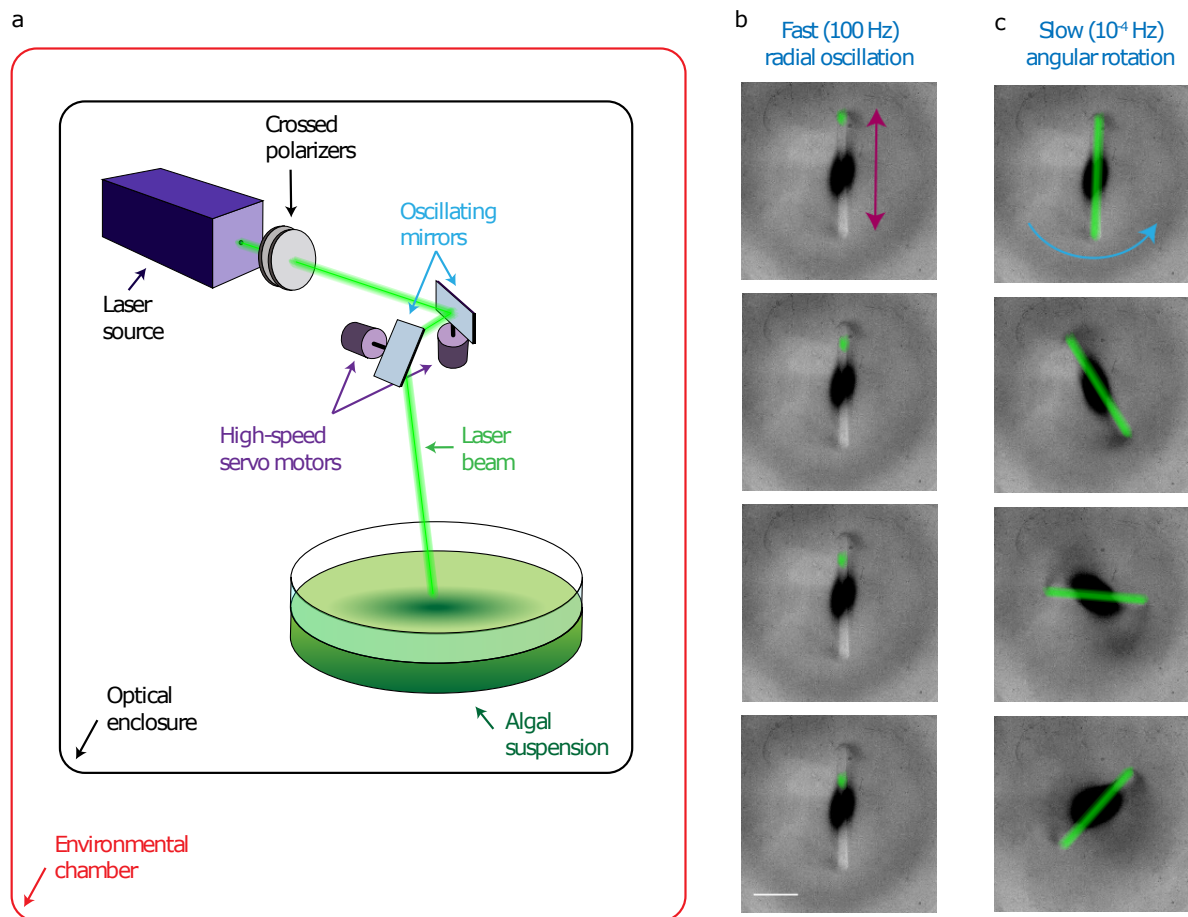


Figure 6.2: Experimental setup for the biomixing study. **a** Sketch of the setup designed to study the influence of bioconvection on cell culture growth. A green laser beam (532nm) is modulated in intensity using cross polarizers before being deflected by two mirrors oscillating at high speed around perpendicular axes. The moving laser dot is projected on an algal suspension covered with a lid (not represented for clarity). Images can be acquired during experiments using a homogeneous red light field passing through the suspension, as described in the previous chapters. The red panel light is not represented either. **b** The moving laser dot oscillates in the radial direction with a high frequency (100Hz) and a projected amplitude around 4cm. During the acquisition timescale of the picture (~ 1 s), the green laser dot oscillates back and forth many times and appear as a clear rod on the picture and to the naked eye. The vertical series of image is a sketch illustrating the fast radial motion of the green dot but this motion is not actually captured by the camera. Algae accumulate around the laser light, as can be seen in the dark region surrounding the path of the laser dot. The scale bar is 3 cm. **c** Pictures of the experiment taken every 5 minutes and illustrating the slow rotation of the optical pattern, which appear to the naked eye as a rotating green rod.

coordinates of the circular vessel containing the algal suspension (Figure 6.2.b), on top of which a much slower rotation frequency (10^{-4} Hz) was added (Figure 6.2.c).

The requirement for the control experiment was mainly to bring to the algal suspension the exact same amount of photons (per unit of time), and at precisely the same wavelength, as spatially homogeneously as possible, in order to avoid triggering bioconvective

flows. To this end, a *pseudo-random* pattern was created by oscillating the laser dot at a high frequency (100Hz) along the radial coordinates and, instead of slowly varying its orientation, a new random orientation was chosen every second according to a uniform distribution in the interval $[0, 2\pi]$. The number of photon is the same for each light patterns. This choice of pattern for the control experiment, which was also constrained by technical limitations of the DAC, does not produce a completely homogeneous light intensity field and it may induces a small amount of bioconvection as a result since, once averaged over time, the number of photons will be highest at the center of the light-intensity field. Cell accumulation at the center over time was indeed noted in these control experiments but the magnitude of these accumulation was much smaller than in the experiments where bioconvection was triggered on purpose.

6.2.2 Microalgae preconditioning

One of the main challenges that needed to be overcome before we could study the impact of bioconvection on growth was to be able to induce phototaxis over timescales comparable to the timescale of cell division in *Chlamydomonas reinhardtii* (~ 8 hours). In particular, because the phototactic response of *Chlamydomonas reinhardtii* is tightly linked to the circadian rhythm of the algae, it usually decreases during the day (Stavis and Hirschberg 1973). In order to circumvent this problem, we used unsynchronized cell cultures continuously exposed to light during their growth before the experiments in this chapter.

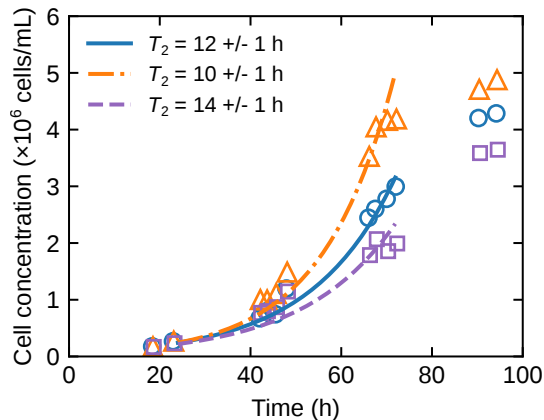


Figure 6.3: Growth curve of unsynchronized liquid cultures. The growth of 3 unsynchronized liquid cultures (different symbols) was monitored by measuring the cell concentration of samples of the cultures at different times. Cells were introduced in their liquid culture medium at $t = 0$. For $24 \text{ h} \leq t \leq 72 \text{ h}$, the growth is well described by an exponential growth of cell doubling time T_2 .

Unsynchronized liquid cultures were grown as described in appendix A.2.3. The growth of *Chlamydomonas reinhardtii* liquid cultures consists of a succession of different phases that starts when cells are introduced in the liquid culture medium. The first phase

is termed the “lag phase”. It is essentially a phase during which cells adapt to their new environment and during which no noticeable growth is detected. In particular, the duration of this lag phase can vary from one culturing method to the other.

Following the lag phase, an exponential growth phase occurs during which we intend to perform our experiments. In this phase, cells have a maximum growth rate and a cell doubling time (the time required for a culture to double in concentration) can be calculated to measure the effect of external factors on growth. The phototactic response is also maximum during the exponential growth phase. At the end of the exponential growth phase, the growth rate gradually decreases and cells enter a stationary phase where they reach a maximum cell concentration (typically 3×10^6 cells/mL). We thus monitored the growth of unsynchronized liquid cultures to identify their exponential growth phase, as shown in Figure 6.3. An exponential growth was found for $24 \text{ h} \leq t \leq 72 \text{ h}$ with a typical cell doubling time of $T_2 \gtrsim 10 \text{ h}$.

6.2.3 Experimental protocol

The experiments with and without bioconvection were performed using the following protocol. First, because of the high sensitivity of cultures of micro-algae to small environmental perturbation, the entire experimental setup was placed in a large environmental growth chamber with controlled temperature, humidity and lighting condition.

In order to check whether cell accumulation, and hence bioconvection, occurred in each experiment, we used transmitted dim red light to image the concentration field in the growth vessel. A computer controlled Nikon D700 digital camera was used to acquire one picture every 10min. Although the red light has little to no effect on phototaxis, it might still affect *Chlamydomonas reinhardtii* metabolism and it was thus kept at the same intensity in all experiments. Pictures were analyzed with the ImageJ software. At the end of the experiments, Petri dishes were weighted to assess the volume of suspension evaporated during the duration of the experiments. Algal suspensions were homogenized before measuring its absorption spectrum and optical density.

We performed experiments with unsynchronized liquid culture grown during 60h to 72h before the experiments. Thus, cells were close to the end of their exponential growth with fully developed phototaxis. In order to maintain cells in the exponential growth and to possibly measure significant growth in the experiments, suspensions were diluted according to the procedure described in A.3.2. The initial concentration before the experiments was typically adjusted to $c_0 \approx 6 \times 10^5$ cells/mL.

Experiments lasted $\Delta t_{\text{exp}} = 24$ hours, and measurements of the cell concentration were performed in triplicate both at the beginning (c_0) and at the end of the experiments (c_f). The cell doubling time T_2 was calculated for each experiment using these six measurements as:

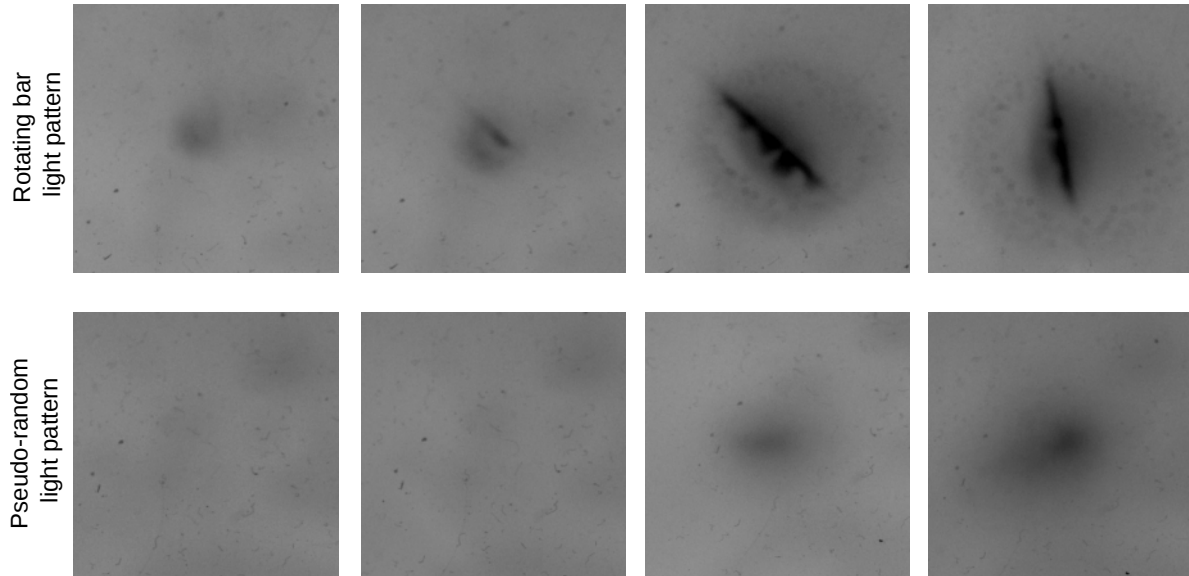


Figure 6.4: Series of images showing the response to the two spatio-temporal light patterns used in the experiments. Red channel of the images of the cell concentration field seen from above in 2 experiments. **Top:** Images 6h apart during a 24 hours-long experiment from 2:00 pm to 2:00 show the sustained phototaxis. The first image was taken at 8:00 pm. The *rotating bar* light pattern (see section 6.2.1) was used to trigger bioconvection on purpose. **Bottom:** Images 6h apart during a 24 hours-long experiment from 3:00 pm to 3:00 pm. The first image was taken at 09:00 pm. The *pseudo-random* light pattern was used to avoid triggering bioconvection (see section 6.2.1). In both experiments, the liquid height $H = 2$ mm with an initial cell concentration $c_0 = 6 \times 10^5$ cells/mL.

$$T_2 = \Delta t_{\text{exp}} \frac{\ln 2}{\ln(c_f/c_0)} \quad (6.1)$$

Finally, in order for bioconvection to have a significant effect on growth, the limiting factor for culture growth must be the availability (or accumulation) of dissolved gases, such as O_2 or CO_2 .

We investigated light-induced mixing for $H = 2$ mm and $H = 6$ mm and compared how *Chlamydomonas reinhardtii* grew in the presence or in the absence of bioconvection.

6.3 Results

6.3.1 Sustained phototaxis

A first result is that we did observe long sustained phototaxis as shown in Figure 6.4. This is especially evidenced in the top series of images where the accumulation of cells around the slow *rotating bar* was clearly visible. On the bottom series of images, we also see a cell accumulation at the center over time, as mentioned previously due to the higher number of photons at the center of the light-intensity field.

6.3.2 Effect of bioconvection on culture growth

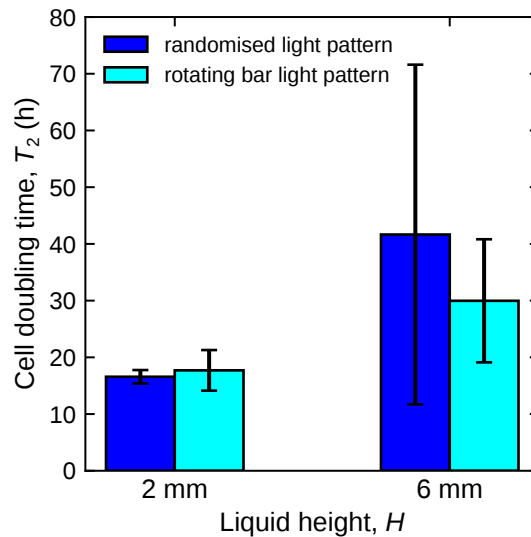


Figure 6.5: Effect of bioconvection on growth. Cell doubling time in suspensions under two different illumination patterns at two different liquid heights. The heights of the bars and the error bars respectively represent the mean value and the standard deviation between the three replicates.

We then investigated the effect of light-induced mixing on the culture growth mixing for $H = 2$ mm and $H = 6$ mm and in the presence or in the absence of bioconvection by measuring the cell doubling time in each case. This is represented in Figure 6.5. We see at first that for small culture depth ($H = 2$ mm), no significant changes in cell doubling time were measured when we changed the projected light pattern. In the case of deeper cultures, we observe an overall significant increase in the cell doubling time, indicating that the range of parameters used in our experiments is indeed relevant and that the diffusion of gases is indeed the limiting factor for the chosen values of the light intensity and wavelength, temperature, humidity, and pre-conditioning of the micro-organisms.

Although the average value of the cell doubling time in absence of bioconvection is indeed 10 hours larger than the average doubling time in the presence of bioconvection, the large error bars in the determination of the cell doubling time prevent us from being conclusive on the effect of bioconvection on cell culture growth. On the other, it strongly calls for additional experiments.

6.4 Conclusion

We investigated the possibility to use light to induce self-mixing in suspensions of *Chlamydomonas reinhardtii* and enhance growth. We developed an original experimental setup with the possibility to project spatially and temporally structured light fields on suspensions of *Chlamydomonas reinhardtii*. We performed experiments with a dynamic

inhomogeneous light field used to trigger bioconvection during a timescale comparable to the timescale of cell division. The effect of bioconvection was studied by measuring cell doubling time and by comparison with experiments in which a quasi homogeneous light intensity field was used. When the liquid height was increased, gas dissolution seemed to become a limiting factor and a smaller doubling time could be measured in the presence of bioconvection, but with large error bars in the determination. Additional experiments will be performed with deeper suspensions.

CHAPTER 7

Conclusion

7.1 Results

The main goal of this thesis was to understand the collective response of populations of the model photosynthetic microalgae *Chlamydomonas reinhardtii* to complex space and time dependent light fields. This collective response involves the coupling between the ability to swim in light intensity gradients - phototaxis - and self-generated macroscopic flows that originates from density gradients - bioconvective flows. We have both studied these phenomena separately and the result of their coupling.

In a first step, the phototactic response of *Chlamydomonas reinhardtii* has been characterized in dilute suspensions under heterogeneous light fields. In these experiments, we spatially controlled stationary light intensity gradients and studied equilibrium cell concentration profiles resulting from the balance between cell diffusion and a phototactic drift. We proposed a constitutive law where the drift is proportional to the light intensity gradient and measured the corresponding phototactic susceptibility as a function of the spatially swept light intensity. On one hand, our macroscopic approach did not model the mechanisms by which individual cells swims in a light intensity gradient. On the other hand, it offered a quantitative description of phototaxis at the population scale, validated by the robustness to a wide range of light intensity and light intensity gradients. We not only have recovered the general trend that phototaxis is positive at low intensity and negative at strong light intensity, but we have also shown with a curve of the phototactic susceptibility that the phototactic response is highly sensitive and nonlinear.

At the heart of this thesis, we have exploited this nonlinear phototactic response to generate complex and self-sustained macroscopic bioconvective flows in moderately concentrated, yet shallow, suspensions of *Chlamydomonas reinhardtii* using spatially controlled light intensity gradients. These flows are driven by density gradients that originate from the light-induced local accumulation of the microalgae which are negatively buoyant. In the experiments, the heterogeneous light fields consisted of vertical light beams projected at the center of the suspensions of different widths. We have found that in these bioconvective flows, the cells self-organize in patterns which, observed from above, can be

classified as a function of two parameters: the beam width and the pseudo-Rayleigh number Ra which controls the magnitude of bioconvective flows. In particular, the cell concentration field undergoes remarkable instabilities with breakings of the initial axisymmetry when the beam width exceeds the suspension depth. Both of these instabilities which, we referred to as *dendrites* and *directional growth*, have been quantitatively described. We have also proposed an asymptotic model for light-controlled bioconvection which qualitatively reproduces some of the experimental observation and evidences that the cells self-organization results from a complex interplay between phototaxis, self-generated advection and viscous torques exerted by the flow. In this model, key elements were the cell repartition throughout the thickness of the suspension and both the structure and the magnitude of the flows, but these quantities could not be measured in the experiments. Still, this study demonstrates the richness of the nonlinear physics controlling the behavior of active fluids, and the possibility to control complex self-generated flows using light in suspensions of *Chlamydomonas reinhardtii*.

Next, we have developed an experimental setup based on the tracking of fluorescent particles to quantitatively study bioconvective flows. These flows were also induced by light in a vertical, two-dimensional confined geometry and have been measured for the first time, simultaneously with the acquisition of the cell concentration field. In these experiments, we have successfully seen the flow field and its effect of the cell repartition, both on the vertical and horizontal directions, qualitatively in agreement with what was expected for bioconvective flows induced by horizontal density gradients. We quantitatively characterized the structure and the magnitude of the flows and investigated their relationship with the cell concentration field. We have found that the magnitude of the flow scales with the liquid height. Its structure on the other hand is controlled by the whole geometry and is to some extent correlated to the structure of the concentration field. At the local scale, we have found a relationship between the local variations of the velocity field and of the cell concentration field. This study also highlighted some effects of increasing the cell concentration that are not captured by simple models of classical bioconvection.

Finally, a work in progress addresses practical applications of the collective long-time response of *Chlamydomonas reinhardtii* to complex space and time dependent light fields. We are interested in the following question: can we use light to enhance growth by inducing biomixing in suspensions? An experimental setup has been developed to provide a spatio-temporal control of complex light fields which does induce long sustained bioconvection, on a timescale comparable to that of cell division and a protocol has been developed to measure the effect of light-controlled bioconvection on growth.

7.2 Outlook

The first encouraging results on the study of the effect of light-controlled bioconvection on growth will direct the immediate future works. They suggest to repeat experiments with deeper cultures in order to possibly enhance the effect of bioconvective flows.

In our exploitation of the phototactic ability of *Chlamydomonas reinhardtii*, we have found two different behaviors. The long term phototaxis response is well described by a nonlinear susceptibility that depends on light intensity. At shorter timescale, a transient negative phototaxis escaped our full control. Factors that influence this transition could be investigated in a first step towards understanding this feature. On the individual scale, the subcellular mechanisms that steer cells in light intensity gradients are still unknown. At a much larger scale, constitutive laws of collective phototaxis in microbes, as the one we obtained for the phototactic susceptibility of *Chlamydomonas reinhardtii*, may help to understand environmental phenomena like algal bloom formation or the diel vertical migration of planktons.

Finally, our measurements of bioconvective flows in Hele-Shaw liquid chambers have evidenced non trivial effects of the geometry and of increasing the cell concentration. This could motivate to further study the effects of confinement or of increasing the volume fraction in suspension of *puller*-type microswimmers. In such studies, it should be of great help to be able to couple microscopic observations of cells with larger scales of observations.

CHAPITRE 8

Résumé détaillé en français

Conformément aux règles d'école doctorale Physique en Île-de-France et de l'Université de Paris, nous proposons un résumé détaillé de ces travaux de thèse en français.

Au croisement entre la matière active et la physique des fluides complexes, cette thèse vise à comprendre la réponse collective, à l'échelle d'une population, de la microalgue photosynthétique modèle *Chlamydomonas reinhardtii* en présence de champs lumineux complexes dépendant de l'espace et du temps.

8.1 Introduction

8.1.1 Suspensions actives

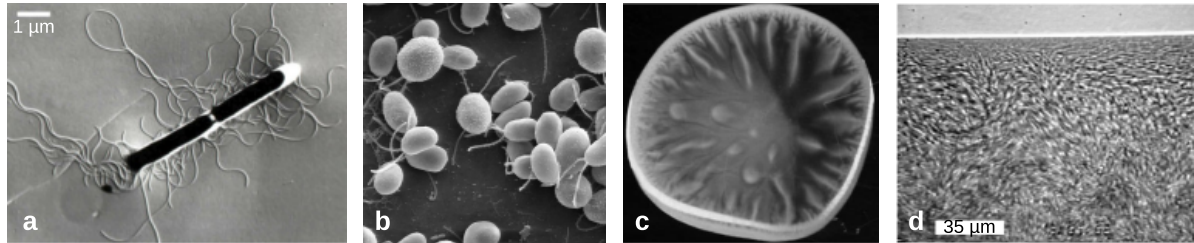


Figure 8.1 : Exemples de micronageurs et de phénomènes d'auto-organisation dans les suspensions actives. **a**, Bactérie *Bacillus subtilis* (CISNEROS 2008). **b**, Microalgues *Chlamydomonas reinhardtii* de diamètre 10 μm (Dartmouth College). **c,d**, Deux échelles d'organisation dans une goutte de 1 cm de *B.subtilis* (DOMBROWSKI et al. 2004). **c**, Plumes de bioconvection visibles dans toute la goutte. **d**, Mouvement collectif dans une zone très concentrée.

Les suspensions actives contiennent des micronageurs capables de s'auto-propulser en convertissant de l'énergie chimique en travail mécanique. Ces micronageurs peuvent être des bactéries ou des microalgues (fig. 8.1.a,b). Parmi les phénomènes observés, on peut citer que la diminution de la viscosité des suspensions par les bactéries (LÓPEZ et al. 2015) contre l'augmentation de la viscosité par les microalgues (RAFAÏ, JIBUTI et PEYLA 2010). Dans ce travail, on s'intéresse à l'auto-organisation dans ces suspensions. DOMBROWSKI et al. 2004 ont observé plusieurs échelles d'organisation dans des gouttes de bactéries. Ils ont observés de la bioconvection à l'échelle de la goutte (fig. 8.1.c). et des mouvements collectifs ont été observés à l'échelle mésoscopique (fig. 8.1.d).

8.1.2 Bioconvection

Alors que les mouvements collectifs ont pour origine des interactions entre nageurs, la bioconvection apparaît dans des suspensions relativement diluées. C'est une instabilité hydrodynamique qui a pour origine des gradients de concentration cellulaire qui peuvent être instables à cause de la gravité lorsque la densité des cellules diffère de celle du liquide.

En l'absence de stimulus, le mouvement des micronageurs peut être décrit par une marche aléatoire avec persistance et un processus de diffusion. Les gradients de concentration sont expliqués par des taxies qui biaisent les mouvements des micronageurs en réponse (active ou passive) à des stimuli extérieurs. On peut citer la chimiotaxie, la gravitaxie ou encore la phototaxie.

La bioconvection peut apparaître spontanément lorsque des micronageurs plus denses que l'eau nagent en moyenne vers le haut, par exemple par aérotaxie des bactéries ou par gravitaxie (à cause d'un couple gravitationnel) des microalgues. Des plumes séparées

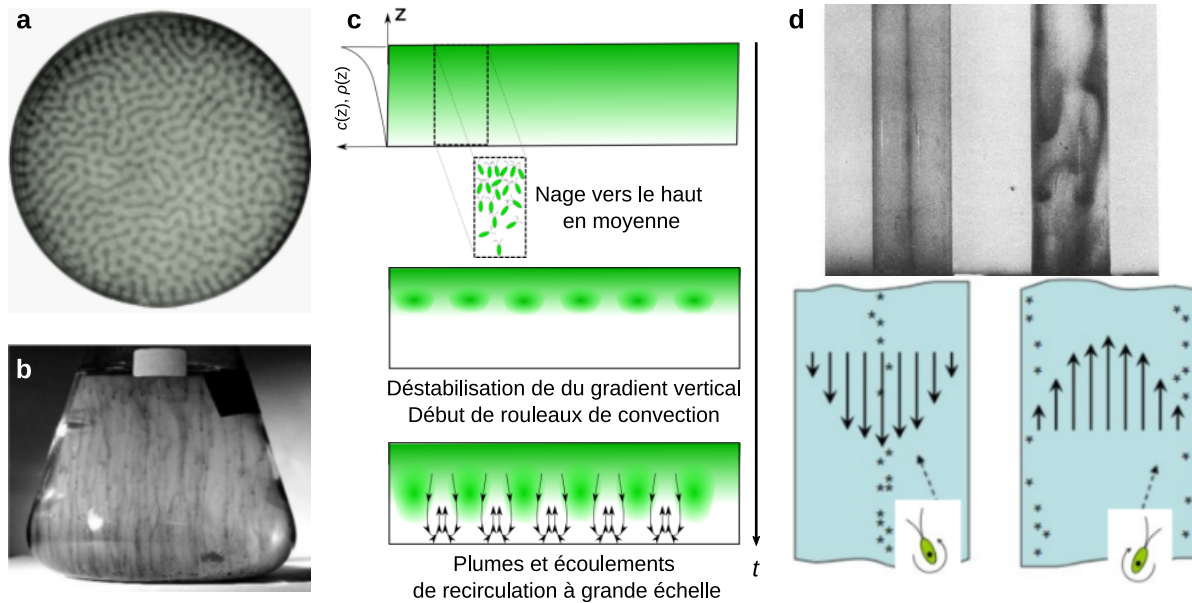


Figure 8.2 : Images et mécanismes de la bioconvection due à la nage vers le haut. **a**, Bioconvection dans une boîte de Pétri (BEES 1996). **b**, Bioconvection dans une fiole Erlenmeyer (WILLIAMS et BEES 2011a). **c**, Mécanisme de renversement. **d**, Focalisation gyrotactique (KESSLER 1985).

par des régions de faible concentration sont alors visibles dans toute la suspension (Figure 8.2.a,b). Deux mécanismes peuvent être impliqués. Dans le mécanisme de renversement, un gradient vertical de densité devient instable et la suspension s'organise dans des rouleaux de convection auto-entretenus (fig. 8.2.c). Dans le mécanisme de focalisation gyrotactique, les écoulements descendants sont renforcés par focalisation des organismes nageant vers le haut (fig. 8.2.c). Cela s'explique par une compétition entre la vorticit  de l' coulement et l'orientation privil gi e des microorganismes. Lorsqu'ils nagent dans le sens contraire de l' coulement, ils sont focalis s le long son axe. Cela a pu  tre montr  lorsque l'orientation privil gi e est donn e par la gravitaxie (KESSLER 1985), mais aussi par la phototaxie (GARCIA, RAFA  et PEYLA 2013) ou encore la magn totaxie (WAISBORD et al. 2016). Les efforts dans l' tude de la bioconvection se sont surtout concentr s sur la quantification des longueurs d'onde des champs de concentration (BEES et HILL 1997; WILLIAMS et BEES 2011a). Aucune quantification des  coulements n'a  t  rapport e. Un effet du m lange par les  coulements de bioconvection sur la croissance des microorganismes n'est pas non plus connu   ce jour.

Nombre de Rayleigh

Qualitativement, l' mergence des instabilit s de bioconvection est contr l e par un pseudo nombre de Rayleigh qui compare le temps caract ristique de diffusion   celui de convection par flottabilit  n gative. Il s' crit :

$$\text{Ra} = \frac{\tau_{\text{diff}}}{\tau_{\text{conv}}} = \frac{\rho_0 g \beta H^3 c_0}{D \eta} \quad \text{avec} \quad \beta = \frac{\rho_{\text{cell}} - \rho_0}{\rho_0} V_{\text{cell}} \quad (8.1)$$

H et c_0 sont la hauteur et la concentration en microorganismes de la suspension. Le coefficient de diffusion des micronageurs D et la viscosité de la suspension η sont supposés indépendants de la concentration.

Photo-bioconvection locale

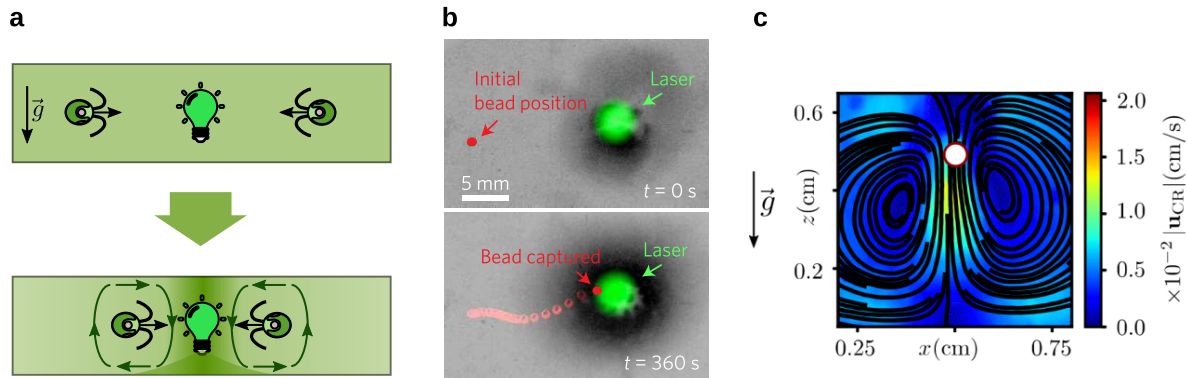


Figure 8.3 : Photo-bioconvection locale dans des suspensions de microalgues phototactique. **a**, Schéma de principe montrant la formation d'un gradient latéral de densité par accumulation autour de la lumière et les rouleaux de convection auto-entretenus. **b**, Vue de dessus du transport d'une bille de verre sur la surface libre d'une suspension de microalgues où la bioconvection est localisée autour d'un faisceau laser (DERVAUX, CAPELLAZZI RESTA et BRUNET 2017). **c**, Lignes de courant de recirculation des algues autour d'un faisceau laser (ARRIETA et al. 2019).

Récemment, DERVAUX, CAPELLAZZI RESTA et BRUNET 2017 et ARRIETA et al. 2019 ont contrôlé la bioconvection de façon locale en projetant un faisceau lumineux sur des suspensions de microalgues phototactiques (fig. 8.3). Cela ouvre la possibilité de contrôler la bioconvection par un contrôle spatial et temporel de champs lumineux inhomogènes. De façon intéressante, ces deux études ont aussi mis en évidence de façon qualitative les écoulements de bioconvection : soit par la manipulation hydrodynamique d'objet, soit par la recirculation des algues.

8.1.3 Le micronageur phototactique modèle *Chlamydomonas Reinhardtii*

Nous avons travaillé avec des suspensions de la microalgue photosynthétique *Chlamydomonas reinhardtii*, une espèce de *Chlamydomonas* schématisée fig. 8.4. Elle est avant tout très utilisée en sciences de la vie et est un candidat pour la production de biohydrogène et de biocarburants. C'est aussi un micronageur modèle utilisant ses deux flagelles pour nager à $100 \mu\text{m/s}$, de densité $\rho_{\text{CR}} = 1.05 \text{ g/cm}^3$. Le stigma répond en lumière verte et bleue pour la phototaxie mais ne répond pas en lumière rouge.

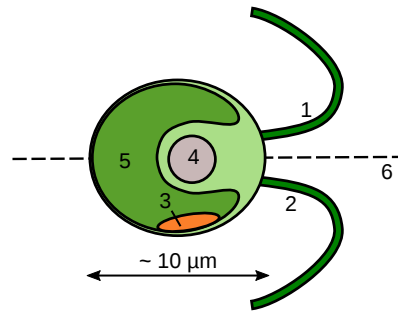


Figure 8.4 : Schéma de *Chlamydomonas*. Flagelles en position *trans* (1) et *cis* (2) par rapport au stigma (3) ou oeil rudimentaire. Noyau (4), chloroplaste pour la photosynthèse (5), axe postérieur-antérieur (6) ou axe principal.

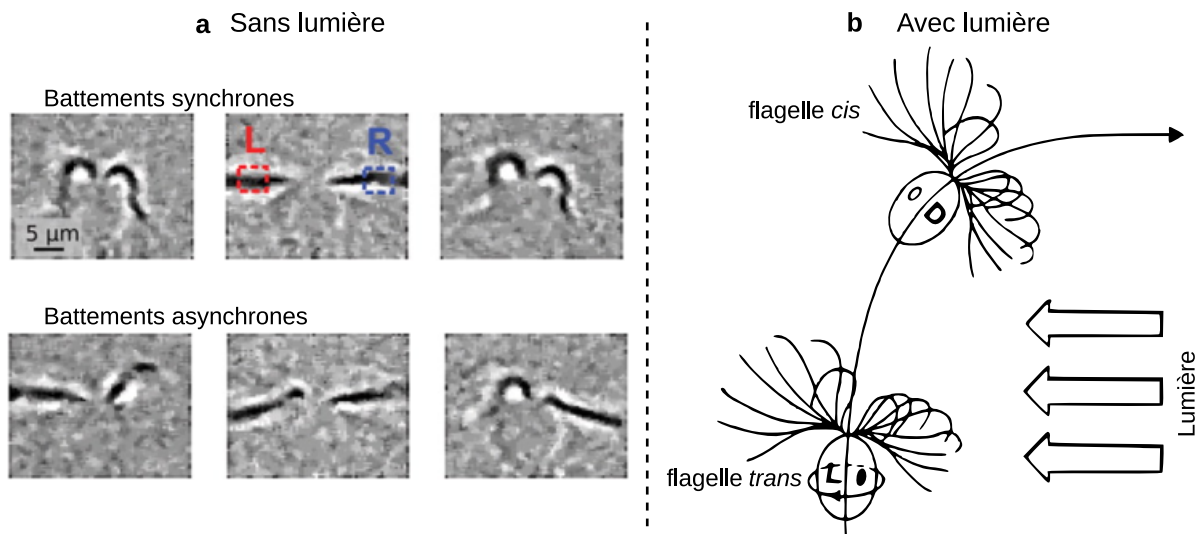


Figure 8.5 : Contrôle de la motilité de *Chlamydomonas* par ses flagelles. a, Battements synchrones et asynchrones contrôlant la marche aléatoire en l'absence de lumière (Par POLIN et al. 2009). b, Changement transitoire de l'équilibre des flagelles pour l'orientation vers la lumière : d'abord en faveur de la flagella *trans* lors de l'exposition du stigma puis en faveur de la flagelle *cis* lorsque le stigma est caché (Par RÜFFER et NULTSCH 1991).

La motilité de *Chlamydomonas* est contrôlée par ses deux flagelles comme illustré fig. 8.5. En l'absence de lumière, *Chlamydomonas* effectue une marche aléatoire avec persistance. Des longues périodes de battements synchrones correspondent à des portions de trajectoires quasiment rectilignes alors que de brèves périodes de battements asynchrones correspondent à des grands virages (fig. 8.5.a, POLIN et al. 2009). Durant sa trajectoire, *Chlamydomonas* tourne en fait autour de son axe principal et le stigma scanne le champ lumineux. La modulation du signal lumineux sur le stigma lorsqu'une lumière se trouve sur le côté déclenche une réorientation vers la lumière ou loin de celle-ci par un changement de l'équilibre des flagelles (fig. 8.5.b pour le cas vers la lumière, RÜFFER et NULTSCH 1991). Il reste encore à quantifier le lien entre une vitesse de dérive phototactique et l'intensité lumineuse.

8.1.4 Plan de la thèse

Le but principal de cette thèse est de comprendre la réponse collective, à l'échelle d'une population, de la microalgue photosynthétique et phototactique *Chlamydomonas reinhardtii* à des champs lumineux complexes dépendants du temps et de l'espace. Ce but se divise en les objectifs suivants :

1. Proposer une loi phénoménologique de la vitesse de dérive phototactique pour une population de *Chlamydomonas reinhardtii* dans des gradients d'intensité lumineuse en fonction de l'intensité lumineuse.
2. Étudier l'auto-organisation des cellules dans des écoulements de photo-bioconvection locale avec un contrôle du champ lumineux inhomogène et du pseudo nombre de Rayleigh.
3. Quantifier l'amplitude et la structure des écoulements de bioconvection, étudier leur relation avec le champ de concentration et les comparer avec un modèle classique de bioconvection.
4. Étudier un possible effet de la photo-bioconvection maintenue dans le temps sur le taux de croissances de cultures d'algues, avec un tête une application pour les photo-bioréacteurs.

8.2 Susceptibilité phototactique de *Chlamydomonas* dans les gradients d'intensité lumineuse

Dans un premier temps, nous avons caractérisé la réponse phototactique de *Chlamydomonas reinhardtii* dans des gradients d'intensité lumineuse à l'échelle d'une population.

8.2.1 Dispositif expérimental

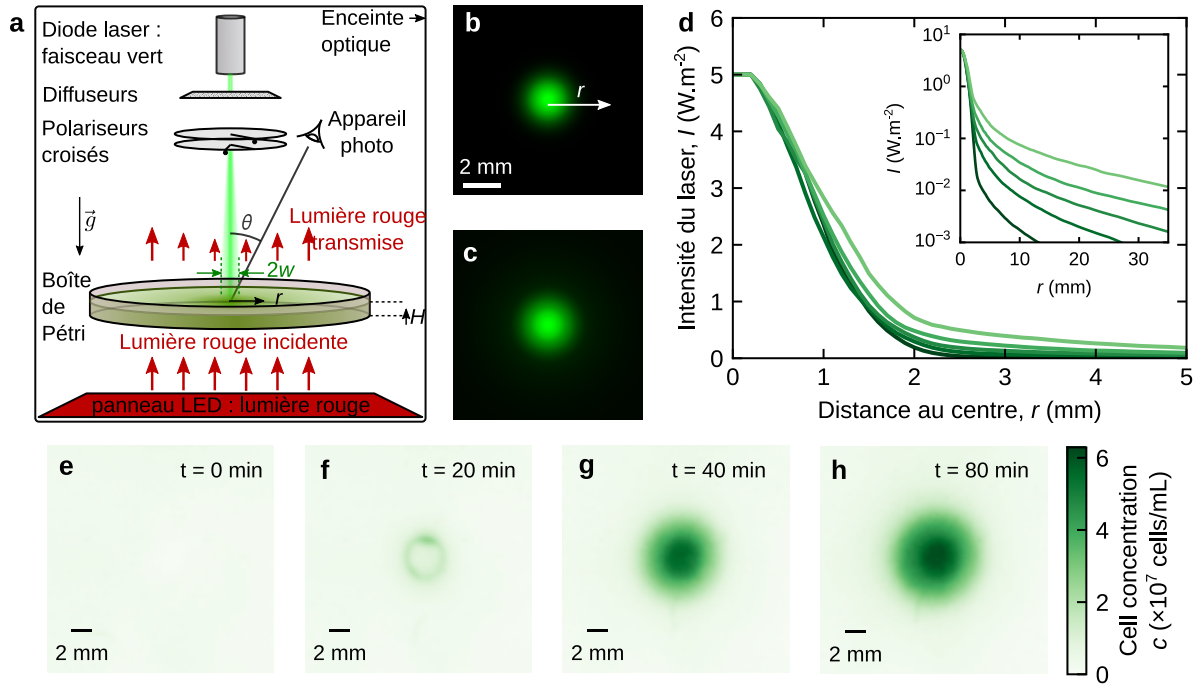


Figure 8.6 : Dispositif expérimental pour étudier l'interaction entre la lumière et les algues. **a**, On étudie la réponse des algues à des faisceau lumineux vert à symétrie radiale projetés au centre de la suspension. Leur étalement et leur intensité sont respectivement contrôlés par des diffuseurs et des polariseurs croisés. Le champ de concentration est imagé en vue de dessus par transmission de la lumière rouge. **b,c**, Deux images du laser correspondant aux profils d'intensité lumineuse le plus fin (**b**) et le plus large (**c**) en (**d**). **d**, Profils d'intensité lumineuse lorsque le maximum est fixé à $5 \text{ W}/\text{m}^2$. **e-h**, Accumulation d'algues au centre du faisceau laser dans le temps.

La réponse phototactique à un gradient d'intensité lumineuse $\vec{\nabla}I$ se traduit par un terme de flux $c\vec{v}_{\text{drift}}$. Ce flux définit une susceptibilité phototactique χ selon $\vec{v}_{\text{drift}} = \chi(I)\vec{\nabla}(I)$. Nous l'avons mesurée avec le dispositif décrit fig. 8.6

8.2.2 Mesure de la susceptibilité phototactique

Nous avons utilisé approche de type Keller-Segel (fig. 8.7). L'évolution de χ sur 7 décades de I montre que réponse phototactique de *Chlamydomonas reinhardtii* est hautement sensible et non-linéaire. La valeur du seuil de détection ($I_{\text{thresh}} \sim 10^{-3} \text{ W}/\text{m}^2$) est en accord avec des valeurs précédemment rapportées dans la littérature (FEINLEIB et CURRY

1971 ; FOSTER et al. 1984 ; HEGEMANN, HEGEMANN et FOSTER 1988) et correspondant à une valeur remarquablement symbolique de 1 photon absorbé/cell/s. La valeur de de seuil d'inversion ($I_{\text{crit}} \sim 10^2 \text{ W/m}^2$) vers la phototaxie négative suggère que toute la gamme des états d'isomérisation des photorécepteurs est utilisée dans la gamme de phototaxie positive, ce qui laisse ouverte la question du mécanisme de la phototaxie négative.

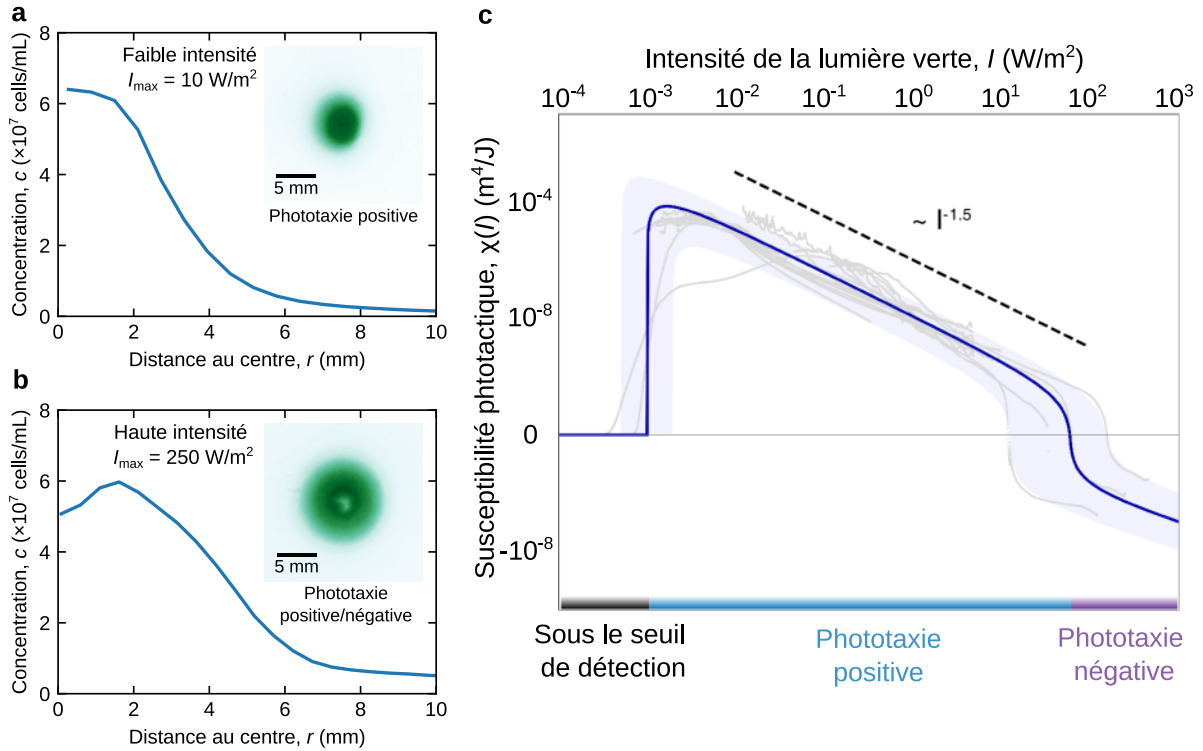


Figure 8.7 : Mesure de la susceptibilité phototactique à partir de profils de concentration à l'équilibre. Le pseudo nombre de Rayleigh est assez faible pour négliger la convection. Les profils radiaux de concentration stationnaires sont le résultat de l'équilibre entre la diffusion et la phototaxie. **a**, Profil de concentration avec seulement de la phototaxie positive à faible $I_{\text{max}} = I(r=0)$. **b**, Profil de concentration avec de la phototaxie positive/ négative à grand I_{max} . **c**, Évolution de la susceptibilité phototactique en fonction de l'intensité lumineuse. Courbes en gris clair : courbes paramétriques $\{I(r), \chi(r)\}$ obtenues avec la formule $\chi(r) = (D \frac{\partial c}{\partial r}) / (c \frac{\partial I}{\partial r})$ et en changeant le profil $I(r)$ d'une expérience à l'autre. Courbe bleue : courbe maîtresse.

8.3 Formation de motifs avec la photo-bioconvection locale

Avec le même dispositif expérimental, nous avons ensuite exploité la phototaxie pour générer des écoulements de bioconvection locale. Nous avons étudié l'auto-organisation des cellules dans ces écoulements.

8.3.1 Paramètres de contrôle

Nous avons contrôlé l'étalement du faisceau lumineux (largeur w) en fixant $I_{\text{max}} = 5 \text{ W/m}^2$ (voir profils fig. 8.6.d). Étant donnée la grande sensibilité de $\chi(I)$, w a été défini

avec les queues de distribution, soit $w \in [2.7, 20]$ mm. Nous avons contrôlé le pseudo nombre de Rayleigh Ra avec la concentration initiale $c_0 \in [1.5, 3.0] \times 10^6$ cells/mL et la hauteur de liquide $H \in [1, 5]$ mm, soit $Ra \in [10, 1000]$.

8.3.2 Diagramme de phase et propriétés globales des motifs de concentration

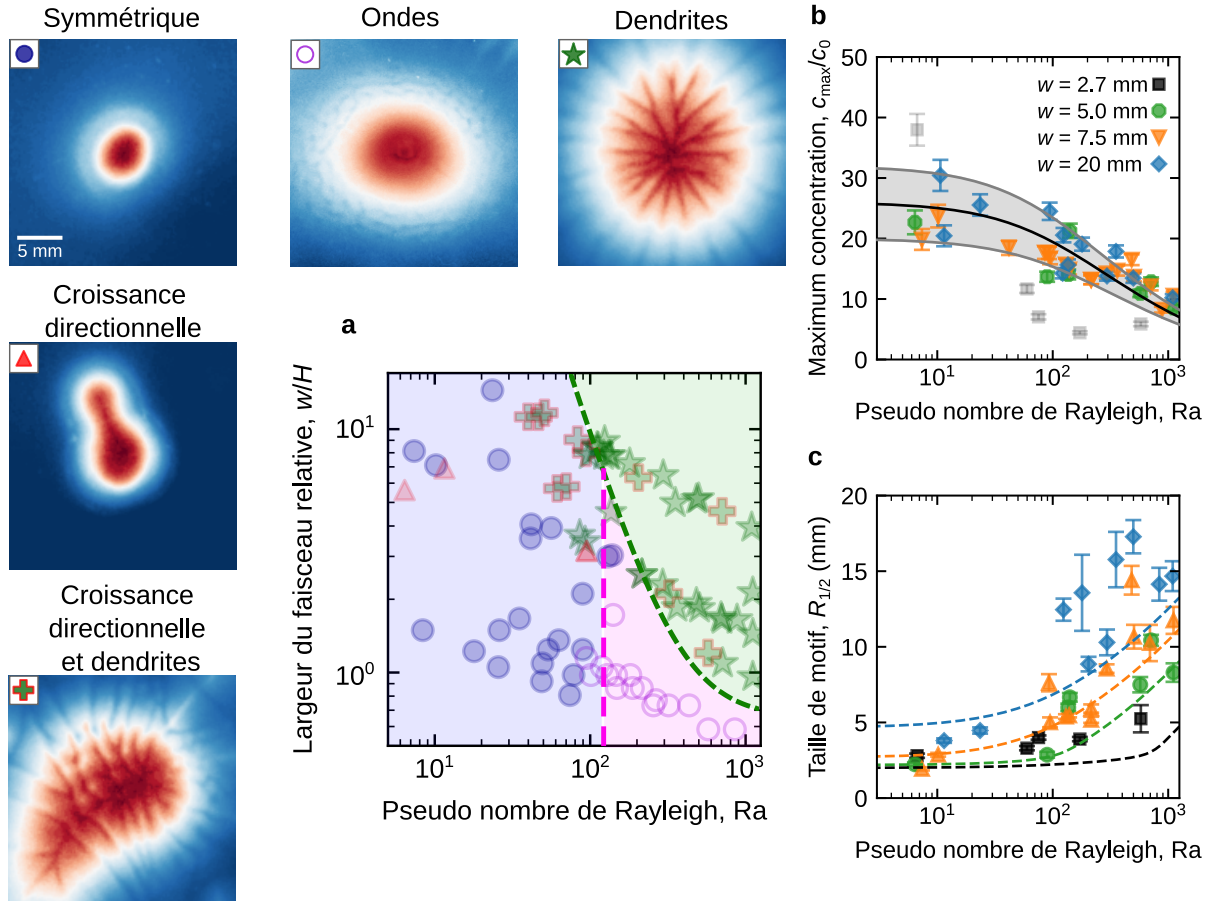


Figure 8.8 : Effet du nombre de Rayleigh Ra et de la largeur de faisceau w sur la formation de motifs de concentration. a, Diagramme de phase montrant : des structures symétriques stationnaires à faible Ra , des ondes de propagations se propageant du centre vers la périphérie à grand Ra et petit w/H , des structures en dendrites stationnaires à grands Ra et w/H , de la croissance directionnelle instationnaire à partir de motifs initialement symétrique ou en dendrites à grand w/H . b-c, Deux propriétés globales des motifs en fonction de Ra pour différents w : maximum de concentration normalisé (b) et taille de motif (c). c_{max}/c_0 et $R_{1/2}$ sont définies pour des motifs dont l'extension radiale est fixe et à partir de profils de concentration moyennés dans le temps et selon la direction angulaire. Un modèle asymptotique permet d'ajuster les frontières du diagramme de phase (a), une courbe maîtresse en (b) avec sa barre d'erreur (zone grise) et les lignes discontinues en (c).

Nous avons obtenu un diagramme des phase de la formation de motifs de concentration dans les écoulements de photo-bioconvection locale en fonction de Ra et de w/H (fig. 8.8.a). À faible w/H , DERVAUX, CAPELLAZZI RESTA et BRUNET 2017 avaient montré

qu'une structure stationnaire et symétrique se déstabilise pour émettre des ondes pour $Ra > 100$. Ici, nous avons montré que lorsque w dépasse H , le champ de concentration se déstabilise en de remarquables brisures de l'axisymétrie initiale (*croissance directionnelle* et *dendrites*). Nous avons aussi montré l'effet de Ra et de w sur deux propriétés globales des motifs : le maximum de concentration et la taille de motif (fig .8.8.b et c). La diminution de c_{\max}/c_0 et l'augmentation de $R_{1/2}$ avec Ra traduisent que la convection tend à étaler le champ de concentration avec un écoulement dirigé du centre vers la périphérie dans la partie inférieure de la suspension. La forte augmentation de $R_{1/2}$ avec w (pour $Ra > 100$) traduit la grande sensibilité de $\chi(I)$ aux queues de distribution des faisceaux lumineux.

8.3.3 Caractérisation des instabilités en dendrites et de croissance directionnelle

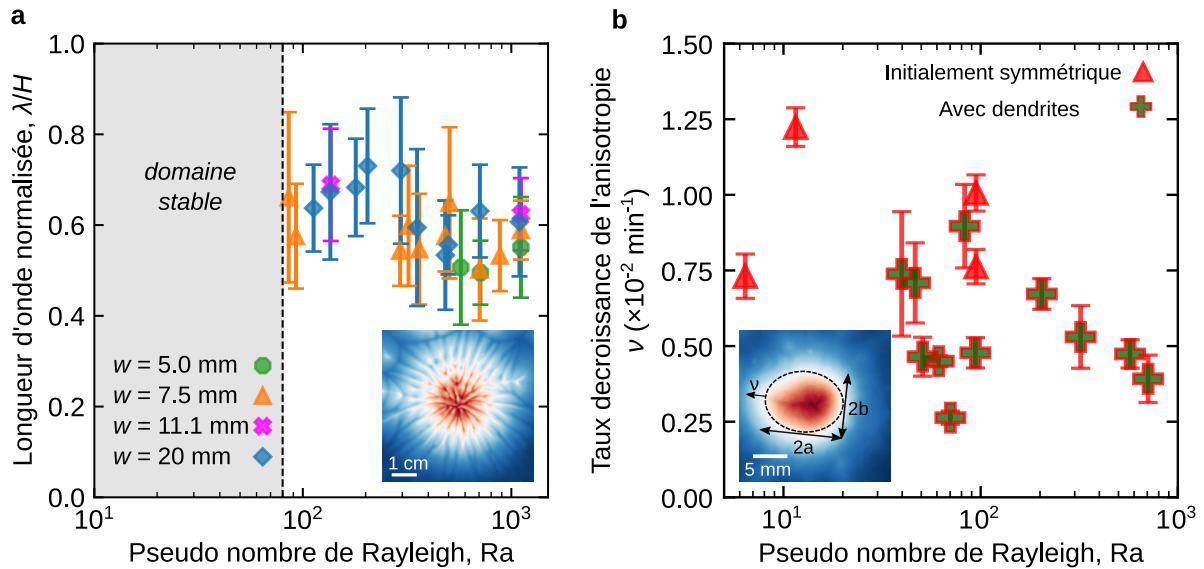


Figure 8.9 : Caractérisation des instabilités en dendrites et de croissance directionnelle. a, Longueur d'onde orthoradiale normalisée λ/H en fonction de Ra . b, Vitesse de croissance de l'anisotropie $\nu = \frac{d(a/b)}{dt}$ en fonction de Ra .

Nous avons caractérisé de façon quantitative les instabilités à grand w/H . Nous avons mesuré la longueur d'onde orthoradiale λ des structures en *dendrites* et montré qu'elle est pilotée H (fig. 8.9.a). Nous avons mesuré la vitesse de croissance de l'anisotropie ν (fig. 8.9.b) et montré qu'elle reflète la grande sensibilité du système à toute légère asymétrie - en particulier un léger défaut d'inclinaison $< 0.1^\circ$ - lorsque la largeur du faisceau est augmentée.

8.3.4 Modèle asymptotique pour la photo-bioconvection en couche mince

Nous avons alors proposé un modèle asymptotique de la photo-bioconvection locale en couche mince pour rendre compte de ces observations. Le champ de concentration

peut être décrit par une équation de diffusion-drift (adimensionnée et moyennée dans l'épaisseur) avec une matrice de diffusion effective anisotrope non linéaire \mathbf{D} et un flux phototactique $\bar{c}\mathcal{T}_{\parallel}\vec{e}_r$ ($\mathcal{T}_{\parallel} = \chi\frac{H}{D}\frac{\partial I}{\partial r}$).

$$\frac{\partial \bar{c}}{\partial t} = \vec{\nabla} \cdot (\mathbf{D}\vec{\nabla}\bar{c} - \bar{c}\mathcal{T}_{\parallel}\vec{e}_r) \quad (8.2)$$

Avec :

$$\mathbf{D} = \underbrace{\begin{pmatrix} 1 & 0 \\ 0 & 1 \end{pmatrix}}_{\text{diffusion linéaire}} + \underbrace{\begin{pmatrix} \alpha_0 \text{Ra} \cdot \bar{c} & 0 \\ 0 & \alpha_0 \text{Ra} \cdot \bar{c} \end{pmatrix}}_{\text{advection}} + \underbrace{\begin{pmatrix} 0 & 0 \\ 0 & -\gamma_0 \text{G}_y \text{Ra} \cdot \bar{c} \end{pmatrix}}_{\text{gyrotaxis}} \quad (8.3)$$

Cette écriture montre que les instabilités sont contrôlées par un coefficient convectif α_0 et un coefficient gyrotactique γ_0 (G_y est un nombre gyrotactique) et sont des instabilités à grand $\text{Ra} \cdot \bar{c}$. Ce modèle reproduit qualitativement l'apparition de *dendrites* comme un couplage complexe entre la phototaxie, l'advection auto-générée et l'action de la gyrotaxie sur la dérive verticale. En ajustant un paramètre dont dépendent α_0 et γ_0 , ce modèle donne aussi des prédictions en accord avec les résultats expérimentaux (voir fig .8.8).

8.4 Quantification des écoulements de bioconvection induits par la lumière

8.4.1 Dispositif expérimental

Ensuite, une méthode de vélocimétrie par images de particules basée sur la fluorescence a été développée pour permettre la quantification directe des écoulements de bioconvection dans une cellule de Hele-Shaw, comme cela est montré fig. 8.10.

Nous avons au passage montré que la réponse phototactique dépend en réalité du temps avec une phototaxie négative pendant ~ 10 min avant un passage en phototaxie positive. Nous avons effectué les mesures de vitesses et de champ de concentration dans l'état pseudo-stationnaire avant le passage en phototaxie positive (fig. 8.10.c). Le champ de vitesse est alors constitué de deux rouleaux principaux des deux côtés de la cellule de Hele-Shaw avec un écoulement descendant sur les côtés. Les motifs de concentration sont localisés sur les côtés et sont étalés par la convection dans la partie inférieure de la suspension.

8.4.2 Amplitude des écoulements

Nous avons quantifié l'amplitude des écoulements en mesurant la vitesse de descente sur les côtés v_{sink} en fonction de H et de c_0 . Cette vitesse augmente proportionnellement à H pour c_0 assez faible (fig. 8.11.a). Elle diminue de façon surprenante avec c_0 (fig. 8.11.b). Cet effet surprenant de c_0 pourrait venir d'une augmentation de la viscosité effective,

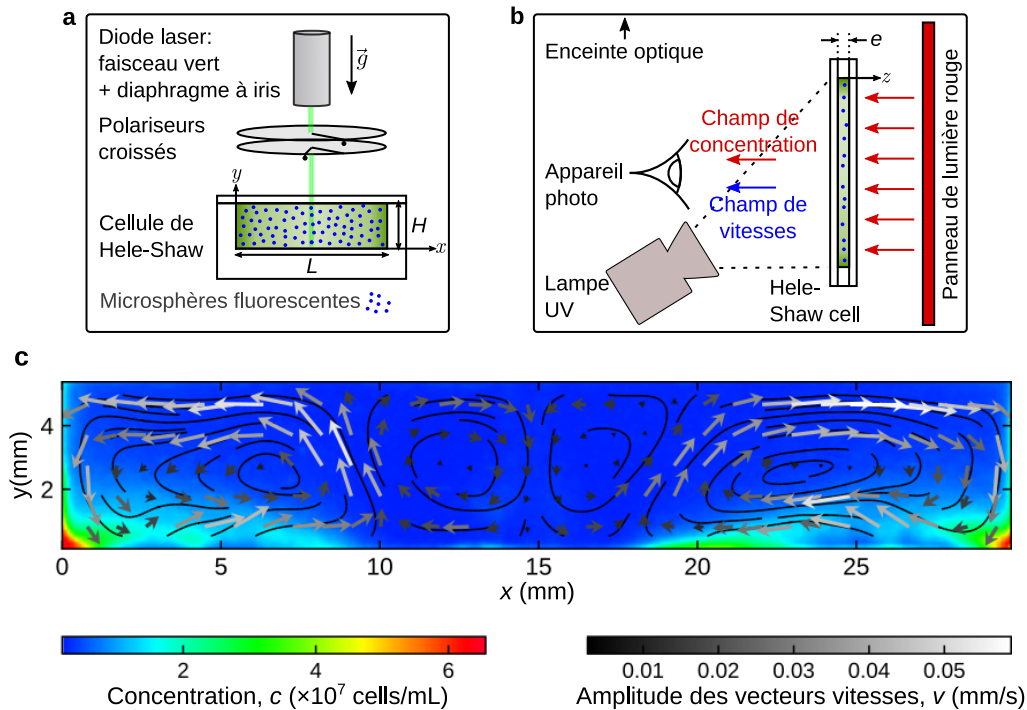


Figure 8.10 : Dispositif expérimental pour quantifier les écoulements de bioconvection induits par la lumière. a-b, Schémas en vue de face (a) et de dessus (b) du dispositif. Un faisceau lumineux vert de taille millimétrique est projeté pour induire une réponse phototactique et des écoulements de bioconvection dans une suspension contenue dans une cellule de Hele-Shaw de dimensions $(L, H, e = 2.1 \text{ mm})$. Le champ de concentration est imagé par transmission de la lumière rouge. Le champ des vitesses est acquis grâce à des traceurs passifs qui sont des microsphères fluorescentes excitées par des flashes UV dont l'intensité est maintenue aussi faible que possible et reste biocompatible. c, Superposition d'un champ de concentration et d'un champ de vitesse lorsque les algues répondent par phototaxie négative au faisceau lumineux et nagent vers les côtés de la cellule de Hele-Shaw.

d'effets de bords ou encore d'effets collectifs.

8.4.3 Relation entre les structures des champs de concentration et des vitesses

Nous avons ensuite comparé la structure des écoulements à celle du champ de concentration. Nous avons mesuré d'une part la longueur de rouleau de convection $L_{\text{roll},1/2}$ et d'autres part la longueur de motif de concentration L_{pattern} . Ces deux grandeurs normalisées sont représentées l'une en fonction de l'autre fig. 8.12.a. Le graphe montre que pour des motifs de concentration bien séparés avec $L_{\text{pattern}}/L < 0.25$ (exemple fig. 8.12.b), $L_{\text{roll},1/2}/L$ et L_{pattern}/L sont corrélés positivement. Cette région du graphe correspond à des faibles c_0 et H . Pour des motifs de concentration peu séparés avec $L_{\text{pattern}}/L > 0.25$ (exemple fig. 8.12.c,d), $L_{\text{roll},1/2}/L$ sature et la corrélation avec L_{pattern}/L est perdue. Cette région du graphe correspond à des grandes valeurs de c_0 ou de H .

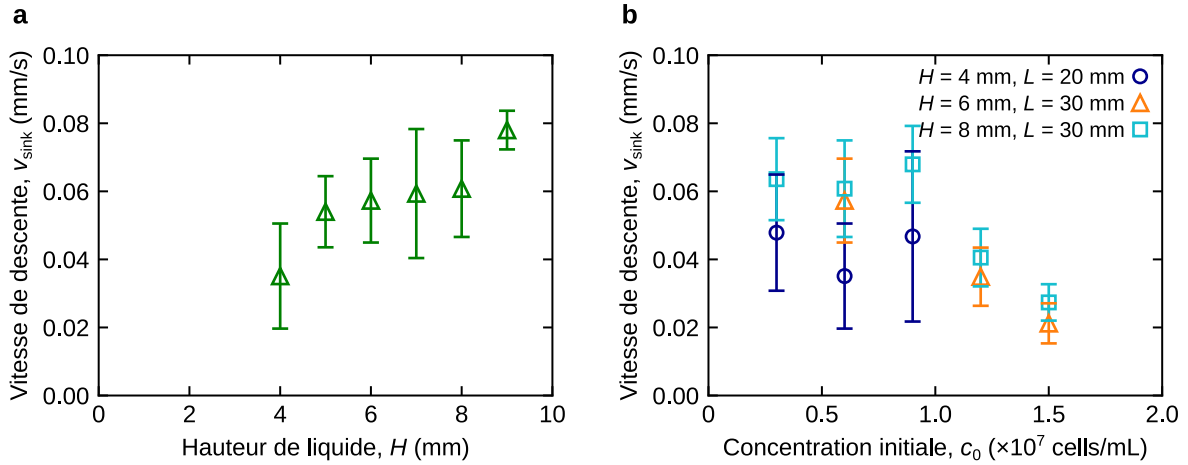


Figure 8.11 : Vitesse de descente des écoulements. a, En fonction de la hauteur de liquide à $c_0 = 6.0 \times 10^6$ cells/mL. b, En fonction de la concentration initiale pour différentes tailles de cellule de Hele-Shaw. Un point correspond à une moyenne sur 3 expériences et la barre d'erreur à correspond l'écart type.

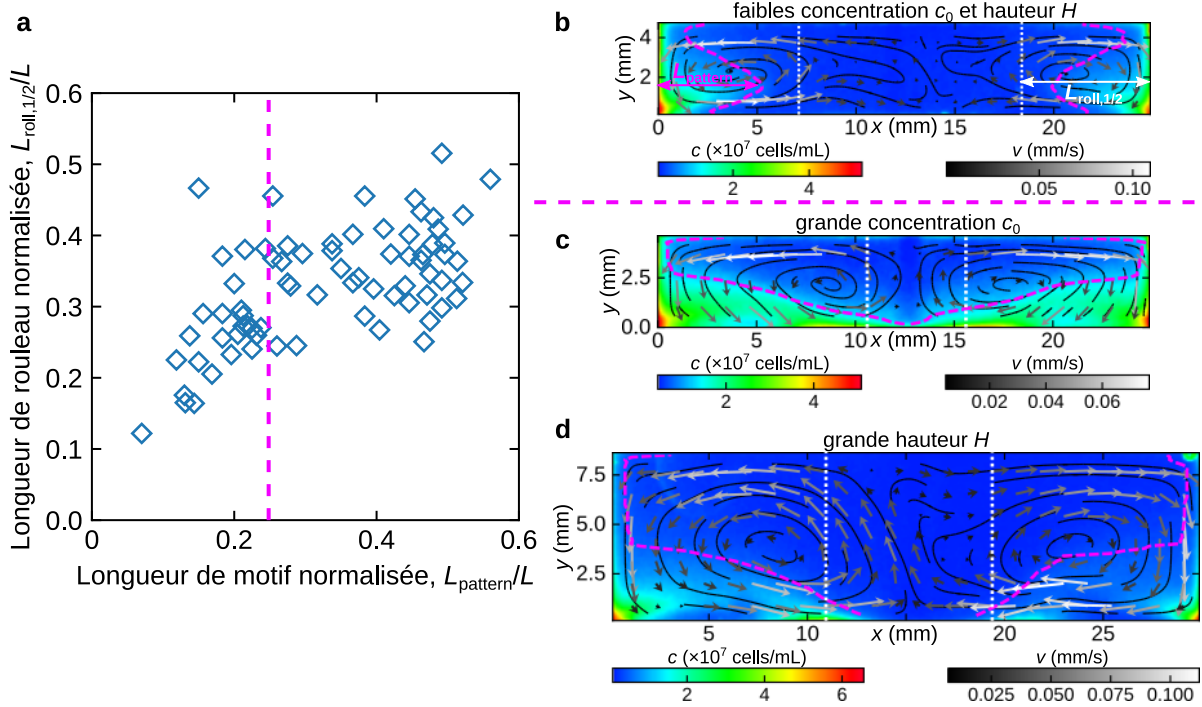


Figure 8.12 : Relation entre la structure des écoulements et celle du champ de concentration. a, Longueur de rouleau normalisée $L_{\text{roll},1/2}/L$ en fonction de la longueur de motif normalisée L_{pattern}/L . L_{pattern} est mesuré à partir des limites iso $c(x, y) = c_0$ des motifs (lignes discontinues en magenta b-d). $L_{\text{roll},1/2}$ est calculé à partir de la décroissance de vitesse horizontale avec la distance aux bords (matérialisé par des lignes en pointillé blanches b-d). Ligne verticale à $L_{\text{pattern}}/L = 0.25$ séparant le graphe en deux régions. b-d. Superposition de champs de concentration et des vitesses représentatifs des différents cas. b, Faibles c_0 et H , $L_{\text{pattern}}/L < 0.25$. c, Grand c_0 , $L_{\text{pattern}}/L > 0.25$. d, Grand H , $L_{\text{pattern}}/L > 0.25$.

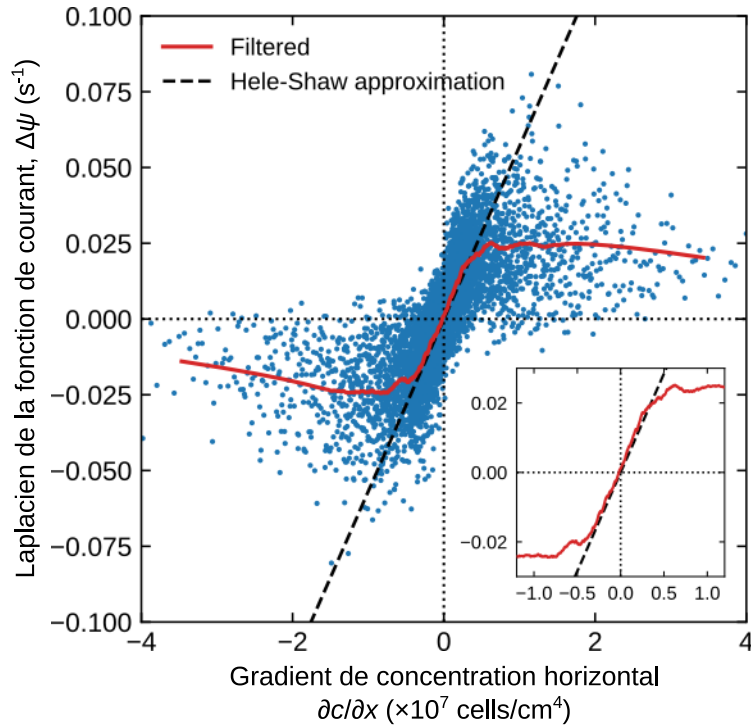


Figure 8.13 : Relation entre le laplacien de la fonction de courant et le gradient horizontal de concentration dans les expériences . Le nuage de points correspond aux différentes valeurs de $\Delta\psi$ et $\frac{\partial c}{\partial x}$ à différentes positions (x, y) dans les expériences. La courbe rouge est obtenue en filtrant le nuage de point. La droite en pointillé correspond à la prédiction théorique dans l'approximation de Hele-Shaw.

8.4.4 Analyse locale

Enfin, un modèle 2D dans l'approximation de Hele-Shaw prédit une relation entre les variations du champ de concentration et celles du champ des vitesses moyennés dans l'épaisseur e :

$$\Delta\psi = B_{\text{th}} \frac{\partial c}{\partial x} \quad \text{où} \quad B_{\text{th}} = \frac{\rho_0 \beta g e^2}{12\eta} \quad (8.4)$$

ψ est la fonction de courant définie par :

$$\bar{v}_x = -\frac{\partial\psi}{\partial y} \quad \text{and} \quad \bar{v}_y = \frac{\partial\psi}{\partial x} \quad (8.5)$$

Nous avons testé cette prédiction sur les données expérimentales (fig. 8.13). La proportionnalité entre $\frac{\partial c}{\partial x}$ et $\Delta\psi$ est vérifiée seulement à faible gradient de concentration. Une analyse de donnée supplémentaire a révélé que l'écart à la relation linéaire intervient à $|\frac{\partial c}{\partial x}|$ d'autant plus petit que c_0 augmente, ce qui est un nouvel effet surprenant de c_0 .

8.5 Mélange par la lumière, une perspective

Dans une dernière partie, une étude préliminaire est en cours sur les effets photo-bioconvection sur le taux de croissances de cultures, avec pour objectif à long terme une application aux photo-bioréacteurs. Le but des expériences est d'induire des écoulements de photo-bioconvection sur des durées comparables au temps de division cellulaire et de comparer des taux de croissance avec et sans bioconvection. Le dispositif utilisé est illustré fig. 8.14. Les résultats préliminaires sont encourageants quant à l'effet de la bioconvection sur le taux de croissance des suspensions.

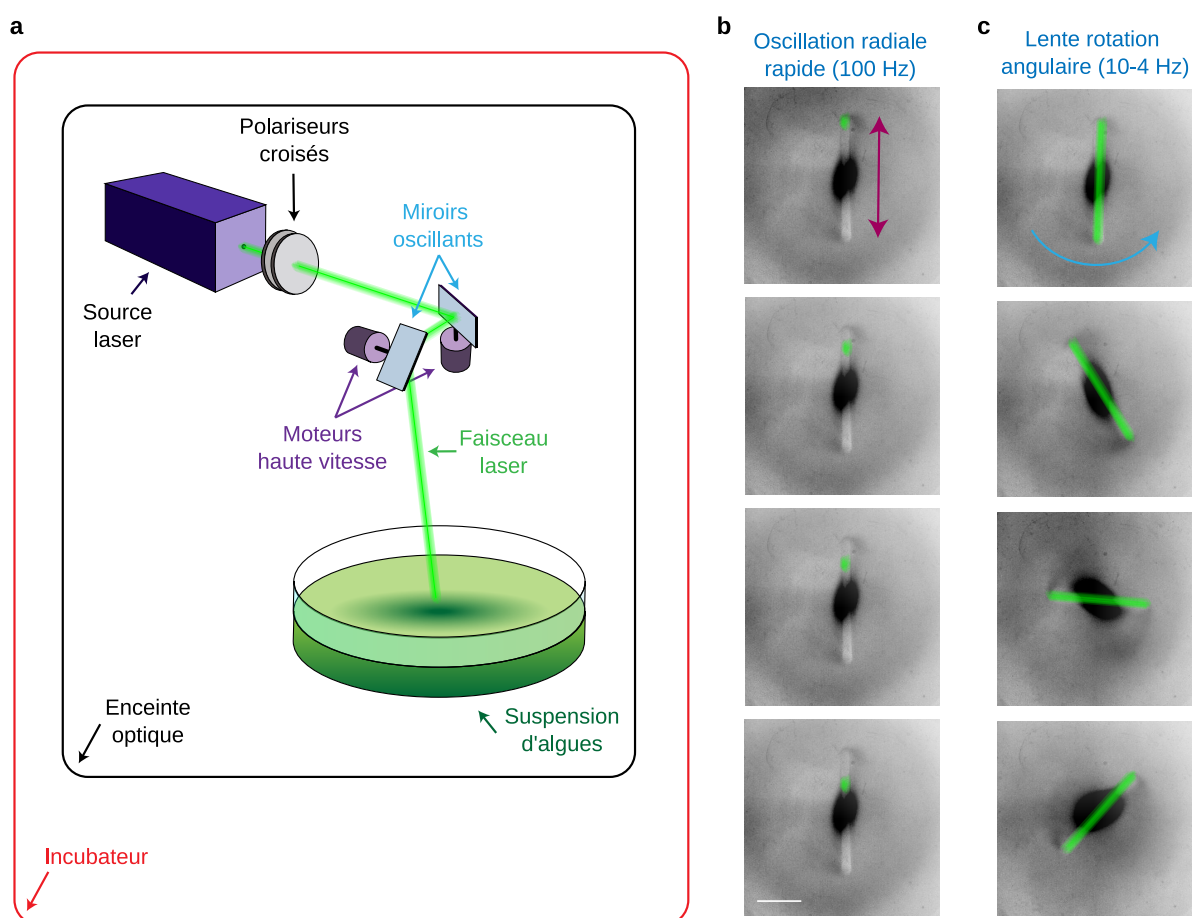


Figure 8.14 : Dispositif pour l'étude de l'effet de la photo-bioconvection sur le taux de croissance d'une suspension. **a**, Deux miroirs oscillants permettent un contrôle spatio-temporel d'un champ lumineux inhomogène projeté sur une suspension d'algue. **b-c**, Un motif lumineux en barre tournant est obtenu en combinant une oscillation radiale rapide et une lente oscillation angulaire. Il favorise des écoulements de bioconvection instationnaires par rapport à une illumination aléatoire avec le même nombre de photons à la même longueur d'onde.

APPENDIX A

Microalgae preparation

All experiments in this work were performed with the strain CC-124 of the unicellular green microalgae *Chlamydomonas reinhardtii*. In this section, I explain its culturing in laboratory and the suspensions preparation for the experiments. The methods can be used for other strains of *Chlamydomonas reinhardtii*.

A.1 Microalgae strain and culture medium

A.1.1 *Chlamydomonas reinhardtii* vegetative cells cultivation

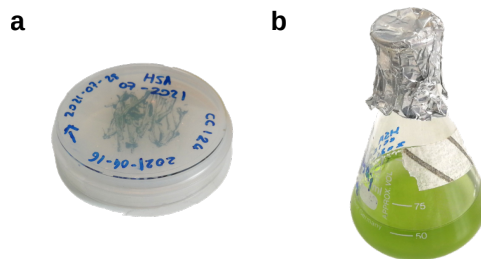


Figure A.1: Pictures of *Chlamydomonas reinhardtii* cultures. **a**, A solid culture in a Petri dish¹. **b**, A liquid culture in an Erlenmeyer flask.

We cultivated CC-124 vegetative cells provided by the Chlamydomonas Resource Center. Cells were either grown on gels made of liquid medium mixed with agar to give solid cultures or in liquid medium to give liquid cultures (see Figure A.1, and more details in A.2). We cultivated synchronized cultures with day/night cycles to synchronize phototaxis during the day and cells division during the night. We also cultivated unsynchronized cultures with continuous light exposition for cells that would be exposed to light during a long period in the experiments.

To avoid contamination, we worked under sterile conditions for cultivation. Both the culture media and the glassware were autoclaved. Microbiology manipulations were performed under a flame with Petri dishes, pipettes and inoculation loops all sterile. Petri

¹Petri dishes were kept upside down with the cells aggregate facing the ground to prevent condensation droplets to fall on the cells

dishes were sealed using parafilm and the top of the Erlenmeyer flasks were covered with autoclaved aluminium.

A.1.2 Culture medium

We use Sueoka's high salt medium with acetate (HSA) for both liquid and agar plates culture medium. The supplier provided both 4 stock solutions for the preparation of HSA solutions and the following formulation based on the stock solutions for 1L of water :

- 5 ml Beijerinck's solution
- 5 ml of phosphate solution
- 5 mL of sodium acetate solution
- 1 ml of Hutner trace elements

The composition of the stock solutions can be found at on the Chlamydomonas Resource Center website². The composition of the HSA medium can be determined from this formulation and is given in Table A.1.

Major components (mM)			
NH_4^+	9.4	Cl^-	9.7
Mg^{2+}	0.081	SO_4^{2-}	0.17
Ca^{2+}	0.14	K^+	21.8
HPO_4^{2-}	8.3	H_2PO_4^-	5.3
$\text{C}_2\text{H}_3\text{O}_2$	14.7	Na^+	14.7
Minor components (μM)			
EDTA	171	Zn^{2+}	76.5
BO_3^{3-}	184	Mn^{2+}	25.6
Co^{2+}	6.7	Cu^{2+}	6.3
HPO_4^{2-}	8.3	H_2PO_4^-	5.3
Mo^{6+}	6.2	Fe^{2+}	4.0

Table A.1: Composition of the HSA growth medium

For HSA agar plates, we added 15g of agar per liter of liquid solution. After the solution was autoclaved, the plates were prepared under an extractor hood. Petri dishes were filled (~ 4 mm) with the solution, still hot and liquid, and then covered. After at least 3 hours of gelification and cooling at room temperature, the Petri dishes were sealed.

Both HSA solutions and gels could be kept in the fridge, which slowed the development of contaminations. Before use, the agar plate or the desired volume of liquid HSA were thermalized at room temperature. Another possibility was to store HSA solutions and gels at room temperature. Contaminations could appear faster but were detected more easily.

²<http://www.chlamycollection.org/Sueoka.html>

A.2 Solid and liquid cultures preparation

Solid cultures were used to keep cells and perpetuate the strain on the long term. They were prepared by cells transfers from plates to plates. Small fractions of cells were taken from old solid cultures with inoculation loops and spread on fresh HSA agar plates.

Liquid cultures were prepared if needed for experiments with two possible methods :

- Solid-liquid transfer, where cells are grown by inoculating a small fraction of a solid culture in fresh liquid growth medium
- Liquid-liquid transfer, where cells are grown by introducing a small volume of a fully grown liquid culture in fresh liquid growth medium, with a typical dilution factor $\sim (2/50)$ (v/v).

A.2.1 Solid cultures

After inoculation, solid cultures were first grown in an incubator at 25°C with a 12h/12h day/night cycle with a white light at 2.5 kLux during the day cycle. Then, they were stored for longer preservation in a second incubator at 20°C with a 12h/12h day/cycle with a white light at 2 kLux during the day cycle. New solid cultures were prepared roughly monthly. However, in the case of contaminated cultures, a few months old healthy solid culture could still be used to transfer cells. Transfers were done more often until healthy growth was safe again. We restarted cultures from a new sample provided by the supplier every 1-2 years.

A.2.2 Synchronized liquid cultures

Synchronized liquid cultures were either prepared by solid-liquid or liquid-liquid transfers. Synchronized liquid cultures were grown in an incubator at 25°C with continuous agitation and a 12h/12h day/night cycle with white light at 2.5 kLux during the day cycle. We performed experiments with 3 days old liquid cultures, at the end of the exponential growth. Every one to two weeks, we restarted liquid cultures from solid cultures.

A.2.3 Unsynchronized liquid cultures

Unsynchronized liquid cultures were prepared by liquid-liquid transfer, with synchronized liquid cultures as mother solutions. They were placed in an incubator, at 20°C, and left unagitated. They were exposed to a continuous continuous white light of 3.5 kLux. They were grown between 60h to 72h before being used in the experiments.

A.3 Microalgae suspensions preparation for experiments

A.3.1 Suspensions cells concentration measurements

The cells concentration of a suspension was accessed using absorption spectroscopy with a 7310 Jenway spectrometer. We measured the optical density OD_{580} at 580 nm.

It quantifies the degree to which the light intensity is reduced by passing through the solution and is defined with the light intensity transmission coefficient : $OD = -\log_{10} T$. According to Beer Lambert's law, it has a linear relationship with the concentration for dilute suspensions with optical density values not greater than 1. Cell counting was previously performed with a Malassez cell on an inverted microscope and gave a cells concentration of $(3.0 \pm 0.6) \times 10^6$ cells/mL for an optical density $OD_{580} = 1$ and a path length of 1 cm. For a averaged cell diameter and volume of respectively 10 μm and 500 μm^3 , this is equivalent to a cells volume fraction of $\sim 1.5 \times 10^{-3}$. Higher cells concentrations were measured by diluting cultures samples to reach OD_{580} values smaller than 1. In the litterature, measured cells concentration are sometimes expressed in OD_{580} , with fixed values of conversion to cells/mL and to volumic fraction, which would be here 3×10^6 cells/mL and 1.5×10^{-3} respectively.

A.3.2 Suspensions of arbitrary cells concentration

Cells concentration of grown liquid cultures typically ranged from 1.5×10^6 to 3.0×10^6 cells/mL, or equivalently to OD_{580} from 0.5 to 1.0. Increasing the cell concentration of a suspension was obtained by centrifugation and removing the adequate volume of supernatant. To lower the cells concentration of a suspension, we diluted the culture with the supernatant obtained by centrifuging another aliquot of the same culture. Cultures were centrifuged at 3000 g for 3 min.

APPENDIX B

Pattern formation experiments : additional material and figures

B.1 Experimental procedure

Before each experiment of phototaxis-driven pattern formation, we first measured the cells concentrations of the suspension. For an experiment, the global cells concentration c_0 was either that of a grown liquid culture, for most of the time, or set to a specific value as described in A.3.2. Microalgae were then conditioned to seek dim light by keeping the suspension in the dark from 30 to 60 min before the laser is switched on.

In the mean time, the horizontality of the Petri dish was adjusted and controlled with a bubble level of precision 0.05° . It was then filled with HSA liquid medium to minimize cell adhesion to boundaries. Then, we shaped the green light beam to a known light intensity profile (see 2.2.2). We used a green laser diode from Thorlabs (CPS532, 532 nm, 4.5 mW). We modified the light intensity and the shape of the light beam profile with crossed polarizers and diffusers. We used overlays of grey photographic films as diffusers.

The Petri dish (inner diameter 139 mm) was then filled again with algal suspension to the desired liquid height and placed in the enclosure. We turned on the green light beam. To observe the pattern formation around the light beam from top view, we used a dim red light background below the Petri dish at 230 lux obtained with a white light LED pannel and a red filter (high pass with a cutoff at 610 nm). Images were recorded using a Nikon D700 digital camera equipped with a Zeiss objective. The intensity values on the red pixels of the images were converted to local cells concentration after calibration.

One experiment lasted 1 to 2 hours during which we measured that the evaporation was typically 1-2 mL, which represents 1-10% of the total volume ranging from 10 to 50 mL. The temperature was not precisely controlled and could rise inside the enclosure because of a slight heating of the LED pannel. The same sample of an algal suspension was not used more than twice. Images and data analysis were performed with Python.

B.2 Laser calibration

We calibrated the acquisition of laser light intensity profiles. We used pictures of light beams projected on a white paper screen placed on an empty Petri dish.

B.2.1 Green light intensity calibration

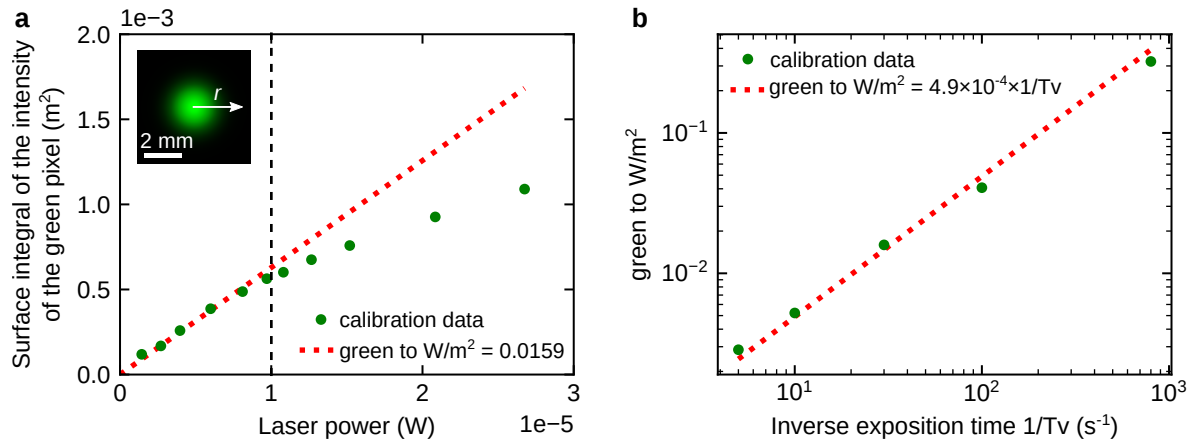


Figure B.1: Calibration of the laser intensity on the green channel. **a**, Evolution of the surface integral of the green pixel intensity with the laser power at fixed ISO (Lo-1) and exposition (1/30 s). At low enough laser power, the evolution is linear with a conversion from green pixel intensity to light intensity of $0.0159 \pm 0.0005 \text{ W/m}^2$. **b**, Conversion 8-bits green value to light intensity for different expositions at fixed ISO (Lo 1). The evolution is linear with the inverse exposition time with a slope $(4.9 \pm 0.4) \times 10^{-4} \text{ W s/m}^2$. Pixel intensity values range from 0 to 255.

For the light intensity calibration, we used pictures of laser beams at different powers with a fixed gaussian shape, as shown in Figure B.1. Green pixel intensity radial profiles were acquired on the green channel at fixed camera ISO. Surface integrals of those profiles $2\pi \int_0^\infty \text{green pix}(r) r dr$ were calculated and plotted against the laser power (Figure B.1.a). As green pixel intensities range from 0 to 255, surface integrals eventually saturate at high laser power. However, at low enough laser power, the relationship is linear and gives a conversion from green pixel intensity values to light intensities in W/m^2 . Then, we repeated this calibration at different camera exposures and fixed ISO. The green to W/m^2 conversion factor has a linear relationship with the inverse of the exposition time (Figure B.1.b). Thus conversion factors could be calculated at any camera exposure at this fixed ISO.

B.2.2 Green light intensity profiles acquisition

To measure radial light intensity profiles over several decades (see Figure 2.2), we used pictures of the laser beams at different camera exposures. At each exposure, a portion of green pixel intensity profile was converted to light intensity. Remembering that the

conversion to light intensities is linear for low green pixel intensities, we used the largest exposure for the tails and decreased it when moving to the center.

B.3 Top view cells concentration imaging calibration

We used the transmitted red light to access the depth averaged cells concentration field. The camera axis had an angle $\theta \sim 20^\circ$ with the vertical axis, which was corrected by a perspective transformation of the images. The conversion from pixel intensity values on the red channel to depth averaged cells concentration was done using homogeneous algal suspensions of different liquid heights and cells concentrations. The calibration curve is shown in Figure B.2.

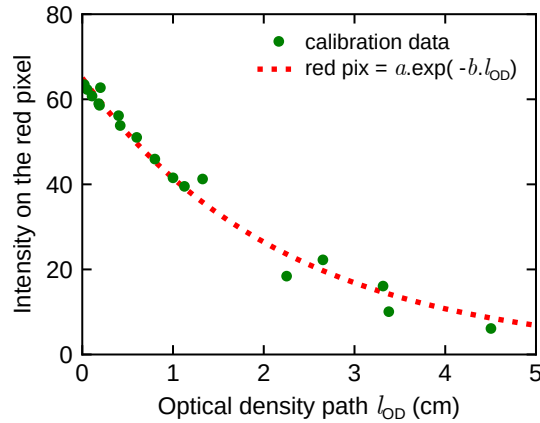


Figure B.2: Calibration curve of top view cells concentration imaging. The intensity on the red pixel is plotted against the optical density path $l_{OD} = H \times c_0/c_{ref}$ with c_0 the global cells concentration c_0 and $c_{ref} = 3 \times 10^6$ cells/mL. The calibration data are fitted with an exponential decay with an amplitude $a = 65 \pm 1$ and a decay constant $b = 0.45 \pm 0.02 \text{ cm}^{-1}$. Pixel intensity values range from 0 to 255.

According to Beer Lambert's law, we stated that the transmitted red light intensity should be constant at fixed product of the cells concentration with the liquid height. We measured the red pixel intensity for different values of the product $l_{OD} = H \times c_0$. For a given liquid height H , the local depth-averaged cells concentration $c(r, \theta)$ could then be calculated in OD_{580} by using the exponential fit in Figure B.2 :

$$c(r, \theta)/c_{ref} = \frac{1}{b.H} \ln\left(\frac{a}{\text{red pix}(r, \theta)}\right)$$

B.4 Additional figures

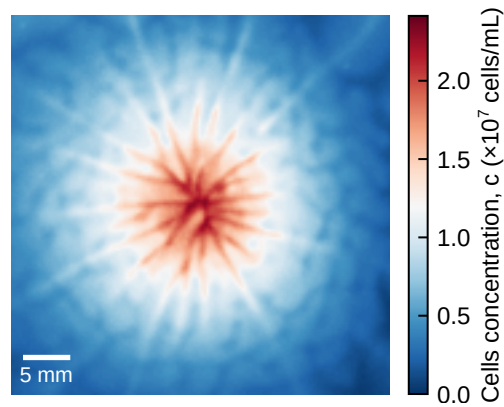


Figure B.3: Dendrites patterns superimposed with waves. Dendrites with well defined splits in branches, a stationary radial extension and superimposed with propagating waves of concentration. $Ra = 710$ ($H = 0.46$ mm, $c_0 = 2.3 \times 10^6$ cells/mL) and $w = 5.0$ mm.

APPENDIX C

Experiments in Hele-Shaw geometry: additional material and figures

C.1 Front view cells concentration imaging calibration

The conversion from pixel intensity values on the red channel to thickness averaged cells concentration was done using homogeneous algal suspensions of concentrations. The calibration curve is shown in Figure C.1. The local cells concentration $c(x, y)$ could then be calculated by using the exponential fit in Figure C.1 :

$$c(x, y)/c_{\text{ref}} = \frac{1}{b} \ln\left(\frac{a_0}{\text{red pix}(x, y) - a_1}\right)$$

The resolution of cell concentration fields was such that $c(x, y) = 3 \times 10^6$ cells/mL corresponds to 30 cells/px.

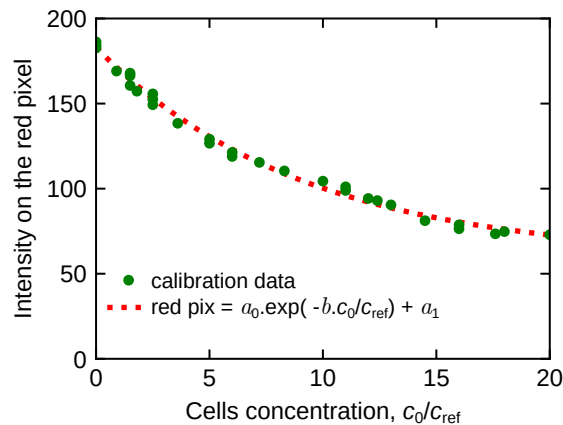


Figure C.1: Calibration curve of side view cells concentration imaging. The intensity on the red pixel is plotted against the cells concentration c_0/c_{ref} , where $c_{\text{ref}} = 3 \times 6$ cells/mL. The calibration data are fitted with an exponential decay with an amplitude $a_0 = 124 \pm 1$, a decay constant $b = 0.110 \pm 0.007$ and an offset $a_1 = 59 \pm 3$. Pixel intensity values range from 0 to 255.

C.2 Tests on the time dependency of the phototactic response

We tested the reproducibility of the time dependence of phototaxis described in section 5.1.2 with repeated exposition to the green light beam. After cells accumulated around the laser beam, we quickly rehomogenized the sample. Then, cells again showed a transient negative phototaxis followed by positive phototaxis.

Then, we tested different green light intensities and cells conditioning prior to the experiments. In all cases, negative phototaxis was observed in the first minutes of the experiments (sometimes mixed with positive phototaxis), and followed by accumulation around the light beam. It should be noted that the switch from negative to positive phototaxis was not due to the value of the maximum light intensity I_{\max} . Positive phototaxis towards the light beam could be observed even when the maximum light intensity at the center exceeded the critical inversion intensity $I_{\max} > I_{\text{crit}}$ because the light beam width was kept fairly small. We tested different I_{\max} . When decreasing the light intensity, phototaxis was still negative in the first minutes. However, we found that cells concentration gradients generally appeared slower and were less pronounced with lower light intensities. We also tested the effect of cells conditioning prior to the experiments. When cells were kept in white light during 30 to 60 min before the experiments, only negative phototaxis was observed during the first minutes. When they were kept in the dark before the experiments, they showed both negative and phototaxis during the first minutes, resulting in a mixed concentration pattern similar to that of Figure 5.4.c.

C.3 Experiments on UV flashes and their biocompatibility in *Chlamydomonas reinhardtii*

In the experiments, we used 500 ms UV flashes at $\sim 10 \text{ W/m}^2$ every 2 s. We investigated the effect of such UV flashes on cells. More precisely, we compared the interaction between algae and light in the absence and in the presence of UV flashes. In Figure C.2.a, y -averaged concentrations profiles at different times after the green light beam was turned on correspond to the images in Figure 5.4 that show the time dependency of the phototactic response. The negative phototactic response is evidenced by lateral concentration gradients pointing to the side in the first minutes. The sign of the gradients is reversed with the sign of phototaxis. In Figure C.2.b, cells of the same suspension were exposed to periodic UV flashes during the acquisition of the concentration fields (the total acquisition 20 min corresponds to 600 flashes). The same negative phototactic response is observed during the first minutes and is not disturbed by UV flashes. However, this is not followed by a turn to positive phototaxis. We concluded that UV flashes at least disturb *Chlamydomonas reinhardtii* phototaxis, if not more, on timescale of minutes, but can safely be

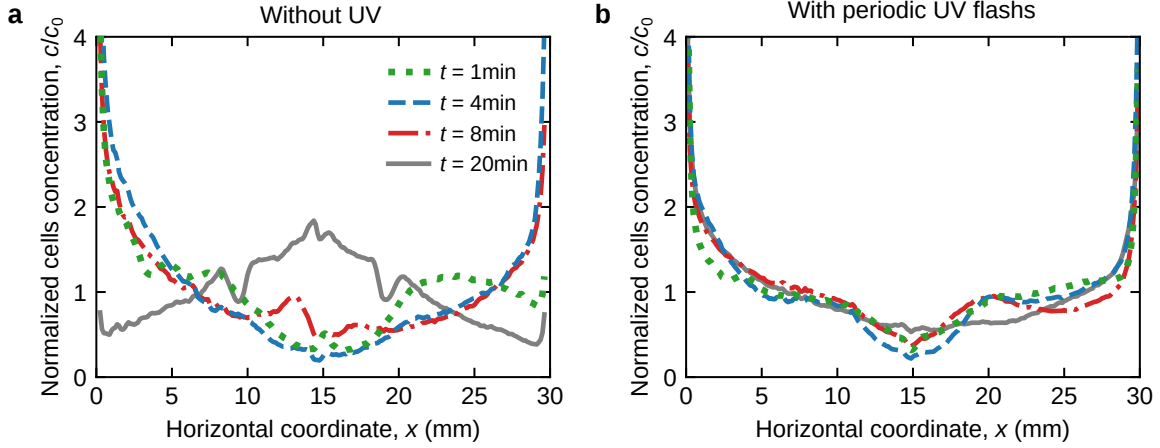


Figure C.2: Effect of the UV on the interaction between algae and light Normalized depth averaged cells concentration profiles at different times. **a,b**, At $t = 0$, the green light beam is turned on with $I_{\max} = 125 \text{ W/m}^2$. The global cells concentration is $c_0 = 6 \times 10^6 \text{ cells/mL}$, the liquid height is $H = 7 \text{ mm}$. In the experiment **b**, cells were additionally exposed to periodic UV flashes (500 ms at $\sim 10 \text{ W/m}^2$, 1500 ms off).

used when limited in number (typically ten flashes).

C.4 Experimental procedures and data analysis

C.4.1 Hele-Shaw liquid chambers assembly

The design of a liquid chamber is illustrated in 5.3. Liquid chambers of different lengths L and heights H were cut in plexiglas plates of constant 2.1 mm thickness with a laser cutting machine in the workshop of the laboratory. Then, two microscope glass slides were glued on the sides with Loctite SuperGlue-3 Glass. A bar was also cut from a plexiglas plate to cover the liquid chamber. Before the experiments, liquid chambers were successively cleaned with ethanol, distilled water and then filled with HSA.

C.4.2 Fluospheres purification

We used stock solutions of blue FluoSpheresTM Polystyrene Microspheres from Thermo Fisher Scientific of diameter $15 \mu\text{m}$, density 1.06 g/cm^3 , and concentration $1 \times 10^6 \text{ beads/mL}$. Micro-algae did not react well to the beads suspension medium, probably because it contains mercury (0.02% of thimerosal, an organomercury compound) (Elbaz et al. 2010). Samples of the stock solution were thus purified in centrifuge microtubes before use. The beads were left sedimenting in centrifuge microtubes and the supernatant was replaced by water. This purification was repeated until 99 % of the medium was replaced.

C.4.3 Main experiments

Main experiments were performed at 5 global cells concentration $c_0/c_{\text{ref}} = \{1, 2, 3, 4, 5\}$ with $c_{\text{ref}} = 3 \times 10^6 \text{ cells/mL}$. Suspensions were concentrated with the procedure described

in appendix A.3.2. Microalgae were then exposed to white light at 2.5 kLux during 30 min before the experiment to get them into condition for swimming away from strong light (see C.2). The green laser maximum light intensity was set to 125 W/m^2 (same green laser diode and polarizers as in 2.2, without diffuser). Then, it was shrunk with an iris diaphragm (total power reduced by $1/4$).

The liquid chamber was placed on the holder (see Figure 5.3.a) in the optical enclosure and filled with algal suspension. The suspension was then seeded with tracer particles and homogenized before the liquid chamber was closed with the plexiglas cover. We turned on the green light beam to start the experiment. Images were recorded using a Nikon D5600 digital camera equipped with a SIGMA macro objective. After a few minutes, a pronounced cells concentration pattern induced by negative phototaxis was visible on the red channel of the images and a pseudo steady state was reached. We then switched to flow field imaging by turning a UV LED on (Thorlabs, SOLIS-365C 365nm) powered by a driver with pulse modulation (Thorlabs, DC2200) to excite the fluorescent passive tracer particles. The UV lamp and the camera were synchronized with Arduino? 6 periodic UV pulses (500 ms on at $\sim \text{W/m}^2$, 1500 ms off) were shot to perform Fluorescent Particle Image Velocimetry. The time step gave a 2 particles apparent diameter displacement at $50 \mu\text{m/s}$.

The same sample of a suspension was only used once. Images and data analysis of concentration fields were treated with Python. Flow fields were calculated with PIVlab on MATLAB and then analysed with Python.

C.4.4 Fluorescent PIV settings

We used PIVlab, a GUI based open source tool developed by Thielicke and Stamhuis 2014 for performing PIV flow analysis with MATLAB. The Figure C.3 shows how the images were enhanced before correlation.

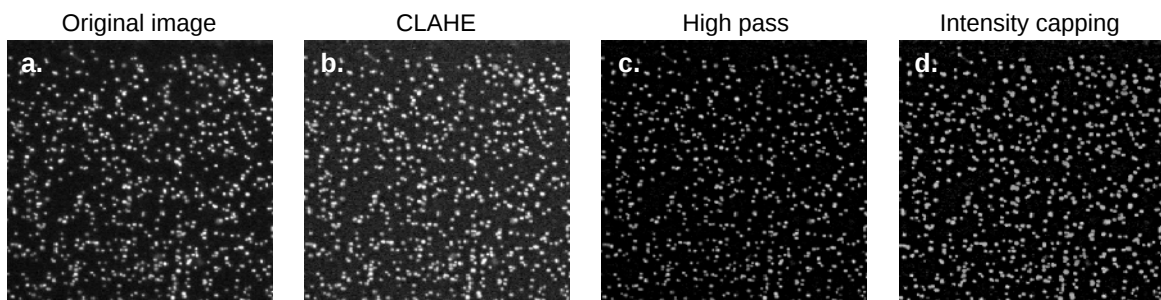


Figure C.3: Pre-processing of the images for PIV. Pre-processing techniques implemented in PIVlab were applied to the chain. **a**, Original image. **b**, CLAHE with a window size of 20 px. **c**, High pass with a kernel size of 50 px. **d**, Intensity capping enabled.

The contrast was enhanced locally with Contrast limited adaptive histogram equalization (CLAHE). A high pass filter was used to conserve most of the particle fluorescence

information and remove background information. Intensity capping prevented brighter spots to contribute statistically more to the correlation signal by adjusting the saturation.

We used the FFT window deformation algorithm which worked with multiple passes and interrogation windows. Three square interrogation windows were in decreasing size order : 256 px, 192 px and 128 px. The large interrogation area gives the better signal-to-noise ratio while the small interrogation area sets the resolution. When excited in UV light, the tracer particles had a fluorescent apparent diameter ~ 4 times larger than their actual diameter, corresponding to 10 px on the blue channel. Their concentration corresponding to ~ 10 particles inside the small interrogation window was $\sim 10^4$ beads/mL. We seeded the algal suspension with 2-3 times this concentration to compensate for sedimentation. The image sequencing was time resolved. Each of the fluorescence images was correlated with the following one : 1-2, 2-3, 3-4, We obtained 5 velocity fields from which one average velocity field was calculated and compared. Velocity field analysis were performed on such averaged velocity fields.

C.5 Additional figures

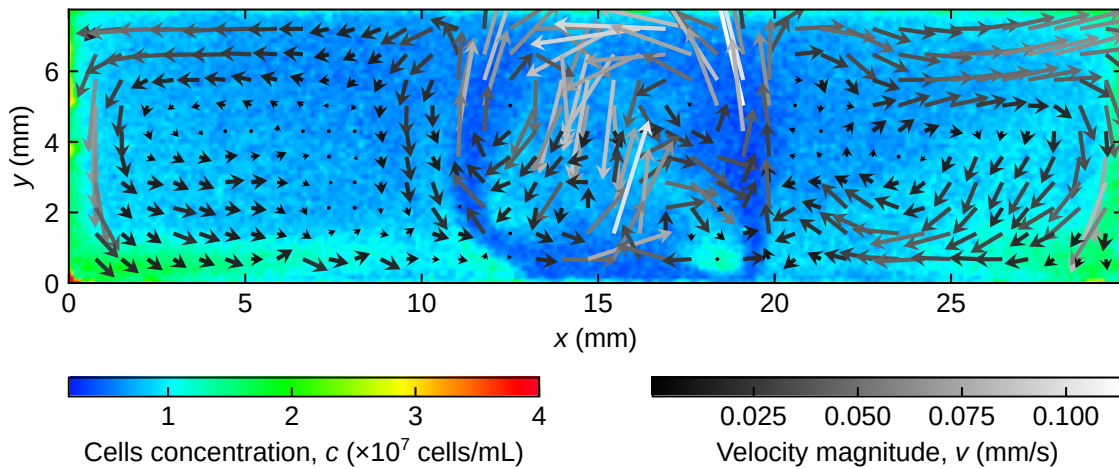


Figure C.4: Velocity and cells concentration fields with mixed phototaxis

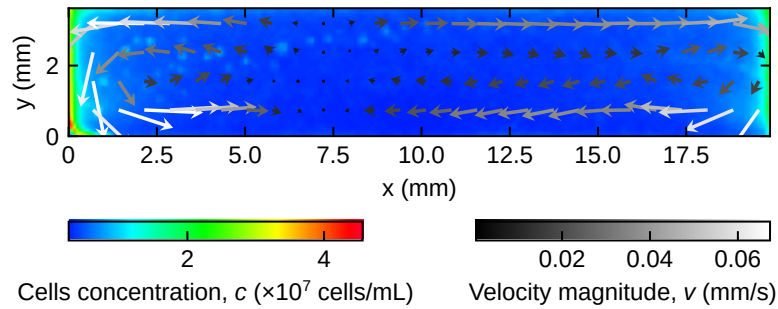


Figure C.5: Superimposition of a highly asymmetric flow field and a quite symmetric concentration field. A quiver plot displays velocity vectors on a colormap of the cells concentration field. The velocity field is highly asymmetric compared to the concentration field. Both cells patterns and convection rolls were measured. On the left side : $L_{\text{pattern}} = 2.4 \pm 0.2$ mm and $L_{\text{roll},1/2} = 4.5 \pm 0.4$ mm. On the right side : $L_{\text{pattern}} = 3.0 \pm 0.2$ mm and $L_{\text{roll},1/2} = 9.3 \pm 0.4$ mm. Parameters : $c_0 = 6 \times 10^6$ cells/mL, $H = 4$ mm, $L = 20$ mm.

Bibliography

- [1] Firoz Alam, Saleh Mobin, and Harun Chowdhury. “Third Generation Biofuel from Algae”. In: *Procedia Engineering* 105 (2015), pp. 763–768.
- [2] Jorge Arrieta et al. “Phototaxis beyond Turning: Persistent Accumulation and Response Acclimation of the Microalga *Chlamydomonas Reinhardtii*”. In: *Sci Rep* 7.1 (2017), p. 3447.
- [3] Jorge Arrieta et al. “Light Control of Localized Photobioconvection”. In: *Phys. Rev. Lett.* 123.15 (2019), p. 158101.
- [4] Thomas J. Böddeker et al. “Dynamic Force Measurements on Swimming *Chlamydomonas* Cells Using Micropipette Force Sensors”. In: *J. R. Soc. Interface.* 17.162 (2020), p. 20190580.
- [5] Barry Bean. “Geotactic Behavior of *Chlamydomonas*”. In: *The Journal of Protozoology* 24.3 (1977), pp. 394–401.
- [6] Max Beckmann and Peter Hegemann. “In Vitro Identification of Rhodopsin in the Green Alga *Chlamydomonas*”. In: *Biochemistry* 30.15 (1991), pp. 3692–3697.
- [7] Laura L Beer et al. “Engineering Algae for Biohydrogen and Biofuel Production”. In: *Current Opinion in Biotechnology* 20.3 (2009), pp. 264–271.
- [8] M. A. Bees. “Nonlinear Pattern Generation by Swimming Micro-Organisms”. University of Leeds, 1996.
- [9] M A Bees and N A Hill. “Wavelengths of Bioconvection Patterns”. In: *Journal of Experimental Biology* 200 (1997), pp. 1515–1526.
- [10] Martin A Bees. “Advances in Bioconvection”. In: *Annu. Rev. Fluid Mech.* 52 (2019), pp. 449–476.
- [11] Rachel R. Bennett and Ramin Golestanian. “A Steering Mechanism for Phototaxis in *Chlamydomonas*”. In: *J. R. Soc. Interface.* 12.104 (2015), p. 20141164.
- [12] Howard C. Berg and Douglas A. Brown. “Chemotaxis in *Escherichia Coli* Analysed by Three-dimensional Tracking”. In: *Nature* 239.5374 (1972), pp. 500–504.
- [13] S. Childress, M. Levandowsky, and E. A. Spiegel. “Pattern Formation in a Suspension of Swimming Microorganisms: Equations and Stability Theory”. In: *J. Fluid Mech.* 69.3 (1975), pp. 591–613.

- [14] Sujeet Kumar Choudhary, Aparna Baskaran, and Purna Sharma. “Reentrant Efficiency of Phototaxis in *Chlamydomonas Reinhardtii* Cells”. In: *Biophysical Journal* 117.8 (2019), pp. 1508–1513.
- [15] Luis Cisneros. “The Organized Melee: Emergence of Collective Behavior in Concentrated Suspensions of Swimming Bacteria and Associated Phenomena”. University of Arizona, 2008.
- [16] Eric Clement et al. “Bacterial Suspensions under Flow”. In: *Eur. Phys. J. Spec. Top.* 225.11-12 (2016), pp. 2389–2406.
- [17] Julien Dervaux, Marina Capellazzi Resta, and Philippe Brunet. “Light-Controlled Flows in Active Fluids”. In: *Nature Phys* 13.3 (2017), pp. 306–312.
- [18] Christopher Dombrowski et al. “Self-Concentration and Large-Scale Coherence in Bacterial Dynamics”. In: *Phys. Rev. Lett.* 93.9 (2004), p. 098103.
- [19] K. Drescher et al. “Fluid Dynamics and Noise in Bacterial Cell-Cell and Cell-Surface Scattering”. In: *Proceedings of the National Academy of Sciences* 108.27 (2011), pp. 10940–10945.
- [20] Knut Drescher et al. “Direct Measurement of the Flow Field around Swimming Microorganisms”. In: *Phys. Rev. Lett.* 105.16 (2010), p. 168101.
- [21] Abdelrahman Elbaz et al. “Mercury-Induced Oxidative Stress and Impact on Antioxidant Enzymes in *Chlamydomonas Reinhardtii*”. In: *Ecotoxicology* 19.7 (2010), pp. 1285–1293.
- [22] Mary Ella Harman Feinleib and George M. Curry. “The Relationship between Stimulus Intensity and Oriented Phototactic Response (Topotaxis) in *Chlamydomonas*”. In: *Physiologia Plantarum* 25.3 (1971), pp. 346–352.
- [23] Kenneth W. Foster and Robert D. Smyth. “Light Antennas in Phototactic Algae”. In: *Microbio rev.* (1980), p. 59.
- [24] Kenneth W. Foster et al. “A Rhodopsin Is the Functional Photoreceptor for Phototaxis in the Unicellular Eukaryote *Chlamydomonas*”. In: *Nature* 311.5988 (1984), pp. 756–759.
- [25] Sean D. Gallaher et al. “*Chlamydomonas* Genome Resource for Laboratory Strains Reveals a Mosaic of Sequence Variation, Identifies True Strain Histories, and Enables Strain-Specific Studies”. In: *Plant Cell* 27.9 (2015), pp. 2335–2352.
- [26] Michaël Garcia. “Hydrodynamique de micro-nageurs”. University of Grenoble, 2013.
- [27] Michaël Garcia et al. “Random Walk of a Swimmer in a Low-Reynolds-number Medium”. In: *Phys. Rev. E* 83.3 (2011), p. 035301.

- [28] Xabel Garcia, Salima Rafai, and Philippe Peyla. “Light Control of the Flow of Phototactic Microswimmer Suspensions”. In: *Phys. Rev. Lett.* 110.13 (2013), p. 138106.
- [29] Andrea Giometto et al. “Generalized Receptor Law Governs Phototaxis in the Phytoplankton *Euglena Gracilis*”. In: *Proc Natl Acad Sci USA* 112.22 (2015), pp. 7045–7050.
- [30] Simon Gluzman, Dmitry A. Karpeev, and Leonid V. Berlyand. “Effective Viscosity of Puller-like Microswimmers: A Renormalization Approach”. In: *J. R. Soc. Interface.* 10.89 (2013), p. 20130720.
- [31] Hartmann Harz and Peter Hegemann. “Rhodopsin-Regulated Calcium Currents in Chlamydomonas”. In: *Nature* 351.6326 (1991), pp. 489–491.
- [32] Yashodhan Hatwalne et al. “Rheology of Active-Particle Suspensions”. In: *Phys. Rev. Lett.* 92.11 (2004), pp. 118101–1–4.
- [33] Selig Hecht, Simon Shlaer, and Maurice Henri Pirene. “Energy, Quanta, and Vision”. In: *Journal of General Physiology* 25.6 (1942), pp. 819–840.
- [34] P. Hegemann, U. Hegemann, and K. W. Foster. “Reversible Bleaching of Chlamydomonas Reinhardtii Rhodopsin in Vivo”. In: *Photochemistry and Photobiology* 48.1 (1988), pp. 123–128.
- [35] Peter Hegemann, Markus Fuhrmann, and Suneel Kateriya. “Algal Sensory Photoreceptors”. In: *Journal of Phycology* (2001), p. 10.
- [36] Peter Hegemann and Wolfgang Marwan. “Single Photons Are Sufficient to Trigger Movement Responses in Chlamydomonas Reinhardtii”. In: *Photochemistry and Photobiology* 48.1 (1988), pp. 99–106.
- [37] N A Hill and T J Pedley. “Bioconvection”. In: *Fluid Dyn. Res.* 37.1 (2005), pp. 1–20.
- [38] N.A. Hill and D.-P. Häder. “A Biased Random Walk Model for the Trajectories of Swimming Micro-organisms”. In: *Journal of Theoretical Biology* 186.4 (1997), pp. 503–526.
- [39] Qingshan Huang et al. “Design of Photobioreactors for Mass Cultivation of Photosynthetic Organisms”. In: *Engineering* 3.3 (2017), pp. 318–329.
- [40] Takahiro Ide et al. “Identification of the Agg1 Mutation Responsible for Negative Phototaxis in a “Wild-Type” Strain of Chlamydomonas Reinhardtii”. In: *Biochemistry and Biophysics Reports* 7 (2016), pp. 379–385.
- [41] Takuji Ishikawa and T. J. Pedley. “The Rheology of a Semi-Dilute Suspension of Swimming Model Micro-Organisms”. In: *J. Fluid Mech.* 588 (2007), pp. 399–435.
- [42] Nahoko Isogai, Ritsu Kamiya, and Kenjiro Yoshimura. “Dominance between the Two Flagella during Phototactic Turning in Chlamydomonas”. In: *Zoological Science* 17.9 (2000), pp. 1261–1266.

- [43] A. Javadi et al. “Photo-Bioconvection: Towards Light Control of Flows in Active Suspensions”. In: *Phil. Trans. R. Soc. A.* 378.2179 (2020), p. 20190523.
- [44] Azusa Kage et al. “The Shape-Effect of Flagella Is More Important than Bottom-Heaviness on Passive Gravitactic Orientation in *Chlamydomonas Reinhardtii*”. In: *Journal of Experimental Biology* (2020), jeb.205989.
- [45] R Kamiya and G B Witman. “Submicromolar Levels of Calcium Control the Balance of Beating between the Two Flagella in Demembrated Models of *Chlamydomonas*.” In: *Journal of Cell Biology* 98.1 (1984), pp. 97–107.
- [46] John O. Kessler. “Hydrodynamic Focusing of Motile Algal Cells”. In: *Nature* 313.5999 (1985), pp. 218–220.
- [47] J. Kompenhans et al. “Particle Image Velocimetry in Aerodynamics: Technology and Applications in Wind Tunnels”. In: *J Vis* 2.3-4 (2000), pp. 229–244.
- [48] Jens Kuhne et al. “Unifying Photocycle Model for Light Adaptation and Temporal Evolution of Cation Conductance in Channelrhodopsin-2”. In: *Proc Natl Acad Sci USA* 116.19 (2019), pp. 9380–9389.
- [49] Eric Lauga and Thomas R Powers. “The Hydrodynamics of Swimming Microorganisms”. In: *Rep. Prog. Phys.* 72.9 (2009), p. 096601.
- [50] Jibuti Levan et al. “Effective Viscosity of a Suspension of Flagellar-Beating Microswimmers: Three-dimensional Modeling”. In: 96.5 (2017), pp. 52–61.
- [51] Peter. S Lovely and F.W. Dahlquist. “Statistical Measures of Bacterial Motility and Chemotaxis”. In: 50 (1975), pp. 477–496.
- [52] Héctor Matías López et al. “Turning Bacteria Suspensions into Superfluids”. In: *Phys. Rev. Lett.* 115.2 (2015), p. 028301.
- [53] Vincent A. Martinez et al. “A Combined Rheometry and Imaging Study of Viscosity Reduction in Bacterial Suspensions”. In: *Proc Natl Acad Sci USA* 117.5 (2020), pp. 2326–2331.
- [54] Teresa M. Mata, António A. Martins, and Nidia. S. Caetano. “Microalgae for Biodiesel Production and Other Applications: A Review”. In: *Renewable and Sustainable Energy Reviews* 14.1 (2010), pp. 217–232.
- [55] Matthias Mussler et al. “Effective Viscosity of Non-Gravitactic *Chlamydomonas Reinhardtii* Microswimmer Suspensions”. In: *EPL* 101.5 (2013), p. 54004.
- [56] Wilhelm Nultsch. “Effect of External Factors on Phototaxis of *Chlamydomonas Reinhardtii*, II. Carbon Dioxide, Oxygen and pH”. In: *Arch. Microbiol.* 112 (1977), pp. 179–185.

- [57] Wilhelm Nultsch. “Effect of External Factors on Phototaxis of *Chlamydomonas Reinhardtii*, III. Cations”. In: *Arch. Microbiol.* 123 (1979), pp. 93–99.
- [58] Jérémie Palacci et al. “Sedimentation and Effective Temperature of Active Colloidal Suspensions”. In: *Phys. Rev. Lett.* 105.8 (2010), p. 088304.
- [59] T J Pedley. “Hydrodynamic Phenomena in Suspensions of Swimming Microorganisms”. In: *Annu. Rev. Fluid Mech.* 24.1 (1992), pp. 313–358.
- [60] T. J. Pedley. “Instability of Uniform Micro-Organism Suspensions Revisited”. In: *J. Fluid Mech.* 647 (2010), pp. 335–359.
- [61] T. J. Pedley and J. O. Kessler. “A New Continuum Model for Suspensions of Gyrotactic Micro-Organisms”. In: *J. Fluid Mech.* 212 (-1 1990), p. 155.
- [62] Timothy J. Pedley, Nicholas A. Hill, and John O. Kessler. “The Growth of Bioconvection Patterns in a Uniform Suspension of Gyrotactic Micro-Organisms.” In: *Journal of fluid mechanics* 195 (1988), pp. 223–237.
- [63] John R. Platt. “”Bioconvection Patterns” in Cultures of Free-Swimming Organisms”. In: *Science* 133.3466 (1961), pp. 1766–1767.
- [64] Milton S. Plesset and Howard Winet. “Bioconvection Patterns in Swimming Microorganism Cultures as an Example of Rayleigh-Taylor Instability”. In: *Nature* 248.5447 (1974), pp. 441–443.
- [65] Marco Polin et al. “*Chlamydomonas* Swims with Two “Gears” in a Eukaryotic Version of Run-and-Tumble Locomotion”. In: *Science* 325.5939 (2009), pp. 487–490.
- [66] E.M. Purcell. “Life at Low Reynolds Number”. In: *Am. J. Phys.* 45 (1976), pp. 3–11.
- [67] Salima Rafai, Levan Jibuti, and Philippe Peyla. “Effective Viscosity of Microswimmer Suspensions”. In: *Phys. Rev. Lett.* 104.9 (2010), p. 098102.
- [68] Osborne Reynolds. “IV. On the Theory of Lubrication and Its Application to Mr. Beauchamp Tower’s Experiments, Including an Experimental Determination of the Viscosity of Olive Oil”. In: *Phil. Trans. R. Soc* 177 (1886), pp. 157–234.
- [69] U. Ruffer and W. Nultsch. “High-Speed Cinematographic Analysis of the Movement of *Chlamydomonas*”. In: *Cell Motility* 5.3 (1985), pp. 251–263.
- [70] Ursula Ruffer and Wilhelm Nultsch. “Flagellar Photoresponses of *Chlamydomonas* Cells Held on Micropipettes: II. Change in Flagellar Beat Pattern: Flagellar Beat Pattern Change in *Chlamydomonas*”. In: *Cell Motil. Cytoskeleton* 18.4 (1991), pp. 269–278.
- [71] A. M. Roberts. “Mechanisms of Gravitaxis in *Chlamydomonas*”. In: *The Biological Bulletin* 210.2 (2006), pp. 78–80.

- [72] K. Schaller, R. David, and R. Uhl. “How Chlamydomonas Keeps Track of the Light Once It Has Reached the Right Phototactic Orientation”. In: *Biophysical Journal* 73.3 (1997), pp. 1562–1572.
- [73] Klaus Schaller and Rainer Uhl. “A Microspectrophotometric Study of the Shielding Properties of Eyespot and Cell Body in Chlamydomonas”. In: *Biophysical Journal* 73 (1997), p. 6.
- [74] A. Sokolov et al. “Swimming Bacteria Power Microscopic Gears”. In: *Proceedings of the National Academy of Sciences* 107.3 (2010), pp. 969–974.
- [75] Andrey Sokolov and Igor S. Aranson. “Reduction of Viscosity in Suspension of Swimming Bacteria”. In: *Phys. Rev. Lett.* 103.14 (2009), p. 148101.
- [76] T. Sommer et al. “Bacteria-Induced Mixing in Natural Waters: Bacteria Induced Mixing in Natural Waters”. In: *Geophys. Res. Lett.* 44.18 (2017), pp. 9424–9432.
- [77] Robert L. Stavis and Rona Hirschberg. “Phototaxis in *Chlamydomonas Reinhardtii*”. In: *The Journal of Cell Biology* 59.2 (1973), pp. 367–377.
- [78] Tetsuo Takahashi and Masakatsu Watanabe. “Photosynthesis Modulates the Sign of Phototaxis of Wild-Type *Chlamydomonas Reinhardtii*: Effects of Red Background Illumination and 3-(3',4'-Dichlorophenyl)-1,1-Dimethylurea”. In: *FEBS Letters* 336.3 (1993), pp. 516–520.
- [79] William Thielicke and Eize J. Stamhuis. “PIVlab – Towards User-friendly, Affordable and Accurate Digital Particle Image Velocimetry in MATLAB”. In: *Journal of Open Research Software* 2 (2014).
- [80] Noriko Ueki et al. “Eyespot-Dependent Determination of the Phototactic Sign in *Chlamydomonas Reinhardtii*”. In: *Proc Natl Acad Sci USA* 113.19 (2016), pp. 5299–5304.
- [81] Harold Wager. “On the Effect of Gravity upon the Movements and Aggregation of Euglena Viridis, Ehrb., and Other Micro-Organisms”. In: *Philos. Trans. R. Soc. Lond.* 201.274-281 (1911), pp. 333–390.
- [82] Nicolas Waisbord et al. “Destabilization of a Flow Focused Suspension of Magnetotactic Bacteria”. In: *Phys. Rev. Fluids* 1.5 (2016), p. 053203.
- [83] K.-i. Wakabayashi et al. “Reduction-Oxidation Poise Regulates the Sign of Phototaxis in *Chlamydomonas Reinhardtii*”. In: *Proceedings of the National Academy of Sciences* 108.27 (2011), pp. 11280–11284.
- [84] H. H. Wensink et al. “Meso-Scale Turbulence in Living Fluids”. In: *Proceedings of the National Academy of Sciences* 109.36 (2012), pp. 14308–14313.
- [85] C. R. Williams and M. A. Bees. “A Tale of Three Taxes: Photo-Gyro-Gravitactic Bioconvection”. In: *Journal of Experimental Biology* 214.14 (2011), pp. 2398–2408.

- [86] C. R. Williams and M. A. Bees. “Photo-Gyrotactic Bioconvection”. In: *J. Fluid Mech.* 678 (2011), pp. 41–86.
- [87] Xiao-Lun Wu and Albert Libchaber. “Particle Diffusion in a Quasi-Two-Dimensional Bacterial Bath”. In: *Phys. Rev. Lett.* 84.13 (2000), pp. 3017–3020.
- [88] Yukio Yamamoto et al. “Relation of Pattern Formation to External Conditions in the Flagellate, *Chlamydomonas Reinhardtii*”. In: *Europ. J. Protistol.* 28.4 (1992), pp. 415–420.